Properties and Hydrogen Atom Transfer Reactivity of Copper(III)-Hydroxide Complexes

A Dissertation

SUBMITTED TO THE FACULTY OF

UNIVERSITY OF MINNESOTA

BY

Debanjan Dhar

IN PARTIAL FULFILLMENT OF THE REQUIREMENTS

FOR THE DEGREE OF

DOCTOR OF PHILOSOPHY

William B. Tolman, Advisor

January, 2018

© Debanjan Dhar, 2018

Acknowledgements

I'm indebted to all of the professors at the University of Minnesota (Prof. Andrew Taton, Prof. Kent. Mann, Prof. Andreas Stein, Prof. John Ellis, Prof. Connie Lu and Dr. Victor Young), who have taken the time to teach and guide me over the past five years. I am thankful to Prof. Lawrence Que, Prof. John Lipscomb and Prof. Ian Tonks for agreeing to be my thesis committee memebers and providing me with helpful suggestions. I would like to thank all the non-teaching and technical staff at the Department of Chemistry for their help.

I'm especially grateful to my advisor and mentor, Prof. William B. Tolman, who has played an instrumental role in my development as a chemist and independent researcher. Bill, you have always been there to guide me and lend support when needed. I am particulalrly thankful to you for the scientific freedom that you have provided with regards to taking intellectual ownership of my research projects, and I believe this has been pivotal in my growth as a scientist. You have been an excellent role model and I have learnt a lot from you, both scientifically and professionally. I sincerely thank you for providing me with the opportunity of working with you and instilling in me the importance of scientific communication and professionalism.

I am thankful to all my previous teachers at Presidency College (Kolkata) and Indian Institute of Technology Kanpur for their intergral role in my development as a chemist. I am particulalrly thankful to my M.Sc. thesis advisor, Prof. R. N. Mukherjee, without whose support and guidance I would not be where I am now.

I'm extremely grateful to all of my lab mates in the Tolman group, past and present for being amazing cohorts. It has been an absolute pleasure working alongside all of you. I would like to especially thank all the members in the Tolman group who have

collaborated with me to some extent during my tenure (Hongtu Zhang, Dr. David Boyce, Dr. Andrew Spaeth, Dr. Benjamin Neisen and Nicole Gagnon). I would like to take this opportunity to particularly thank Dr. Gereon Yee, with whom I have worked very closely. Some of the work presented in this thesis (Chapter 4 and parts of Chapter 2) was done in very close collaboration with him. Gereon, you have been an amazing partner in crime and I have thoroughly enjoyed working with you. I feel that working alongside you has helped me grow as a researcher and I admire your dedication, work ethic, scientific curiosity and enthusiasm. I would also like to take this opportunity to thank my collaborators Prof. Chrisopher Cramer, Prof. James Mayer, Büsra Dereli, Dr. Mohammadreza Momenitaheri and Dr. Todd Markle for their help and scientific support.

I am and will be ever indebted to all my family members, particularly my mother, uncle and father for their constant encouragement and support. This would never have been possible without you. I am also thankful to Sukanya for being extremely patient with me over the last one year. Words cannot express my gratitude towards my friends, both near and far. They have always stood by me through thick and thin and have been there to cheer me up and encourage me when things looked gloomy.

Dedicated to everyone who made this possible,

particularly my Mother for being my constant source of inspiration.

Abstract

The conversion of C-H bonds in hydrocarbons to C-O bonds is one of the grand challenges in chemistry as it involves the energy demanding preliminary step of removing a hydrogen atom from the strong C-H bond via an initial hydrogen atom transfer step. A number of high-valent reactive transition metal-oxygen species are proposed to be the key intermediates that perform such hydrogen atom transfer reactions in biological and synthetic systems. The mononuclear copper(III)-hydroxide unit has been demonstrated to be a potent reactive species in this regard. The work in this thesis is focused on the chemistry of such synthetic mononuclear copper(III)-hydroxide cores generated using strongly electron donating pyridine di-carboxamido based ligand scaffolds. In particular the spectroscopic properties and hydrogen atom transfer reactivity of a series of such copper(III)-hydroxide complexes is explored in the light of the well established proton-coupled-electron transfer theory. The effects of ligand electronic perturbations on the properties and reactivity patterns of these compounds is explored through detailed spectroscopic and mechanistic invetsigations, with the ultimate aim of elucidating the intrinsic factors that contribute to the high efficiency of such species as hydrogen atom transfer reagents. A key conclusion from all of these studies is that the thermodynamic driving force plays a crucial role in determining the rates and mechanism of such hydrogen atom transfer reactions, and that a systematic tuning of the supporting ligand electronics modulates these intrinsic thermodynamic driving forces.

Table of Contents

List of Tables viii

List of Figures and Schemes x

Chapter 1 : Metal-Oxygen Complexes and Their Role in Hydrogen Atom Transfer 1

1.1. Introduction 1

1.2. Previous studies on the mononuclear copper(III)-hydroxide $[CuOH]^{2+}$ core 3

1.3. Hydrogen atom transfer 6

1.3.1. Thermodynamics of HAT reactions 8

1.3.2. Influence of HAT thermodynamics on the rates of HAT reactions 10

1.3.3. Mechanistic implications of the thermodynamics of HAT reactions 12

1.4. Hydrogen atom transfer from C-H bonds by high-valent metal-oxo/hydroxo complexes 14

1.5. Research objectives 20

Chapter 2 : Thermodynamics and Kinetics of Hydrogen Atom Transfer From Hydrocrabons by Copper(III)-Hydroxide Cores 24

2.1. Introduction 24

2.2. Evaluation of HAT therodynamics via determination of O-H BDE in copper(II)-aqua complex ($LCuOH_2$) 27

2.2.1. Determination of $pK_{a(1)}$ 28

2.2.1.1.Experimental evaluation of the ligand exchange equilibrium using different spectroscopic methods 29

2.2.1.2. Determination of the pK_a of the $LCuOH_2$ by using the composite equilibrium analysis 33

2.2.2. Determination of $E°_{(1)}$ 34

2.2.3. Determination of the O-H BDE in the $LCuOH_2$ and implications of the determined HAT thermodynamic parameters 37

2.3. Kinetics of Hydrogen atom transfer from hydrocarbons performed by LCuOH 38

2.3.1. Reactivity of LCuOH with THF 38

2.3.2. Reactivity of LCuOH with a range of hydrocarbons and interdependence between the rates of HAT and thermodynamic driving forces 43

2.3.3. Role of quantum mechanical tunneling in HAT reactions with DHA 47

2.4. Effects of ligand electronic perturbations on the $[CuOH]^{2+}$ core 49
2.4.1. Spectroscopic manifestations of the ligand electronic perturbations 50
2.4.1.1. Spectroscopic characterization of copper(II)-hydroxide complexes 50
2.4.1.2. Spectroscopic characterization of the copper(III)-hydroxide complexes 52
2.4.2. Effects of ligand electronic perturbations on the thermodynamics and kinetics of HAT for the copper(III)-hydroxide complexes 54
2.5. Summary and conclusions 55
2.6. Experimetal section 57

Chapter 3 : Effects of Anionic Substituents on the Properties of the Copper(III)-Hydroxide Core 64
3.1. Introduction 64
3.2. Synthesis and Characterization of the ligand $[i\text{Pr}_2\text{EtNH}]_2[^{SO3}\text{LH}_2]$ 67
3.3. Synthesis and structural characterization of copper(II) complexes 70
3.3.1. Synthesis of the copper(II)-hydroxide complex 70
3.3.2. X-ray crystallographic characterization of the copper(II)-hydroxide complex 71
3.3.3. Synthesis and structural characterization of other copper(II)-complexes 76
3.3.3.1. A sulfonato bridged dimer: $[(Et_4N)_2(^{SO3}\text{LCu})]_2$ 76
3.3.3.2. $[Na(15\text{-crown-}5)]_3[^{SO3}\text{LCuCl}]$ 77
3.4. Spectroscopic studies on $[K(18\text{-C-}6)]_3[^{SO3}\text{LCuOH}]$ 79
3.4.1. UV-vis absorption spectroscopy 80
3.4.2. EPR spectroscopy 81
3.4.3. Electrochemical measurements 84
3.5. Characterization of $[CuOH]^{2+}$ complexes 86
3.6. Evaluation of HAT thermodynamics via determination of the O-H BDE in the copper(II)-aqua complex $[^{SO3}\text{LCuOH}_2]^{2-}$ 88
3.6.1. Determination of O-H BDE via cross HAT experiments between LCuOH_2 and $[K(18\text{-C-}6)]_2[^{SO3}\text{LCuOH}]$ 88
3.6.2. Determination of the O-H BDFE (Bond Dissociation Free Energy) in water through the determination of the basicity and redox potential of $[K(18\text{-C-}6)]_3[^{SO3}\text{LCuOH}]$ 92
3.7. Kinetics of HAT from 9,10-dihydroantracene (DHA) performed by $[CuOH]^{2+}$ 95
3.8. Summary and conclusions 98
3.9. Experimental section 99

Chapter 4 : A Mechanistic Dichotomy in Reactions of the Copper(III)-Hydroxide Unit with Phenols **107**
4.1. Introduction 107
4.2. Stopped-flow kinetics experiments 111
4.2.1. Overview of experimental setup and kinetic workup 111
4.2.2. Reactions of LCuOH with ^{X}ArOH 112
4.2.3. Reactions of ^{NO2}LCuOH with ^{X}ArOH 124
4.2.4. Implication of the rates of reaction of LCuOH and ^{NO2}LCuOH with ^{X}ArOH 127
4.3. Analysis of products for reactions with ^{X}ArOH with X = NMe_2, OMe, Me, H, and Cl 128
4.4. Analysis of Products for Reactions with ^{X}ArOH with X = NO_2 and CF_3 132
4.5. Evidence for a PT Mediated Pathway 136
4.5.1. Identification of $[LCu(OH_2)]^+$ as an intermediate in reactions of LCuOH with ^{X}ArOH (X = NO_2 or CF_3) 137
4.5.2. Linear free energy relationships and thermodynamic arguments 144
4.6. Summary and conclusions 151
4.7. Experimental section 152

Chapter 5 : Targeting Mononuclear Copper(III)-Phenolate Complexes **164**
5.1. Introduction 164
5.2. Synthesis and characterization of copper(II)-phenolate complexes 167
5.2.1. Synthesis and structural characterization 167
5.2.2. Spectroscopic characterization of the copper(II)-phenolate complexes 171
5.2.2.1. UV-vis absorption spectroscopy 171
5.2.2.2. EPR spectroscopy 172
5.2.2.3. Cyclic voltammetry 176
5.3. Characterization of the corresponding one-electron oxidized complexes of the copper(II)-phenolate compounds 178
5.3.1. UV-vis absorption spectroscopy 179
5.3.1.1. One-electron oxidation of $[Bu_4N]$[**1a**] 179
5.3.1.2. One-electron oxidation of $[Et_4N]$[**1b-c**] 180
5.3.1.3. One-electron oxidation of $[Bu_4N]$[**1d**] 182
5.3.2. EPR spectroscopy 183
5.3.3. Resonance Raman spectroscopy 184
5.4. Summary and conclusions 186
5.5. Experimental section 187

References **193**

List of Tables

Table 1.1. Summary of HAT parameters from DHA for selected high-valent metal-oxo/hydroxo complexes (Data adapted from Ref 33). ***16***

Table 2.1. EPR spectral simulation parameters for LCu(THF) in anhydrous and H_2O saturated THF. ***31***

Table 2.2. The ligand exchange equilibrium constant values as determined from simulation of the cyclic voltammograms at different titration points. ***32***

Table 2.3. Scan rate dependence of relevant electrochemical parameters for the copper(III/II)-hydroxide couple in THF solvent. ***35***

Table 2.4. Scan rate dependence of relevant electrochemical parameters for the copper(III/II)-hydroxide couple in DFB solvent. ***37***

Table 2.5. The rate constants of C-(H/D) activation from solvent obtained from electrochemical simulations. ***41***

Table 2.6. The second order HAT rate constants for reactions between LCuOH and a series of hydrocarbon substrates. ***44***

Table 2.7. Experimental (from spectral fitting) vs. predicted Cu Hyperfine Coupling Constants (HFCC's) along with Mulliken spin population analysis. ***52***

Table 2.8. Summary of selected properties of $[CuOH]^{2+}$ complexes. ***54***

Table 3.1. Selected interatomic distances (Å) for Cu(II) Complexes. ***73***

Table 3.2. g-values for EPR spectra of $[CuOH]^{+}$ complexes. ***83***

Table 3.3. Hyperfine Parameters for Cu, N(amide), and N(pyridine/piperidine) Nuclei (MHz). ***83***

Table 4.1. Thermodynamic properties of *para*-subsituted phenols ^{X}ArOH. ***111***

Table 4.2. Second-order rate constants for pseudo first-order reactions of LCuOH with ^{X}ArOH. ***113***

Table 4.3. Second-order rate constants for stoichiometric reactions of LCuOH with ^{X}ArOH determined from initial rates. ***122***

Table 4.4. Second-order rate constants for stoichiometric reactions of ^{NO2}LCuOH with ^{X}ArOH determined from initial rates ***125***

Table 4.5. Second-order rate constants (*k*) for the reactions of LCuOH and ^{NO2}LCuOH with ^{X}ArOH at –80 ºC. ***128***

Table 4.6. . Hydrogen bond donor activities of the phenols used in this study. ***145***

Table 4.7. Second-order rate constants (*k*) for the reactions of LCuOH and ^{NO2}LCuOH with ^{X}ArOH at –80 ºC, converted from THF to DMSO. ***145***

Table 5.1. Structural parameters for the compounds [Bu_4N][**1a**], [Et_4N][**1b**], [Et_4N][**1c**] and [Bu_4N][**1d**]. ***171***

Table 5.2. Simulated g-values for EPR spectra of corresponding copper complexes [R'$_4$N][**1a-d**] ***173***

Table 5.3. Simulated hyperfine parameters^{a} for Cu, amido N (N_{am}), and pyridyl N (N_{py}) nuclei for complexes [R'$_4$N][**1a-d**]. ***174***

Table 5.4. Redox potential for the 1 electron oxidation of [R'$_4$N**][1a-d**] and the redox potential for the one-electron oxidation of the corresponding free phenolate species. ***177***

Table 5.5. Relevant vibrational frequencies in the Resonance Raman spectra (in cm^{-1}) and the proposed assignments for the corresponding vibrations. ***185***

List of Figures and Schemes

Figure 1.1. $[CuOH]^{2+}$ core supported by a pyridine dicarboxamide ligand framework ***2***

Figure 1.2. (Left) Cyclic voltammogram, displaying the reversible $[LCuOH]/[LCuOH]^{-}$ redox couple. (Right) Low temperature UV-vis spectra of $Bu_4N[LCuOH]$ (blue, dashed trace) and upon addition of 1 eq. of $[Fc]PF_6$ (black trace). Inset displays the oxidized (purple) and reduced reaction solutions (light blue). Reprinted with permission from Ref 8. Copyright 2011, American Chemical Society ***4***

Scheme 1.1. HAT reaction between DHA and LCuOH, producing anthracene and $LCuOH_2$ as the corresponding reaction products. ***5***

Figure 1.3. Generic square scheme depicting the HAT/CPET reaction between the two reactants X-H and $Y^{\bullet}$ ***7***

Figure 1.4. The thermodynamic square scheme for a HAT reagent X-H. ***8***

Figure 1.5. (Left) Linear correlation between rates of HAT and BDE of the formed O-H bond, between DHA and a series of H-atom acceptors including organic radicals and manganese complexes, where L_2 is phenanthroline. (Right) Linear correlation between HAT rates and ΔH for reactions of $[Bu_4N][MnO_4]$ with a range of substrates. Adapted with permission from Ref 22b. ***11***

Figure 1.6. (Top) HAT reaction between DHA and the iron(III)bis-imidazoline complex $[Fe^{III}Hbim]^{2+}$, where the other ligands are the bidentate neutral H_2bim. (Bottom) The thermodynamic parameters in the square scheme for the two reactants participating in the HAT reaction. Data adapted from Ref 28. ***12***

Figure 1.7. The HAT square scheme for metal-oxo/hydroxo complexes denoting the key thermodynamic parameters. ***16***

Figure 1.8. Potential energy curves along with the corresponding Arrhenius plots displaying characteristics of semi-classical (top) barrier crossing as well as the semi-classical case with a tunneling correction (bottom). Adapted from Ref 35b. ***18***

Figure 1.9. Experimental and computationally predicted trends of rates for HAT reactions from DHA with a series of Fe(IV)-oxo complexes, $[Fe^{IV}(O)(TMC)(L_{ax})]^{z+}$ (z =1,2). Adapted with permission from Ref 37a. ***19***

Figure 1.10. Targeted complex using pendant anionic sulfonate groups on the ligand backbone ***21***

Figure 1.11. Reaction of LCuOH with a series of *para* substituted phenols. ***22***

Figure 1.12. Oxidation chemistry of copper(II)-phenolate complexes targeted. ***23***

Figure 2.1. The reported mononuclear copper(III)-hydroxide complex along with the corresponding HAT reaction performed with DHA. ***25***

Figure 2.2. The PCET square scheme for LCuOH showing all involved components and the corresponding thermodynamic parameters. ***27***

Figure 2.3. Representation of the X-ray crystal structure of LCu(THF), showing all non-hydrogen atoms as 50% thermal ellipsoids. Selected interatomic distances (Å) and angles (deg): Cu1-N1, 1.883(13); Cu1-N2, 1.947(14); Cu1-N3, 1.948(11); Cu1-O3, 1.974(11); N1-Cu1-N2, 81.9(5); N1-Cu1-N3, 81.1(6); N2-Cu1-N3, 162.5(5); N1-Cu1-O3, 171.4(6); N2-Cu1-O3, 99.9(5); N3-Cu1-O3, 97.5(5). ***28***

Figure 2.4. (Left) UV-vis spectroscopic changes observed upon addition of increasing amounts of H_2O to solution of LCu(THF) in THF (1 mM, green), culminating in the red spectrum (540 eq. H_2O added). (Right) Representative multicomponent deconvolution of an intermediate equilibrium spectrum depicting the two components of LCu(THF) in green and $LCuOH_2$ in red. The experimental spectrum is depicted by the black dashed trace and the overall modeled spectrum by the navy trace. ***30***

Figure 2.5. (Left) X-band EPR spectra of LCu(THF) in anhydrous THF (green), and LCu(THF) in THF saturated with H_2O (red), recorded at 125K, 9.3863 GHz. The brackets highlight the differences between the spectra in the $g_{||}$ region. (Right) Experimental (black) and simulated (red) spectra for the two cases depicted at the top and bottom respectively. Reprinted with permission from Ref 13. Copyright 2015, American Chemical Society. ***31***

Figure 2.6. (Left) Cyclic voltammograms of LCu(THF) in anhydrous THF (green, bottom) and in the presence of variable amounts of added H_2O, culminating in a wave assigned to $LCu(H_2O)$ (red, top). Conditions: THF, 0.2 M $TBAPF_6$, 200 mV/s. (Right) Representative overlays of the experimental and simulated cyclic voltammograms at different titration points with the experimental spectra depicted as a black trace and the simulated spectra depicted as a red trace. ***33***

Figure 2.7. (Left) UV-vis spectroscopic changes observed upon addition of increasing amounts of $[Et_3NH]OTf$ to solution of $[Bu_4N][LCuOH]$ in THF (1 mM, navy), culminating in the green spectrum for LCu(THF). (Right) Representative multicomponent deconvolution of an intermediate equilibrium spectrum depicting the two components of LCu(THF) in green and $[Bu_4N][LCuOH]$ in navy. The experimental spectrum is depicted by the black dashed trace and the overall modeled spectrum by the red trace. . ***34***

Figure 2.8. (Left) Scan rate normalized cyclic voltammograms depicting the first oxidation event for $[Bu_4N][LCuOH]$ in THF. Conditions: 0.3 M $[Bu_4N][PF_6]$, 20 °C. (Right) Cyclic voltammogram of the same complex across a wider potential sweep at a scan rate of 1 V/s. Conditions: 0.3 M $[Bu_4N][PF_6]$, 20 °C. ***35***

Figure 2.9. Scan rate normalized cyclic voltammograms for $[Bu_4N][LCuOH]$ in 1,2-DFB solvent. Conditions: 0.3 M $[Bu_4N][PF_6]$, 20 °C. ***36***

Figure 2.10. Cyclic voltammograms of $[Bu_4N][LCuOH]$ in THF (black, 200 mV/s) overlaid with one at higher scan rate (left, red, 1000 mV/s) or at same scan rate in THF-d_8 (right, red, 200 mV/s). Conditions: 0.3 M $TBAPF_6$, 20 °C. Reprinted with permission from Ref 13.Copyright 2015, American Chemical Society. ***39***

Figure 2.11. Representative experimental (black) and simulated (red) cyclic voltammograms of $[Bu_4N][LCuOH]$ in THF (top) at two different scan rates of 100 mV/s (left) and 500 mV/s (right), and in THF-d_8 (bottom) at two different scan rates of 100 mV/s (left) and 300 mV/s (right). Conditions : 1 mM analyte, 0.3 M $TBAPF_6$, 20 °C. Reprinted with permission from Ref 13. Copyright 2015, American Chemical Society. ***40***

Figure 2.12. Plot of reaction rate vs. $[THF]_0$ for the reaction of LCuOH with THF in DFB. The red trace is a fit to eq. 2.8 (R^2 = 0.9925), yielding K_{eq} = 0.1688 M^{-1} and k_3 = 0.0371 s^{-1}. . ***42***

Figure 2.13. The two plausible pathways of HAT from THF which are consistent with a saturation kinetics.Reprinted with permission from Ref 13. Copyright 2015, American Chemical Society. ***43***

Figure 2.14. Plots of k_{obs} vs. [substrate] for the reactions of LCuOH with the substrates in DFB at -25 °C. The second order rate constants k_2 were determined from the slopes of the indicated linear fits (R^2 = 0.9816, 0.9821, 0.9625, 0.9602, 0.9773, and 0.9871, respectively) ***45***

Figure 2.15. Plot of log *k* (where *k* is the second order rate constant k_2 or k_3K_{eq}) vs. BDE for the reaction of LCuOH with the indicated substrates. The linear fit depicted in red has a $R^2 = 0.9264$. ***46***

Figure 2.16. Plot of log *k* (where *k* is the second order rate constant k_2 or k_3K_{eq}) vs. pK_a (left) and $E_{1/2}$ (right) of the different hydrocarbon substrates used for HAT reactions with LCuOH. ***47***

Figure 2.17. (Left) Eyring plots of ln(*k*/T) vs. 1/T with linear least square fits to the data for reactions of LCu(OH) (black circles with DHA (solid line) or DHA-d_4 (dashed line) in CH_2Cl_2. (Right) (a) Representative optimized HAT TS structure for LCuOH. Dotted lines indicate the forming and breaking O-H and C-H bonds, respectively. Atoms are copper (green), nitrogen (blue), oxygen (red), carbon (grey), and hydrogen (white). (b) A drawing emphasizing the forming and breaking O-H and C-H bonds, with calculated interatomic distances indicated. Adapted with permission from Ref 14. Copyright 2016, American Chemical Society. ***48***

Figure 2.18. The two electronic variants of LCuOH. ***50***

Figure 2.19. (Left) Cyclic Voltammograms of $[Bu_4N][^{pipMe}LCuOH]$ (red dash trace), $[Bu_4N][LCuOH]$(black solid trace) and $[Et_4N][^{NO2}LCuOH]$ (blue dotted trace) in 1,2-DFB solvent, Conditions : 0.3 M $[Bu_4N][PF_6]$, 20 °C, Scan rate of 50 mV/s. (Right) X-band EPR spectra THF frozen solutions of $[Bu_4N][^{pipMe}LCuOH]$ (red), $[Bu_4N][LCuOH]$(black) and $[Et_4N][^{NO2}LCuOH]$ (blue) depicting the respective Cu-hyperfine splitting constants. ***51***

Figure 2.20. UV-Vis spectra for $^{pipMe}LCuOH$ (red dash trace), LCuOH (black solid trace) and $^{NO2}LCuOH$ (blue dotted trace) in 1,2-DFB solvent at -25 °C. ***53***

Figure 2.21. Combined plot of log(*k*) vs. Δ*H* for reactions of $^{NO2}LCuOH$ (blue), LCuOH (black), and $^{pipMe}LCuOH$ (red) with DHA (filled circle), cyclohexene (open circle), diphenylmethane (filled square), toluene (filled star), THF (open square), and cyclohexane (open star). ***55***

Figure 2.22. Proposed tautomerization between $[CuO]^{+}$ and $[CuOH]^{2+}$ unit within the active site of LPMO that involves deprotonation of the amino terminus of the 'histidine brace" concomitant with a protonation of the $[CuO]^{+}$ to yield a $[CuOH]^{2+}$ core. ***56***

Figure 3.1. Previously studied copper(III)-hydroxide complexes. ***65***

Figure 3.2. New copper complex targeted in the current study. ***66***

Scheme 3.1. Synthesis of the ligand $[(i\text{Pr}_2\text{EtNH})_2(^{SO3}\text{LH}_2)]$. ***68***

Figure 3.3. ^{1}H-NMR (400 MHz) spectrum of $((i\text{Pr})_2\text{EtNH})_2(^{SO3}\text{LH}_2)$. (*solvent residual signal in D_2O). ***69***

Figure 3.4. The X-ray structure of the ligand $[(i\text{Pr}_2\text{EtNH})_2(^{SO3}\text{LH}_2)]$ depicting the presence of the two ammonium counter cations, with the inset showing the H-bond interaction (dotted bond) between the acidic proton on the ammonium and the oxygen atom of the sulfonate. Key H-bonding parameters between the donor an acceptor (N-H : 0.98 Å, H-O : 1.85 Å, N-O : 2.816 Å, and N-H-O bond angle : 166.6°). ***70***

Scheme 3.2. Synthesis of the copper(II)-hydroxide complex $[K(18\text{-C-}6)]_3[^{SO3}\text{LCuOH}]$ ***70***

Figure 3.5. (Top) X-ray crystal structure of $[K(18\text{-C-}6)]_3[^{SO3}\text{LCuOH}]$ with non-hydrogen atoms depicted at 50% thermal ellipsoids. (Bottom) The coordination polymer network in the solid state structure depicting the repeating units (faded) and the key coordinating components (highlighted). ***72***

Figure 3.6. (Top) X-ray structure of anionic component of [K(Krptofix-222)]$_3$[^{SO3}LCuOH] with non-hydrogen atoms depicted at 50% thermal ellipsoids (counter ions are omitted for clarity). (Bottom) Depiction of secondary sphere interaction between a disordered K^{+} (which is not encapsulated completely by the cryptand cavity) with one of the counter-ions and one sulfonate group on the ligand. ***75***

Figure 3.7. (Top) Chemical structure of $[(Et_4N)_2(^{SO3}\text{LCu})]_2$. (Bottom) X-ray structure of $[(Et_4N)_2(^{SO3}\text{LCu})]_2$ depicting non-hydrogen atoms at 50% thermal ellipsoids (counter ions are omitted for clarity). Selected bond distances in Å (standard deviation in parenthesis) Cu1-N1: 1.927(3), Cu1-O3: 1.944(2) Cu1-N2: 1.994(2), Cu1-N3: 1.995(2), S1-O4: 1.440(3), S1-O5: 1.443(3), S1-O3: 1.484(2). ***77***

Figure 3.8. The X-ray structure of $[Na(15\text{-}C\text{-}5)]_3[^{SO3}LCuCl]$ depicting the repeating unit (top) and the coordination polymer chain (bottom) with non-hydrogen atoms depicted at 50% thermal ellipsoids. ***79***

Figure 3.9. (Left) UV-Vis spectra of $[K(18\text{-}C\text{-}6)]_3[^{SO3}LCuOH]$ (blue trace), $[K(18\text{-}C\text{-}6)]_3[^{SO3}LCuOH]$ in the presence of 100 eq [Na(15-C-5)]OTf (red trace), and $[Bu_4N][LCuOH]$ (black dashed trace). Conditions : 1,2-DFB solvent 25 °C. (Right) UV-vis spectra of $[K(18\text{-}C\text{-}6)]_3[^{SO3}LCuOH]$ of in water recorded at 25 °C. ***80***

Figure 3.10. EPR signal for $[K(18\text{-}C\text{-}6)]_3[^{SO3}LCuOH]$ in 1,2-DFB solvent recorded at 30 K (black trace represents the experimental spectrum, red trace represents the simulated spectrum). ***82***

Figure 3.11.Comparison of the EPR spectra of $[K(18\text{-}C\text{-}6)]_3[^{SO3}LCuOH]$ in the absence (black trace) and presence of 100 eq of [Na(15-C-5)]OTf (blue trace).The dashed line shows the increase in the Cu-hyperfine coupling along the z-direction for the latter. ***82***

Figure 3.12. EPR spectrum of $[K(18\text{-}C\text{-}6)]_3[^{SO3}LCuOH]$ in water (blue trace) and 1,2-DFB (black trace). ***84***

Figure 3.13. (Left) Scan rate normalized Cyclic voltammograms of $[K(18\text{-}C\text{-}6)]_3[^{SO3}LCuOH]$ recorded in 1,2-DFB solvent using 0.3 M $[Bu_4N]PF_6$ as the supporting electrolyte. (Right) Overlay of the Cyclic vaoltammograms of $[K(18\text{-}C\text{-}6)]_3[^{SO3}LCuOH]$ in the absence (black trace) and presence of 100 eq. [Na(15-C-5)]OTf (red trace). There is an anodic shift of ~180 mV in the $E_{1/2}$ that is observed. ***85***

Figure 3.14. (Left) UV-Vis spectrum obtained upon the oxidation of $[K(18\text{-}C\text{-}6)]_3[^{SO3}LCuOH]$ (blue trace). The UV-Vis absorption feture for [LCuOH] is depicted as the black dashed trace for comparison. (Right) Titration curve with oxidant, revealing a 1:1 reaction stoichiometry. ... ***87***

Figure 3.15. Overlay showing the difference in the LMCT features observed upon the one-electron oxidation of $[K(18\text{-}C\text{-}6)]_3[^{SO3}LCuOH]$ in the absence (blue trace) and presence of 100 eq. [Na(15-C-5)]OTf (red trace). ***88***

Scheme 3.3. Cross-HAT scheme. ***89***

Figure 3.16. Changes in the UV-Vis absorption spectrum of $[K(18\text{-}C\text{-}6)]_2[^{SO3}LCuOH]$ with increasing equivalents of $LCuOH_2$. ***90***

Figure 3.17. Representative deconvolution traces depicting the modeled spectra and experimental spectra. In all cases, the black dashed trace represents the experimental equilibrium spectrum, the red trace represents LCuOH, the blue trace represents $[^{SO3}LCuOH]^{2-}$ and the pink trace represents the overall modeled spectrum. ***92***

Figure 3.18. (Left) UV-vis spectra of $[K(18\text{-}C\text{-}6)]_3[^{SO3}LCuOH]$ in water at a pH of 4.75 (red trace) and at pH of 11.35 (black trace). (Right) Observed changes in the UV-Vis spectra during the course of the titration from pH 11.35 to pH 4.75. ***93***

Figure 3.19. Cyclic Voltammogram of $[K(18\text{-}C\text{-}6)]_3[^{SO3}LCuOH]$ in water recorded at pH 10. Conditions : 2 mM analyte, 0.1 M $NaClO_4$ supporting electrolyte, Glassy Carbon working electrode, Scan rate 100mV/s. ***95***

Figure 3.20. (Left) Representative UV-vis spectrum over time for the reaction of $[K(18\text{-}C\text{-}6)]_2[^{SO3}LCuOH]$ with 10 eq of DHA at -25 $^{\circ}$C. (Right) Representative absorbance vs. time plots showing the single exponential fit in red and the corresponding second-order plot. ***96***

Figure 3.21. Second order plots depicting the variation in the rates of HAT from DHA to $[^{SO3}LCuOH]^{2-}$ as a function of the added electrolyte. ***98***

Scheme 4.1. Synthesis and reactivity of $[CuOH]^{2+}$ complexes. ***108***

Scheme 4.2. Scheme of Reactions of $[CuOH]^{2+}$ with *para*-substituted phenols. ***110***

Figure 4.1. (Left) Representative pseudo first-order UV-vis decay trace of LCuOH in the presence of $^{Me}ArOH$, as monitored by stopped-flow studies. The final blue spectrum matches that of the LCu(THF) adduct (see Figure 4.15 below), which forms as a result of ligand exchange with $LCu(OH_2)$. (Right) Representative fits of the absorbance at 548 nm to a single exponential decay function. ***113***

Figure 4.2. Second-order plots for pseudo-first-order reactions of LCuOH with *p*-OMe- (top left), *p*-Me- (top right), *p*-H- (middle left), *p*-Cl- (middle right), *p*-NO_2- (bottom left), and *p*-CF_3-phenol (bottom right). Pseudo first-order rate constants (k_{obs}) were determined using single wavelength analysis, exemplified in Figure 4.1 above. ***114***

Figure 4.3 Second-order plots for pseudo-first-order reactions of LCuOH with *p*-OMe- (top left), *p*-Me- (top right), *p*-H- (middle left), *p*-Cl- (middle right), *p*-NO_2- (bottom left), and *p*-CF_3-phenol (bottom right). Pseudo first-order rate constants (k_{obs}) determined from global fitting with Olis Global Works™ program, exemplified in Figure 4.4 below. ***115***

Figure 4.4. . (Left) Representative spectral components obtained from the global kinetic analysis using Olis Global Works™ for ^{Me}ArOH reacting with LCuOH under pseudo-first-order conditions in which reactant is in black and product is in red. (Right) The relative contribution of the respective spectral components (or eigenvectors, E.V.) to the overall observed spectrum over the course of time, which is representative of the time course evolution of the various species involved in the reaction. The inset shows the residuals as a function of time. ***116***

Figure 4.5. (Left) Representative UV-vis spectra as a function of time (1 ms to 100 s) for the reaction of LCuOH (prepared by reaction of Bu_4N[LCuOH] with [Fc]BAr^F_4) with ^{NO2}ArOH (5 equiv). Only selected data shown for clarity. (Right) The plot of k_{obs} vs. [^{NO2}ArOH]$_0$ for the growth of the feature at 400 nm. ***117***

Figure 4.6. Representative spectral components obtained from the global kinetic analysis using Olis Global Works for *p*-NO_2-phenol reacting with LCuOH under pseudo-first order conditions when the kinetic model A→ B → C involving an intermediate C is used; reactant is in black, intermediate is in navy and product is in red (top left). Relative contribution of the respective spectral components (or eigen vectors, E.V.) to the overall observed spectrum over the course of time; this represents the time course evolution of the various species involved in the reaction (top right). Plot of residuals (bottom left). Overlay of residuals from a step-wise mechanism (red) and the mechanism involving a single kinetic step (blue, bottom right). ***118***

Figure 4.7. Representative spectral components obtained from the global kinetic analysis using Olis Global Works for *p*-CF_3-phenol reacting with LCuOH under pseudo-first order conditions when the kinetic model A→ B → C involving an intermediate C is used; reactant is in black, intermediate is in navy and product is in red (top left). Relative contribution of the respective spectral components (or eigen vectors, E.V.) to the overall observed spectrum over the course of time; this represents the time course evolution of the various species involved in the reaction (top right). Plot of residuals (bottom left).

Overlay of residuals from a step-wise mechanism (red) and the mechanism involving a single kinetic step (blue, bottom right). ***119***

Figure 4.8. . Representative spectral components obtained from the attempted global kinetic analysis using a simple kinetic model (A→ B) on Olis Global Works for *p*-NO_2-phenol reacting with LCuOH under pseudo-first order conditions in which reactant is in black and product is in red (left). Relative contribution of the respective spectral components (or eigen vectors, E.V.) to the overall observed spectrum over the course of time; this represents the time course evolution of the various species involved in the reaction (center). Plot of residuals indicating a systematic error in the fits (right). ***120***

Figure 4.9. Representative spectral components obtained from the attempted global kinetic analysis using a simple kinetic model (A→ B) on Olis Global Works for *p*-CF_3-phenol reacting with LCuOH under pseudo-first order conditions in which reactant is in black and product is in red (left). Relative contribution of the respective spectral components (or eigen vectors, E.V.) to the overall observed spectrum over the course of time; this represents the time course evolution of the various species involved in the reaction (center). Plot of residuals indicating a systematic error in the fits (right). ***120***

Figure 4.10. Plots of [LCuOH] vs. time (black) along with linear fits to the first 5% of data (10% in the case of *p*-OMe-phenol) for stoichiometric reactions of LCuOH with *p*-OMe- (top left), *p*-Me- (top right), *p*-H- (middle left), *p*-Cl- (middle right), *p*-NO_2-(bottom left), and *p*-CF_3-phenol (bottom right). ***121***

Figure 4.11. Plots of [$LCu^{III}OH$] vs. time (black) along with linear fits (red) to the first three-four data points for stoichiometric reactions of LCuOH (in red). ***122***

Figure 4.12. Representative concentration vs. time plots for reactions of LCuOH with *p*-CF_3- (left) and *p*-NO_2-phenol, displaying fits to Eq.4.2 (solid red) and 4.5 (dashed blue), along with the corresponding residual plots (inset). The improved fits to the expanded kinetic model are evident from the residuals. ***124***

Figure 4.13. Plots of ^{NO2}LCuOH vs. time (black) along with linear fits (blue) to the first three-four data points for stoichiometric reactions with *p*-NMe_2-phenol. ***125***

Figure 4.14. Plots of [^{NO2}LCuOH] vs. time (black) along with linear fits to the first 5% of data (10% in the case of *p*-OMe-phenol) for stoichiometric reactions of ^{NO2}LCuOH with *p*-OMe- (top left), *p*-Me- (top right), *p*-H- (middle left), *p*-Cl- (middle right), *p*-NO_2-(bottom left), and *p*-CF_3-phenol (bottom right). ***126***

Figure 4.15. Representative concentration vs. time plots for reactions of ^{NO2}LCuOH with *p*-CF_3- (left) and *p*-NO_2-phenol, displaying fits to Eq. 5.2 (solid red) and Eq. 5.5 (dashed blue), along with the corresponding residual plots (inset). The improved fits to the expanded kinetic model are evident from the residuals. ***127***

Scheme 4.3. Formation of Pummerer's ketone from the *ortho-para* coupling of two *p*-cresol phenoxyl radicals (only one resonance form of each of the reacting radicals is shown). ***129***

Figure 4.16. (Left) EPR spectra for reactions of LCuOH with 2,4,6-tri-*t*-butylphenol (black) and TEMPOH (red), confirming the formation of organic radical species in these reactions (conditions: 1 mM concentration, 77 K, 0.0002 mW microwave power). (Right) Product EPR spectrum for the reaction of ^{NO2}LCuOH with 2,4,6-tri-*t*-butylphenol confirming the formation of phenoxyl radical in this reaction (conditions: 0.1 mM concentration, 30 K, 0.063 mW microwave power). The inset shows a zoomed-in view to highlight the copper features that are also observed. ***130***

Figure 4.17. UV-vis traces of reaction between LCuOH and 2 eq. 2,4,6-tri-*t*-butylphenol in THF monitored at -80 °C. The inset shows the spectrum of the phenoxyl radical obtained after subtracting out the spectral contribution from other species in solution. ***131***

Figure 4.18. (Left) Final decay spectra of pseudo first-order stopped-flow reactions between LCuOH and ^{Me}ArOH (red), ^{H}ArOH (blue), ^{Cl}ArOH (green), and ^{OMe}ArOH (pink), all overlayed with an independent spectrum of LCu(THF) (black), supporting the identity of this species as the final inorganic product from these reactions. (Right) Final decay spectra of stoichiometric stopped-flow reactions between ^{NO2}LCuOH and ^{OMe}ArOH (black), ^{Me}ArOH (red), ^{H}ArOH (blue), and ^{Cl}ArOH (green). ***131***

Figure 4.19. UV-vis traces showing the reaction between LCuOH (left) or ^{NO2}LCuOH (right) with 1 eq. of ^{NMe2}ArOH and the corresponding decay spectra after prolonged warming at room temperature. The starting spectra of LCuOH/^{NO2}LCuOH are shown in black, the resulting spectra after the addition of 1 eq. of ^{NMe2}ArOH are shown in red, and the decay spectra are shown in blue. ***132***

Figure 4.20. UV-vis spectra of ^{NO2}ArO^{-} (left) and corresponding Beer's law plot (right) of the absorbance at 400 nm for [Bu_4N][^{NO2}ArO]. ***133***

Figure 4.21. Final decay spectra of pseudo first-order stopped-flow reactions between LCuOH and ^{NO2}ArOH (left) and ^{CF3}ArOH (right) at the concentrations listed. Molar

extinction values were approximated by using the total copper concentration (0.03 mM). The spectra are overlayed with that of the LCu(THF) adduct for comparison. ***134***

Figure 4.22. (Left) Overlay of the UV-vis spectra for a 0.03 mM solution of [Fc][BAr^F_4] (black) with the product solution of the reaction between LCuOH and 100 eq. of ^{NO2}ArOH (red). (Right) An overlay of the EPR spectra for a 1 mM [Fc]BAr^F_4 solution (red) and the product solution of the reaction of LCuOH and 2 eq. of ^{NO2}ArOH (black) with the features due to Fc^+ shown in the insets. ***135***

Figure 4.23. (Left) UV-vis spectrum of the product mixture for the reaction between LCuOH and ^{NO2}ArOH in THF at -80 °C (black spectrum; total Cu concentration is 0.5 mM), as well as the corresponding spectra of the same solution upon the addition [Fc]BAr^F_4 in of 0.25 eq. (red spectrum), 0.5 eq. (blue spectrum), 0.75 eq (pink spectrum), 1.0 eq. (green spectrum), and 1.25 eq (purple spectrum) increments. The inset shows the original product mixture after baseline correction, which was done to approximate the absorbance solely due to Fc^+ in the product mixture. (Right) Standard addition plot for the addition of [Fc][BAr^F_4] to the product mixture corresponding to the UV-vis absorption changes shown in the figure to the left. The absorbance after baseline correction was used to approximate the concentration of Fc^+ in the product mixture from the linear fit. ***135***

Scheme 4.4. Mechanisms that would yield the phenolate $^{NO2}ArO^-$. ***136***

Figure 4.24. UV-vis spectra for the reaction of LCuOH (prepared by reaction of [Bu_4N][LCuOH] with (p-tolyl)$_3N^{+\bullet}$) with ^{NO2}ArOH in THF at -80 °C. (Black) initial spectrum of LCuOH. (Grey) intermediate spectra as a function of time (4-834 s). (Blue) final spectrum stable at -80 °C. (Red) spectrum resulting from warming to room temperature. ***138***

Figure 4.25. (Left) UV-Vis traces for the reaction between LCuOH (black spectrum; generated by addition of 1 eq. of [$C_{12}H_8S_2$]PF_6 to a 0.1 mM solution of [Bu_4N][LCuOH] in THF at -80 °C) and 1 eq of 2,4,6-trimethylpyridinium triflate (blue spectrum) in THF at -80 °C. (Right) UV-vis absorption spectrum of the independently generated [$LCu(OH_2)]^+$ intermediate, formed by the addition of 1 eq of [$C_{12}H_8S_2$]PF_6 to a 0.1 mM solution of LCu^{II}(THF) dissolved in wet Acetone (red) at -80 ºC. ***139***

Figure 4.26. (Left) UV-vis absorption spectra of LCu^{II}(THF) in THF (black), [LCu^{III}(THF)]$^+$ in THF generated by addition of 1 eq of [$C_{12}H_8S_2$]PF_6 (red), and the corresponding decay spectrum of the oxidized species upon warming up to room temperature (blue). All spectra were recorded at -80 ºC. (Right) UV-Vis absorption

spectra of a THF solution of $Bu_4N[LCu^{II}OAr^{NO2}]$ (black), after the addition of 1 eq of $[(p\text{-tolyl})_3N]PF_6$ (red), and the final decay spectrum of the oxidized species after warming up to room temperature (blue). All spectra were recorded at -80 °C. ***140***

Figure 4.27. Crystal structure of $[Bu_4N][LCuOAr^{NO2}]$ with thermal ellipsoids drawn at 50% probability. Green, blue, red, and gray atoms represent Cu, N, O, and C, respectively. H-atoms, counter-ion, and solvent molecules omitted for clarity. ***140***

Figure 4.28. Overlay of the UV-vis spectra corresponding to the intermediate identified from global fitting of the reaction between LCuOH (from stopped-flow studies, generated by treatment of $Bu_4N[LCuOH]$ with 1 eq. of Fc^+) and ^{NO2}ArOH (black) and the experimentally measured spectrum of $[LCu^{III}(OH_2)]^+$ generated by treatment of LCu(THF) in wet acetone with 1 eq. of $[C_{12}H_8S_2]PF_6$ at -80 ºC (red). The spectra are normalized. ***141***

Figure 4.29. UV-Vis traces on treatment of LCuOH (generated with $(p\text{-tolyl})_3NPF_6$)) with 2 eq *p*-cresol monitored in THF at -80 °C. ***143***

Figure 4.30. (Top Left) Plots of $\log k_{DMSO}$ vs. $E_{1/2}(^{X}ArOH^{+\bullet}/^{X}ArOH)$ (X indicated) for their reactions with LCuOH (black) and ^{NO2}LCuOH (red). Linear fits have slopes of -2.5 (R^2 = 0.84) and -2.1 (R^2 = 0.76), respectively. (Top Right) Plots of $\log k_{DMSO}$ vs. pK_a of the phenols ^{X}ArOH (X indicated) for their reactions with LCuOH (black) and ^{NO2}LCuOH (red). Linear fits do not include the data points for X = NO_2 and have slopes of 1.1 (R^2 = 0.85) and 0.94 (R^2 = 0.93), respectively. The wide arrow indicates the X = NO_2 outliers. (Bottom) Plots of $\log k_{DMSO}$ vs. $\log K_{CPET}$ for reactions of LCuOH (black) and ^{NO2}LCuOH (red) with phenols ^{X}ArOH (X labeled). Linear fits have slopes of 0.47 (R^2 = 0.94) and 0.44 (R^2 = 0.84), respectively. Adapted from Ref 15. ***146***

Figure 4.31. The plot of ΔG for corresponding PT (red) or CPET (black) reactions with LCuOH (squares) and ^{NO2}LCuOH (circles). The dashed region represents where there is potential for thermodynamic overlap (i.e., both PT and CPET are feasible). ***149***

Figure 5.1. ORTEP representation (50% probability) of $[CuSal]^+SbF_6^-$, excluding hydrogen atoms. Selected interatomic distances (Å) and angles (deg): Cu(1)−O(1), 1.831(6); Cu(1)−O(2), 1.838(6); Cu(1)−N(1), 1.877(6); Cu(1)−N(2), 1.880(6); N(1)−C(7), 1.290(9); N(2)−C(14), 1.292(10); O(1)−C(1), 1.317(10); O(2)−C(20), 1.317(9); O(1)−Cu(1)−O(2), 86.5(3); O(1)−Cu(1)−N(1), 94.3(3); O(2)−Cu(1)−N(2), 93.8(3); N(1)−Cu(1)−N(2), 85.7(3). Adapted from Ref. 94a. ***165***

Scheme 5.1. The copper(II)-phenolate complexes presented in this chapter and the possible electronic descriptions of the one-electron oxidized species. ***167***

Scheme 5.2. Synthetic route for the copper(II)-phenolate complexes. ***168***

Figure 5.2. Representation of the X-ray crystal structure of the anionic components of [R'$_4$N][**1a-d**], showing all nonhydrogen atoms as 50% thermal ellipsoids where counterions and solvents have been omitted for clarity. (Top left) [Bu$_4$N][**1a**], (Top right) [Et$_4$N][**1b**], (Bottom left) [Et$_4$N][**1c**], and (Bottom right) [Bu$_4$N][**1d**] depicted as a ball and stick model. Relevant bond Cu-N/O bond distances are listed in Table 5.1. ***170***

Figure 5.3 UV-Vis absorption spectrum of the copper(II)-phenolate compounds [R'$_4$N][**1a-d**] in THF at -80 °C showing the entire wavelength region (left) and expanded *d-d* region (right). ***172***

Figure 5.4. X-band EPR spectra of frozen solutions of samples [R'$_4$N][**1a-d**] recorded at 30 K where black trace represents [Bu$_4$N][**1a**], red trace represents [Et$_4$N][**1b**], blue trace represents [Et$_4$N][**1c**], and cyan trace represents [Bu$_4$N][**1d**]. The dashed lines depict the Cu hyperfine splitting constants A_z for [Bu$_4$N][**1a**] and dotted lines depict that for [Bu$_4$N][**1d**]. ***173***

Figure 5.5. Experimental (black) and Simulated (red) spectra for [Bu$_4$N][**1a**] (top left), [Et$_4$N][**1b**] (top right), [Et$_4$N][**1c**] (bottom left), and [Bu$_4$N][**1d**] (bottom right). ***174***

Figure 5.6. Linear correlation (R^2= 0.95) between the A_z*(Cu)* for [R'$_4$N][LCuOAr^R] and σ_{para}(R). ***175***

Figure 5.7. Overlay of the cyclic voltammograms of [R'$_4$N][**1a-d**] in THF solvent ([Bu$_4$N][PF$_6$] as the supporting electrolyte supporting electrolyte, referenced internally with decamethylferrocene, potentials reported against Ferrocene); black trace represents [Bu$_4$N][**1a**] (Scan rate 50 mV/s), red trace represents [Et$_4$N][**1b**] (Scan rate 1000 mV/s), blue trace represents [Et$_4$N][**1c**] (Scan rate 2000 mV/s), and cyan trace represents [Bu$_4$N][**1d**] (Scan rate 50 mV/s). ***176***

Figure 5.8. Cyclic voltammograms of [Et$_4$N][**1b**] (left) and [Et$_4$N][**1c**] (right) depicting the nature of the scan rate dependence. ***177***

Figure 5.9. UV-Vis absorption spectra for the one-electron oxidation of [Bu_4N][**1a**] in THF at -80 °C to yield [**1a**], where black trace represents the starting compound, red trace represents the oxidation product and navy trace represents the decay product. ***180***

Figure 5.10. (Left) UV-Vis absorption spectra for the one-electron oxidation of [Et_4N][**1b**] in THF at -80 °C to yield [**1b**]. (Right) UV-Vis absorption spectra for the one-electron oxidation of [Et_4N][**1c**] in THF at -80 °C to yield [**1c**]; In both cases, the black trace represents the starting compound, red trace represents the oxidation product and blue trace represents the decay product. ***181***

Figure 5.11. UV-Vis absorption spectra for the one-electron oxidation of [Bu_4N][**1d**] in THF at -80 °C to yield [**1d**], where the black trace represents the starting compound, red trace represents the oxidation product and blue trace represents the decay product. ***182***

Figure 5.12. UV-vis absorption spectra for copper(II)-phenolate (solid line) and copper(II)-phenoxyl (dashed line) for a TACN based ligand framework. Adapted with permission from Ref 98a. ***183***

Figure 5.13. Resonance Raman spectra of [Bu_4N][**1a**], **1a**, [Bu_4N][**1d**] and **1d** with the relevant stretching frequencies highlighted (all samples are recorded at 5mM concentration). ***185***

Chapter 1
Metal-Oxygen Complexes And Their Role In Hydrogen Atom Transfer

1.1 Introduction

Elucidating how oxygenations and oxidation reactions of organic molecules operate, with the ultimate goal of developing selective, green, and efficient methods to perform such transformations, are key topics in chemical research.[1] The detailed study of biologically important metalloenzymes and small molecule biomimetic analogs of the active sites of such enzymes involved in oxidation reactions have proven particularly informative.[2] Metalloenzymes play a pivotal role in harnessing the oxidizing power of dioxygen by mediating the $4e^-$ reduction of O_2 to water in cellular respiration and in the incorporation of O-atoms during the biosynthesis of numerous organic compounds. Longstanding goals have been to comprehend the mechanisms of these reactions, unambiguously determine the geometries and electronic structures of intermediates, and unravel structure/function relationships for the catalytic centers. Such knowledge will facilitate the design of new and more selective and/or reactive oxidation catalysts. A useful strategy for achieving these goals involves the synthesis, characterization, and detailed evaluation of the reactivity and mechanisms of reactions of discrete molecules that contain metal-oxygen moieties relevant to proposed reaction intermediates.

The crucial ability of transition metal ions like manganese, iron and copper to shuttle between multiple oxidation states makes them ideal candidates for such studies.[3] These metal centers serve to activate O_2 through preliminary binding and reduction, followed by a cascade of events yielding reactive transition metal-oxygen intermediates that span a wide range of binding motifs and metal/O_2 stoichiometries. In particular, a number of copper-oxygen based intermediates have been characterized and/or implicated in enzymes,[4] heterogeneous and homogenous catalysts that oxidize organic molecules,[5] and in catalysis of the 4-electron interconversion between O_2 and H_2O.[6] The wide

spectrum of spectroscopic and reactivity patterns of such copper-oxygen motifs has been reviewed extensively.[7]

One of the more recently characterized high-valent copper-oxygen motifs is the mononuclear copper(III)-hydroxide core, $[CuOH]^{2+}$, shown supported by a dianionic dicaroxamide ligand system in Figure 1.1. The first successful synthesis and characterization of this $[CuOH]^{2+}$ core was reported by the Tolman group in 2011.[8] This core was particularly notable due to its ability to perform very efficient and rapid Hydrogen Atom Transfer (HAT) from the weak C-H bonds of 9,10-dihydroantracene (DHA), as discussed in more detail below.

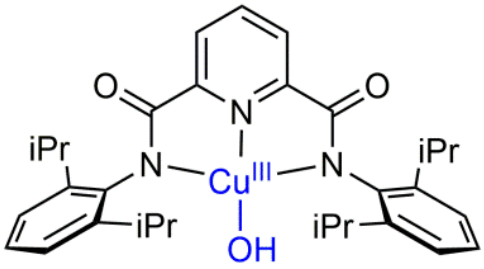

Figure 1.1. $[CuOH]^{2+}$ core supported by a pyridine dicarboxamide ligand framework.

The $[CuOH]^{2+}$ core may be viewed as a protonated version of the elusive copper-oxyl unit $[CuO]^{+}$, which is the copper analog of the well characterized and documented high-valent iron and manganese-oxo species.[9] While the $[CuO]^{+}$ core has been implicated on the basis of computational studies to be the key intermediate in a number of biological and synthetic oxidation reactions,[10,11] it has only been characterized successfully in the gas phase and direct evidence for its involvement in enzymes or model compound systems is lacking.[12] Subsequent studies on the $[CuOH]^{2+}$ core have demonstrated that it is capable of performing HAT from an array of hydrocarbon substrates, including even strong C-H bonds having Bond Dissociation Enthalpies (BDEs) as high as 99 kcal mol^{-1},[13,14] as well as a range of phenolic substrates.[15] Based on these observations of the

ability of the $[CuOH]^{2+}$ to act as an efficient HAT reagent, its potential involvement as a key intermediate in enzymatic oxidation reactions has been proposed.[7g,13]

The focus of my thesis work has been primarily on the chemistry of the $[CuOH]^{2+}$ core, including establishing what factors contribute to its high propensity to act as an efficient HAT reagent and how these intrinsic factors can be modulated to tune its reactivity. The results of my endeavors in this regard are presented in the subsequent chapters, with an additional chapter on related work on copper-phenolate species isolated as reaction products and having intriguing electronic structures. As a preface to the subsequent chapters, in this chapter I will first discuss the characterization of the $[CuOH]^{2+}$ core which was reported prior to my dissertation research. I will then present a general discussion on the thermodynamics of HAT reactions in general, in light of well-established Proton-Coupled-Electron Transfer (PCET) theory. The interdependence of thermodynamic properties and the kinetics and mechanism of HAT reactions also will be discussed. The focus will then shift to a discussion of the HAT reactivities of certain reported metal-oxo/hydroxo complexes. The aim will be to establish what factors play a crucial role in such reactions and to draw key conclusions and lessons, thus setting the stage for discussion of my dissertation research in the subsequent chapters.

1.2 Previous studies on the mononuclear copper(III)-hydroxide $[CuOH]^{2+}$ core

The first characterized copper(III)-hydroxide $[CuOH]^{2+}$ core reported in 2011 by the Tolman group was generated using the dianionic pyridine dicarboxamide ligand framework (Figure 1.1).[8] This initial report provided electrochemical evidence for the reversible oxidation (quasi-reversible cyclic voltammograms) of the copper(II)-hydroxide precursor ($[Bu_4N][LCuOH]$) at mild potentials ($E_{1/2}$ = -0.076 V vs. Fc^+/Fc in acetone, Figure 1.2, left), suggesting a relatively weak oxidizing ability for the copper(III)-hydroxide species (LCuOH). The complex $[Bu_4N][LCuOH]$ was synthesized and isolated by treatment of the copper(II)-solvato adduct LCu(MeCN) with 1 eq of Bu_4NOH.

Chemical oxidation of $[Bu_4N][LCuOH]$ with 1 equivalent of $[Fc][PF_6]$ in acetone at low temperature (-80 °C) resulted in the immediate formation of an intense charge-transfer band in the UV-vis spectrum at ~ 540 nm ($\varepsilon \sim 12{,}400\ M^{-1}\ cm^{-1}$, Figure 1.2, right).

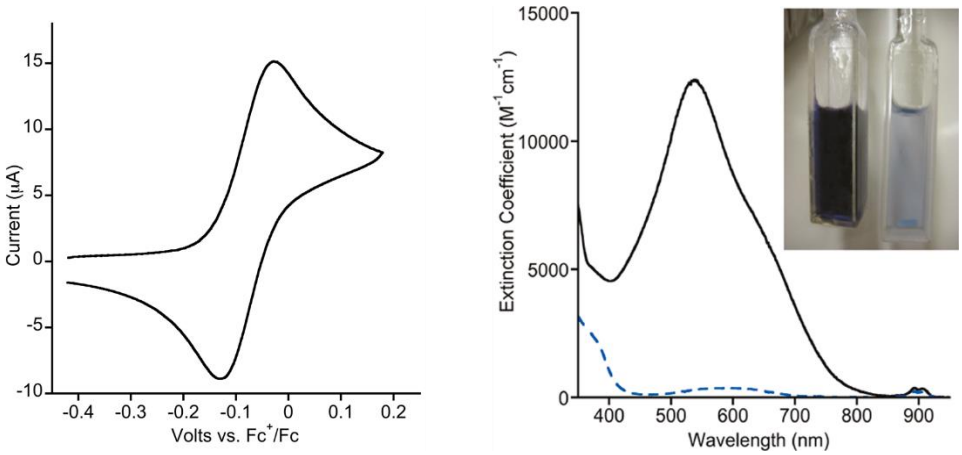

Figure 1.2. (Left) Cyclic voltammogram, displaying the reversible $[LCuOH]/[LCuOH]^-$ redox couple. (Right) Low temperature UV-vis spectra of $Bu_4N[LCuOH]$ (blue, dashed trace) and upon addition of 1 eq. of $[Fc]PF_6$ (black trace). Inset displays the oxidized (purple) and reduced reaction solutions (light blue). Reprinted with permission from Ref 8. Copyright 2011, American Chemical Society.

This charge transfer feature was quenched upon addition of 1 eq of a suitable reductant, decamethylferrocene (Fc*), to give the spectrum of the starting complex $[Bu_4N][LCuOH]$. This species could again be re-oxidized to form LCuOH. This chemical reversibility experimental result coupled with the reversibility in the cyclic voltammograms support the reversible one-electron oxidation of $[Bu_4N][LCuOH]$ to generate LCuOH. Oxidation at the metal center was corroborated by EPR silence of the oxidized samples. More direct evidence favoring the assignment of the oxidation product as a Cu(III) species came from X-ray absorption spectroscopy (XAS). The Cu K pre-edge features of LCuOH show a ~1.7 eV shift to higher energy when compared to $[Bu_4N][LCuOH]$, which clearly reveals oxidation of the copper ion with a concomitant increase in ligand field strength.[8] Also, a 1.1 eV shift in the rising edge was observed upon oxidation, which was attributed to an increase in effective nuclear charge of the

copper. Density Functional Theory (DFT) calculations ruled out the possibility of a ligand-based oxidation which could afford either a triplet or an open shell singlet ground state configuration, as optimizations starting from the structure of $[Bu_4N][LCuOH]$ gave a close-shell singlet structure for LCuOH, consistent with the formulation of a Cu(III) center. Additionally, the CT features in the UV-vis spectrum were identified by time-dependent DFT (TD-DFT) calculations as predominantly derived from a ligand-to-metal charge-transfer transition involving single-electron excitation from the aryl-π orbitals to the Cu $d_{x^2-y^2}$ orbital.[8]

While the complex LCuOH was relatively stable at low temperatures, it decayed rapidly upon warming. Notably, when treated with excess DHA (10-40 eq) at low temperatures, a rapid decay in the LMCT band characteristic of LCuOH concomitant with the growth of sharp CT bands indicative of anthracene formation was observed. Product analysis by GC-MS (Gas Chromatography-Mass Spectrometry) indicated an 85% yield of anthracene, with the inorganic product being the corresponding copper(II)-aqua complex ($LCuOH_2$, Scheme 1.1). All of these data are indicative of a HAT reaction occurring between DHA and LCuOH.

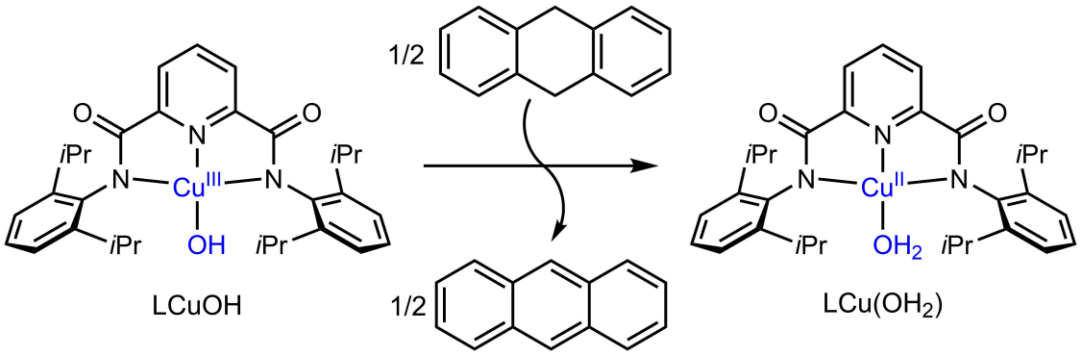

Scheme 1.1. HAT reaction between DHA and LCuOH, producing anthracene and $LCuOH_2$ as the corresponding reaction products.

Kinetic measurements of the reaction with DHA revealed an overall second-order rate constant of ~ 1.1(1) M^{-1} s^{-1} (-80 °C, acetone). Additionally, by using DHA-d_4 as a

substrate, a large, non-classical Kinetic Isotope Effect (KIE) of 44 (-70 °C; extrapolated to 29 at 25 °C) was observed.[8] Eyring analysis of the reactions revealed an enthalpy of activation ($\Delta H^{\ddagger}$) of 5.4(2) kcal mol^{-1} (6.2(3) kcal mol^{-1} for DHA-d_4) and a large, negative entropy of activation ($\Delta S^{\ddagger}$) of -30(2) e.u. (-34(3) e.u for DHA-d_4). Taken together, the results indicate that the rate determining step involves the transfer of the hydrogen atom from DHA to LCuOH, with significant contributions from quantum mechanical tunneling effects implicated by the large KIE values. The rates of HAT from DHA demonstrated by LCuOH are among the highest reported in the literature for high-valent transition metal-oxygen intermediates, thus raising intriguing questions about the reasons for such efficient HAT reactivity.[8]

1.3 Hydrogen atom transfer

Hydrogen Atom Transfer (HAT) is a process within the broader class of Proton Coupled Electron Transfer (PCET) reactions.[16,17] A hydrogen atom can simply be considered as a proton and an electron, and the name HAT simply refers to reactions where a hydrogen atom is transferred.[16,17,18] A variety of reactions of biological and synthetic significance involve the concurrent transfer of protons and electrons.[16,17,18] This transfer is complicated by how and when these two fundamental species are transferred: the transfer may either be concerted, whereby the two are transferred in a single kinetic step without the involvement of any intermediates, or it may occur in stepwise fashion (Figure 1.3). The stepwise transfer can be of two types: (1) proton transfer (PT) is followed by an electron transfer (ET), which is commonly denoted by the notation PT/ET, or (2) electron transfer (ET) is followed by a proton transfer (PT), which is commonly denoted by the notation ET/PT.

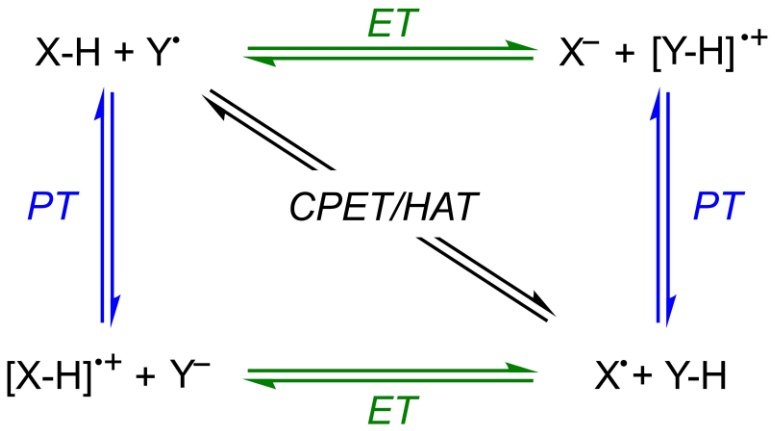

Figure 1.3. Generic square scheme depicting the HAT/CPET reaction between the two reactants X-H and Y•

Historically, while PCET was used to refer to reactions where the proton and electron transfer are concerted, there are many redox reactions where the rate and/or energetics are modulated by one or more protons. Researchers have included these reactions within the scope of "proton coupled electron transfer,"[16] which causes considerable confusion in the literature. As a result, a much broader and now generally accepted definition of PCET has been proposed. The term PCET is used to describe all reactions and half reactions in which both protons and electrons are transferred/involved without any regard to mechanism.[17b] A classic example is the water splitting reaction where both the half reactions are pH dependent, although technically there is no actual transfer of a proton. Savéant *et al* introduced a new term "concerted proton electron transfer" (CPET) which aims to clarify the mechanistic implications of a concerted transfer.[16] However, "concerted" necessarily *does not* imply a synchronous process. HAT reactions form a class of CPET in which the both the proton and electron are transferred from the same donor to the same acceptor. The proton and electron need not be transferred to the same atom or bond – the acceptor/donor sites may be different, but they have to be within the same moiety.[16] A demonstration of this idea is the hydrogen atom abstraction step in the catalytic cycle of cytochrome P450 enzymes, where the proton is transferred to an iron-oxo unit while the electron is transferred to the delocalized

porphyrin radical cation of Compound 1 (in a concerted mechanism), and the overall reaction is best described as a HAT.[19]

Owing to the ubiquitous involvement of such HAT reactions in energy conversion and storage reactions in chemistry and biology, their study has garnered significant interest within the research community, and multiple proposed models/theories have been postulated in the literature that aim at understanding what factors play a crucial role in controlling such reactions.[16-18] In the following sections I will discuss the key factors that are responsible for governing the rates of such HAT reactions in the light of well-established PCET theory.

1.3.1 Thermodynamics of HAT reactions

The thermodynamics for a single proton and electron transfer for a HAT reagent X-H going to $X^{\bullet}$ is given by the square scheme in Figure 1.4.

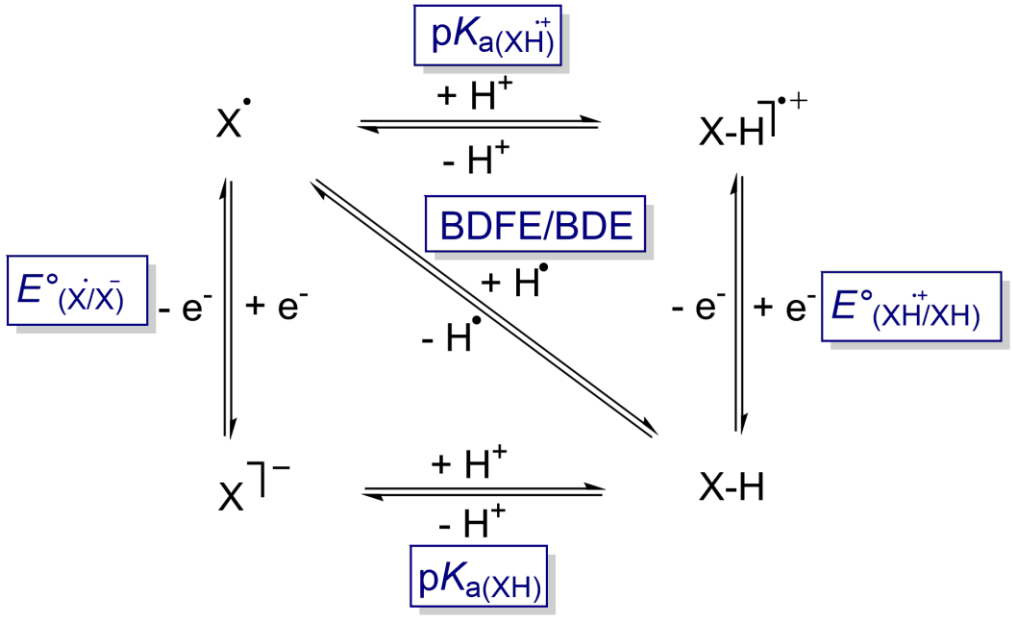

Figure 1.4. The thermodynamic square scheme for a HAT reagent X-H

The key five parameters in the above square scheme include pK_a values of the oxidized and reduced forms ($XH^{\bullet+}$ and XH); the redox potential values for the protonated and deprotonated forms ($E°[XH^{\bullet+}/XH]$ and $E°[X^{\bullet}/X^{-}]$); and the homolytic bond dissociation free energy (BDFE) or homolytic bond dissociation enthalpy (BDE) of the X-H bond.

The free energy change for the proton transfer ($\Delta G°_{PT}$) and free energy change for electron transfer ($\Delta G°_{ET}$) can be expressed using Eq 1.1 and 1.2, respectively, where *R*, *T* and *F* represent the universal gas constant, the temperature (in Kelvin) and the Faraday constant.

$$\Delta G°_{PT} = -RT \ln(K_a) = 2.303RT(pK_a) = 1.37pKa \text{ kcal mol}^{-1} \text{ (at 298 K)} \quad \text{(eq. 1.1)}$$

$$\Delta G°_{ET} = -FE° = -23.06E° \text{ kcal mol}^{-1} \quad \text{(eq. 1.2)}$$

The BDFE of the X-H bond can be calculated using Hess' Law applied to the square scheme; it is a function of the pK_a, the $E°$ and another solvent dependent constant, C_G, which is related to the $H^+/H^\bullet$ standard reduction potential in the solvent (Eq. 1.3).[16,20] This constant includes the free energy of formation of $H^\bullet$ in the gaseous phase and the free energy of solvation of $H^\bullet$ in the specified solvent, and also depends on the nature of the reference electrode. For aqueous conditions the potentials are referenced to the standard hydrogen electrode, while for organic solvents the reference electrode is the Ferrocenium/Ferrocene couple.[16,21]

$$BDFE_{sol}(X\text{-}H) = 1.37pK_a + 23.06E° + C_{G,sol} \quad (\text{kcal mol}^{-1}) \quad \text{(eq. 1.3)}$$

Alternately, the BDE of the X-H bond is given by Eq. 1.4 defined in terms of the pK_a and $E°$, and another solvent dependent constant, C_H, which pertains to only *enthalpic* contributions for the redox couple of $H^+/H^\bullet$.

$$BDE_{sol}(X\text{-}H) = 1.37pK_a + 23.06E° + C_{H,sol} \quad (\text{kcal mol}^{-1}) \quad \text{(eq. 1.4)}$$

The relation between C_H and C_G is given by [$C_H = C_G - T\Delta S°(H^\bullet)_{solv}$], where $\Delta S°(H^\bullet)_{solv}$ represents the standard entropy change of solvation of $H^\bullet$ from H_2.[16] Although BDE values are more commonly used to evaluate the HAT driving force in comparison to BDFE values, the use of BDEs fails to account for entropic changes in HAT reactions. For purely organic HAT reactions, it has been shown that entropy generally does not contribute significantly to free energies of reaction and in many cases this extends to reactions with transition metal complexes, thus enabling the use of BDE values to ascertain the thermodynamic driving force.[22] However, for transition metal mediated

HAT chemistry, this is not always the case, as has been shown in a few notable examples, particularly in cases where the oxidation/reduction of the transition metal ion is associated with a large spin state change.[23]

Finally, for the HAT reaction occurring between the pair of reactants X-H and $Y^{\bullet}$ described in Figure 1.3 above, the overall reaction enthalpy (ΔH_{rxn}) can be taken as the difference in bond dissociation enthalpies (BDE) of the reactant X-H bond and the product Y-H bond according to Hess' Law and is given by Eq. 1.5.[16]

$$\Delta H_{rxn} = \Delta BDE = BDE_{X-H} - BDE_{Y-H} \qquad \text{(eq. 1.5)}$$

The same can be also said for the free-energy of the reaction (ΔG_{rxn}) instead, using the bond dissociation free-energies (BDFEs) for the Y-H and X-H bonds.

1.3.2 Influence of HAT thermodynamics on the rates of HAT reactions

From the study of a wide variety of HAT reactions, it was recognized that for a given reaction series (e.g. reaction of a single H-atom donor with a series of acceptors, or reaction of a single H-atom acceptor with a series of donors) the logarithm of the rate constant ($\log(k)$) correlated linearly with the thermodynamic driving force for the reaction.[16-18] This relationship is illustrated in Figure 1.5, which describes a series of reactions between DHA and a range of H-atom acceptors, and a series of reactions between various hydrocarbon substrates and the single acceptor $[Bu_4N][MnO_4]$. In both cases, it can be seen that the logarithm of the rates of the HAT reaction vary linearly with the driving force of the reaction.

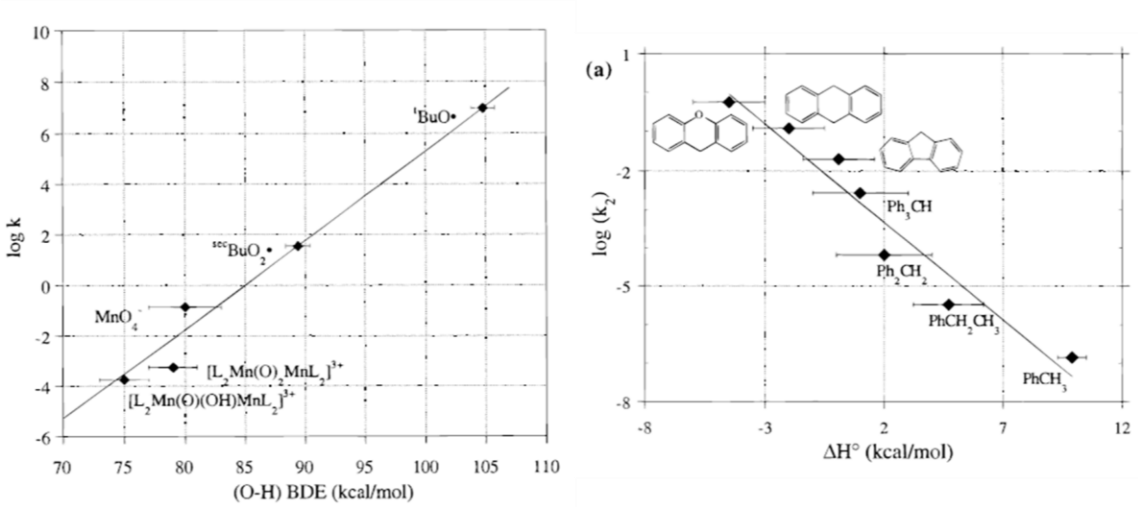

Figure 1.5. (Left) Linear correlation between rates of HAT and BDE of the formed O-H bond, between DHA and a series of H-atom acceptors including organic radicals and manganese complexes, where L_2 is phenanthroline. (Right) Linear correlation between HAT rates and ΔH for reactions of $[Bu_4N][MnO_4]$ with a range of substrates. Adapted with permission from Ref 22b.

This observation is an expression of a linear free energy relationship between the rates of HAT reactions and their thermodynamic driving forces, most commonly given by the reaction enthalpy.[24] While a number of such correlations have been developed for specific sets of reactions, the idea was first generalized in the form of the Bell-Evans-Polanyi relationship given in Eq. 1.6, which relates the activation energy of a reaction (E_a) to the reaction enthalpy, where α and β are constants specific to the reaction.[25]

$$E_a = \beta + \alpha \Delta H^o \qquad \text{(eq. 1.6)}$$

Most notably, Eq. 1.6 has been shown to describe a large number of HAT reactions, ranging from reactions mediated by organic radical species to those for which a transition metal complex is the H-atom abstractor.[22] It was later demonstrated by Mayer and co-workers that the Marcus cross relation could be used as a predictive model in describing the rates of HAT reactions across a wide range of compounds.[22,26] They demonstrated in detail that the free energy of activation ($\Delta G^{\ddagger}$) for HAT reactions varies as the square of the free energy change of the overall reaction ($\Delta G°$), which ultimately translates into a linear correlation between the log(k) and $\Delta G°$, such that an increase in the driving force

for a HAT reaction translates into a higher rate. Similar conclusions have also been reached on the basis of theoretical models used to describe HAT reactions.[27]

1.3.3 Mechanistic implications of the thermodynamics of HAT reactions

As described in Section 1.3.1, once the overall CPET square scheme for a reaction between a pair of compounds is defined, the individual energy changes associated with the stepwise transfer of a proton/electron and that associated with the concerted transfer of the H-atom can be determined. These values are often useful in determining the mechanism of the reaction by helping CPET and step-wise mechanisms to be distinguished. An illustrative example is the HAT reaction between DHA and an iron(III)-bisimidazoline complex (Figure 1.6).[28]

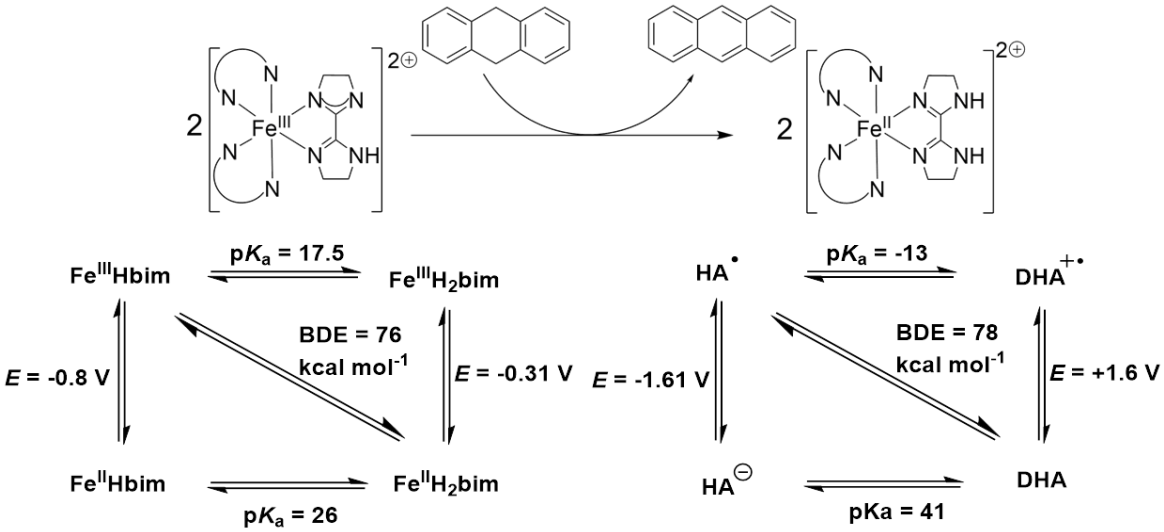

Figure 1.6. (Top) HAT reaction between DHA and the iron(III)bis-imidazoline complex $[Fe^{III}Hbim]^{2+}$, where the other ligands are the bidentate neutral H_2bim. (Bottom) The thermodynamic parameters in the square scheme for the two reactants participating in the HAT reaction. Data adapted from Ref 28.

The respective thermodynamic square schemes depicting the involved thermodynamic parameters for $Fe^{III}HBim$ and DHA also are depicted in Figure 1.5. The initial ET from DHA to $Fe^{III}HBim$ is uphill by ~55 kcal mol^{-1} ($\Delta E°$= 2.4 V) while the initial PT would require an energy of ~32 kcal mol^{-1} (ΔpK_a = 23.5). In contrast, the energy requirement for

the CPET pathway (given by ΔBDE) is only 2 kcal mol^{-1}. The observed free energy of activation for the reaction is 12 kcal mol^{-1}, which is significantly lower than the free energy changes associated with the initial PT or ET. Based on these arguments, it was concluded that the reaction must proceed through a CPET mechanism.[28]

For most reactions there is a large thermodynamic bias in favor of CPET over a stepwise ET/PT or PT/ET mechanism, as the latter mechanisms often require the generation of high energy charged intermediates. However, if the thermodynamic driving force for a stepwise process is lower, as in it is energetically more favorable to achieve a discrete proton/electron transfer first in comparison to the concerted transfer, the reaction tends to proceed through a stepwise mechanism.[9i] This situation has been demonstrated in the reactions of a Mn(IV) and Mn(III)-oxo complex (supported by the same ligand framework) with DHA.[9i] While, the thermodynamic driving force for the CPET reaction (determined by the BDE of the O-H bond in the product Mn(III/II)-OH complexes) is higher for the reaction with Mn(IV)-oxo in comparison to Mn(III)-oxo (BDE for Mn(III)-OH is 89 kcal mol^{-1} and that for Mn(II)-OH is 77 kcal mol^{-1}), the reactions with the Mn(III)-oxo proceed at significantly faster rates ($k^{Mn(III)\text{-}oxo}$ = 0.48(4) M^{-1} s^{-1} and $k^{Mn(IV)\text{-}oxo}$ = 0.026(2) M^{-1} s^{-1} at 20 °C). These observations were rationalized by postulating that the reactions proceeded *via* different mechanisms. While the reaction between Mn(IV)-oxo and DHA proceeds through the CPET pathway, it was proposed that the reaction between Mn(III)-oxo and DHA proceeds through the PT/ET pathway.[29] In support of this notion, the Mn(III)-oxo is significantly more basic than the Mn(IV)-oxo and the initial proton transfer from DHA to Mn(III)-oxo is uphill by only ~3 kcal mol^{-1} (ΔpK_a ~ 2), while the corresponding proton transfer for Mn(IV)-oxo is uphill by ~21 kcal mol^{-1} (ΔpK_a ~ 15). Consequently, the latter prefers the more favorable CPET pathway.[29] It is also worth noting that in the former case (reaction of Mn(III)-oxo with DHA), the overall HAT reaction is almost thermoneutral as the BDE of C-H bond in DHA and the O-H bond in Mn(II)-OH are similar, thus negating any intrinsic thermodynamic driving force for the

CPET pathway, which further propels the reaction to proceed through the PT/ET pathway. Additionally, for a series of reactions taking place between one H-atom abstractor and a series of analogous substrates, a linear correlation between the log(*k*) and ΔH (or BDE of the substrate) is often taken as an indicator for a similar mechanism being operational within the series,[13,16] while a deviation from linearity is indicative of a difference in the mechanism.[30]

1.4 Hydrogen atom transfer from C-H bonds by high-valent metal-oxo/hydroxo complexes

The C-H bonds in hydrocarbons are among the most inert chemical bonds in nature and, as a consequence, the conversion of these C-H bonds to C-X bonds (where X = oxygen, halogen, nitrogen) is one of the key challenges in modern chemistry.[1] In particular, the functionalization of C-H bonds to form C-O bonds has garnered significant interest among researchers because of its multifaceted applications. While an extremely challenging reaction, nature uses a variety of transition-metal based enzymes to carry out similar transformations within biological systems under mild conditions, through the involvement of highly reactive metal-oxygen intermediates. The first proposed step in the conversion of C-H bonds to C-O bonds involves the scission of the C-H bond which is speculated to happen by the loss of a hydrogen atom. Because the C-H bond is so strong and inert, this reaction requires the involvement of an extremely reactive species. In this regard, high-valent transition metal-oxo/hydroxo intermediates have been postulated in the catalytic cycles of enzymes and small molecule mimics as the key reactive species responsible for carrying out the initial HAT step.[9-12,31] Despite overarching similarities in the HAT reactions of high-valent metal-oxo complexes and high-valent metal-hydroxide complexes, there are some distinct differences. The HAT reaction product of most well characterized high-valent Mn and Fe-oxo complexes is the one-electron reduced hydroxide compound, which can itself either participate in a second HAT, or participate

in a “radical rebound” wherein hydroxylation of the substrate organic radical occurs.[9,32] In contrast, for high-valent metal-hydroxide complexes, the corresponding reaction product is the one-electron reduced aqua compound, which is unable to participate in any further reaction.

A wide variety of small molecules containing high-valent metal-oxo/hydroxo cores have been synthesized and characterized and their reactivity towards HAT from hydrocarbons has been investigated.[33] One commonly used hydrocarbon substrate used to probe the HAT reactivity of these metal-oxo/hydroxo complexes is DHA because of its relatively weak C-H bond (BDE ~ 76 kcal mol^{-1})[16] and its propensity to cleanly convert to anthracene (formed as a result of the HAT from DHA) without the complication of side reactions arising from radical coupling reactions. Important mechanistic insights about the nature of the HAT reaction have been obtained in these studies through evaluation of the reaction thermodynamics, in particular the measurement of the bond dissociation enthalpy (BDE) or free energy (BDFE) of the O-H bond formed in the product complex. Examples of such metal-oxo/hydroxo complexes are summarized in Table 1.1, which are selected on the basis of the availability of the thermodynamic parameters in the HAT square scheme for the metal-oxo/hydroxo complex (Figure 1.7) and the availability of the rate of reaction from DHA. The log(k) values (k is the second order rate constant for reactions with DHA (at 25 °C)) also are presented in Table 1.1 for comparison.

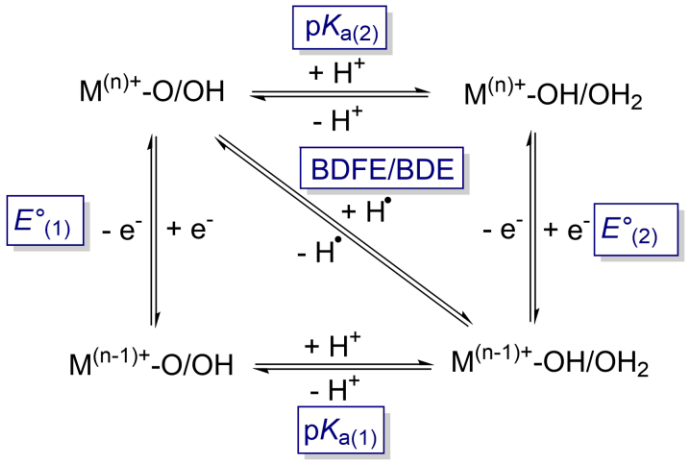

Figure 1.7. The HAT square scheme for metal-oxo/hydroxo complexes denoting the key thermodynamic parameters.

Table 1.1. Summary of HAT parameters from DHA for selected high-valent metal-oxo/hydroxo complexes (Data adapted from Ref 33)

Complex	$E°_1$ (V)[a]	p$K_{a(1)}$	$E°_2$ (V)[a]	p$K_{a(2)}$	BDE (kcal mol^{-1})	log k[d]
$[Mn^{IV}H_3buea(O)]^-$ [e]	-1.0	28.3	-0.18	15.0	89	-1.59
$[Fe^{IV}H_3buea(O)]^-$ [e]	-0.9	25	-0.03	10	87	-
$[(bpy)_2(py)Ru^{IV}O]^{2+}$	<0.48[b]	>13	>1.6[b]	<0	84	2.09
$[Fe^{III}(PY5)OMe]^{2+}$ [f]	0.73	9.1	-	-	84	-2.31
$[Mn^{IV}(Me_2EBC)(O)(OH)]^+$ [g]			0.756	6.86	84	-2.25
$[(PyPz)Fe^{III}(OH)(OH_2)]^{4+}$ [h]	0.9[b]	8	-	-	84	1.8
$[Mn^{IV}(Me_2EBC)(OH)_2]^{2+}$ [g]	0.756	5.87	-	-	83	-3.43
$[(bpy)_2(py)Ru^{III}OH]^{2+}$	0.46[b]	10.6	1.02[b]	0.85	82	-
$[Mn^{III}(PY5)OH]^{2+}$ [f]	0.81	13	-	-	82	-2.80
$[MnO_4]^-$	0.56[b]	7.4	-	-	80	-0.92
$[Fe^{III}(PY5)OH]^{2+}$ [f]	0.55	8.1	-	-	80	-3.36
$[L'_2Mn^{IV}(O)_2Mn^{III}L'_2]^{3+}$ [i]	-0.01	14.6	-	-	79	-2.81
$[Fe^{IV}(O)(N_4Py)]^{2+}$ [j]	0.24[c]	-	-	-	78	1.25
$[Mn^{III}H_3buea(O)]^{2-}$ [e]	-2.0	50.0	-1.51	28.3	77	-0.53
$[L'_2Mn^{III}(O)(OH)Mn^{III}L'_2]^{3+}$ [i]	-0.03	11.5	-	-	75	-3.38
$[Fe^{III}H_3buea(O)]^{2-}$ [e]	-	-	-1.79	25	66	-

[a] vs. Fc/Fc^+ unless otherwise stated. [b] vs. SHE. [c] vs. SCE. [d] k = second order rate constant for the reaction with DHA at 25 °C, either measured directly or extrapolated to this temperature from experimentally determined activation parameters.

[e] H_6buea = tris[(N_3-*tert*-butylureayl)-*N*-ethylene]amine. [f] PY5 = 2,6-bis(bis(2-pyridyl)methoxymethane)pyridine. [g] Me_2EBC = 4,11-dimethyl-1,4,8,11-tetraazabicyclo[6.6.2]hexadecane. [h] PyPz = tetramethyl-2,3-pyridino porphyrazine [i] L' = phenanthroline. [j] N_4Py = *N,N*-bis(2-pyridylmethyl)-bis(2-pyridyl)methylamine.

A survey of the data in Table 1.1 reveals that the BDE of the O-H bond formed varies over a wide range (~ 23 kcal mol^{-1}) and that the rates of the HAT reactions also span a large range (~6 log units). It should be noted, however, that the experimental data obtained for the indicated set of compounds was obtained in different solvents, ranging from aprotic solvents like MeCN to polar protic solvents like H_2O and MeOH. Because of potential solvent effects, direct comparisons should be made with caution. The supporting ligand framework in the complexes varies greatly in terms of the charge and sterics, which influences the HAT parameters. For example, high log *k* values of 2.09 for $[(bpy)_2(py)Ru^{IV}O]^{2+}$ and 1.25 for $[Fe^{IV}(O)(N_4Py)]^{2+}$ have been reported, but these complexes have lower BDE values of 84 and 78 kcal mol^{-1}, respectively, when compared to the Mn(IV)-oxo complex $[Mn^{IV}H_3buea(O)]$, which despite having a higher BDE of 89 kcal mol^{-1}, has a significantly low log(*k*) of -1.59. Among the factors potentially at play, it was speculated that the H-bonding array surrounding the oxo unit in $[Mn^{IV}H_3buea(O)]^-$ inhibits substrate approach and slows down HAT reactions. Another interesting observation is the comparison between the reactivities of the Mn(IV)-oxo $[Mn^{IV}(Me_2EBC)(O)(OH)]^+$ and Mn(IV)-hydroxide $[Mn^{IV}(Me_2EBC)(OH)_2]^{2+}$ complexes using the same supporting ligand framework. While the BDE values of the O-H bond formed in both cases is similar, suggesting that the thermodynamic driving force for the HAT reaction from DHA should be similar, the Mn(IV)-oxo complex reacts faster by almost an order of magnitude.[33f,g] Thus, from these results it can be concluded that while there are indications of linear free energy relationships and useful trends, the drawing of generalized conclusions for metal-oxo/hydroxo complexes is not always straightforward.

An additional feature in the HAT reactivity of metal-oxo/hydroxo complexes with C-H bonds are temperature dependent KIE data that are often attributed to quantum mechanical tunneling. For example, high KIE values, which are beyond the classical limit of ~7,[34] often are observed in these reactions.[8,13,14] Values significantly in excess of ~7 are often attributed to quantum mechanical tunneling of the proton through the activation barrier.[35] As depicted in Figure 1.8, tunneling results in an increased difference in activation barrier (in comparison to the semi-classical case) for the heavier deuterium when compared to the proton, resulting in significantly enhanced values of k_H/k_D. For the HAT reactions of transition metal-oxo/hydroxo species with C-H bonds, it is common to observe KIE values of ~ 2-7. At lower temperatures (198-273 K), larger KIE values (~10-20) are often observed,[35] and extremely large KIEs (k_H/k_D > 40 at room temperature) have also been observed in a few cases.[36]

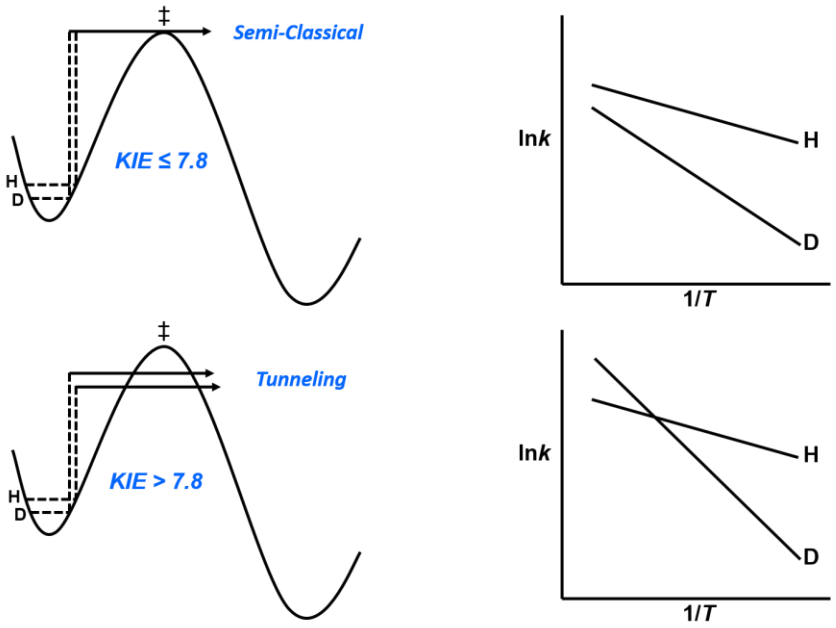

Figure 1.8. Potential energy curves along with the corresponding Arrhenius plots displaying characteristics of semi-classical (top) barrier crossing as well as the semi-classical case with a tunneling correction (bottom). Adapted from Ref 35b.

In some cases, it has been demonstrated that such non-classical tunneling effects play a crucial role in governing the rates of HAT reactions and may be the cause of apparently counterintuitive effects/trends.[37] For example, in a study of a series of Fe(IV)-oxo complexes, $[Fe^{IV}(O)(TMC)(L_{ax})]^{z+}$ (z =1,2), supported by the tetramethylcyclam (TMC) ligand framework and varying only with respect to the degree of electron donation from the axial ligand *trans* to the oxo unit (Figure 1.9), it was demonstrated that tunneling contributions are intricately responsible in governing the trends of the HAT reactions. While, the computationally predicted BDE of the formed O-H bond in all the complexes was found to be very similar (~ 84 kcal mol^{-1}),[33n] there was an observed trend in the HAT rates from DHA, with the more electron donating axial ligand having higher rates (Figure 1.9 (a), right).[38]

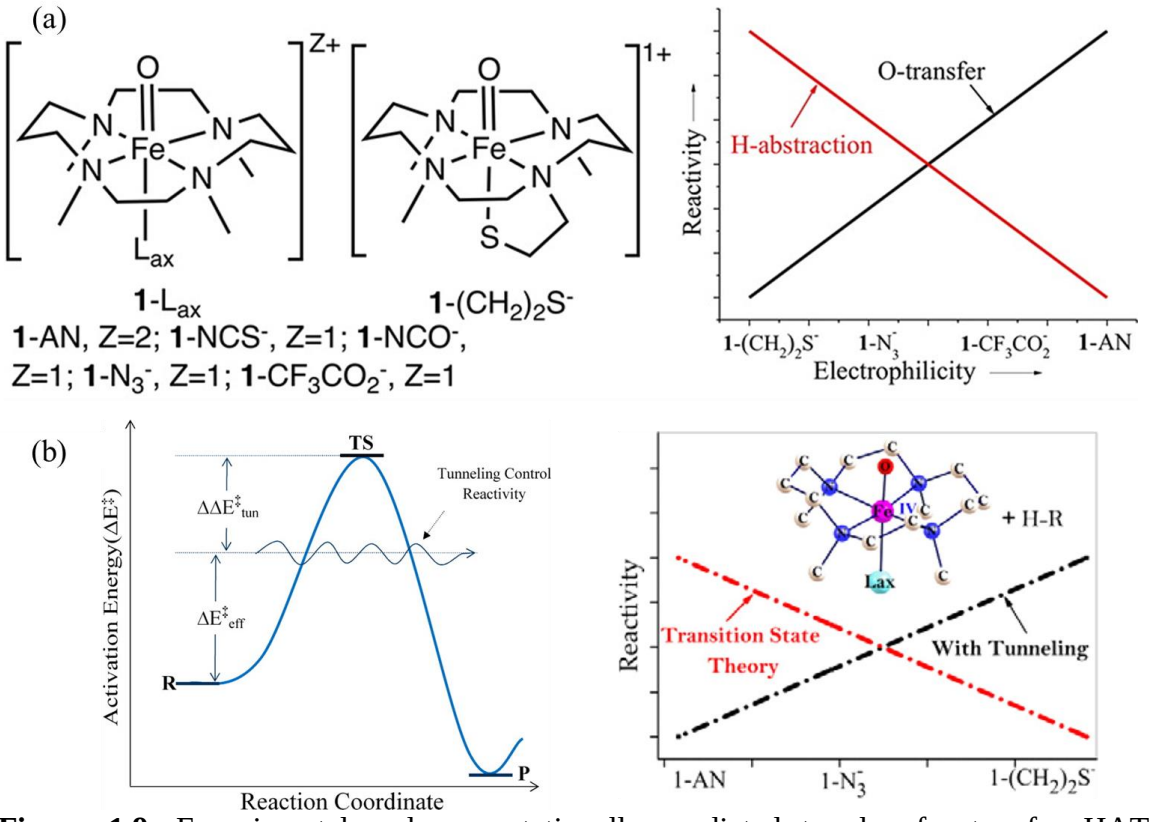

Figure 1.9. Experimental and computationally predicted trends of rates for HAT reactions from DHA with a series of Fe(IV)-oxo complexes, $[Fe^{IV}(O)(TMC)(L_{ax})]^{z+}$ (z =1,2). Adapted with permission from Ref 37a.

The rates of oxygen atom transfer from triphenylphosphine are explained using the more intuitive rationale, wherein making the trans ligand more electron poor increases the electrophilicity of the Fe(IV)-oxo unit which translates to faster rates of reactions. However, the rates of HAT reactions with DHA follow the opposite trend, where the more electrophilic oxo reacts slower (Figure 1.9 (a), right). Shaik and co-workers demonstrated using extensive computations that this apparently counter intuitive HAT rate trend is explained only when one invokes tunneling contributions, which lead to significant lowering of the effective activation barrier in the transition state (Figure 1.9 (b), left).[37a] They propose that the more electron donating *trans* ligands lead to "tighter" transition states, which in turn increases the tunneling contribution in these reactions, causing a significant decrease in the effective energy of activation for the HAT reaction.[37a] Indeed, the computationally predicted rate trends obtained after incorporating the correction due to tunneling are in agreement with the experimental trends, while those predicted on the basis of classical transition-state theory calculations (with no tunneling correction) diverge from the experimental trends ((Figure 1.9 (b), right).

1.5 Research objectives

As described above, the complex LCuOH is notable in its ability to perform very rapid HAT reactions with DHA. In order to put this high reactivity in perspective relative to the log(*k*) values presented in Table 1.1, the log(*k*) for the HAT reaction between DHA and LCuOH at 25 °C (extrapolated from the activation parameters)[8] is calculated to be ~2.27. This is significantly higher than most of the numbers in Table 1.1 by at least 3-4 log units (~10^3-10^4 times larger *k* values). My predominant research focus was aimed at elucidating what factors are responsible for this observed high HAT reactivity for the $[CuOH]^{2+}$ core and how these factors can be systematically tuned to alter the reactivity of the $[CuOH]^{2+}$ unit. The work presented in the subsequent chapters thus focuses on my

findings from extensive kinetic and mechanistic studies on HAT reactions of the $[CuOH]^{2+}$ core.

In Chapter 2, I present the results of my efforts to study the HAT reaction of LCuOH in light of PCET theory. The results of the application of the concepts discussed in Sections 1.3 and 1.4 towards the study of LCuOH will be presented in detail. I describe the experimental determination of the thermodynamic driving forces for HAT (given by the CPET square scheme) with an aim of finding a rationale for the high HAT reactivity. The discussion then turns to evaluating how the thermodynamics of the HAT correlate with the kinetics of the HAT reaction. Finally, a summary of the effects of ligand electronic perturbations to the LCuOH complex on the spectroscopic features and HAT reactivity patterns (thermodynamics and kinetics) is presented.

In Chapter 3, I present the results of alterations in the properties of the $[CuOH]^{2+}$ core derived from installation of anionic sulfonate substituents on the ligand backbone (Figure 1.10). The synthesis and spectroscopic characterization of this novel ligand framework and corresponding copper(II) complexes will be discussed. This section is followed by discussion of the spectroscopy and reactivity patterns of the $[CuOH]^{2+}$ core that was generated using this new ligand. The installation of the pendant anionic sulfonate groups makes the new $[CuOH]^{2+}$ core dianionic (as opposed to the previously described neutral LCuOH), and the potential effects of this secondary coordination sphere modification to the supporting ligand framework are discussed.

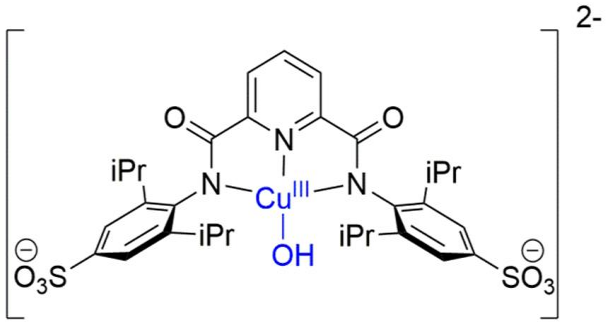

Figure 1.10. Targeted complex using pendant anionic sulfonate groups on the ligand backbone

In Chapter 4, I present the results of kinetic and mechanistic studies of the reactions of $[CuOH]^{2+}$ cores with a series of *para*-substituted phenolic substrates (Figure 1.11). The reaction mechanism for the PCET reaction involving a C-H bond generally involves a concerted proton-electron transfer because C-H bonds are neither innately acidic (poor proton donor) nor reducing (poor electron donor). Reactions with potentially more acidic phenolic substrates were performed with the ultimate goal of investigating if a switch of the mechanism from a concerted proton-electron transfer to a stepwise pathway within a series of analogous phenolic substrates could be achieved by merely altering the electronic properties of the phenol.

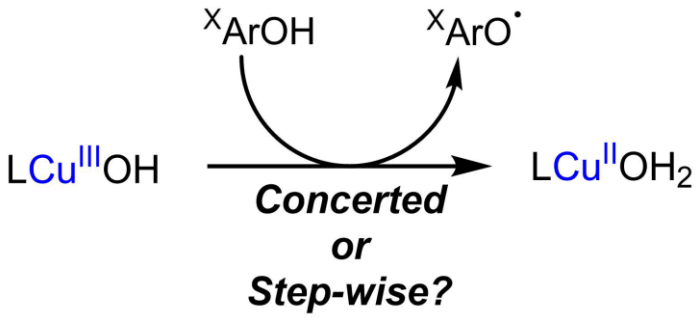

Figure 1.11. Reaction of LCuOH with a series of *para* substituted phenols.

Finally, in Chapter 5, I will present the results of efforts geared towards the synthesis and characterization of novel high-valent copper(III)-phenolate complexes using the strongly electron donating pyridine dicarboxamide ligand framework (Figure 1.12). This ligand framework has been successfully used for the generation of the mononuclear copper(III)-hydroxide core. Additionally, in the previous study of the reactions of the $[CuOH]^{2+}$ unit with the *para*-substituted phenols, we had observed the putative involvement of such high-valent copper(III)-phenolate/copper(II)-phenoxyl complexes as potential intermediates and/or reaction products. Accurately defining the electronic and spectroscopic oxidation states of such species is an underlying theme of this chapter. The synthesis and spectroscopic characterization of a series of electronically varying copper(II)-phenolate complexes will be presented first. This discussion will be

followed by an exploration of the oxidation chemistry of these compounds using multiple spectroscopic methods to unambiguously determine the electronic structure of the oxidized species as either copper(II)-phenoxyl or copper(III)-phenolate species.

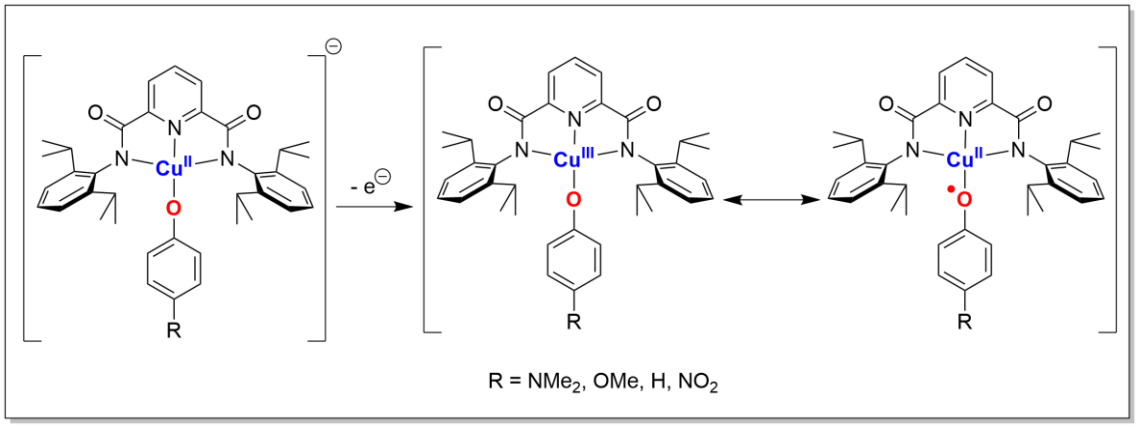

Figure 1.12. Oxidation chemistry of copper(II)-phenolate complexes targeted

Chapter 2

Thermodynamics And Kinetics Of Hydrogen Atom Transfer From Hydrocarbons By Copper(III)-Hydroxide Cores[a]

[a] The results presented in this chapter were previously published in:

(1) Debanjan Dhar, and William B. Tolman*. Hydrogen Atom Abstraction from Hydrocarbons by a Copper(III)-Hydroxide Complex. *J. Am. Chem. Soc.* **2015**, *137*, 1322-1329.

(2) Debanjan Dhar[†], Gereon M. Yee[†], David W. Boyce, Hongtu Zhang, Büsra Dereli, Christopher J. Cramer*, and William B. Tolman*. Perturbing the Copper(III)-Hydroxide Unit Through Ligand Structural Variation. *J. Am. Chem. Soc.* **2016**, *138*, 356-368.

[†]*These authors contributed equally to this work.*

2.1 Introduction

Elucidation of the properties of high-valent copper-oxygen intermediates proposed for oxidation reactions catalyzed by copper based enzymes and other systems is essential for gaining mechanistic insights and developing more efficient catalytic processes. Extensive studies of reactions of dioxygen and other oxidants with copper complexes has led to the identification of a number of crucial copper-oxygen species relevant to metalloenzymes and other catalytic intermediates.[7] Based on these studies a plethora of copper-oxygen intermediates have been proposed for enzymatic systems and they have been suggested to be capable oxidants of organic substrates, but the exact nature of the active oxidant in these reactions is still not completely understood. Hence, much needs to be done *via* synthetic chemistry approaches to evaluate provocative proposals for such motifs involved in oxidation catalysis. Along these lines, a number of computational studies have evaluated the possibility of a $[CuO]^+$ unit ("copper-oxyl" type species) as a potent oxidant in a number of biological and synthetic oxidation reactions.[10]

However, an intermediate of this nature has only been definitively characterized in the gas phase,[12] and direct evidence for its involvement in enzymes or model compound systems is lacking. Towards the ongoing pursuit of this elusive intermediate, in 2011 the Tolman group reported the synthesis and spectroscopic characterization of a mononuclear copper(III)-hydroxide core $[CuOH]^{2+}$ supported by strongly electron donating pyridine dicarboxamide ligand frameworks (Figure 2.1).[8,13,14] This $[CuOH]^{2+}$ core, which can be viewed as a protonated version of the elusive copper-oxyl species, was accessed through a one-electron oxidation of the corresponding copper(II)-hydroxide species ($[Bu_4N][LCuOH]$) at low temperatures. It was also demonstrated that this $[CuOH]^{2+}$ complex was capable of performing rapid hydrogen atom transfer (HAT) from the relatively weak C-H bonds of 9,10-dihydroanthracene (DHA) to form anthracene and the corresponding copper(II)-aqua complex (Figure 2.1, for R = *i*Pr, k = 1-24 $M^{-1}s^{-1}$ from -80 to -30 °C).[8] Additionally, this overall second order reaction featured a large kinetic isotope effect (k_H/k_D = 44 at -70 °C) consistent with a rate-determining HAT process involving significant quantum mechanical tunneling contributions.

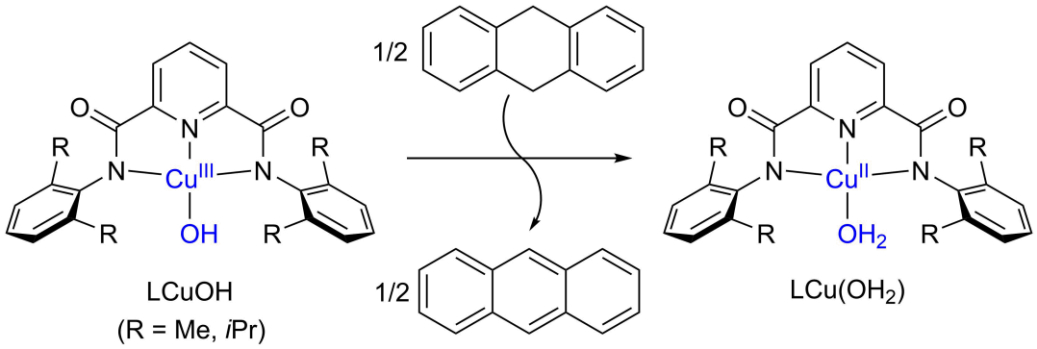

Figure 2.1. The reported mononuclear copper(III)-hydroxide complex along with the corresponding HAT reaction performed with DHA.

The observed rapid rate of HAT is particularly intriguing in view of the fact that LCuOH is a weak oxidant (for R = *i*Pr, $E_{1/2}$ = -0.076 V vs. Fc^+/Fc in acetone).[8] Thus, in order to provide a rationale for this high reactivity and place the properties of LCuOH in

perspective, it is informative to draw comparisons to other characterized metal-oxo/hydroxo complexes from the first transition series that perform similar HAT processes. A wide variety of such high-valent complexes of iron and manganese, for example, have been prepared and their reactivity with substrate C-H bonds has been explored in efforts to understand their intrinsic properties and evaluate their feasibility as catalytic intermediates.[9i,31c,33] Critical mechanistic insights have been obtained in these studies through evaluation of the HAT reaction thermodynamics. In particular, the bond dissociation enthalpy (BDE) or free energy (BDFE) of the O-H bond formed in the product complex as a result of the HAT process was measured and it has been postulated that the strength of this nascent bond is very often a key determinant in such reactions[16,22,26,28,33] as it provides the thermodynamic driving force that is proposed to influence the rates of HAT. Correlations of the BDE/BDFE with reaction rates (i.e., log(*k*) vs. BDE plots) and evaluations of the interplay of redox potential and pK_a that underly the BDE/BDFE values have been shown to be especially useful in predicting and/or explaining the fate of such HAT processes.[16,22,26,28] As described in the previous chapter (Section 1.3.1), the BDE or BDFE may be calculated using Hess' law and a square scheme once the redox potential, the pK_a, and a constant C (associated with the $H^+/H^\bullet$ standard reduction potential in a given solvent) for the corresponding HAT process are determined.

In this chapter, I present the results of the application of such proton-coupled-electron transfer (PCET) thermodynamic analysis pertinent to the HAT reaction kinetics of LCuOH. Additionally, the importance of other factors like quantum mechanical tunneling will also be highlighted through detailed analysis of the rates of HAT reactions with DHA at different temperatures. Finally, comparisons will be drawn to other reported systems along with a brief discussion on how electronic perturbations to the supporting ligand framework of the $[CuOH]^{2+}$ core may influence these parameters.

2.2 Evaluation of HAT thermodynamics via determination of the O-H BDE in the copper(II)-aqua complex ($LCuOH_2$).

The PCET square scheme for LCuOH is shown in Figure 2.2. As discussed above, the BDE of the O-H bond in $LCuOH_2$ is given by Eq. 2.1,[16]

$$\text{BDE (kcal mol}^{-1}) = 1.37\text{pK}_a + 23.06E° + C_H \qquad \text{eq. 2.1}$$

and it can be evaluated by experimental determination of either $pK_{a(1)}$ and $E°_{(1)}$, or $pK_{a(2)}$ and $E°_{(2)}$, in a solvent for which the value of the constant C_H is known. Owing to the ease of accessibility of $[LCuOH]^-$, the preferred parameters that can be experimentally determined are $pK_{a(1)}$ and $E°_{(1)}$. While previous reported experiments were performed using acetone as the solvent,[8] its acidity, the lack of a known C_H value for acetone, and the unavailability of pK_a values in acetone for organic conjugate acid-base pairs for use in evaluating the acid/base equilibrium required the use of an alternate solvent. We chose THF, which lacks acidic functionality, and for which C_H is known to be 66 kcal/mol[21,39] and numerous organic acid-base pK_a values are available.[40]

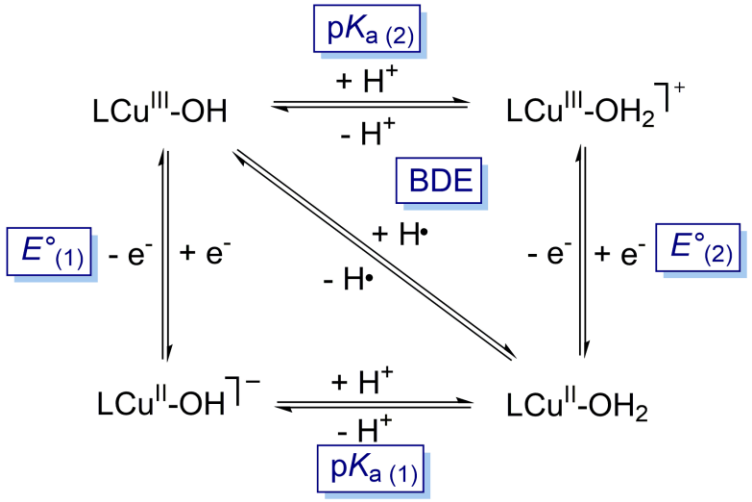

Figure 2.2. The PCET square scheme for LCuOH showing all involved components and the corresponding thermodynamic parameters.

2.2.1 Determination of $pK_{a(1)}$

The value of $pK_{a(1)}$ can in principle be determined by either starting from $[LCuOH]^-$ or $LCuOH_2$, titrating in known amounts of an acid/base for which the pK_a value in THF is known, and measuring the equilibrium constant for the reaction. However, the use of THF led to a complication, as it was discovered that dissolution of brown crystals of $LCuOH_2$ in THF resulted in the formation of a green solution. Working under the initial hypothesis that this color change indicated a ligand exchange reaction involving replacement of the H_2O ligand by solvent THF, solutions of $LCuOH_2$ in THF were treated with a drying agent (3 Å molecular sieves) and the complex re-isolated. The product was identified as the THF adduct, LCu(THF), on the basis of an X-ray crystal structure (Figure 2.3) and elemental analysis. The coordination environment about the copper ion in the crystal structure is best described as pseudo square planar with standard Cu-O and Cu-N bonds lengths of ~1.9 Å and a τ_4 value of 0.185 (where standard τ_4 values are 0 for square planar and 1 for tetrahedral geometries, respectively).[41]

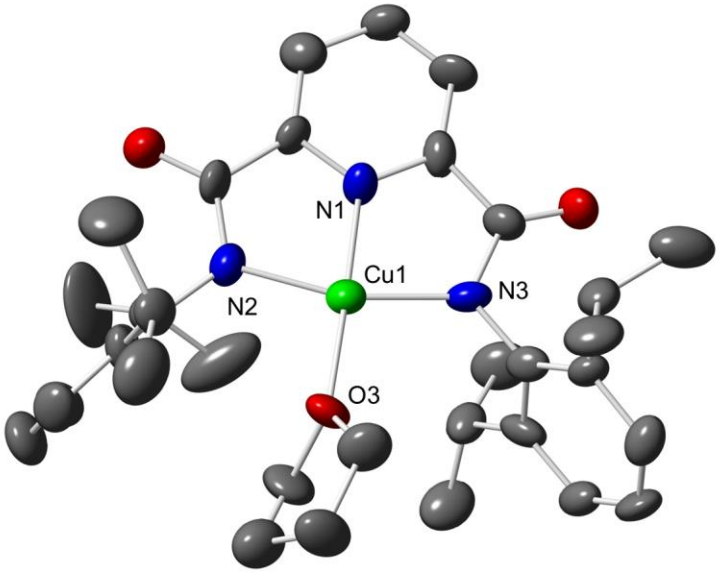

Figure 2.3. Representation of the X-ray crystal structure of LCu(THF), showing all non-hydrogen atoms as 50% thermal ellipsoids. Selected interatomic distances (Å) and angles (deg): Cu1-N1, 1.883(13); Cu1-N2, 1.947(14); Cu1-N3, 1.948(11); Cu1-O3, 1.974(11); N1-Cu1-N2, 81.9(5); N1-Cu1-N3, 81.1(6); N2-Cu1-N3, 162.5(5); N1-Cu1-O3, 171.4(6); N2-Cu1-O3, 99.9(5); N3-Cu1-O3, 97.5(5).

Owing to this complicating ligand exchange phenomenon, we realized that approaching the acid/base equilibrium for $LCuOH_2$/$[LCuOH]^-$ would only be feasible if one started from $[LCuOH]^-$. More importantly, the determination of the equilibrium constant for this acid/base reaction would no longer be the simple equilibrium reaction given by Eq. 2.2 below, as this is a driven equilibrium where the products of Eq. 2.2 (the ones lying to the right side of the reaction arrow) further react as per Eq. 2.3 to form the LCu(THF) complex. Hence, the overall reaction is actually a composite equilibrium reaction given by Eq. 2.4. In order to evaluate the true acid base equilibrium, we would have to independently measure K_2 and K_3 and use these values to calculate K_1. The results of these experiments will be discussed in the following section.

$$(Bu_4N)[LCuOH] + (Et_3NH)(OTf) \overset{K_1}{\rightleftharpoons} LCu(OH_2) + Et_3N + (Bu_4N)(OTf) \quad \text{eq. 2.2}$$

$$LCu(OH_2) + THF \overset{K_2}{\rightleftharpoons} LCu(THF) + H_2O \quad \text{eq. 2.3}$$

$$(Bu_4N)[LCuOH] + (Et_3NH)(OTf) + THF \overset{K_3}{\rightleftharpoons} LCu(THF) + H_2O + Et_3N + (Bu_4N)(OTf) \quad \text{eq. 2.4}$$

2.2.1.1 Experimental evaluation of the ligand exchange equilibrium using different spectroscopic methods.

UV-vis absorption spectroscopy : Solution state UV-vis absorption spectra for the independently generated LCu(THF) in THF and for $LCuOH_2$ dissolved in anhydrous THF were identical, indicating that in the absence of exogenous water, the ligand exchange reaction is almost completely in favor of the THF adduct owing to flooding amounts of THF solvent. Nonetheless, incremental addition of H_2O to solutions of LCu(THF) dissolved in anhydrous THF resulted in a discernable shift of UV-vis spectral features ($LCuOH_2$, λ_{max} = 558 nm; LCu(THF), λ_{max} = 577 nm; Figure 2.4, left), indicating a ligand exchange equilibrium in the presence of water (Eq. 2.3). The reaction was further studied by adding gradual increments of known amounts of H_2O into a solution of a known concentration of LCu(THF) in anhydrous THF and the spectrum at all titration points recorded. Multicomponent spectral deconvolution of the equilibrium

experimental spectrum at all titration points, modeled using pure components of $LCuOH_2$ and LCu(THF), was used to evaluate the equilibrium concentration of all the species. A representative deconvolution trace depicting the two pure components and the overall modeled spectrum is shown in Figure 2.4, right. From these values, the equilibrium constant K_2 = 440 ± 20 (Eq. 2.3) was calculated for the conversion of LCu(THF) to $LCuOH_2$. It is noteworthy that the equilibrium constant of the ligand exchange reaction actually lies in favor of $LCuOH_2$, but in THF solvent, the law of mass action causes the compound to exist almost exclusively as LCu(THF). Also, the observed λ_{max} of 558 nm for $LCuOH_2$ is in good agreement with that previously reported for the same complex in acetone (λ_{max} = 557 nm).[8]

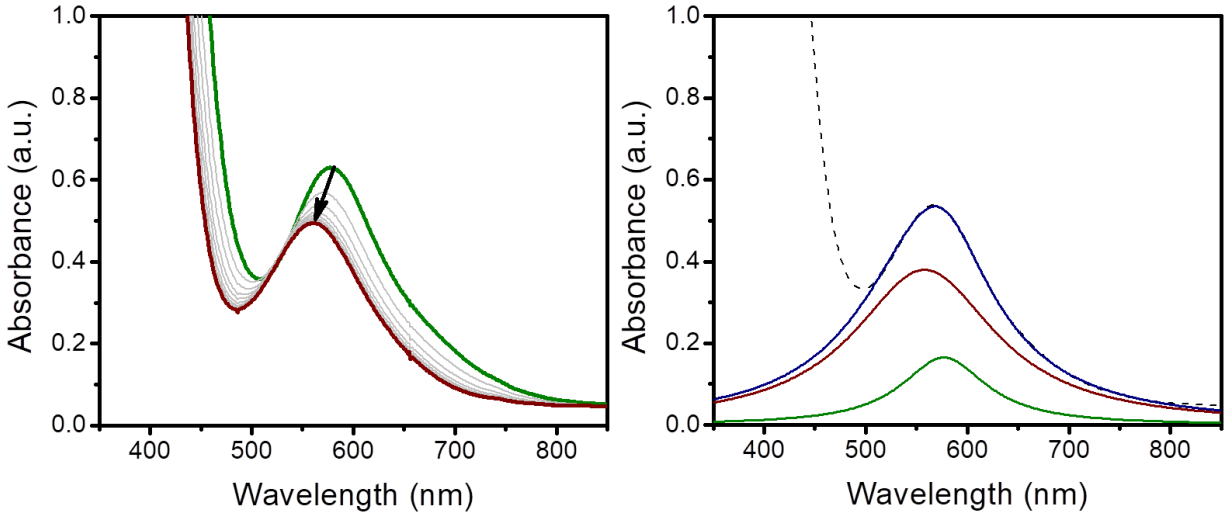

Figure 2.4. (Left) UV-vis spectroscopic changes observed upon addition of increasing amounts of H_2O to solution of LCu(THF) in THF (1 mM, green), culminating in the red spectrum (540 eq. H_2O added). (Right) Representative multicomponent deconvolution of an intermediate equilibrium spectrum depicting the two components of LCu(THF) in green and $LCuOH_2$ in red. The experimental spectrum is depicted by the black dashed trace and the overall modeled spectrum by the navy trace.

EPR spectroscopy: EPR spectral data were consistent with the UV-vis results with respect to indicating the presence of the THF and H_2O-ligated complexes. Thus, axial signals that were distinctly different were observed for pure LCu(THF) in anhydrous THF when compared to the corresponding signals in H_2O-saturated THF (Figure 2.5, left;

simulations in Figure 2.5, right; and simulation parameters in Table 2.1). While the EPR spectra are generally very similar and have the diagnostic characteristics of typical mononuclear pseudo-axial copper(II) complexes, subtle differences are observed from the simulation parameters, most notably in the $g_{||}$ region, with $LCuOH_2$ having a slightly higher observed g value in comparison to LCu(THF).

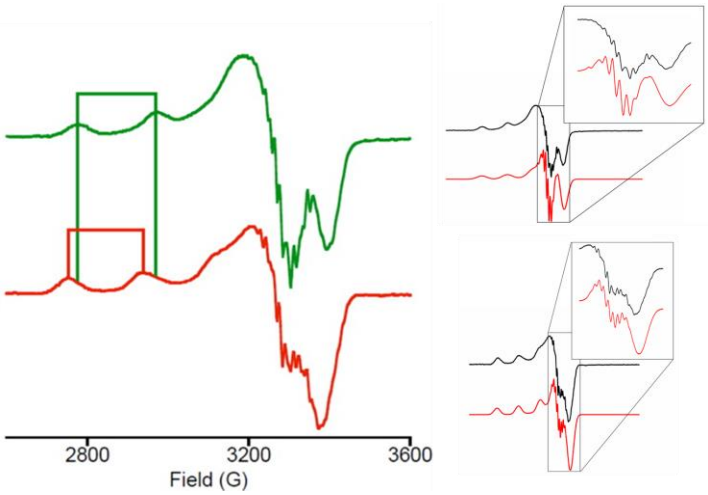

Figure 2.5. (Left) X-band EPR spectra of LCu(THF) in anhydrous THF (green), and LCu(THF) in THF saturated with H_2O (red), recorded at 125K, 9.3863 GHz. The brackets highlight the differences between the spectra in the $g_{||}$ region. (Right) Experimental (black) and simulated (red) spectra for the two cases depicted at the top and bottom respectively. Reprinted with permission from Ref 13. Copyright 2015, American Chemical Society.

Table 2.1. EPR spectral simulation parameters for LCu(THF) in anhydrous and H_2O saturated THF.

	g(x)	**g(y)**	**g(z)**	**A(Cu)**[a]	**A($N_{Pyridine}$)**[a]	**A(N_{Amide})**[a]
LCuTHF in anhy. THF	2.048	2.052	2.190	197	15	17
LCuTHF in H_2O-sat THF	2.020	2.056	2.215	195	13	17

[a] Hyperfine coupling in ($x10^{-4}$ cm^{-1})

Cyclic voltammetry: The ligand exchange equilibrium between H_2O and THF was further corroborated through cyclic voltammetry experiments. Distinct changes in the voltammograms were observed upon addition of H_2O to THF solutions of LCuTHF

(Figure 2.6, left). In anhydrous THF, LCu(THF) exhibits a pseudoreversible wave with $E_{1/2}$ = 0.735 V vs. Fc^+/Fc that was assigned to the $[LCu(THF)]^+/LCu(THF)$ couple (eq. 2.5). Progressive addition of known amounts of H_2O caused this feature to decrease in intensity with the concomitant growth of a new wave with $E_{1/2}$ = 0.345 V, which was assigned to the $[LCuOH_2]^+/LCuOH_2$ couple (eq. 2.6). The experimental voltammograms were simulated using DigiSim 3.03b[42] with the overall chemical model comprising both the redox couples being in equilibrium with each other. The overall mechanism used for the simulation is shown below (Eq. 2.5-2.7) and the known starting concentration of LCu(THF) and concentrations of added water at every titration point were used as the two input parameters during the fit.

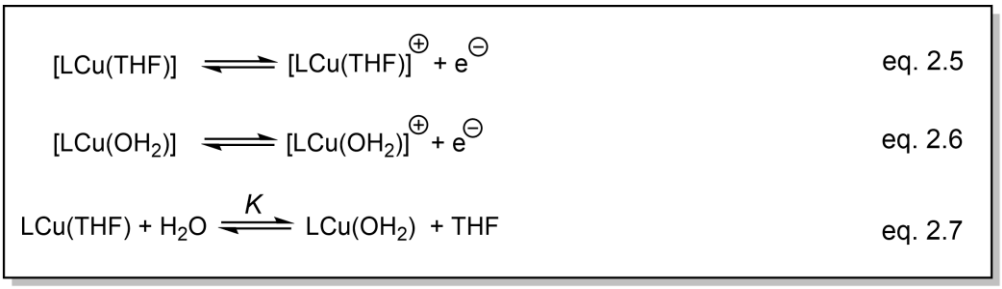

From these simulations (illustrative fits shown in Figure 2.6, right), the value of the equilibrium constant was found to be K = 408 ± 15 (Eq 2.7, Table 2.2), which was in excellent agreement with the value determined from the UV-vis titrations. Additionally, the value of $E°_{(2)}$ (Eq. 2.6, Figure 2.2) was also obtained from these results and it is +0.345 V vs. Fc^+/Fc.

Table 2.2. The ligand exchange equilibrium constant values as determined from simulation of the cyclic voltammograms at different titration points.

Eq. of water added	90	150	210	300	360	450	540
K determined from simulations	384	405	412	428	397	405	422
Average *K* = 408(15)							

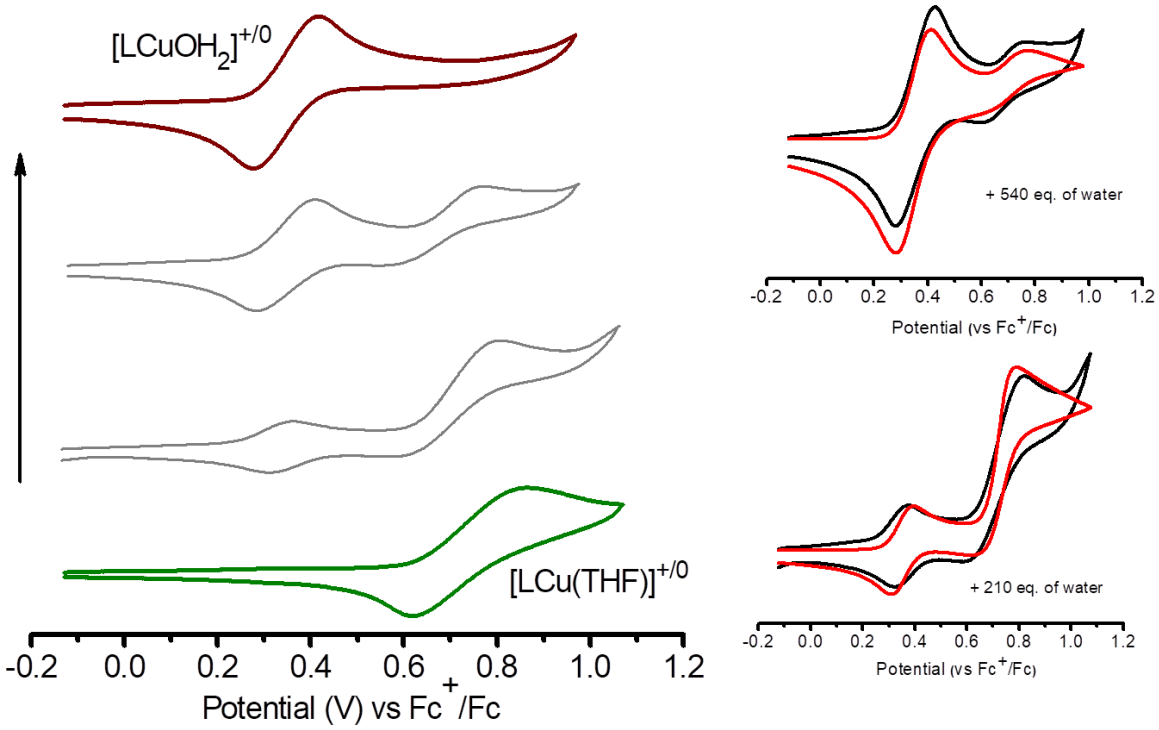

Figure 2.6. (Left) Cyclic voltammograms of LCu(THF) in anhydrous THF (green, bottom) and in the presence of variable amounts of added H_2O, culminating in a wave assigned to LCu(H_2O) (red, top). Conditions: THF, 0.2 M $TBAPF_6$, 200 mV/s. (Right) Representative overlays of the experimental and simulated cyclic voltammograms at different titration points with the experimental spectra depicted as a black trace and the simulated spectra depicted as a red trace.

2.2.1.2 Determination of the pK_a of the $LCuOH_2$ by using the composite equilibrium analysis.

As discussed above, in order to evaluate K_1 (Eq. 2.2), the overall composite equilibrium constant K_3 (Eq. 2.4), needed to be evaluated. In order to achieve this, solutions of a known concentration of [Bu_4N][LCuOH] in THF were treated with known increments of the protic acid, triethylammonium triflate ([Et_3NH]OTf), and the reaction was monitored using UV-vis absorption spectroscopy. It was hypothesized that [Et_3NH]OTf (pK_a = 14.9 ± 1.7 in THF)[40] would be a strong enough acid to perform this reaction. Additionally, the conjugate base triethylamine was expected to be poorly coordinating and hence not capable of performing any unwanted side reactions. Indeed, progressive addition of incremental equivalents of acid to solutions [Bu_4N][LCuOH] in

THF caused characteristic changes in the UV-Vis absorption spectrum (Figure 2.7, left), with the absorption peak shifting from 597 nm (for $[Bu_4N][LCuOH]$) to 577 nm, indicating the formation of LCu(THF). Multicomponent spectral deconvolution of the equilibrium experimental spectrum at all titration points, modeled using pure components of $[Bu_4N][LCuOH]$ and LCu(THF), was used to evaluate the equilibrium concentration of all involved species (a representative deconvolution trace depicting the two pure components and the overall modeled spectrum is shown in Figure 2.7, right). From these values, the equilibrium constant K_3 was evaluated to be 17 ± 1. Using the evaluated values of K_2, K_3 and known pK_a value of $[Et_3NH]OTf$ in THF[40] the value for $pK_{a(1)}$ was found to be 18.8 ± 1.8.[13]

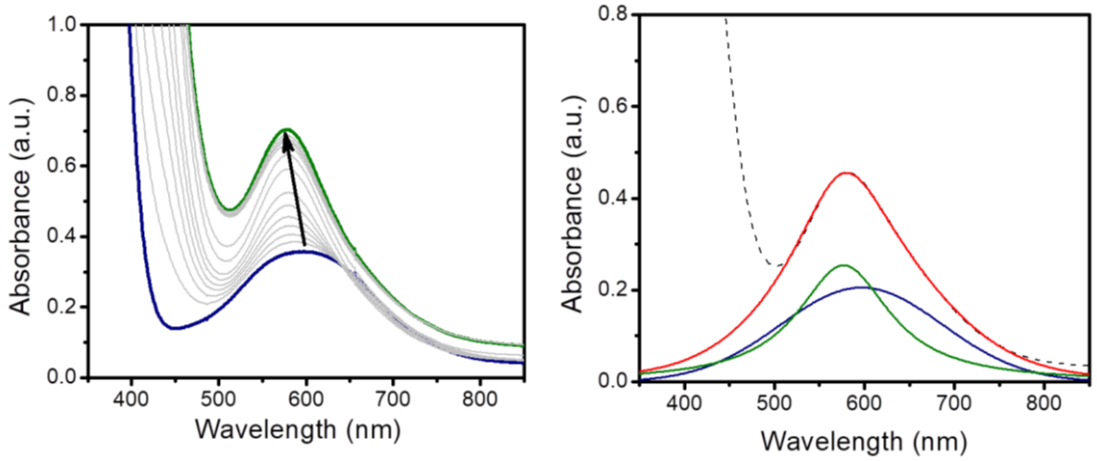

Figure 2.7. (Left) UV-vis spectroscopic changes observed upon addition of increasing amounts of $[Et_3NH]OTf$ to solution of $[Bu_4N][LCuOH]$ in THF (1 mM, navy), culminating in the green spectrum for LCu(THF). (Right) Representative multicomponent deconvolution of an intermediate equilibrium spectrum depicting the two components of LCu(THF) in green and $[Bu_4N][LCuOH]$ in navy. The experimental spectrum is depicted by the black dashed trace and the overall modeled spectrum by the red trace.

2.2.2 Determination of $E°_{(1)}$

Cyclic voltammograms of $[Bu_4N][LCuOH]$ in THF with 0.3 M $[Bu_4N][PF_6]$ at 20 °C exhibited irreversible anodic waves at low scan rates (E_{pa} ~ -0.03 V vs. Fc^+/Fc), but the return wave gained intensity as the scan rate was increased, enabling determination of $E_{1/2}$ = -0.074 V vs. Fc^+/Fc (Figure 2.8, left; Table 2.3). It was previously reported that this

single electron redox feature corresponding to the $[CuOH]^{2+}/[CuOH]^{+}$ couple had a similar $E_{1/2}$ of -0.076 V vs. Fc^{+}/Fc in acetone solvent.[8]

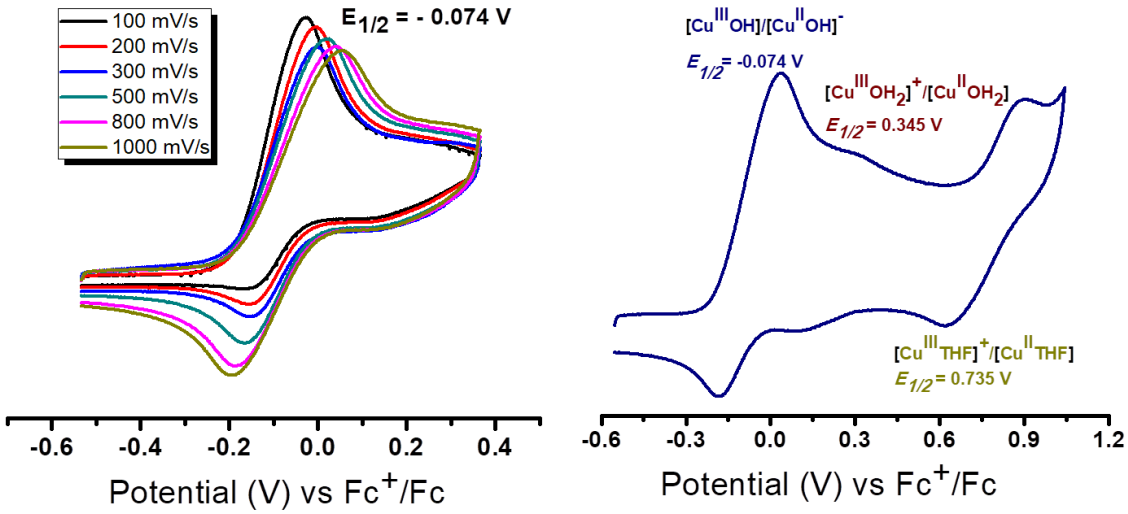

Figure 2.8. (Left) Scan rate normalized cyclic voltammograms depicting the first oxidation event for $[Bu_4N][LCuOH]$ in THF. Conditions: 0.3 M $[Bu_4N][PF_6]$, 20 °C. (Right) Cyclic voltammogram of the same complex across a wider potential sweep at a scan rate of 1 V/s. Conditions: 0.3 M $[Bu_4N][PF_6]$, 20 °C

Table 2.3. Scan rate dependence of relevant electrochemical parameters for the copper(III/II)-hydroxide couple in THF solvent.

Scan Rate (mV/s)	E_{pa} **(V vs. Fc^{+}/Fc)**	E_{pc} **(V vs. Fc^{+}/Fc)**	$E_{1/2}$ **(V vs. Fc^{+}/Fc)**	ΔE **(mV)**	i_{pc}/i_{pa}
100	-0.028	-	-	-	-
200	-0.004	-0.149	-0.077	145	0.15
300	-0.003	-0.150	-0.077	147	0.25
500	0.021	-0.163	-0.071	184	0.36
800	0.041	-0.184	-0.072	225	0.47
1000	0.052	-0.192	-0.070	244	0.52

When a sweep across a wider potential range window was done, two additional pseudo-reversible redox features are seen with $E_{1/2}$ values of ~0.35 V and ~0.73 V vs. Fc^{+}/Fc (Figure 2.8, right). These features were assigned to the one-electron oxidation events corresponding to the $LCuOH_2$ and LCu(THF) complexes, respectively, owing to the similarity to their independently measured redox potential values (Figure 2.6). It was also observed that the current intensity of both the anodic and cathodic peaks of these

subsequent features was inversely dependent on the scan rate. This observation, coupled with the observed cathodic irreversibility of the $[CuOH]^{2+}/[CuOH]^{+}$ couple at low scan rates, led to the hypothesis that upon oxidation, the generated $[CuOH]^{2+}$ reacts with the THF (which has a C-H BDE of 92 kcal mol^{-1})[43] solvent (*via* a HAT pathway) to form the corresponding $LCuOH_2$ and LCu(THF) complexes *in situ*. The implications and detailed analysis of this hypothesis will be presented in a later section (Section 2.3.1).

A further corroboration of the hypothesis that $[CuOH]^{2+}$ reacts with the C-H bonds in THF came from cyclic voltammetry experiments carried out in 1,2-diflurobenzene (DFB) solvent, which lacks weak C-H bonds and is expected to be inert to the postulated HAT reactivity. Cyclic voltammograms of $[Bu_4N][LCuOH]$ in 1,2-DFB under identical conditions to that in THF revealed only one pseudo-reversible oxidation event (corresponding to the single electron oxidation of the $[CuOH]^{+}$ complex) with a $E_{1/2}$ of -0.079 V vs. Fc^{+}/Fc (Figure 2.9). This feature demonstrated enhanced cathodic reversibility even at low scan rates (Table 2.4), indicating that in 1,2-DFB, the formed $[CuOH]^{2+}$ is more stable.

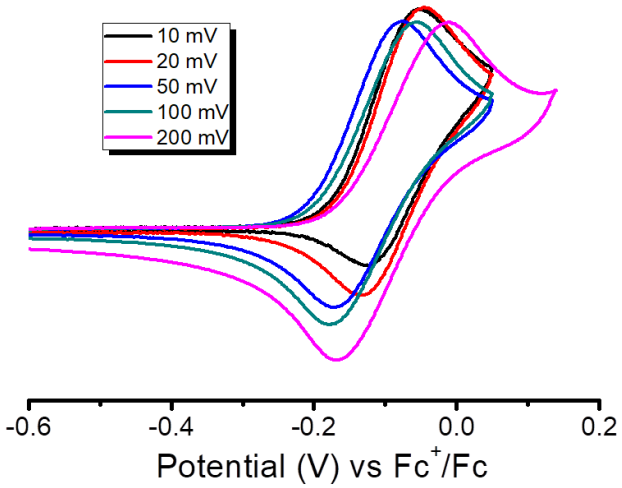

Figure 2.9. Scan rate normalized cyclic voltammograms for $[Bu_4N][LCuOH]$ in 1,2-DFB solvent. Conditions: 0.3 M $[Bu_4N][PF_6]$, 20 °C.

Table 2.4. Scan rate dependence of relevant electrochemical parameters for the copper(III/II)-hydroxide couple in DFB solvent.

Scan Rate (mV/s)	E_{pa} (V vs. Fc^+/Fc)	E_{pc} (V vs. Fc^+/Fc)	$E_{1/2}$ (V vs. Fc^+/Fc)	ΔE (mV)	i_{pc}/i_{pa}
10	-0.054	-0.125	-0.090	71	0.54
20	-0.045	-0.134	-0.090	89	0.65
50	-0.027	-0.121	-0.074	94	0.70
100	-0.009	-0.129	-0.070	120	0.80
200	-0.001	-0.157	-0.079	156	0.91
300	0.006	-0.162	-0.078	168	0.99

2.2.3 Determination of the O-H BDE in the $LCuOH_2$ and implications of the determined HAT thermodynamic parameters

Using the determined values of p$K_{a(1)}$ = 18.8 ± 1.8 (Section 2.2.1), $E°_{(1)}$ = -0.074 V vs. Fc^+/Fc (Section 2.2.2), C_H = 66 kcal mol^{-1} in THF,[21] and Eq. 2.1, we calculated the BDE of the O-H bond formed as a result of a HAT to LCuOH to be 90 ± 3 kcal mol^{-1}.[13] Additionally, using the interdependence of the thermodynamic parameters in eq. 2.1 and Figure 2.2, we estimate the value of p$K_{a(2)}$ to be 11.7 ± 2.2. This relatively high value of the BDE of the formed O-H bond in $LCuOH_2$ represents a significant thermodynamic driving force for HAT reactions with LCuOH. It is well documented in the literature that one of the key factors governing the rates of HAT reactions is the overall thermodynamic force for the reaction and generally there is a dependence between the rates and the thermodynamic force,[25,26,28] with a greater thermodynamic force leading to faster HAT reactions. The HAT reaction between DHA (C-H BDE = 76.3 kcal mol^{-1})[43] and LCuOH (O-H BDE in $LCuOH_2$ = 90 kcal mol^{-1}) is a thermodynamically favored reaction with a driving force of ~14 kcal mol^{-1} (per hydrogen atom transferred), which helps provide a strong rationale for the observed high rates of HAT from DHA to LCuOH.[13]

The evaluated pK_a of ~19 for $LCuOH_2$ indicates that $[LCuOH]^-$ behaves as a very strong base in THF, with its basicity being comparable to that of certain phosphazenes and DBU (pK_a = 19.1).[40] It is noteworthy that in aprotic solvents having low permittivity like THF (ε = 7.39), interionic interactions have an accentuating effect on the pK_a values

of neutral acids such as $LCuOH_2$.[44] For example, neutral phenols and benzoic acids have pK_a values in THF that are 8-13 units higher than in H_2O; e.g. for *p*-nitrophenol pK_a(THF) = 21 vs. pK_a(H_2O) = 7.2.[44c] This effect has been attributed to a significant enhancement of the basicity of the conjugate base in the solvent with a low dielectric constant.[44a] Consequently, it is not surprising that p$K_{a(1)}$ is significantly higher than the reported pK_a values of other $CuOH_2$ complexes which range from 7-13 in water.[45] The high basicity of $[LCuOH]^-$ is consistent with the dianionic, strongly electron donating characteristics of the supporting bis(arylcarboxamido)pyridine ligand, which also underly the low redox potential for the [LCuOH]/$[LCuOH]^-$ couple of -0.074 V vs. Fc^+/Fc. These two counterbalancing parameters combine to yield an O-H BDE of 90 ± 3 kcal mol^{-1}, that is among the highest among most reported metal-oxo/hydroxo complexes.[13] For example, while BDE values of 92-100 kcal mol^{-1} have been estimated for some $[(porphyrin)Fe^{IV}OH]^{n+}$ complexes that are cited as particularly reactive cytochrome P450 analogs,[46] and a value of > 91.6 kcal mol^{-1} was estimated for $(H_2O)_5CrOH^{2+}$,[47] most BDE values for metal complexes are < 90 kcal mol^{-1}.

2.3 Kinetics of hydrogen atom transfer from hydrocarbons performed by LCuOH.

2.3.1 Reactivity of LCuOH with THF

We hypothesized that the scan rate dependence of the electrochemical behavior of $[Bu_4N]$[LCuOH] in THF was caused by competing HAT from the C-H bonds of THF performed by the one-electron oxidized LCuOH. To test this notion, the electrochemistry experiments were repeated in THF-d_8, under the hypothesis that a kinetic isotope effect would result in enhanced stability of LCuOH in that solvent. In THF-d_8, significant cathodic reversibility was observed in the cyclic voltammograms even at low scan rates, unlike what was observed in THF (Figure 2.10). This result supports the hypothesis that the electrochemically generated complex LCuOH indeed reacts with the C-H bonds of

THF. Based on these results, the following ECE (electrochemical process followed by a chemical reaction which produces a product that demonstrates a second electrochemical process) type mechanism is proposed for the cyclic voltammetry experiments for [Bu_4N][LCuOH] in THF/ THF-d_8.

$$[LCuOH]^{\ominus} \rightleftharpoons LCuOH + e^{\ominus} \qquad \text{eq. 2.8}$$

$$LCuOH + THF/THF\text{-}d_8 \xrightarrow{k_{H/D}} LCuOH_2 \qquad \text{eq. 2.9}$$

$$LCuOH_2 \rightleftharpoons [LCuOH_2]^{\oplus} + e^{\ominus} \qquad \text{eq. 2.10}$$

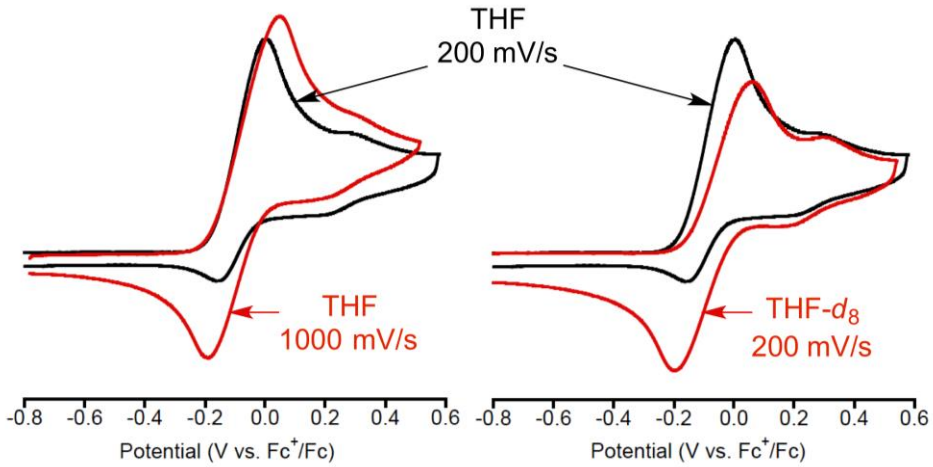

Figure 2.10. Cyclic voltammograms of [Bu_4N][LCuOH] in THF (black, 200 mV/s) overlaid with one at higher scan rate (left, red, 1000 mV/s) or at same scan rate in THF-d_8 (right, red, 200 mV/s). Conditions: 0.3 M $TBAPF_6$, 20 °C. Reprinted with permission from Ref 13.Copyright 2015, American Chemical Society.

Thus, reversible one-electron oxidation of [Bu_4N][LCuOH] (Eq. 2.8) is followed by an irreversible chemical reaction of LCuOH with THF/ THF-d_8 to form $LCuOH_2$ (Eq. 2.9), which itself undergoes a second reversible one-electron oxidation (Eq. 2.10). Through simulations of the cyclic voltammograms in THF and THF-d_8 measured over the range of scan rates 50-1000 mV s^{-1} using DigiSim 3.03b,[42] the rate constants for the chemical reaction and the kinetic isotope effect were determined: k_H = 0.114 ± 0.004 M^{-1} s^{-1}, k_D = 0.0112 ± 0.0003 M^{-1} s^{-1}, k_H/k_D = 10.2 (representative simulation traces shown in

Fig 2.11; rate constants from simulations at different scan rates listed in Table 2.5). These results clearly support attack of LCuOH at the C-H(D) bonds of THF.[13] Attempts to observe differences in rates of reaction with THF and THF-d_8 *via* UV-vis monitoring of the decay of LCuOH prepared chemically at -50 °C using $FcPF_6$ as the oxidant revealed complicated decay kinetics that could not be modeled reasonably. Nonetheless, different approximate $t_{1/2}$ values could be discerned ($t_{1/2}$(THF) = 230 s; $t_{1/2}$(THF-d_8) = 1080 s) that are consistent with attack of the THF C-H(D) bond by LCuOH. It should be noted that in THF solvent, $LCuOH_2$ further undergoes a ligand substitution reaction (as discussed in section 2.2.1.1), but for the sake of the simulations (in order to avoid over parametrization), this process was ignored.

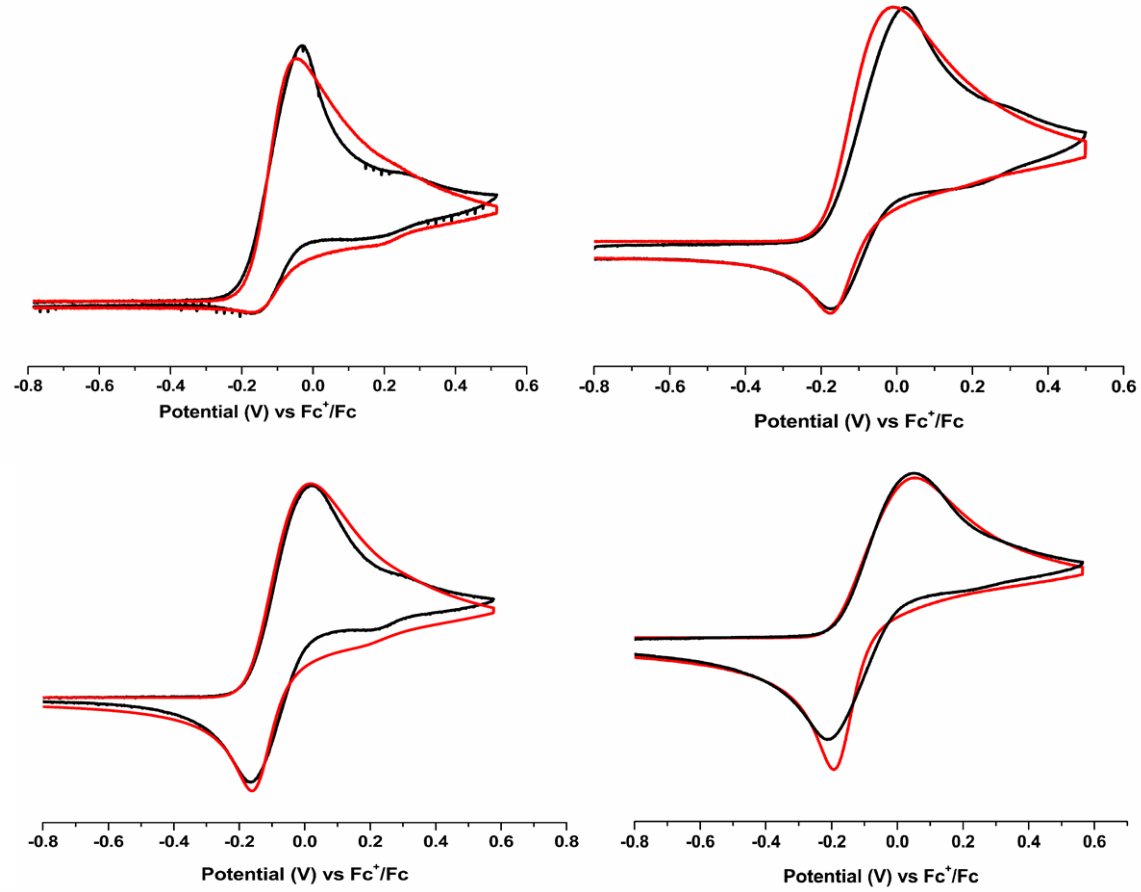

Figure 2.11. Representative experimental (black) and simulated (red) cyclic voltammograms of [Bu_4N][LCuOH] in THF (top) at two different scan rates of 100 mV/s (left) and 500 mV/s (right), and in THF-d_8 (bottom) at two different scan rates of 100

mV/s (left) and 300 mV/s (right). Conditions : 1 mM analyte, 0.3 M $TBAPF_6$, 20 °C. Reprinted with permission from Ref 13. Copyright 2015, American Chemical Society.

Table 2.5. The rate constants of C-(H/D) activation from solvent obtained from electrochemical simulations.

Scan Rate (mV/s)	k_H (M^{-1} s^{-1})	k_D (M^{-1} s^{-1})
50	0.11229	0.01195
100	0.11330	0.01191
200	0.11195	0.01185
300	0.11084	0.01248
500	0.10963	0.01249
700	0.11903	0.01185
1000	0.11951	0.01154
Average	**0.114 ± 0.004**	**0.0112 ± 0.0003**

Further, the observation of a possible HAT reaction from THF (which has a C-H BDE of 92 kcal mol^{-1}),[43] was in agreement with the high BDE of 90 kcal mol^{-1}evaluated for the O-H bond in $LCuOH_2$. Attempts to identify the final organic products of this reaction by allowing LCuOH to decay in THF followed by analyzing the volatile components by GC−MS indicated formation of 2-hydroxytetrahydrofuran and γ-butyrolactone in variable yields (as high as ~40 and 12%, respectively); neither of these compounds were present in control samples of THF solvent. The low and variable yields of these products are consistent with a HAT (radical) process.

In order to further understand the mechanism of this HAT from THF, the reactions were repeated using variable concentrations of THF as substrate with the goal of elucidating the kinetics of this reaction using low temperature UV-vis spectroscopy. For these studies, DFB was used as the solvent as it was observed that LCuOH was significantly more stable in DFB ($k_{self\text{-}decay}$= 3.3 x 10^{-7} s^{-1} at -25 °C). Treatment of a 0.1 mM solution of $[Bu_4N][LCuOH]$ in DFB at -25 °C with one equivalent of $Fc[BAr^F_4]$[48] (where BAr^F_4 = $[B[3,5\text{-}(CF_3)_2C_6H_3]_4]^-$) as oxidant immediately led to the growth of an intense absorption feature at 563 nm (ε = 12,000 M^{-1} cm^{-1})[13,14] indicating the formation of LCuOH. The origin of this charge transfer feature has been previously discussed in detail

as being a Ligand-to-Metal Charge Transfer (LMCT) from the diisopropylphenyl aromatic π-system (HOMO) to the Cu d_{x2-y2} orbital (LUMO).[14] Treatment of this solution with varying concentrations of THF substrate (0.012-9.3 M) at-25 °C under pseudo-first order reaction conditions showed enhanced rates of decay of this absorption feature. Linear fits of the decay trace at 563 nm for the initial 5% of the reaction was used to estimate the initial rate of the reaction. Plotting the initial rate of the reaction vs. $[THF]_0$ revealed saturation behavior (Figure 2.12).

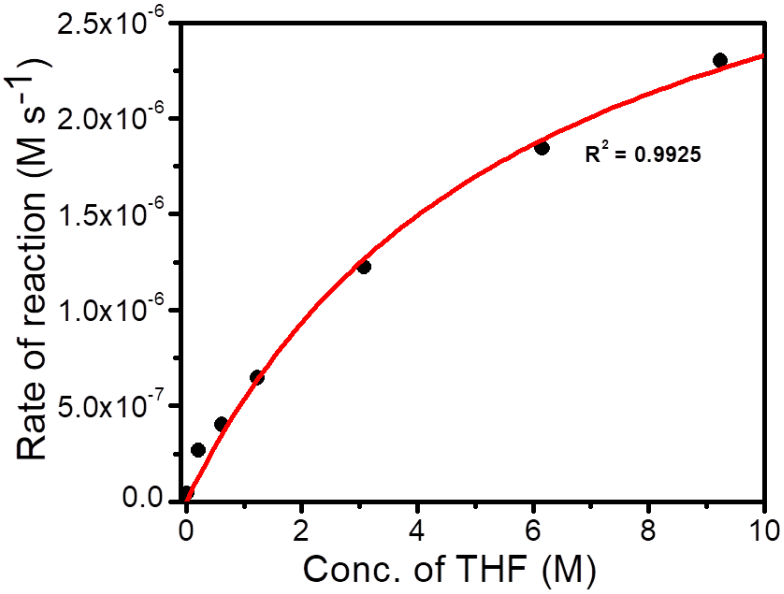

Figure 2.12. Plot of reaction rate vs. $[THF]_0$ for the reaction of LCuOH with THF in DFB. The red trace is a fit to eq. 2.8 (R^2 = 0.9925), yielding K_{eq} = 0.1688 M^{-1} and k_3 = 0.0371 s^{-1}.

The simplest rate expression consistent with saturation kinetics is Eq. 2.11, to which the data fit well (R = 0.997), yielding K_{eq} = 0.1688 M^{-1} and k_3 = 0.0371 s^{-1}.

$$rate = \frac{k_3[1][THF]}{1/K_{eq} + [THF]} \qquad \text{eq. 2.11}$$

The observation of a saturation behavior is indicative of some sort of a pre-equilibrium binding of THF and we considered two possible mechanisms which are consistent with this notion (Figure 2.13). Mechanism **A** (Figure 2.13, parameters K_{eq} and k_3) involves rapid pre-equilibrium coordination of THF to LCuOH followed by rate-determining

attack at a THF C-H bond. An alternative mechanism **B** (Figure 2.13, parameters K'_{eq} and k'_3) is also consistent with the kinetic data. In this pathway, equilibrium THF binding to LCuOH results in inhibition, with intermolecular attack of the unbound form at an exogenous THF molecule (k'_3) being preferred. While both the proposed mechanisms are consistent with the kinetic data and experimental distinction between them is complicated, it seems reasonable that mechanism **A** might be the more favored pathway as (1) axial THF binding to the copper in LCuOH could lead to activation of the α-H on the THF and make it more susceptible to a HAT process, and (2) the expected transition state geometry for the HAT pathway in mechanism **A** should be a geometrically favorable 5-membered one.

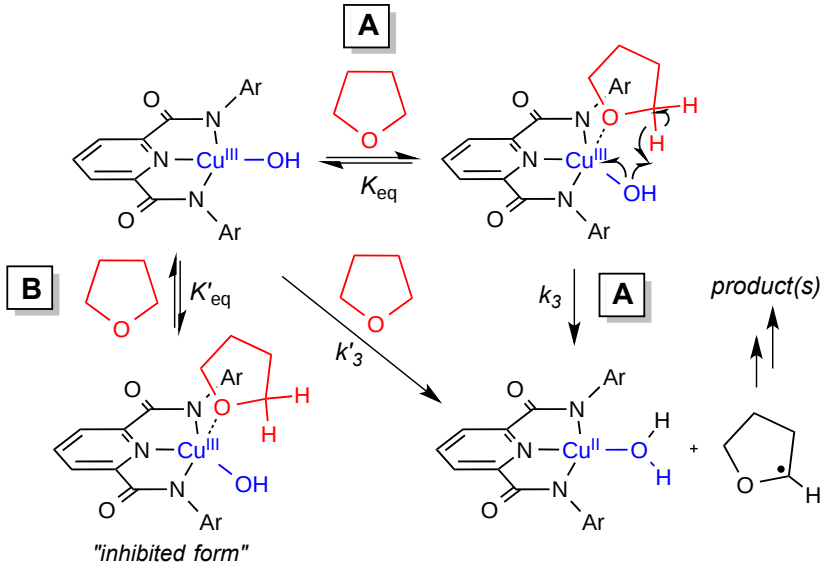

Figure 2.13. The two plausible pathways of HAT from THF which are consistent with a saturation kinetics.Reprinted with permission from Ref 13. Copyright 2015, American Chemical Society.

2.3.2 Reactivity of LCuOH with a range of hydrocarbons and interdependence between the rates of HAT and thermodynamic driving forces.

It had been previously reported that LCuOH was capable of performing very rapid HAT from DHA in acetone solvent at low temperatures.[8] With the finding that the BDE of the O-H bond in $LCuOH_2$ is 90 kcal mol^{-1} and that the formed $[CuOH]^{2+}$ complex was

capable of performing HAT from the strong C-H bonds of THF, the reactivity of LCuOH (prepared in DFB at -25 °C) was examined with a variety of other hydrocarbon substrates (DHA, fluorene, cyclohexene, diphenylmethane, toluene, and cyclohexane) spanning a BDE range of ~23 kcal mol^{-1}.[43] The reactions were monitored by UV-vis spectroscopy by following the decay of the intense absorption associated with LCuOH (0.1 mM) at 563 nm in the presence of excess substrate (0.005-8 M) at -25 °C. In all cases, the decay was accelerated in the presence of substrate, and pseudo first order rate constants (k_{obs}) were determined. In all cases apart from cyclohexane, the decay trace was fit to a single exponential decay function to obtain k_{obs}. For cyclohexane, the method of initial rates was used, whereby the slope of the linear fit of the decay trace monitored over initial 5% of the reaction was used to determine k_{obs}. Linear fits of plots of k_{obs} vs. $[substrate]_0$ yielded second order rate constants k_2 (Figure 2.14, Table 2.6).

Table 2.6. The second order HAT rate constants for reactions between LCuOH and a series of hydrocarbon substrates.

Substrate	***k* (M^{-1} s^{-1}) at -25 °C**	**BDE of C-H bond (kcal mol^{-1})**[a]
DHA	50(8)	76.3
Cyclcohexene	0.16(2)	81.0
Fluorene	0.634(8)	82.0
Diphenylmethane	0.040(6)	84.5
Toluene	0.0042(6)	88.5
THF	0.0063(9)[b]	92.1
Cyclcohexane	2.6(4) x 10^{-5}	99.8

[a] Data taken from Ref. 43 [b] This is the true second order HAT rate constant given by k_3K_{eq} from eq. 2.8

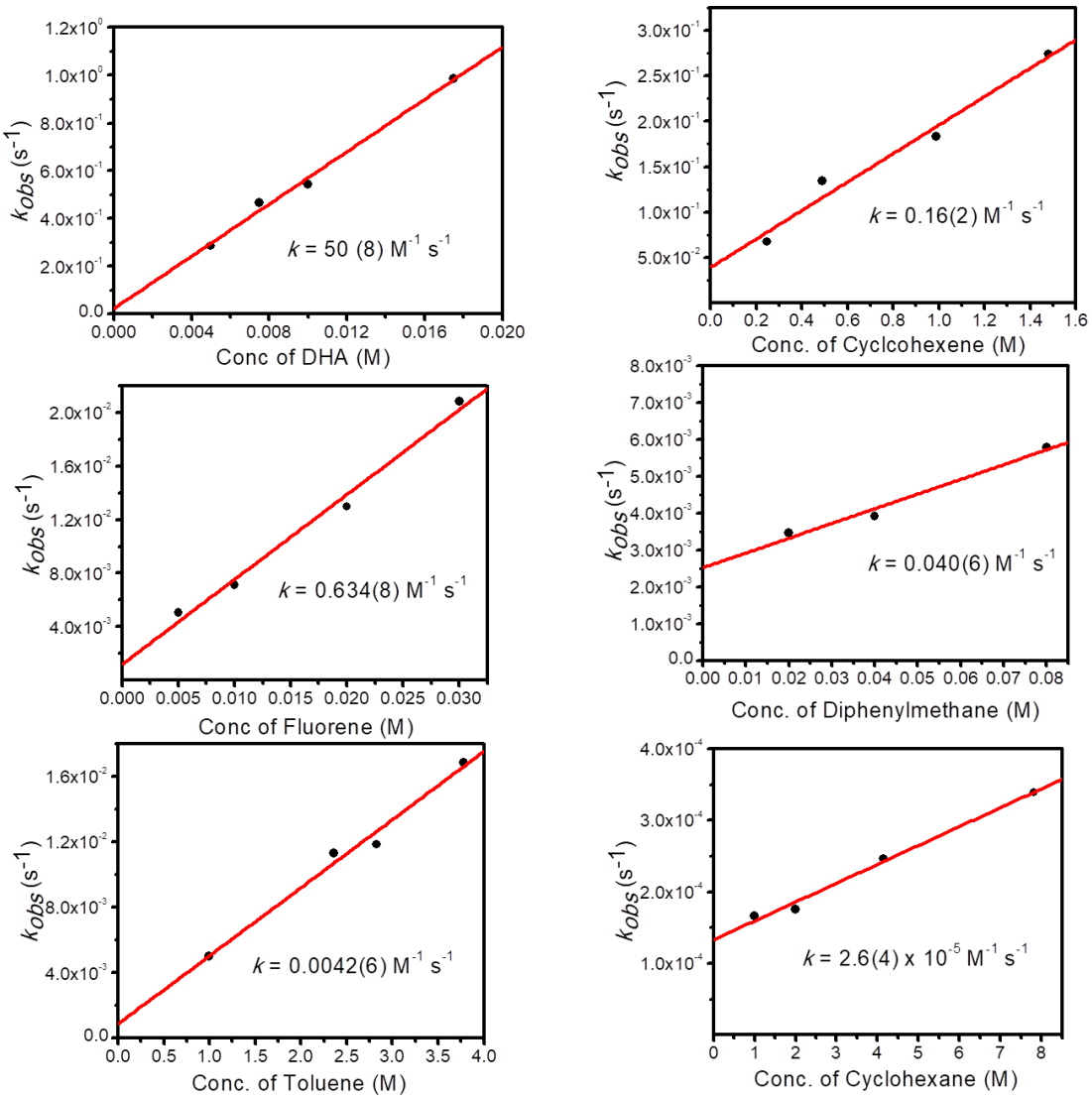

Figure 2.14. Plots of k_{obs} vs. [substrate] for the reactions of LCuOH with the substrates in DFB at -25 °C. The second order rate constants k_2 were determined from the slopes of the indicated linear fits (R^2 = 0.9816, 0.9821, 0.9625, 0.9602, 0.9773, and 0.9871, respectively)

The trends in rates of reaction as a function of substrate C-H bond strength were analyzed through a plot of log(k_2) or, for THF, log(k_3K_{eq}) vs. reported BDE values (Evans-Polanyi relation, Figure 2.15).[13,25] The data are statistically corrected for the number of H atoms susceptible to abstraction. The observed excellent linear dependence on the substrate BDE is congruent with similar plots for other oxidants,[14,16,26,33] and supports a similar HAT pathway across the range of substrates, demonstrating a strong

correlation between the rates of HAT and the thermodynamic driving force for such HAT reactions. Additionally, the lack of such a linear dependence on the substrate pK_a and redox potential (Figure 2.16) further cements the argument in favor of concerted proton-electron transfer (CPET) or HAT mechanism across the hydrocarbon substrates in preference over possible step-wise proton/electron (PT/ET) or electron/proton (ET/PT) pathways. Particularly notable is the fact that LCuOH reacts with excess cyclohexane (BDE = 99 kcal mol^{-1})[43] at a rate approximately 10 times faster than self-decay, illustrating the power of such $[CuOH]^{2+}$ species as an extremely potent HAT reagent and, thus, its potential involvement in oxidation catalysis.

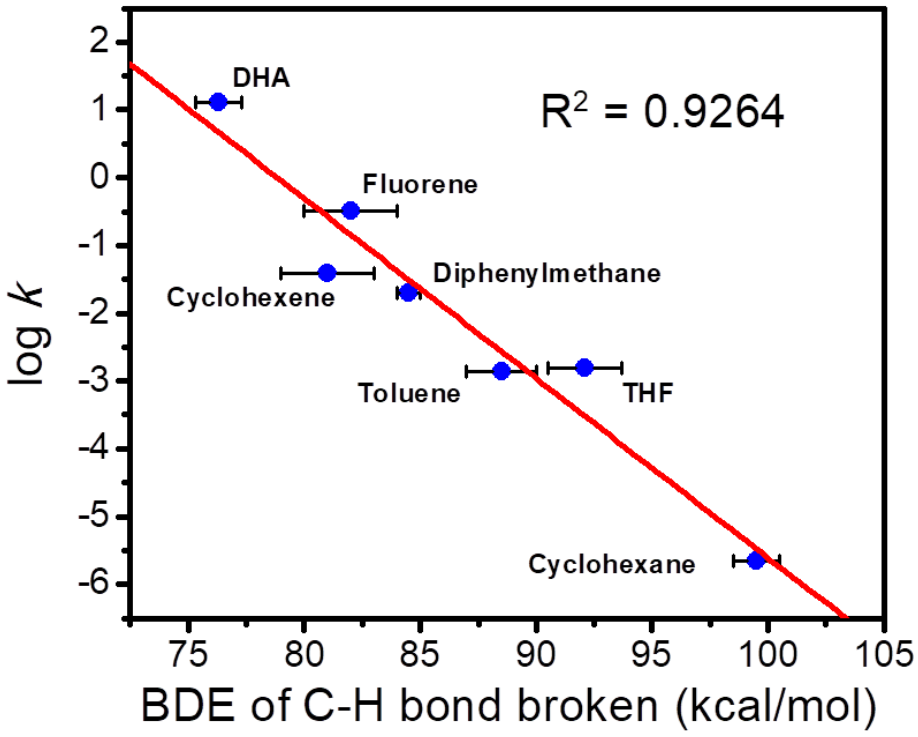

Figure 2.15. Plot of log k (where k is the second order rate constant k_2 or k_3K_{eq}) vs. BDE for the reaction of LCuOH with the indicated substrates. The linear fit depicted in red has a R^2 = 0.9264.

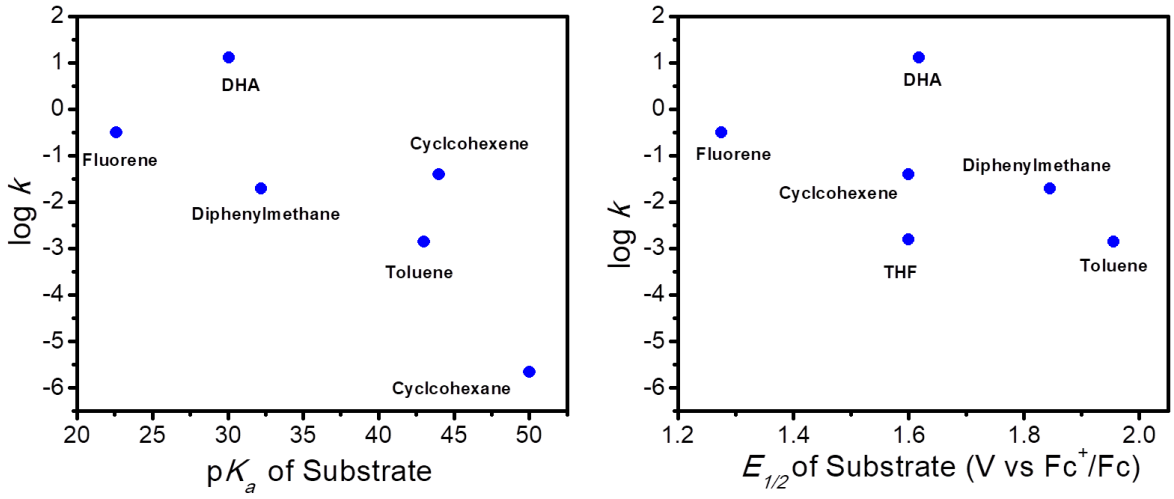

Figure 2.16. Plot of log *k* (where *k* is the second order rate constant k_2 or k_3K_{eq}) vs. pK_a (left) and $E_{1/2}$ (right) of the different hydrocarbon substrates used for HAT reactions with LCuOH.

2.3.3 Role of quantum mechanical tunneling in HAT reactions with DHA

In order to further the understanding of what additional factors play a critical role in the HAT reactions of LCuOH, the dependence of the second order rate constants of HAT from DHA and DHA-d_4 on temperature was evaluated in CH_2Cl_2 solvent across the temperature range -80 to -20 °C. In the experiments, solutions of the complexes [Bu_4N][LCuOH] in the presence of excess substrate were treated with one equivalent of [Fc][$BAr^F{}_4$], which immediately yielded the intense absorption features associated with LCuOH in the UV-vis spectrum. The decay at a single wavelength (563 nm) was monitored by UV-vis spectroscopy and fit to an exponential function to yield a pseudo-first order rate constant (k_{obs}). These experiments were repeated using 3-4 different concentrations of substrate (still in excess), and plots of k_{obs} vs. [substrate] were fit to linear equations to determine the second order rate constants (*k*) at a given temperature. Eyring plots of ln(*k*/T) vs. 1/T are shown in Figure 2.16 (left), which yielded the experimental activation parameters for the reaction as follows: $\Delta H^{\ddagger}_H$ = 5.1(1) kcal mol^{-1}, $\Delta S^{\ddagger}_H$ = -31(3) eu, $\Delta H^{\ddagger}_D$ = 5.5(3) kcal mol^{-1}, $\Delta S^{\ddagger}_D$ = -36(4) eu. In previous work using a slightly different protocol, the kinetics of the reactions of LCuOH with DHA or DHA-d_4

in acetone were measured, and the previously reported activation parameters ($\Delta H^{\ddagger}_{H}$ = 5.4(2) kcal mol^{-1}, $\Delta S^{\ddagger}_{H}$ = -30(2) eu, $\Delta H^{\ddagger}_{D}$ = 6.2(3) kcal mol^{-1}, $\Delta S^{\ddagger}_{D}$ = -34(3) eu) were in reasonable agreement with those determined in this study.[8] The kinetic isotope effect (KIE) at -40 °C was found to be 29, which is significantly higher than the classical limit, suggestive of significant tunneling contributions to the reaction rates.[34-37] However, an interesting conclusion from this study was the observation that the KIE value for the reaction between LCuOH and DHA/DHA-d_4 was relatively insensitive to temperature, as indicated by the roughly parallel H and D lines (Figure 2.17, left).

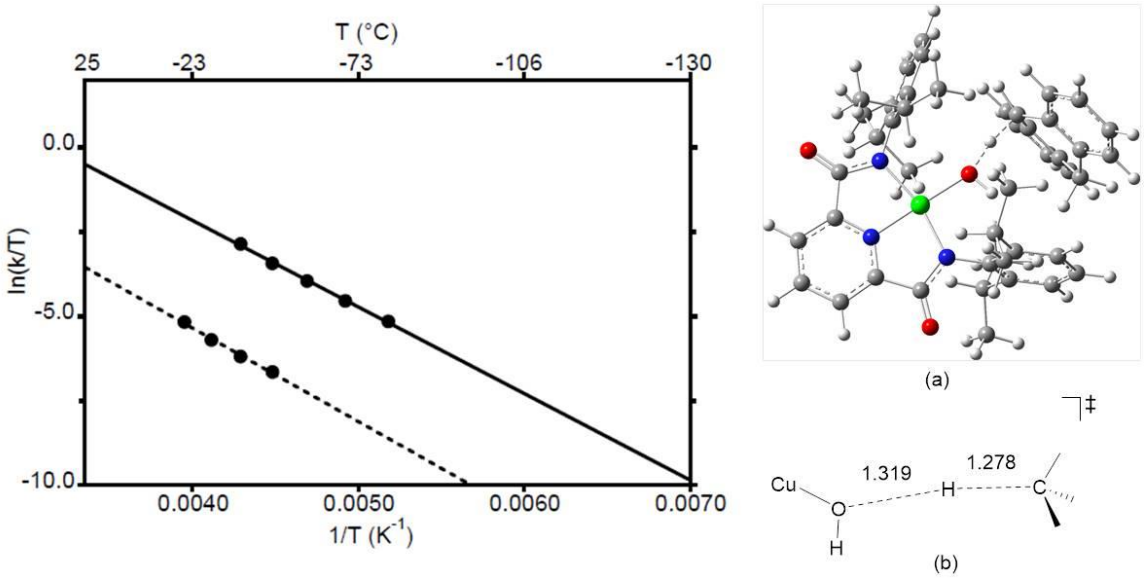

Figure 2.17. (Left) Eyring plots of ln(k/T) vs. 1/T with linear least square fits to the data for reactions of LCu(OH) (black circles with DHA (solid line) or DHA-d_4 (dashed line) in CH_2Cl_2. (Right) (a) Representative optimized HAT TS structure for LCuOH. Dotted lines indicate the forming and breaking O-H and C-H bonds, respectively. Atoms are copper (green), nitrogen (blue), oxygen (red), carbon (grey), and hydrogen (white). (b) A drawing emphasizing the forming and breaking O-H and C-H bonds, with calculated interatomic distances indicated. Adapted with permission from Ref 14. Copyright 2016, American Chemical Society.

Theoretical transition-state (TS) structures for the reaction of LCuOH with DHA were determined through the use of DFT calculations by Büsra Dereli in the group of Prof. Christopher Cramer (Figure 2.16, right). The transition-state structure was found to involve facial approach of the DHA molecule. The relatively short O-H distance of 1.319

Å between the abstracting oxygen (in LCuOH) and hydrogen (in DHA) along with the near linear C-H-O geometry (where C is the donor carbon in DHA) is consistent with a tight transition-state structure, an essential prerequisite for tunneling contributions.[14,37] Additionally, the computationally predicted activation parameters for the reactions ($\Delta H^{\ddagger}_{H(comp)}$ = 5.1 kcal mol^{-1}, $\Delta S^{\ddagger}_{H(comp)}$ = -31.7 eu, $\Delta H^{\ddagger}_{D(comp)}$ = 6.4 kcal mol^{-1}, $\Delta S^{\ddagger}_{D(comp)}$ = -34.3 eu) were found to be in reasonable agreement with the experimentally determined values.[14] Importantly, a large tunneling correction had to be employed in the computations in order to correctly predict the activation parameters for these reactions, further corroborating the non-classical behavior reflected in the low-temperature KIE values and highlighting its crucial role in the HAT reactions for LCuOH.

2.4 Effects of ligand electronic perturbations on the $[CuOH]^{2+}$ core

In an extension of the above mentioned work pertaining to the chemistry of LCuOH, the effects of ligand electronic perturbations on the properties of the $[CuOH]^{2+}$ core were investigated. This work was done in close collaboration with Dr. Gereon M. Yee[14] and parts of this work have been discussed in detail in his thesis.[49] However, a brief overview of the key results will be presented here, with the aim of elucidating how the ligand electronic perturbations affect the HAT thermodynamics and kinetics for the $[CuOH]^{2+}$ core. The two electronic variants of LCuOH were synthesized using the two new supporting ligand frameworks $^{pipMe}LH_2$ ($^{pipMe}L$ = *N*,*N*'-bis(2,6-diisopropylphenyl)-1-methylpiperidine-2,6-dicarboxamide) and $^{NO2}LH_2$ (^{NO2}L = *N*,*N*'-bis(2,6-diisopropyl-4-nitrophenyl)pyridine-2,6-dicarboxamide). In the first case, the electron donation from the ligand framework is enhanced in comparison to the supporting ligand framework for LCuOH, by means of incorporating a stronger piperidine donor. The greater basicity and sigma donor properties of piperidine relative to pyridine ($\Delta pK_a \sim 6$)[50] was expected to lower the redox potential (stabilize the higher copper oxidation state), but increase the basicity (destabilize the deprotonated form of the product aqua complex). In the second

case, the electron donation from the ligand framework is reduced by incorporation of electron withdrawing *para*-NO_2 substituents on the flanking aryl groups of the supporting ligand framework, which should result in the generation of a stronger oxidant and weaker base when compared to the parent LCuOH. The chemical structures of the corresponding copper(III)-hydroxide complexes are shown below in Figure 2.18. In the following, I summarize the key manifestations of the electronic perturbations on spectroscopic characteristics and HAT reactivity patterns of the $[CuOH]^{2+}$ cores.

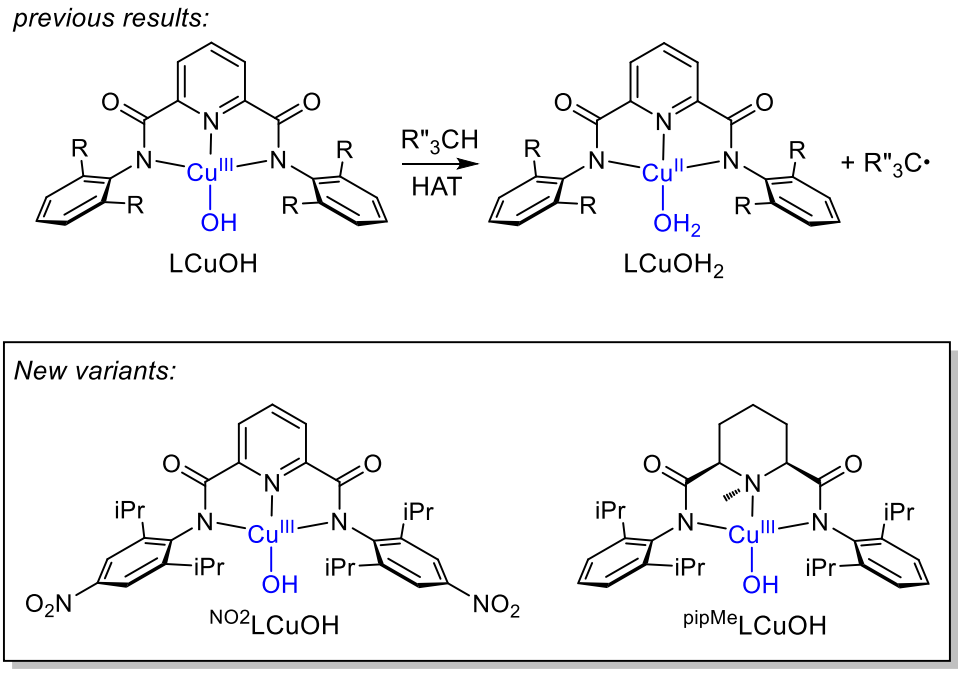

Figure 2.18. The two electronic variants of LCuOH

2.4.1 Spectroscopic manifestations of the ligand electronic perturbations

2.4.1.1 Spectroscopic characterization of copper(II)-hydroxide complexes

The effects of the ligand electronic perturbations on the spectroscopic characteristics of the copper hydroxide complexes were examined using cyclic voltammetry, EPR and UV-vis spectroscopy. In particular, the redox potential of the one-electron oxidation for the $[CuOH]^{2+}/[CuOH]^{+}$ couple obtained from cyclic voltammetry experiments (Figure 2.19, left) reflect the anticipated electronic perturbations. While the

more electron donating ligand framework ($^{pipMe}LH_2$) resulted in a lowering of the one-electron oxidation potential for the [^{pipMe}LCuOH]/[^{pipMe}LCuOH]$^-$ by ~180 mV when compared to the redox potential for [LCuOH]/[LCuOH]-$^-$, the opposing electronic perturbation using the electron deficient ligand framework ($^{NO2}LH_2$) causes the corresponding oxidation potential for the [^{NO2}LCuOH]/[^{NO2}LCuOH]$^-$ couple to be shifted to a higher potential by ~200 mV.[14]

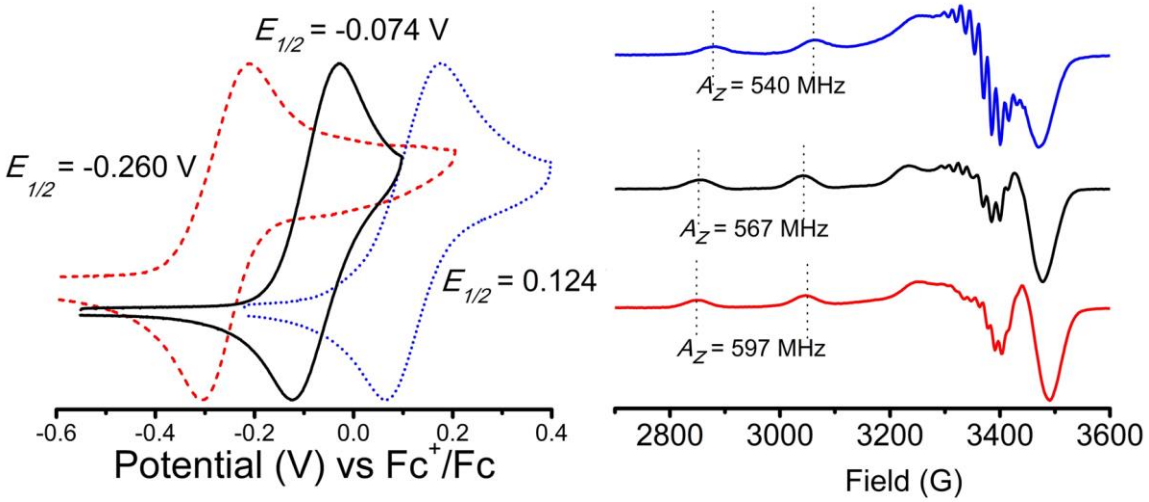

Figure 2.19. (Left) Cyclic Voltammograms of [Bu_4N][^{pipMe}LCuOH] (red dash trace), [Bu_4N][LCuOH](black solid trace) and [Et_4N][^{NO2}LCuOH] (blue dotted trace) in 1,2-DFB solvent, Conditions : 0.3 M [Bu_4N][PF_6], 20 °C, Scan rate of 50 mV/s. (Right) X-band EPR spectra THF frozen solutions of [Bu_4N][^{pipMe}LCuOH] (red), [Bu_4N][LCuOH](black) and [Et_4N][^{NO2}LCuOH] (blue) depicting the respective Cu-hyperfine splitting constants.

The electronic perturbations are also indicated in the EPR spectra of the corresponding copper(II)-hydroxide complexes. In general, the EPR spectra for the copper(II)-hydroxide complexes display very similar pseudo-axial signals with g_x ~2.03, g_y ~2.05, and g_z ~2.19, as well as resolved Cu hyperfine and rich superhyperfine splitting patterns attributed to the ligand N atoms in the coordination sphere (which are magnetically isolated from the nearby H atoms). These data are consistent with very similar solution state structures of these complexes which differ only slightly with respect to the nature of the electron donation from the supporting ligand framework. However, a subtle trend in the Cu hyperfine splitting constants A_z (g_z ~ 2.19), which are 597 MHz

([Bu_4N][^{pipMe}LCuOH]), 567 MHz ([Bu_4N][LCuOH]), and 540 MHz ([Et_4N][^{NO2}LCuOH]) is observed (Figure 2.19, right). Notably, this trend in the experimental Cu hyperfine splitting is reproduced in the calculated A_z values (determined from DFT calculations) and Mulliken spin densities (Table 2.7), both of which provide a measure of the localized spin density at the copper(II) center.[14] Taken together, these results indicate that for the above series of copper(II)-hydroxide complexes, a more electron-rich ligand set results in greater localization of spin density on the copper center, as indicated by the larger Cu-A_z value for [Bu_4N][^{pipMe}LCuOH] compared to both [Bu_4N][LCuOH] and [Et_4N][^{NO2}LCuOH], as well as its larger Mulliken spin density. Making the ligand set more electron-poor as in the case of [Et_4N][^{NO2}LCuOH] results in both a smaller Cu-A_z value and Mulliken spin density relative to the other two hydroxide complexes, indicative of greater delocalization of the unpaired electron.

Table 2.7. Experimental (from spectral fitting) vs. predicted Cu Hyperfine Coupling Constants (HFCC's) along with Mulliken spin population analysis

Complex	Experimental Cu HFCC (A_z in MHz)	Predicted Cu HFCC (A_z in MHz)	Mulliken Cu Spin Population
Bu_4N[^{pipMe}LCuOH]	597	479	+0.4538
Bu_4N[LCuOH]	567	387	+0.4522
Et_4N[^{NO2}LCuOH]	540	321	+0.4358

2.4.1.2 Spectroscopic characterization of the copper(III)-hydroxide complexes

As indicated in Section 2.1, the copper(II)-hydroxide complexes can be oxidized using a one-electron chemical oxidant to generate the corresponding copper(III)-hydroxide ($[CuOH]^{2+}$) complexes at low temperatures.[13] A diagnostic spectroscopic feature of the $[CuOH]^{2+}$ complexes is an intense ligand-to-metal charge transfer absorption in the UV-vis spectrum. On the basis of TD-DFT calculations, the origin of this charge transfer feature has been shown to be from the from the diisopropylphenyl aromatic π-system (HOMO) to the Cu d_{x2-y2} orbital (LUMO).[8,13,14] We hypothesized that

varying the ligand electronics on the supporting ligand would result in an observable difference in this LMCT feature resulting from perturbations to the corresponding HOMO and LUMO in the $[CuOH]^{2+}$ complexes. In order to test this hypothesis, the $[CuOH]^{2+}$ complexes were characterized using UV-vis spectroscopy in 1,2-DFB solvent (chosen for the observed inertness of the solvent to HAT reactions, as discussed in Section 2.2.2) at -25 °C. As anticipated, both ^{NO2}LCuOH and ^{pipMe}LCuOH depict intense charge transfer bands with λ_{max} (ε) = 513 nm (15,000 M^{-1} cm^{-1}) and 544 nm (11,000 M^{-1} cm^{-1}) respectively, akin to LCuOH which has a strong absorption band (ε =12,000 M^{-1} cm^{-1}) at 563 nm (Figure 2.20). However, the electron withdrawing *p*-NO_2 substituent in ^{NO2}LCuOH causes a greater stabilization of the HOMO resulting in an increased HOMO-LUMO gap when compared to LCuOH, which results in the observed blue shift in the absorption spectrum. On the contrary, for ^{pipMe}LCuOH both orbitals are destabilized by the σ-donating piperidine donor, but the effect is accentuated for the LUMO, again increasing the HOMO-LUMO gap and blue-shifting the LMCT transition.[14]

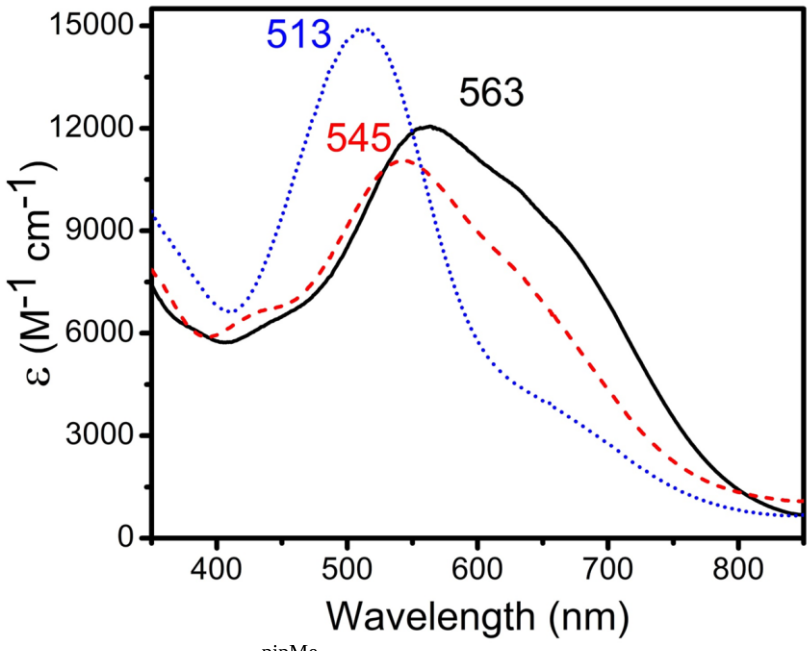

Figure 2.20. UV-Vis spectra for ^{pipMe}LCuOH (red dash trace), LCuOH (black solid trace) and ^{NO2}LCuOH (blue dotted trace) in 1,2-DFB solvent at -25 °C.

2.4.2 Effects of ligand electronic perturbations on the thermodynamics and kinetics of HAT for the copper(III)-hydroxide complexes

With the aim of understanding the effects of the ligand electronic perturbations on the thermodynamic parameters in the PCET square scheme (Figure 2.2), analogous experiments to those discussed in Section 2.2 were performed using ^{pipMe}LCuOH and ^{NO2}LCuOH. The key parameters p$K_{a(1)}$, $E°_{(1)}$, and BDE of the corresponding copper(II)-aqua complexes are summarized below in Table 2.8.[14]

Table 2.8. Summary of selected properties of $[CuOH]^{2+}$ complexes.

Compound	$E_{1/2}$ (V)[a]	pK_a	BDE (kcal mol^{-1})[b]
^{pipMe}LCuOH	-0.260	20 ± 2	88 ± 3
LCuOH	-0.074	18.8 ± 1.8	90 ± 3
^{NO2}LCuOH	0.124	16.2	91

[a] V vs. Fc^+/Fc. [b] O-H BDE of corresponding $[CuOH_2]^{2+}$ complexes.

From the above listed parameters it can be seen that increasing electron donation from the supporting ligand framework in the case of ^{pipMe}LCuOH leads to a lower oxidation potential and higher basicity for $[^{pipMe}LCuOH]^-$. On the contrary, decreased electron donation from the supporting ligand framework in the case of ^{NO2}LCuOH causes $[^{NO2}LCuOH]^-$ to behave as a weaker base, but ^{NO2}LCuOH is now a stronger oxidant. These two counterbalancing effects partially offset the BDE of the O-H bond in the corresponding copper(II)-aqua complexes, causing a net trend in the observed BDE values given by $^{NO2}LCuOH_2$ > $LCuOH_2$ > $^{pipMe}LCuOH_2$.[14] Additionally, other experimental and theoretical data also support the anticipated trend in electron donation $^{pipMe}L^{2-}$ > L^{2-} > $^{NO2}L^{2-}$.[14] Detailed examination of the HAT reactivity for ^{pipMe}LCuOH and ^{NO2}LCuOH with a wide range of hydrocarbon substrates (as used for LCuOH) in DFB solvent at -25 °C reveals an overarching correlation between HAT rates and thermodynamic driving forces for such reactions. For example, the rates of HAT from

DHA for the three complexes are 25(4) M^{-1} s^{-1}, 50(8) M^{-1} s^{-1}, and 346(52) M^{-1} s^{-1} for ^{pipMe}LCuOH, LCuOH, and ^{NO2}LCuOH respectively. The plot in Figure 2.21 of log(*k*) vs. Δ*H* (equivalent to the ΔBDE, given as the difference in the BDE of the copper(II)-aqua complex and the substrate C-H bond) for the three compounds shows a rough linear correlation between the two parameters consistent with similar HAT processes across the series and an underlying relationship between the rate of HAT and the thermodynamics of the reaction.[14]

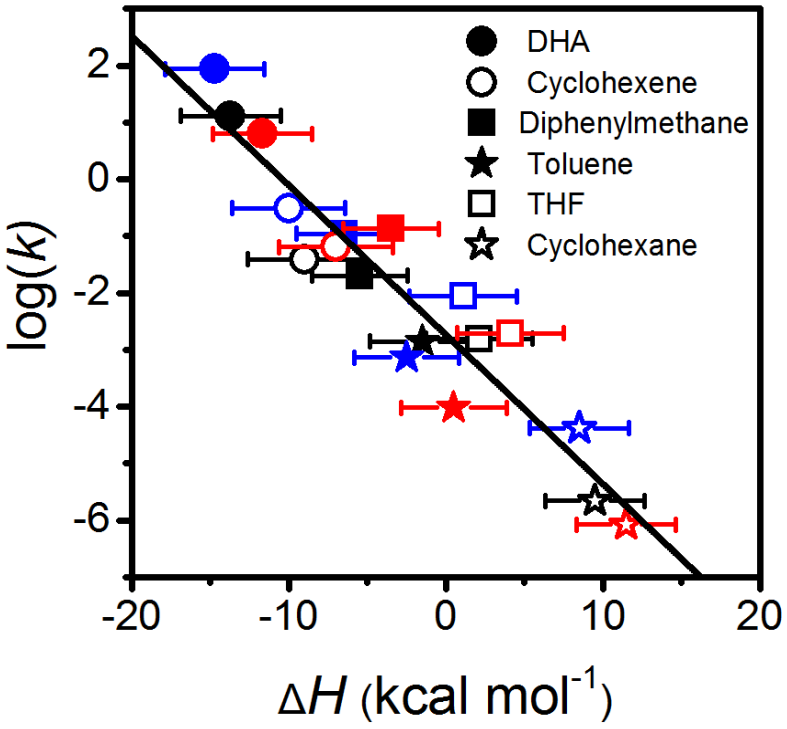

Figure 2.21. Combined plot of log(*k*) vs. Δ*H* for reactions of ^{NO2}LCuOH (blue), LCuOH (black), and ^{pipMe}LCuOH (red) with DHA (filled circle), cyclohexene (open circle), diphenylmethane (filled square), toluene (filled star), THF (open square), and cyclohexane (open star).

2.5 Summary and conclusions

The BDE of the O-H bond in $LCuOH_2$ was determined through evaluation of its pK_a and redox potential of $[Bu_4N][LCuOH]$ in THF, after defining the ligand substitution equilibrium with THF through UV-vis and EPR spectroscopy and cyclic voltammetry. Although LCuOH is a weak oxidant, the high basicity of $[LCuOH]^-$ results in a high BDE

of 90 ± 3 kcal mol^{-1} and a corresponding high rate of HAT from DHA. Detailed analysis of CV data revealed that LCuOH reacts with solvent THF/THF-d_8 *via* attack at its C-H(D) bonds with an isotope effect of 10.2. Substrates with a variety of C-H bond strengths were found to react with LCuOH in DFB solution, and a linear relationship between log(*k*) and BDE for the substrate C-H bond was established. Additionally, the effects of ligand electronic perturbations to the $[CuOH]^{2+}$ core were explored, including on thermodynamic parameters like basicity, redox potential and bond strengths. Measurement of the redox potential and pK_a parameters for HAT by the $[CuOH]^{2+}$ complexes revealed only partial compensation of these parameters and, thus, a trend in the corresponding O-H BDE values for the corresponding aqua complexes $^{NO2}LCuOH_2$ > $LCuOH_2$ > $^{pipMe}LCuOH_2$. This trend is qualitatively reflected in a similar trend in the rates of HAT from substrates with a range of C-H bond strengths. The discovery that $[CuOH]^{2+}$ attacks strong C-H bonds in a variety of substrates attests to its viability as a possible reactive species in oxidation catalysis, including by copper enzymes, with its high O-H BDE in the reaction product being a key basis for its efficient HAT capabilities.

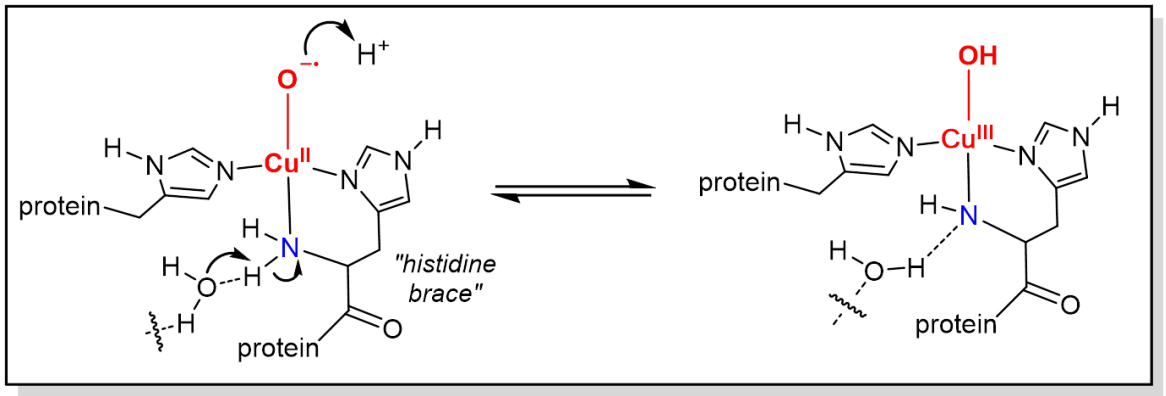

Figure 2.22. Proposed tautomerization between $[CuO]^+$ and $[CuOH]^{2+}$ unit within the active site of LPMO that involves deprotonation of the amino terminus of the 'histidine brace" concomitant with a protonation of the $[CuO]^+$ to yield a $[CuOH]^{2+}$ core.

Importantly, based on the observation that the $[CuOH]^{2+}$ core is capable of performing HAT reactions from robust C-H bonds, it is postulated that it might be

considered as a potential reactive intermediate in the enzymatic catalytic cycles of enzymes like Lytic Polysaccharide Monooxygenase (LPMO). The active site of LPMO contains a single copper ion in a tetragonal geometry with meridional binding of a monodentate His imidazolyl and a bidentate motif called a 'histidine brace' comprising an imidazolyl and amino group (Figure 2.22). Two pathways for attack at the C-H bond of the saccharide unit have been considered for LPMO, involving (a) either direct HAT from an initially formed copper(II)-superoxide $[CuOO]^+$ intermediate or (b) a $2e^-/2H^+$ O-O homolysis of this intermediate to yield the highly reactive "copper-oxyl" $[CuO]^+$ unit that then reacts with the C-H bond of the substrate. Theoretical work suggests that the latter has a lower energy barrier.[11] Based on our observations that $[CuOH]^{2+}$ unit is a potent HAT reagent, we propose that an alternate tautomeric form of the aforementioned $[CuO]^+$ core involving deprotonation of the amino arm of the histidine brace and protonation of the $[CuO]^+$ to yield a $[CuOH]^{2+}$ unit should also be considered as a viable intermediate in the proposed catalytic cycle.[13] The synthetic chemistry we accomplished thus provides precedence for a new mechanistic notion for an enzyme.

2.6 Experimental section

Materials and Methods. All reagents and solvents were purchased from commercial sources and used as received unless otherwise noted. Tetrahydrofuran (THF) and diethyl ether was passed through solvent purification columns containing activated alumina and used directly (Glass Contour, Laguna, California). 1,2-Difluorobenzene (DFB), acetonitrile, and dichloromethane were dried over calcium hydride and vacuum distilled.. All solvents were stored over 3 Å molecular sieves in a N_2 filled glove-box prior to use. All samples for kinetic measurements were prepared in a Vacuum Atmospheres glove-box under an inert atmosphere of nitrogen. HPLC grade water was degassed by sparging with N_2 for 15 min prior to use in titration experiments. Elemental analyses were performed by Robertson Microlit Laboratory (Ledgewood, NJ). UV-vis

spectra were obtained using an HP8453 (190-1100) diode array spectrophotometer. Variable temperature UV-vis experiments were performed using a Unisoku low temperature cell holder. Cyclic voltammograms were recorded using an EC Epsilon potentiostat from BASi, a glassy-carbon working electrode, and a Ag^+/Ag reference electrode; they were referenced internally using decamethylferrocene. In particular, the electrochemistry for $[Bu_4N][LCuOH]$ in THF was recorded using both a glassy-carbon and Pt-working electrode to confirm that the nature of the electrode surface does not affect the reactivity of the generated species. The final potentials were then converted vs. the standard Fc^+/Fc couple using standard conversion factors.[51] The experimental cyclic voltammograms were modeled using the DigiSim 3.03b software package from BASi. For X-ray diffraction measurements, data collection was done using CuKα radiation and a Bruker D8 Photon 100 CMOS diffractometer using normal parabolic mirrors as monochromators. EPR spectra were recorded on a CW X-band EleXsys E500 EPR spectrometer and simulations were performed using Bruker SimFonia software (version 1.25). All GC-MS experiments were conducted on an Agilent Technologies 7890A GC system and 5975C VL MSD. The GC column was a HP-5 ms with dimensions 30 m x 0.25 mm. The standard method used for all runs involved an initial oven temperature of 50 °C (held for 2 min) followed by a 20 °C min^{-1} ramp to 70 °C (held for 6 min), followed by a final 20 °C min^{-1} ramp to 230 °C (held for 15 min). The flow rate was 1 ml/min and inlet temperature was 250 °C. NMR spectra were recorded on either VI-300 or VI-500 spectrometers at room temperature. Chemical shifts (δ) for ^1H and ^{13}C NMR spectra were referenced to residual protium in the deuterated solvent (^1H) or the characteristic solvent resonances of the solvent nuclei (^{13}C). $[Et_3NH]OTf$ was prepared by adding AgOTf (257 mg, 1 mmol) to $[Et_3NH]Cl$ (137 mg, 1 mmol) dissolved in dry acetonitrile (5 ml) in the glove-box. After stirring for 20 min, the precipitated AgCl was removed by filtration and solvent was removed from the filtrate in vacuo to yield the product as a colorless viscous liquid (210 mg, 85%). ^1H-NMR (DMSO-d_6): δ 1.15 (t, *J* =

7.2 Hz, 9H), 3.09 (m, 6H), 8.84 (s, 1H) ppm. The ligand H_2L and the corresponding metal complexes $[Bu_4N][LCuOH]$ and $LCuOH_2$ were synthesized using previously reported procedures.[8] The compounds DHA-*d*$_4$,[33k] and $Fc[BAr^F_4]$[48] were synthesized using previously reported procedures.

Synthesis of LCu(THF). A solution of $LCuOH_2$ (200 mg, 0.35 mmol) in dry THF (10 mL) was stirred over 3 Å molecular sieves for 3 h. The mixture was filtered to remove the pulverized molecular sieves and the filtrate was evaporated to yield a green colored solid. The isolated solid was then dissolved in THF/Et_2O (1:1 by volume, 10 mL) and stirred for a further 30 min, following which the solvents were removed in vacuo to yield the product as a fine powdery green solid (160 mg, 75%). Small prismatic green crystals for analysis by X-ray crystallography were grown by vapor diffusion of pentanes into a THF solution of the solid at -19 °C. UV-vis (THF, 25 °C) λ_{max}, nm (ε): 397 (2700), 577 (630). Anal. calculated for $C_{35}H_{45}CuN_3O_3$: C, 67.88; H, 7.32; N, 6.79. Found: C, 67.63; H, 7.67; N, 7.27.

Synthesis of [AcFc][BAr$^F_4$]. A dry 250 mL Schlenk flask was charged with N_2 gas, AgOTf (1.00 g, 3.89 mmol), and 125 mL of dry Et_2O. Dry $NaBAr^F_4$ (3.62 g, 4.09 mmol) was added under N_2 flow, followed by acetylferrocene (0.933 g, 4.09 mmol), which resulted in the immediate formation of a yellow-green solution and a grey precipitate. The reaction was stirred at room temperature for 1 h, after which filtration under N_2 yielded a green filtrate. Subsequent solvent removal gave an orange-brown residue, which was washed repeatedly with copious amounts of pentanes to remove any remaining acetylferrocene, finally leaving a blue precipitate which was collected by vacuum filtration. Recrystallization was achieved by dissolution into minimal amounts of dry Et_2O, followed by the dropwise addition of toluene which yielded deep blue crystals. To ensure the full removal of any remaining NaOTf, this material was again taken up into Et_2O (~15 mL), filtered through celite twice, concentrated to ~5 mL, and filtered through

celite once more. The dropwise addition of toluene to the filtrate gave deep blue crystals which were collected by filtration. To ensure that no toluene remained in the product, this material was taken up into dry CH_2Cl_2, filtered through celite, and precipitated by addition of pentanes (15 mL) to give a blue powder. This was repeated once more to give the final product (1.12 g, 26.4 %). Titration against ferrocene as monitored by UV-vis confirmed a 1:1 stoichiometry. Anal. Calcd for $C_{44}H_{24}BF_{24}FeO$: C, 48.43; H, 2.22; N, < 0.02. Found: C, 48.39; H, 1.91; N, < 0.02.

Reactions of LCu(THF) with H_2O. *UV-vis.* To a solution of LCu(THF) in dry THF (3 mL, 1 mM) in a cuvette under nitrogen at room temperature was added HPLC grade degassed water in 5 μL increments. UV-vis spectra were recorded (Figure 3) and simulated using two separate Lorentzian functions centered at 577 nm (for LCu(THF)) and 558 nm (for $LCuOH_2$) *via* the program Fityk (0.9.8). The extinction coefficient for $LCuOH_2$ in THF was estimated to be ~500 M^{-1} cm^{-1} based on the absorbance at the end of the titration assuming complete conversion of LCu(THF) to $LCuOH_2$ (evidenced by no further shifts and only dilution effects beyond addition of 540 eq. of water).

EPR. To a solution of LCu(THF) in dry THF (0.6 ml, 5 mM) in a cuvette under nitrogen at room temperature was added 2.3 ml dry THF and 0.1 ml degassed HPLC grade water so as to generate a 1 mM solution of $LCuOH_2$ in THF (in the presence of excess water). The formation of the species was confirmed by UV-vis spectroscopy and then this solution was used for EPR measurements. EPR measurements of LCu(THF) were taken on a separately prepared 1 mM solution of LCu(THF) in dry THF. All EPR spectra were recorded at 125 K, 9.3863 GHz.

Cyclic Voltammetry. To a solution of LCu(THF) in dry degassed THF (6 ml, 3 mM; 0.2 M $[Bu_4N][PF_6]$) under argon, incremental amounts of degassed HPLC grade water were added and the cyclic voltammogram subsequently recorded. The voltammograms at every titration point were then simulated using two reversible redox couples for $[LCu(THF)]^+$/

LCu(THF) and $[LCuOH_2]^+$/ $LCuOH_2$ assuming an equilibrium between LCu(THF) and $LCuOH_2$. In order to initially obtain reasonably optimized chemical parameters for the chemical reaction involving equilibrium between LCu(THF) and $LCuOH_2$, the transfer coefficient (α) and heterogeneous electron transfer rate constant (k_s) for all electrochemical reactions were fixed at 0.5 and 0.02 cm/s, while the diffusion coefficient of all involved species were taken to be 10^{-5} cm^2/s.[52] Following this, all parameters were allowed to refine freely, except for α (restrained between 0.3 and 0.7) until the fitting converged. Finally, the capacitance and resistance were manually varied until a satisfactory visual fit was obtained between the simulated and the experimental voltammograms. In particular, the value of the resistance was found to be 50 Ω while that for the capacitance was found to be 3 x 10^{-6} F, which is in close agreement with previously reported values.[52] In general, a semi-infinite diffusion model at a planar electrode geometry having a surface area of 0.07 cm^2 (for glassy-carbon electrode) was employed for the simulations.

Titration of $[Bu_4N][LCuOH]$ with $[Et_3NH]OTf$. To a solution of $[Bu_4N][LCuOH]$ in dry THF (2 mL, 1 mM) in a cuvette under nitrogen at room temperature was added a solution of $[Et_3NH]OTf$ in THF (5 mM) in 0.05 mL increments. UV-vis spectra were recorded (Figure S5) and simulated to determine the relative amounts of the species in solution as described above, here using a Gaussian function centered at 597 nm ($[Bu_4N][LCuOH]$) and a Lorentzian function centered at 577 nm (LCu(THF)) (Figure S6). The concentrations of $[Bu_4N][LCuOH]$ and LCu(THF) were determined using the extinction coefficients 350 ± 3 M^{-1} cm^{-1} and 630 ± 12 M^{-1} cm^{-1}, respectively, determined from independently analyzed Beers' Law plots.

Simulation of Cyclic Voltammograms of $[Bu_4N][LCuOH]$ in THF and THF-d_8. The experimental voltammograms of $\mathbf{1}^-$ in both solvents (across scan rates ranging from 50 to 1000 mV/s) were simulated using DigiSim 3.03b with an *ECE* mechanism. In

order to initially obtain reasonably optimized chemical parameters for the chemical reaction involving LCuOH and the solvent, the transfer coefficient (α) and heterogeneous electron transfer rate constant (k_s) for all electrochemical reactions were fixed at 0.5 and 0.02 cm/s, while the diffusion coefficient of all involved species were taken to be 10^{-5} cm^2/s.[52] In addition, recognizing that the chemical reaction is essentially irreversible, the equilibrium constant for the same was fixed to be 10^5. Following this, all parameters were allowed to refine freely, except for α (restrained between 0.3 and 0.7) until the fitting converged. Finally, the capacitance and resistance were manually varied until a satisfactory visual fit was obtained between the simulated and the experimental voltammograms. In particular, the value of the resistance was found to be 50 Ω while that for the capacitance was found to be 3 x 10^{-6} F, which is in close agreement with previously reported values.[52] In general, a semi-infinite diffusion model at a planar electrode geometry having a surface area of 0.02 cm^2 (for platinum electrode) was employed for the simulations.

Procedure for kinetic studies with different substrates in DFB. To a 1.8 mL solution of a known concentration of the substrate in DFB in a cuvette, 0.1 mL of a 2 mM solution of $[Bu_4N][LCuOH]$ was added under nitrogen and the contents were cooled to -25 °C for 10 min. To this solution 0.1 mL of a 2 mM solution of $Fc[BAr^F_4]$ in DFB was added, resulting in the immediate appearance of a feature at 563 nm associated with formation of LCuOH. Subsequent decay of the absorption peak at 563 nm was monitored over time by UV-vis spectroscopy. For all substrates except cyclohexane and THF, the decay trace of the peak was fit to a single exponential decay function to obtain the pseudo-first order rate constant (k_{obs}). For cyclohexane and THF, the method of initial rates was used, whereby the slope of the linear fit of the decay trace monitored over initial 5% of the reaction was used to determine the pseudo-first order rate constant (cyclohexane) or rate (THF). For all substrates except THF, linear fitting of plots of k_{obs}

vs. the substrate concentration afforded the second order rate constant. For THF, the plot of initial rate vs. the concentration of THF was fit to Eq. 2.11.

General procedure for measuring kinetics of reactions of the copper(III)-hydroxide complexes with DHA/DHA-*d*$_4$ in CH_2Cl_2. Under an atmosphere of N_2, a 3.0 mL cuvette was charged with 1.8 mL of a known concentration of substrate (1-10 mM for DHA, 1-20 mM for DHA-*d*$_4$) in CH_2Cl_2. The cuvette was cooled to the desired temperature (-80 °C to -20 °C) for approximately 10 min, after which 0.1 mL (2 mM solution) of $[R_4N][^{X}LCuOH]$ was added (R = Et for ^{NO2}LCuOH and R=Bu for ^{pipMe}LCuOH and LCuOH). After 2 min, to this was added 0.1 mL (2mM solution) of the corresponding oxidant ($[Fc][BAr^F_4]$, in case of ^{pipMe}LCuOH, LCuOH and $[AcFc][BAr^F_4]$ in case of ^{NO2}LCuOH), which resulted in the immediate appearance of the intense UV-vis absorption feature consistent with formation of LCuOH (563 nm), ^{NO2}LCuOH (513 nm), or ^{pipMe}LCuOH (544 nm), respectively. The decay of this feature over time was monitored by UV-vis spectroscopy by recording spectra until no further change was observable. The decay trace of absorbance at the respective λ_{max} was then fit to a single exponential decay function to obtain the pseudo-first order rate constants (k_{obs}). Linear fitting of the k_{obs} vs. substrate concentration afforded the corresponding second order rate constants. These second order rate constants were then used for the Eyring analyses over the temperature range (-80 °C to -40 °C for DHA and -50 °C to -20 °C for DHA-*d*$_4$).

Chapter 3

Effects Of Anionic Substituents On The Properties Of The Copper(III)-Hydroxide Core

3.1 Introduction

Among the wide variety of high-valent copper-oxygen motifs implicated with relevance to catalytic oxidations in biological and synthetic systems,[7] the recently well characterized mononuclear copper(III)-hydroxide core ($[CuOH]^{2+}$) is notable with respect to its ability to be an excellent hydrogen atom abstraction reagent.[8,14,15] The high reactivity of such species towards hydrogen atom transfer (HAT) reactions has been attributed to the high thermodynamic driving force associated with such reactions, which is derived from the strong O-H bond formed (BDE ~ 90 kcal/mol) in the resultant product copper(II)-aqua $[CuOH_2]^{2+}$ complexes.[13,14] It has been demonstrated that electronic perturbations on the supporting ligand cause a systematic alteration in the BDE of the $[CuOH_2]^{2+}$ complexes, which is in turn manifested in differences among the rates of HAT from various substrates.[14] Previous work has demonstrated how ligand electronic perturbations affect the spectroscopy and reactivity trends across a range of three different $[CuOH]^{2+}$ cores ($[^{pipMe}LCuOH]$, [LCuOH] and $[^{NO2}LCuOH]$ in Figure 3.1) generated using supporting ligands with varying degrees of electron donation to the copper center (see Chapter 2 for details). One key conclusion drawn from these studies was that, in general, making the supporting ligand framework more electron deficient makes the resulting copper-hydroxide moiety a stronger oxidant and a weaker base. These counterbalancing effects are only partially offset, which results in the stronger oxidant having the highest thermodynamic driving force for the hydrogen atom transfer.

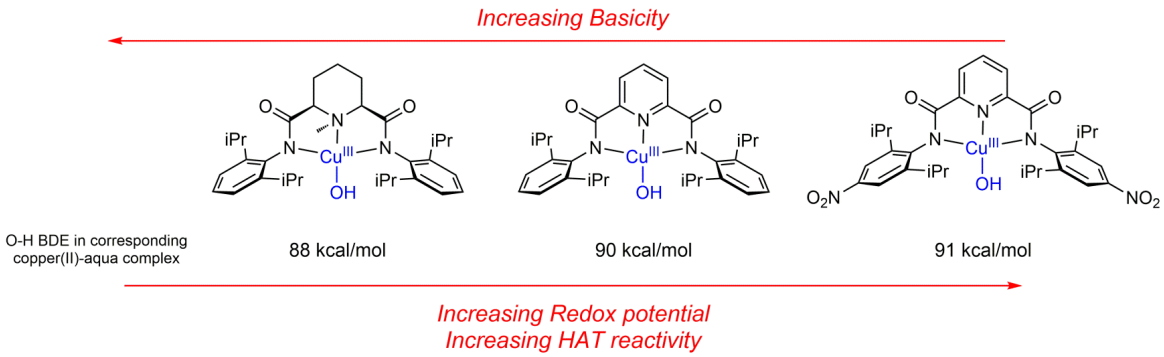

Figure 3.1. Previously studied copper(III)-hydroxide complexes

However, in the previous study one underlying theme was that the electronic perturbations were centered on the primary coordination sphere around the copper, wherein the donation abilities of the three N atoms were modulated by either (1) altering the hybridization (sp^2 in pyridine to sp^3 in methyl-piperidine, thus making it a stronger σ donor), or (2) installing conjugated electron withdrawing $–NO_2$ groups at the *para* position of the donor carboxamide nitrogen atoms in the aryl ring. Guided by these results, we then sought to explore the effects of more distal electronic modifications in this present study. In particular, we aimed to understand the effects of installation of anionic sulfonate groups on the *para* position of the flanking aryl rings (Figure 3.2). Additionally, we envisioned that the charged residues on the supporting ligand would render the copper complexes soluble in water, unlike the previously reported hydrophobic analogs. This effect would enable us to determine key parameters like the basicity, redox potential and other relevant properties under aqueous conditions, which could, in turn, provide valuable insight into the behavior of the proposed $[CuOH]^{2+}$ motif in hydrophilic active sites of enzymes.

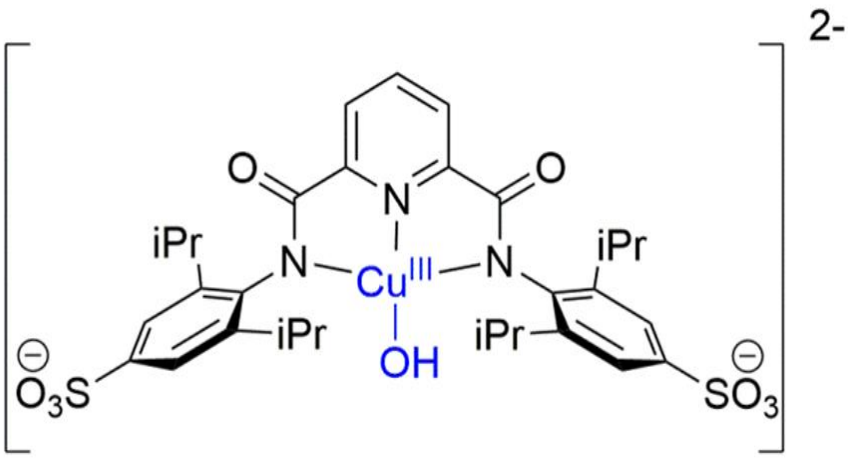

Figure 3.2. New copper complex targeted in the current study

With the incorporation of the anionic *para*–SO_3^- functionalities, an interesting question concerns how this electronic perturbation might affect the basicity and redox potential of the copper-hydroxide species. On the one hand, it would cause the current $[CuOH]^{2+}$ species to be dianionic as opposed to the previous analogs that were neutral, and it might be expected that the current system thus should be more electron-rich based on strictly electrostatic arguments. On the other hand, *para*–SO_3^- groups are intrinsically electron withdrawing in nature, as evidenced from their Hammett constant (σ_p = 0.35), which is roughly comparable to that of *para*-CHO (σ_p = 0.44).[53] Literature examples that explore such electronic effects of sulfonate groups are scarce. In one recent example, a series of sulfonate-substituted phenyl substituents at the *meso* positions of a heme-iron system were investigated in aqueous medium.[54] It was shown that inclusion of an additional SO_3^- group on each phenyl ring (net increase of four SO_3^- groups on the entire moiety) altered the oxidation potential of the porphyrin ring by less than 50 mV and the pK_a by less than 1 unit. However, this study was performed in water where efficient stabilization of charged species is achieved by means of hydration; similar trends might not translate in non-polar solvents. Additionally, there are some literature reports that implicate the Lewis basicity of the pendant sulfonate functionalities as key determinants in altering reactivity by means of secondary coordination sphere effects.[55] In one case, it

was demonstrated that the pendant anionic SO_3^- group in a mononuclear ruthenium water oxidation catalyst binds to a Lewis acidic Ce(IV) ion, which results in an enhancement in the activity of the catalyst. This "Ce^{+4} capture" has been postulated to be crucial in facilitating the O-O bond formation reaction step as it properly orients the hydroxide group bound to the Ce(IV) and enables a facile nucleophilic attack on the electrophilic Ru-oxo moiety.[55a] In a second example, it was shown that the presence of an anionic SO_3^- group on the supporting ligand framework of a catalyst was crucial in enhancing the activity of copper-catalyzed Chan-Evans-Lam coupling reactions because it causes precoordination of the electrophilic boronic acid substrate.[55b,c]

In this chapter, the synthesis and spectroscopic characterization of the novel sulfonate based ligand framework and its corresponding copper(II)-complexes will be presented. Emphasis will be placed on the spectroscopy of the copper(II)-hydroxide complex of the new ligand. Subsequently, the oxidation chemistry of the complex will be discussed, with the ultimate goal of exploring how the inclusion of the sulfonate groups on the supporting ligand framework affects the properties and HAT reactivity patterns of the $[CuOH]^{2+}$ core.

3.2 Synthesis and Characterization of the ligand $[i\mathrm{Pr_2EtNH}]_2[^{\mathrm{SO3}}\mathrm{LH_2}]$

The synthesis of bis(*N*-ethyl-*N*-isopropylpropan-2-aminium)4,4'-((pyridine-2,6-dicarbonyl)bis(azanediyl))bis(3,5-diisopropylbenzenesulfonate) or $[(i\mathrm{Pr_2EtNH})_2(^{\mathrm{SO3}}\mathrm{LH_2})]$ is outlined in Scheme 3.1.

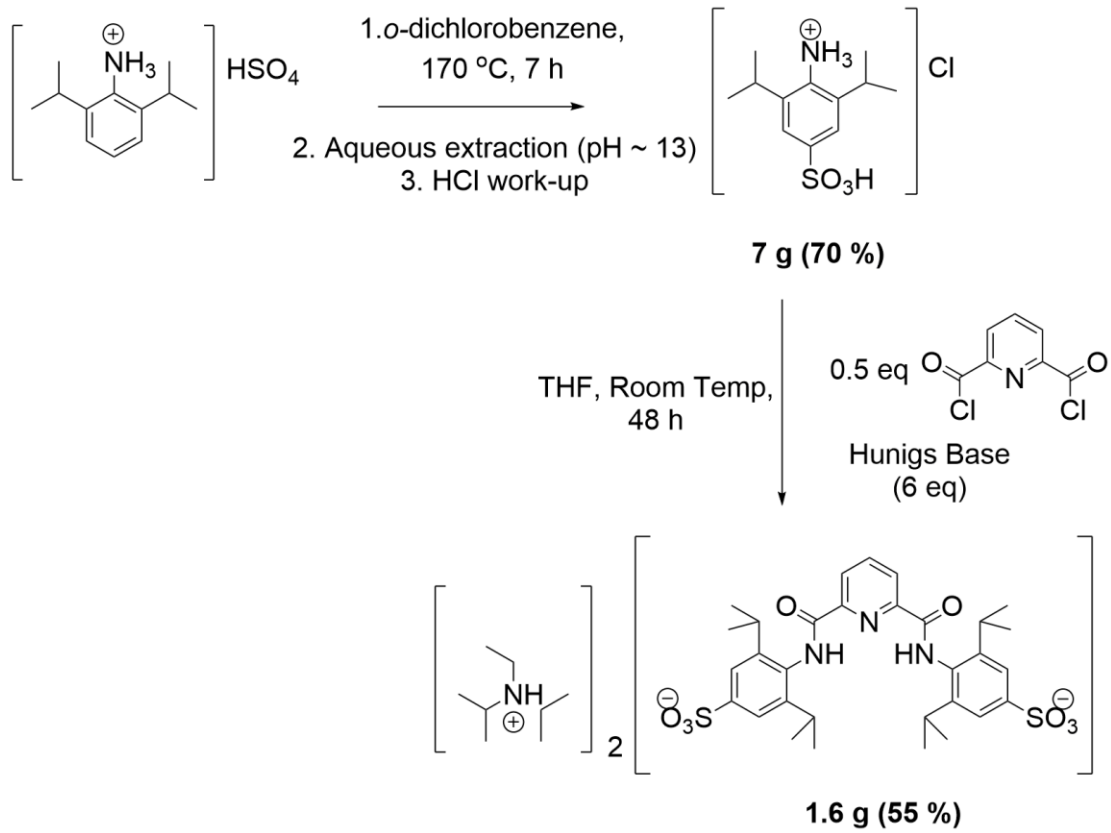

Scheme 3.1. Synthesis of the ligand $[(i\text{Pr}_2\text{EtNH})_2(^{SO3}\text{LH}_2)]$

In the first step, the precursor *p*-sulfonated anilinium salt 4-amino-3,5-diisopropylbenzenesulfonic acid hydrochloride was synthesized from 2,6-diisopropylanilinium hydrogen sulfate using a modification of a reported procedure for an analogous compound.[56] Heating of a suspension of diisopropylanilinium hydrogen sulfate in 1,2-dichlorobenzene (reaction medium chosen because of its high boiling point and inertness towards electrophilic aromatic substitution reactions) at 170 °C led to an intermolecular rearrangement and sulfonation at the desired *para* position of the activated aromatic ring of the 2,6-diisopropylaniline. An aqueous acidic workup led to the isolation of 4-amino-3,5-diisopropylbenzenesulfonic acid as the corresponding hydrochloride salt, which was confirmed on the basis of NMR spectroscopy and elemental analyses. In the second step, treatment of this salt with 0.5 eq of 2,6-pyridinedicarbonyl dichloride in the presence of excess Hünig's base (*N*,*N*-diisopropylethylamine) produced the desired

sulfonated pyridine di-carboxamide ligand as the corresponding ammonium salt in good yield. The presence of the two ammonium counter cations in the pro-ligand [(*i*Pr$_2$EtNH)$_2$(^{SO3}LH$_2$)] was confirmed on the basis of ^{1}H-NMR spectroscopy (Figure 3.3) and elemental analysis. It should be noted that the acidic N-H protons (both in the carboxamide functionality of the ligand backbone and the ammonium counter cation) are not seen in the ^{1}H-NMR spectrum and it is hypothesized that this is due to exchange with D_2O solvent.

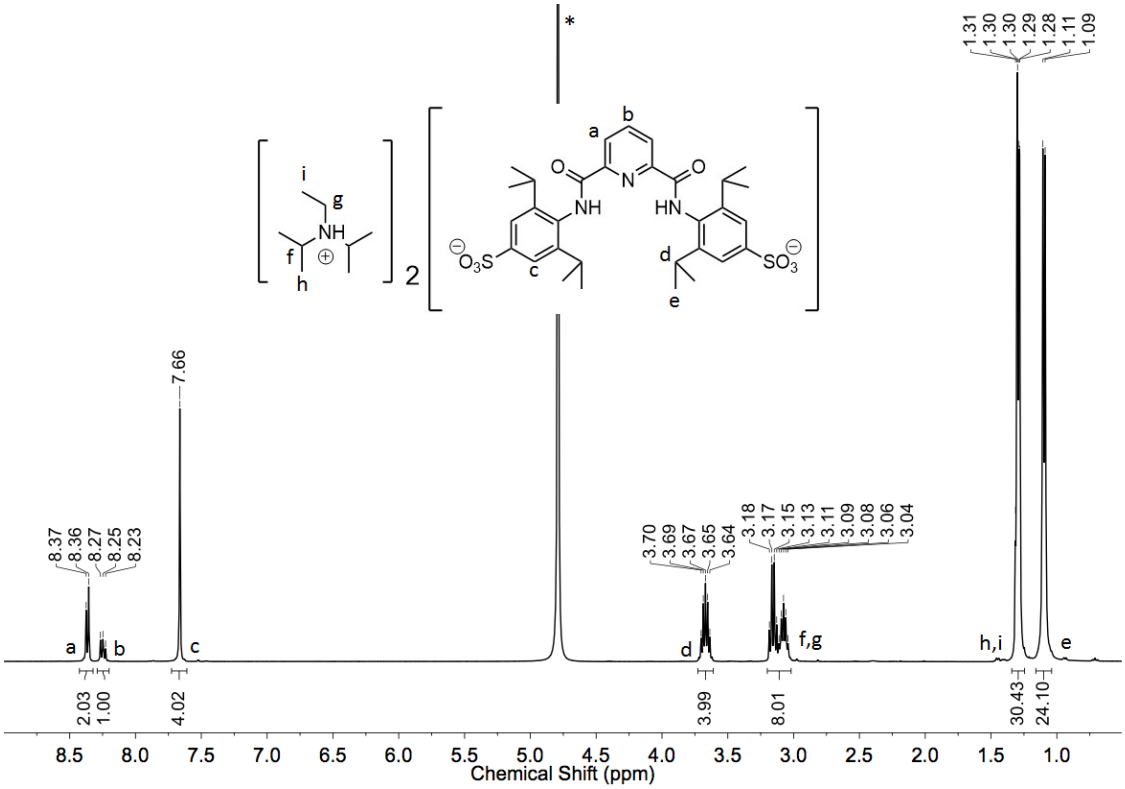

Figure 3.3. ^{1}H-NMR (400 MHz) spectrum of ((*i*Pr)$_2$EtNH)$_2$(^{SO3}LH$_2$). (*solvent residual signal in D_2O).

Proof of the formulation of the ligand came from determination of its X-ray crystal structure (Figure 3.4), which also depicts the presence of the two protonated ammonium counter cations. The acidic proton on the counter cation is involved in a H-bonding interaction with one of the oxygen atoms of the sulfonate group, with a N-H-O distance of ~2.8 Å and N-H-O bond angle 166.6°, both of which are within the standard range for a moderate H-bonding interaction.[57] The other bond distances within the

molecule are similar to those reported for analogous compounds, having standard aromatic C-C and C-N distances (within the ligand backbone) ~ 1.35 Å, the C-O (carboxamide) ~1.23 Å and S-O (sulfonate) bond distance ~ 1.44 Å.

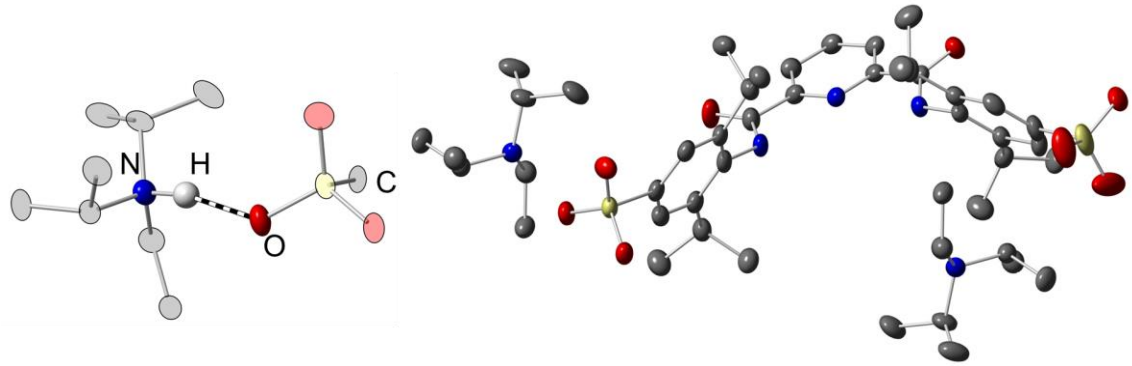

Figure 3.4. The X-ray structure of the ligand [(*i*Pr$_2$EtNH)$_2$(^{SO3}LH$_2$)] depicting the presence of the two ammonium counter cations, with the inset showing the H-bond interaction (dotted bond) between the acidic proton on the ammonium and the oxygen atom of the sulfonate. Key H-bonding parameters between the donor an acceptor (N-H : 0.98 Å, H-O : 1.85 Å, N-O : 2.816 Å, and N-H-O bond angle : 166.6°).

3.3 Synthesis and structural characterization of copper(II) complexes

3.3.1 Synthesis of the copper(II)-hydroxide complex

The synthetic scheme for the generation of the copper(II)-hydroxide complex is outlined in Scheme 3.2. Owing to the water solubility of the pro-ligand (isolated as a dianionic ammonium salt), a direct metalation strategy in aqueous conditions was employed for the synthesis of the [CuOH]$^+$ complex, in contrast to the previously reported procedures which required the synthesis of copper(II)-solvato precursors.[8,14]

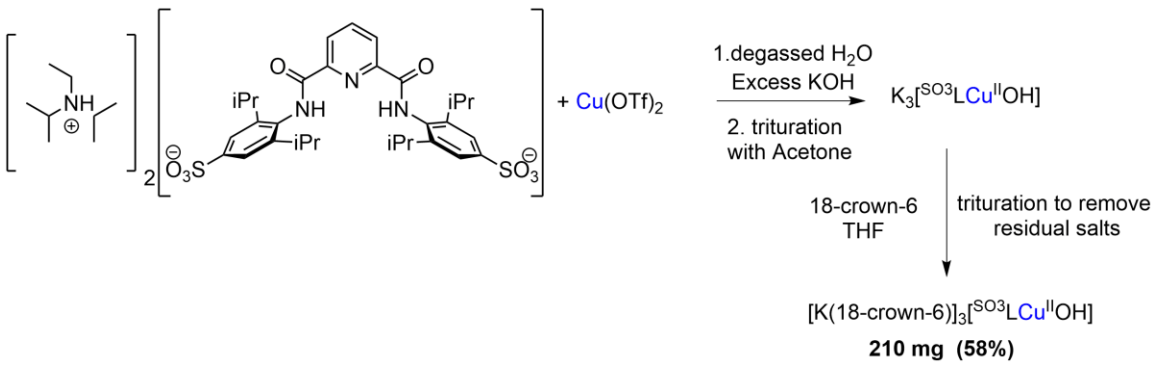

Scheme 3.2. Synthesis of the copper(II)-hydroxide complex [K(18-C-6)]$_3$[^{SO3}LCuOH]

Treatment of a degassed aqueous solution of the pro-ligand $((i\text{Pr})_2\text{EtNH})_2(^{SO3}\text{LH}_2)$ with 1 eq of $Cu(OTf)_2$ in the presence of excess KOH led to the formation of an intense blue solution of the copper(II)-hydroxide complex. Partial removal of the solvents from this reaction mixture followed by trituration with acetone (to remove salt impurities) led to the precipitation of blue-purple solid. This solid was then triturated overnight in THF with excess 18-crown-6 (18-C-6) and filtration of the reaction mixture on a fine porosity glass frit yielded the corresponding compound $[K(18\text{-C-}6)]_3[^{SO3}\text{LCuOH}]$ as a fine blue solid in reasonable yield. Its identity as the [K(18-C-6)] adduct was verified on the basis of elemental analyses and X-ray crystallographic analysis. In contrast to the other analogous $[CuOH]^+$ compounds synthesized previously,[14] the current complex is insoluble in solvents like THF and CH_2Cl_2, presumably due its trianionic constitution. It is soluble in polar solvents like 1,2-diflurobenzene (DFB), dimethylformammide (DMF) and water, however. Attempted synthesis of the analogous $[CuOH]^+$ complex with tetraalkylammonium counter cations (to avoid using phase transfer reagents like 18-C-6) proved unsuccessful with regards to getting pure complexes owing to the insoluble nature of the isolated compounds.

3.3.2 X-ray crystallographic characterization of the copper(II)-hydroxide complex

X-ray quality single crystals of $[K(18\text{-C-}6)]_3[^{SO3}\text{LCuOH}]$ were grown by vapor diffusion of diethyl ether into a 1,2-DFB solution at -20 °C. The X-ray structure is depicted in Figure 3.5. The coordination environment around the copper(II)-center is best described as distorted square planar having a τ_4 value of ~0.16 (where the standard τ_4 value is 0 for square planar and 1 for tetrahedral geometries, respectively).[41] The Cu-O bond distance is ~1.83 Å, while the Cu-N bond distances are around 1.9-2.0 Å (Cu-Npy : 1.92, Cu-Nam : 2.0). These bond metrics are similar to those observed for the previously reported analogous $[CuOH]^+$ complexes (Table 3.1).[8,14,58]

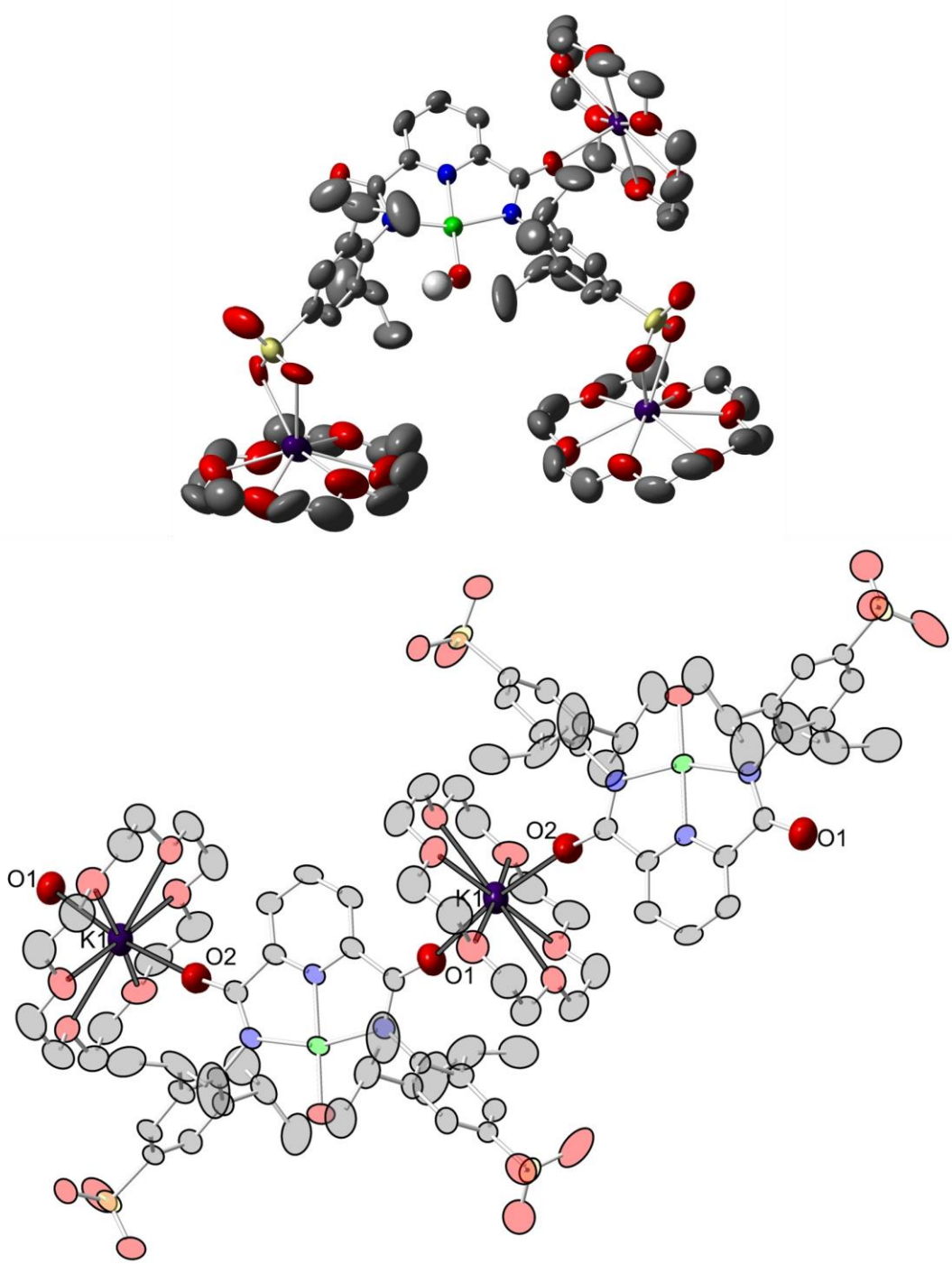

Figure 3.5. (Top) X-ray crystal structure of $[K(18\text{-}C\text{-}6)]_3[^{SO3}LCuOH]$ with non-hydrogen atoms depicted at 50% thermal ellipsoids. (Bottom) The coordination polymer network in the solid state structure depicting the repeating units (faded) and the key coordinating components (highlighted).

Table 3.1. Selected interatomic distances (Å) for Cu(II) Complexes.[a]

Compound	Cu-O	Cu-N_{py}	Cu-N_{am}	τ_4
$[Bu_4N][LCuOH]$[b]	1.845(4)	1.924(3)	2.016(3), 2.019(3)	0.16
$[Et_4N][^{NO2}LCuOH]$[c]	1.859(2)	1.936(2)	2.005(1), 1.998(1)	0.17
$Na[^{pipMe}LCuOH]$[c,d]	1.885(2)	2.032(3)	1.963(3), 1.958(3)	0.20
$[K(18\text{-}C\text{-}6)]_3[^{SO3}LCuOH]$	1.829(4)	1.915(4)	1.996(4), 2.012(4)	0.16
$[K(Krytpofix\text{-}222)]_3[^{SO3}LCuOH]$	1.848(3)	1.937(3)	2.006(3), 2.012(3)	0.15

[a] Estimated standard deviations are indicated in parenthesis. [b] Ref 58 [c] Ref 14
[d] Na^+ is coordinated to the hydroxide.

Two interesting features emerge from the crystal structure. First, the Lewis basic nature of the sulfonate functionality is demonstrated *via* its binding with the Lewis acidic $[K(18\text{-}C\text{-}6)]^+$ counter cation. Two of the three $[K(18\text{-}C\text{-}6)]^+$ cations in the structure are bound to the SO_3^- in a bidentate fashion having a K-O bond distance of ~2.8 Å. However, this ionic interaction between the SO_3^- group and the $[K(18\text{-}C\text{-}6)]^+$ is accompanied by severe positional disorder in the X-ray structure, which results from the rotation of the SO_3^- group that is coupled with rotational disorder in the crown moieties. As a result, both the SO_3^- groups and the coupled $[K(18\text{-}C\text{-}6)]^+$ fragments needed to be modeled using a two part disorder component. The second interesting feature in the crystal structure is the fact that it exists as a coordination polymer (Figure 3.5, bottom) in the solid state formed through interaction between the carbonyl oxygen on the di-carboxamide ligand and the third $[K(18\text{-}C\text{-}6)]^+$ counter ion (K-O distance of ~2.6 Å).

Inspired by the finding in the above crystal structure that the SO_3^- is bound with the $[K(18\text{-}C\text{-}6)]^+$ counter ion through an ionic interaction, it was hypothesized that this interaction could be prevented by using a more efficient encapsulating reagent like a cryptand. Additionally, it was also hypothesized that this would yield better quality X-ray data by circumventing the severe positional disorder described above. In order to test this

hypothesis, excess (5 eq) Kryptofix-222 was added to a solution of [K(18-C-6)]$_3$[^{SO3}LCuOH] in 1,2-DFB, and vapor diffusion of diethyl ether into this solution at -20 °C afforded needle-shaped blue crystals suitable for X-Ray diffraction analysis. The X-ray structure is depicted in Figure 3.6.

Indeed, as hypothesized the more rigid encapsulating cryptand successfully mitigates the secondary interactions observed in the previous solid state structure and leads to the formation of better quality crystals with fewer disorder issues. In this case, two of the [K(Kryptofix-222)]$^+$ counter ions do not exhibit any additional coordination as the central K^+ is coordinatively saturated by binding with the six oxygen and two nitrogen donors from the cryptand. Also, one of the SO_3^- groups on the ligand does not interact with any countercations. Interestingly, however, the third [K(Kryptofix-222)]$^+$ cation exhibits a bonding interaction with the other sulfonate. This interaction is indicated by the observation that the central K^+ is slightly disordered, having a 15 % disordered component which sits outside the central cryptand cavity and is involved in a bonding interaction with the sulfonate group in a similar bidentate fashion as observed in the previous solid state structure (K-O distance is ~2.8 Å). This observation highlights the innately high propensity of the SO_3^- to be involved in bonding interactions that cause the K^+ to be partially dislodged from even the extremely rigid cryptand cavity.

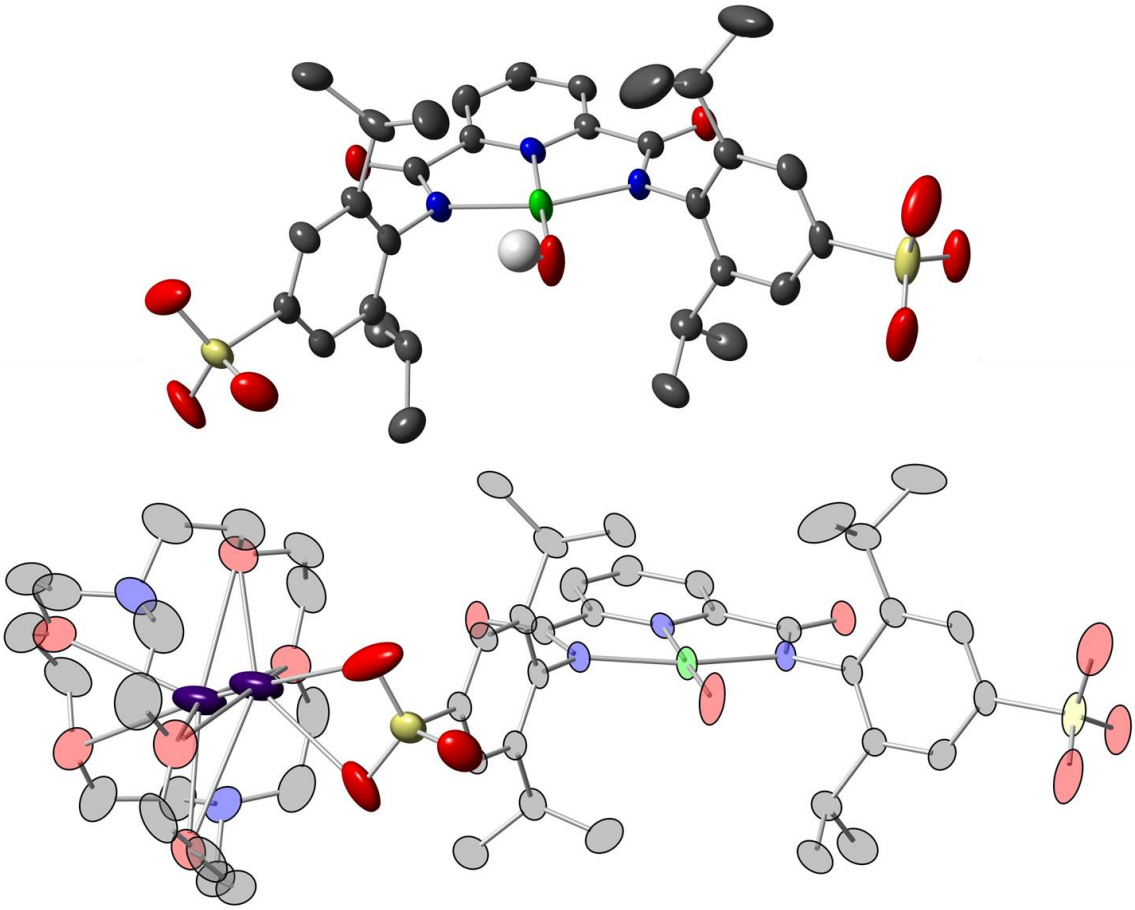

Figure 3.6. (Top) X-ray structure of anionic component of [K(Krptofix-222)]$_3$[^{SO3}LCuOH] with non-hydrogen atoms depicted at 50% thermal ellipsoids (counter ions are omitted for clarity). (Bottom) Depiction of secondary sphere interaction between a disordered K^+ (which is not encapsulated completely by the cryptand cavity) with one of the counter-ions and one sulfonate group on the ligand.

The coordination environment about the copper(II)-ion remains mostly conserved and the geometry is best described as pseudo square planar, having τ_4 ~0.15.[41] The key bond-metrics along with the bond metrics for the other analogous $[CuOH]^+$ complexes are listed in Table 3.1. While the Cu-N bonds in the structure with the cryptand encapsulated counter cation is similar to what was observed before (Cu-N_{py} : ~1.94 Å, Cu-N_{am} : ~2.0 Å), the Cu-O bond distance shows a subtle increase to ~1.85 Å. While this represents an approximate difference of 0.02 Å in the Cu-O bond distance between the two [^{SO3}LCuOH]$^{3-}$ structures, caution is taken in drawing any conclusion from this

because this subtle change might be a consequence of crystal packing effects in the solid state.

3.3.3 Synthesis and structural characterization of other copper(II)-complexes

3.3.3.1 A sulfonato bridged dimer: $[(Et_4N)_2(^{SO3}LCu)]_2$

Treatment of a degassed aqueous solution of $((i\text{Pr})_2\text{EtNH})_2(^{SO3}LH_2)$ with 1 eq $Cu(OTf)_2$ and 4 eq Et_4NOH led to the formation of a blueish green solution. Removal of the solvents from the reaction mixture produced an oily blue green residue, which was stirred overnight with excess acetone to afford a fine forest green solid. This solid was isolated by filtration and washed thoroughly with boiling acetone to remove all salt impurities. The remaining solid was then dried thoroughly and isolated. This solid was found to be soluble only in a handful of solvents such as methanol, dimethylformamide, and water. Slow evaporation of a solution of this isolated solid in a water:acetone (5:95 v/v) solvent mixture afforded green needle shaped crystals, which were identified on the basis of elemental analyses and X-ray crystallography to be the sulfonate bridged dimeric compound depicted in Figure 3.7. The observed sulfonate coordination mode in the solid state crystal structure reflects the Lewis basic nature of the SO_3^- group and its tendency to bind to Lewis acidic centers. The coordination environment around the copper(II)-ion is pseudo square planar (consisting of the three N-donors from the supporting pyridine di-carboxamide and a fourth oxygen from the SO_3^- group on a neighboring molecule, having a τ_4 ~0.18) with Cu-N/O bond distances in line with the previously reported similar complexes.[55b,c] The S-O bond distance for the oxygen atom in the sulfonate that is coordinated to the copper is significantly longer than the others, measuring 1.48 Å as opposed to 1.44 Å in the other S-O bonds. Such asymmetry in coordinated sulfonates has been reported previously in the literature.[55b,c,59]Additionally, similar interactions between a Lewis acidic copper center and the O-donors from a $–NO_2$ substituent in the ligand backbone was previously observed in copper complexes of a substituted β-diketiminate ligand.[60]

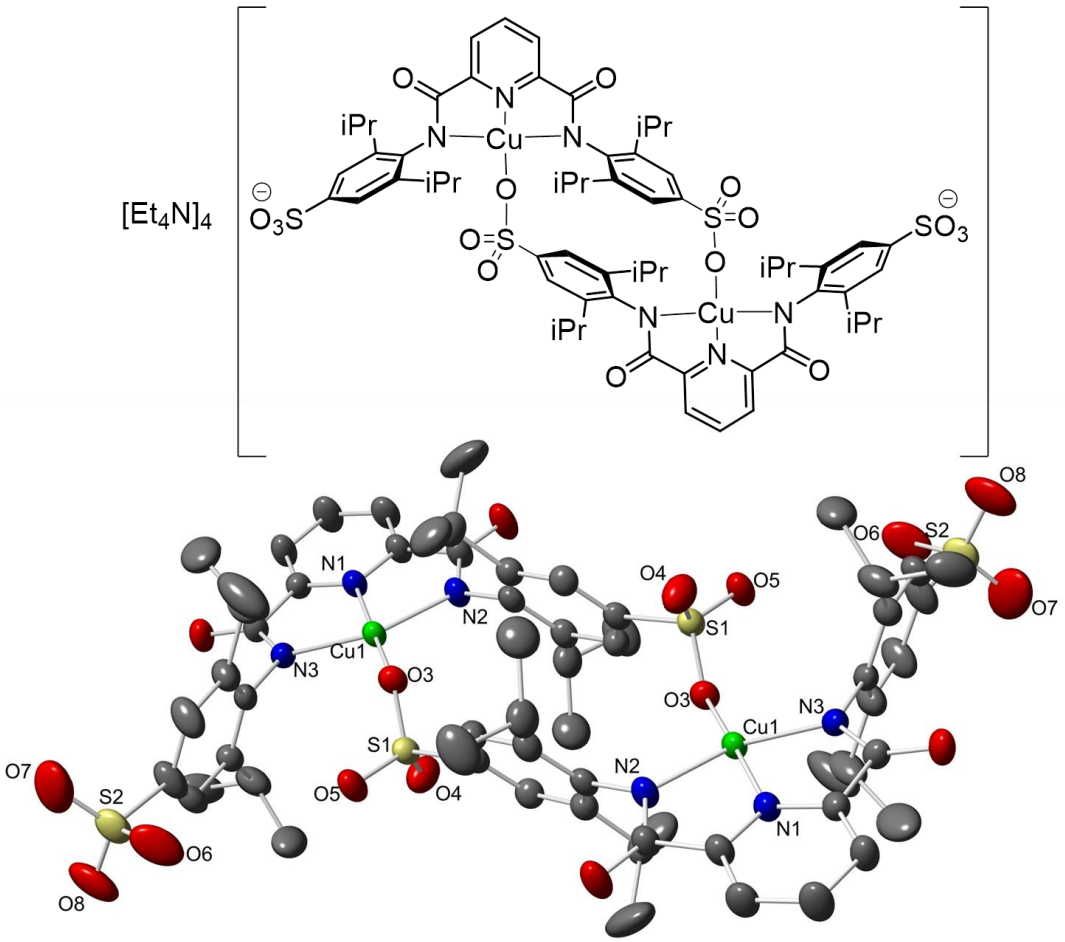

Figure 3.7. (Top) Chemical structure of $[(Et_4N)_2(^{SO3}LCu)]_2$. (Bottom) X-ray structure of $[(Et_4N)_2(^{SO3}LCu)]_2$ depicting non-hydrogen atoms at 50% thermal ellipsoids (counter ions are omitted for clarity). Selected bond distances in Å (standard deviation in parenthesis) Cu1-N1: 1.927(3), Cu1-O3: 1.944(2) Cu1-N2: 1.994(2), Cu1-N3: 1.995(2), S1-O4: 1.440(3), S1-O5: 1.443(3), S1-O3: 1.484(2).

3.3.3.2 $[Na(15\text{-crown-}5)]_3[^{SO3}LCuCl]$

Based on the observation that the SO_3^- group interacts with the K^+ counterion, it was envisioned that replacement of the K^+ by the more Lewis acidic Na^+ might lead to different ionic interactions, which might be manifested in the metric parameters in the X-ray structure. However, attempts to obtain a crystal structure of $[Na(15\text{-crown-}5)]_3[^{SO3}LCuOH]$ proved unsuccessful. We thus chose to explore the possibility of obtaining structural insight from the analogous copper(II)-chloride complex instead. A

suspension of $[(Et_4N)_2(^{SO3}LCu)]_2$ in CH_2Cl_2 was treated with 3 eq (per copper center) of NaCl and excess 15-crown-5 (15-C-5), which immediately led to the generation of a deep green solution, diagnostic of the generation of copper(II)-chloride complexes supported by analogous pyridine di-carboxamide ligand frameworks.[8] Slow evaporation of this solution produced X-ray quality crystals as dark green blocks. The X-ray structure is shown in Figure 3.8. The structure of $[Na(15\text{-}C\text{-}5)]_3[^{SO3}LCuCl]$ is similar to that for $[K(18\text{-}C\text{-}6)]_3[^{SO3}LCuOH]$, with almost identical Cu-N distances of 1.9337(11) Å for Cu-$N_{py,}$ 1.9973(11) and 2.0002(11) for Cu-N_{am}, and a τ_4 of ~0.16. The Cu-Cl bond distance of 2.2030(4) Å is larger than the corresponding Cu-O, as expected. All of the bond metrics are in line with those reported for an analogous $[Bu_4N][LCuCl]$ complex reported previously.[8] Additionally, the compound forms a coordination polymer in the solid state (Figure 3.8). The key Na-O(SO_3) distance is ~2.37 Å (vs. 2.8 Å K-O distance in K-crown-hydroxide structure). This shortening of the bond by 0.43 Å is more than what can be accounted for by the difference in the ionic radii (0.36 Å) between Na^+ and K^+ (1.02 and 1.38 Å respectively),[61] indicating that the interaction between $[Na(15\text{-}C\text{-}5)]^+$ and SO_3^- is significantly stronger.

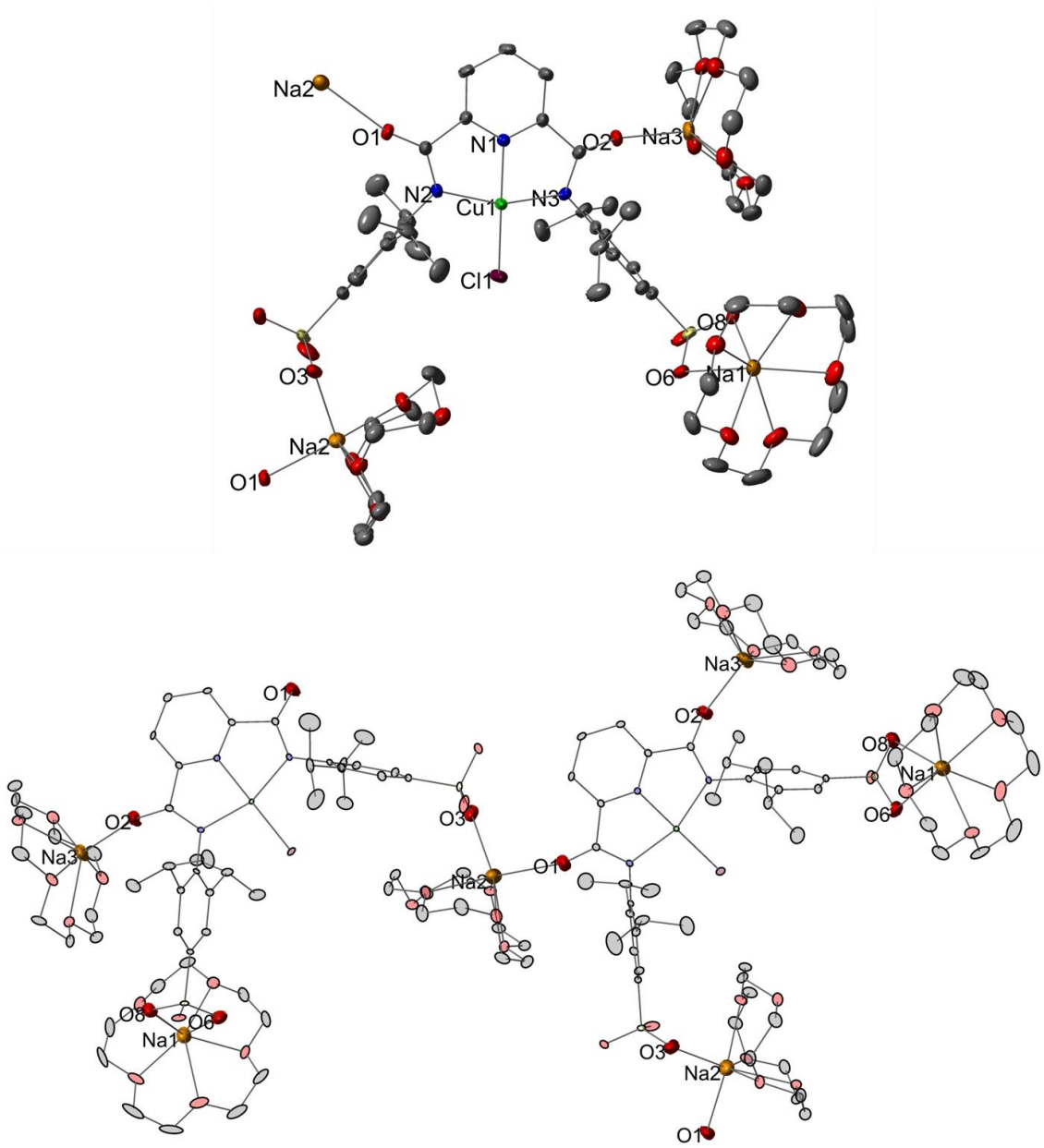

Figure 3.8. The X-ray structure of $[Na(15\text{-}C\text{-}5)]_3[^{SO3}LCuCl]$ depicting the repeating unit (top) and the coordination polymer chain (bottom) with non-hydrogen atoms depicted at 50% thermal ellipsoids.

3.4 Spectroscopic studies on $[K(18\text{-}C\text{-}6)]_3[^{SO3}LCuOH]$

In order to understand the effects of the inclusion of the anionic SO_3^- functionality on the $[CuOH]^+$ species and draw comparisons to previously reported analogs,[8,13,14] the spectroscopic characterization of $[K(18\text{-}C\text{-}6)]_3[^{SO3}LCuOH]$ was performed in 1,2-DFB. Also, because of the charged residues we were able to

characterize some spectroscopic properties in aqueous conditions. This section will summarize the key findings and conclusion from these spectroscopic experiments.

3.4.1 UV-vis absorption spectroscopy

The UV-vis spectrum of $[K(18\text{-}C\text{-}6)]_3[^{SO3}LCuOH]$ in 1,2-DFB solvent recorded at 25 °C is shown in Figure 3.9 (left, blue trace). It contains a $d \rightarrow d$ band centered around 597 nm, as well as an intense charge transfer feature at ~310 nm (off scale, not shown) with a weaker shoulder appearing at ~380 nm. These features very similar to those observed for similar mononuclear $[CuOH]^+$ complexes reported previously (UV-vis spectra for $[Bu_4N][LCuOH]$ shown in Figure 3.9 (left, black trace) for the sake of comparison).[13,14] The similarity between these spectra shows that incorporation of the anionic sulfonate groups does not alter the solution state geometry and ligand field around the central copper(II) ion. In order to check if ionic interactions would affect the UV-Vis spectroscopy, the UV-vis spectrum was measured in the presence of 100 eq of [Na(15-C-5)]OTf. The UV-Vis spectrum was unchanged from that measured in the absence of any added electrolyte, however, suggesting either no change in the ionic interactions or no effect of changed ionic interactions on the electronic structure of the complex.

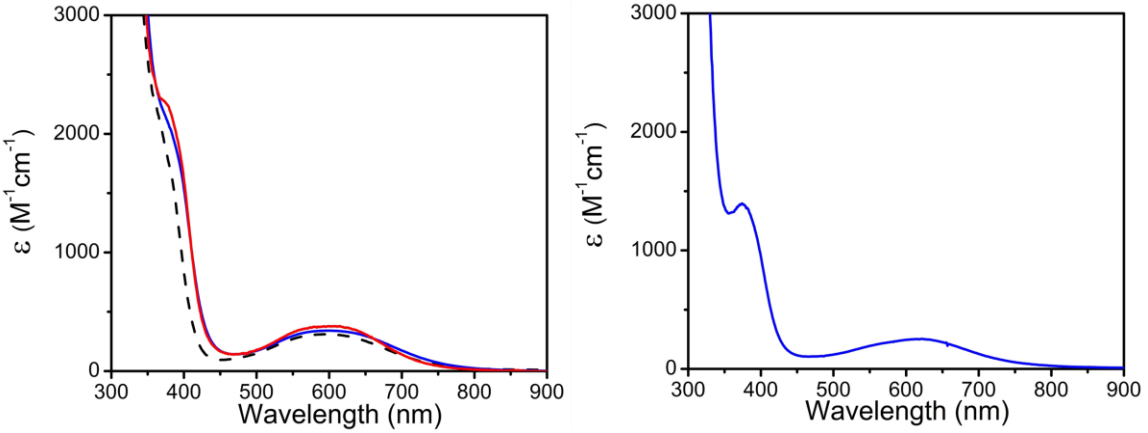

Figure 3.9. (Left) UV-Vis spectra of $[K(18\text{-}C\text{-}6)]_3[^{SO3}LCuOH]$ (blue trace), $[K(18\text{-}C\text{-}6)]_3[^{SO3}LCuOH]$ in the presence of 100 eq [Na(15-C-5)]OTf (red trace), and $[Bu_4N][LCuOH]$ (black dashed trace). Conditions : 1,2-DFB solvent 25 °C. (Right) UV-Vis spectra of $[K(18\text{-}C\text{-}6)]_3[^{SO3}LCuOH]$ of in water recorded at 25 °C.

The UV-Vis spectrum for $[K(18\text{-}C\text{-}6)]_3[^{SO3}LCuOH]$ in water (at a pH of 12 at 25 °C) was also recorded and is shown in Figure 3.9 (right). The aqueous spectrum is very similar to that recorded under non-aqueous conditions, depicting a similar broad $d \rightarrow d$ band centered around ~606 nm with a more intense charge transfer feature at ~400 nm. These findings indicate that the copper(II)-hydroxide complex has a conserved square planar geometry in both the solvents used.

3.4.2 EPR spectroscopy

Figure 3.10 shows the EPR spectrum of $[K(18\text{-}C\text{-}6)]_3[^{SO3}LCuOH]$ recorded in 1,2-DFB at 30 K (experimental spectrum depicted in black trace and simulated spectra depicted in red trace). The spectrum contains a diagnostic S=1/2 pseudo-axial EPR signal with g_x, g_y, and g_z values of approximately 2.03, 2.05, and 2.19, respectively, as well as well-resolved Cu hyperfine and rich superhyperfine splitting patterns attributed to the ligand N atoms (which are magnetically isolated from the nearby H-atoms) in the primary coordination sphere. These observations are in line with what was observed previously for the reported $[CuOH]^+$ complexes.[14] The simulation parameters obtained from the modelling of the EPR spectra are listed in Tables 3.2 and 3.3.[14] The fitted g_z parameter is significantly different from g_x and g_y (Table 3.2), which are both similar in magnitude, as is the characteristic of pseudo-axial signals. The hyperfine and superhyperfine splitting (Table 3.3) were modeled using one Cu nucleus and three N-nuclei, with two of the N-nuclei being identical. The copper-hyperfine splitting is displayed predominantly in the z-component of the A_{Cu} hyperfine tensor, with the superhyperfine splitting resulting from the *N*,*N*,*N*-binding pocket being expressed predominantly in the x- and y-components of the A_{am} and A_{py} tensors. The EPR spectrum of $[K(18\text{-}C\text{-}6)]_3[^{SO3}LCuOH]$ in the presence of 100 eq. [Na(15-C-5)]OTf was also measured and is shown in Figure 3.11. It reveals a nearly identical spectrum bearing similar line shapes and *g* values, with only a subtle difference noticeable in the z-component of the A_{Cu} hyperfine tensor, depicting a slightly higher coupling. All of these observations are consistent with the notion that

[^{SO3}LCuOH]$^{3-}$ has a solution state structure similar to those of the previously reported mononuclear copper(II)-hydroxide complexes that differ only slightly with respect to the electronic structure of the copper(II) center.

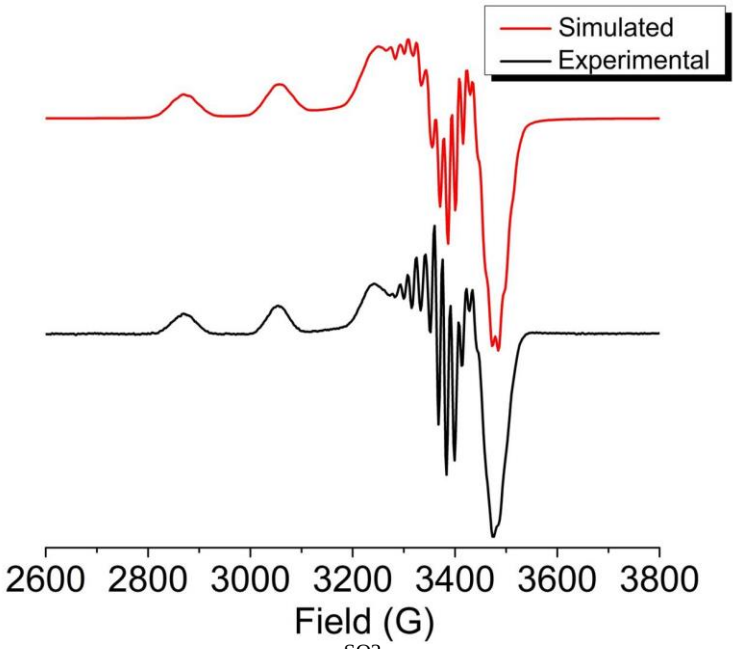

Figure 3.10. EPR signal for [K(18-C-6)]$_3$[^{SO3}LCuOH] in 1,2-DFB solvent recorded at 30 K (black trace represents the experimental spectrum, red trace represents the simulated spectrum).

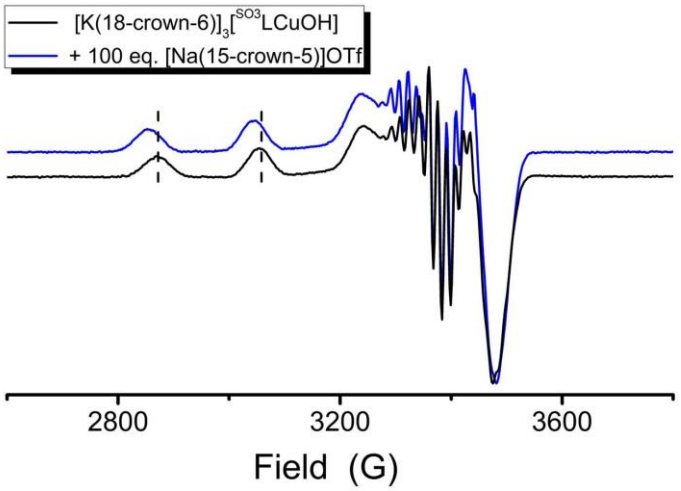

Figure 3.11. Comparison of the EPR spectra of [K(18-C-6)]$_3$[^{SO3}LCuOH] in the absence (black trace) and presence of 100 eq. of [Na(15-C-5)]OTf (blue trace). The dashed line shows the subtle increase in the Cu-hyperfine coupling along the z-direction for the latter.

Table 3.2. g-values for EPR spectra of $[CuOH]^+$ complexes.

Compound	g(x)	g(y)	g(z)
$[Bu_4N][LCuOH]$	2.0255	2.0465	2.1939
$[K(18\text{-C-}6)]_3[^{SO3}LCuOH]$	2.0300	2.0550	2.1875
$[Et_4N][^{NO2}LCuOH]$	2.0330	2.0540	2.1850
$[Bu_4N][^{pipMe}LCuOH]$	2.0300	2.0490	2.1900

Table 3.3. Hyperfine Parameters for Cu, N(amide), and N(pyridine/piperidine) Nuclei (MHz)

Compound	A^{Cu} (x)	A^{Cu} (y)	A^{Cu} (z)	A^{am} (x)	A^{am} (y)	A^{am} (z)	A^{py} (x)	A^{py} (y)	A^{py} (z)
$[K(18\text{-C-}6)]_3$ $[^{SO3}LCuOH]$	65	60	555[a]	40	55	50	40	40	30
$[Bu_4N]$ $[LCuOH]$	57	57	567	32	50	30	30	50	30
$[Et_4N]$ $[^{NO2}LCuOH]$	70	60	540	45	47	45	40	40	45
$[Bu_4N]$ $[^{pipMe}LCuOH]$	45	45	597	40	45	40	35	45	40

[a] Increases to ~ 561 MHz upon the addition of 100 eq. [Na(15-C-5)]OTf.

In previous studies on $[CuOH]^+$ complexes it was observed that $A_{Cu}(z)$ showed a correlation with the spin density on the copper(II), and thus was a measure of the electron donating ability of the supporting ligand framework (Table 3.3).[14] In particular, it was noted that stronger electron donation from the supporting ligand resulted in an increase in $A_{Cu}(z)$, while incorporation of the electron withdrawing *p*-NO_2 substituent on the flanking aryl ring of the ligand in the case of $[Et_4N][^{NO2}LCuOH]$ caused a decrease in $A_{Cu}(z)$ of 27 MHz when compared to $[Bu_4N][LCuOH]$. According to these results, we conclude that the *p*-SO_3^- substituents in $[K(18\text{-C-}6)]_3[^{SO3}LCuOH]$, which has a lower $A_{Cu}(z)$ when compared to $[Bu_4N][LCuOH]$, are electron withdrawing, consistent with its Hammett constant (σ_p = 0.35).[53] Thus, while incorporation of the anionic substituents cause a net 2-unit increase in the negative charge on the copper-complex, the overall

effect of the charge increase at the Cu(II) ion is negated by the intrinsic electron withdrawing ability of the sulfonate group.

The EPR spectra of $[K(18\text{-}C\text{-}6)]_3[^{SO3}LCuOH]$ in water also was measured (Figure 3.12). While the spectrum shows the characteristic 4-line hyperfine splitting typical for mononuclear copper(II)-complexes, the superhyperfine coupling from the N-atoms is not as distinct, consistent with the known line-broadening effects of solvent water.[62] Importantly, the overall nature of the EPR spectrum (with regards to the position of the dominant absorption and derivative features) is very similar to that observed in 1,2-DFB, indicating a conserved geometry in both the solvents.

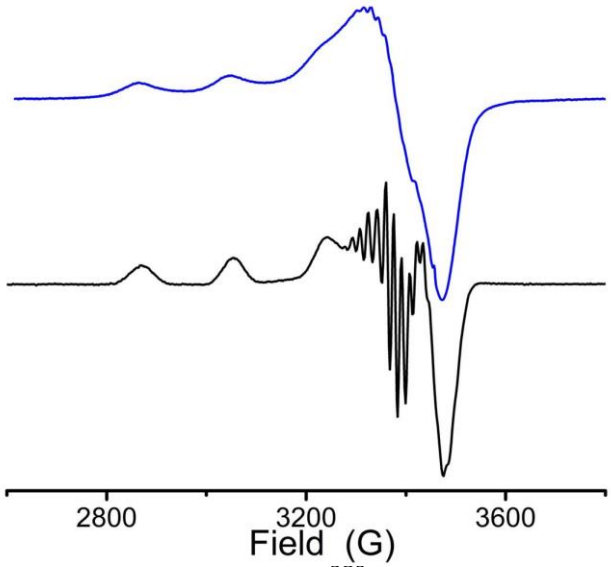

Figure 3.12. EPR spectrum of $[K(18\text{-}C\text{-}6)]_3[^{SO3}LCuOH]$ in water (blue trace) and 1,2-DFB (black trace).

3.4.3 Electrochemical measurements

In order to elucidate the effects of the anionic $p\text{-}SO_3^-$ groups on the redox behavior of the copper center, cyclic voltammetry experiments on $[K(18\text{-}C\text{-}6)]_3[^{SO3}LCuOH]$ were performed in 1,2-DFB solvent using $[Bu_4N]PF_6$ as the supporting electrolyte (Figure 3.13, left). The one- electron oxidation event for $[K(18\text{-}C\text{-}6)]_3[^{SO3}LCuOH]$ is best described as being quasi-reversible (i_{pa}/i_{pc} ~0.99 and ΔE ~ 90 mV

at a scan rate of 50 mV/s) with the $[CuOH]^{2+}/[CuOH]^{+}$ couple having an $E_{1/2}$ of -0.135 V (vs. Fc^{+}/Fc). This is lower than the $E_{1/2}$ for [LCuOH]/$[LCuOH]^{-}$, which has a value of -0.076 V (vs. Fc^{+}/Fc).[13] The lower value of the oxidation potential can be rationalized on the basis of the fact that the incorporation of the anionic *p*-SO_3^{-} groups makes the corresponding copper(II)-hydroxide species trianionic, thus enabling a more facile oxidation when compared to the previous monoanionic analogs.

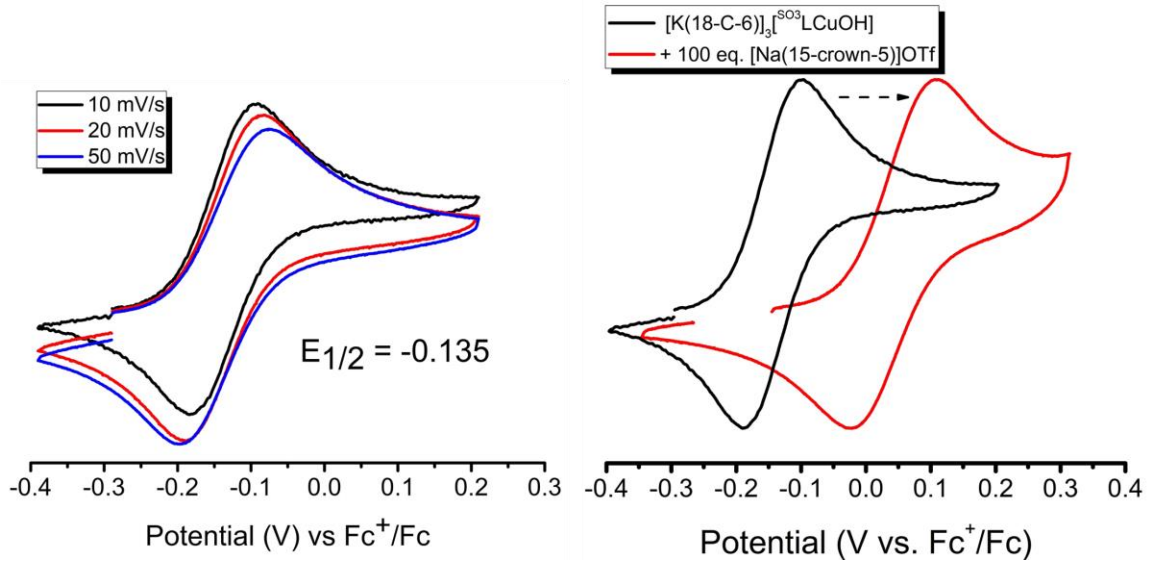

Figure 3.13. (Left) Scan rate normalized Cyclic voltammograms of $[K(18\text{-}C\text{-}6)]_3[^{SO3}LCuOH]$ recorded in 1,2-DFB solvent using 0.3 M $[Bu_4N]PF_6$ as the supporting electrolyte. (Right) Overlay of the Cyclic vaoltammograms of $[K(18\text{-}C\text{-}6)]_3[^{SO3}LCuOH]$ in the absence (black trace) and presence of 100 eq. [Na(15-C-5)]OTf (red trace). There is an anodic shift of ~180 mV in the $E_{1/2}$ that is observed.

The cyclic voltammetry experiments were then repeated under identical conditions except in the presence of 100 eq of [Na(15-C-5)]OTf (Figure 3.13, right). Surprisingly, the $E_{1/2}$ for the $[CuOH]^{2+}/[CuOH]^{+}$ couple is now shifted to a value of 0.043 V (vs. Fc^{+}/Fc), a considerable anodic change of ~180 mV when compared to the value obtained in the absence of the added Na^{+} electrolyte. The magnitude of this shift to a higher potential by mere alteration of the counter-ion is comparable to the increase in the redox potential observed when going from [LCuOH] to $[^{NO2}LCuOH]$ ($\Delta E_{1/2}$ ~ 200 mV).

This observation suggests that there is a significant difference between the interactions of the pendant SO_3^- groups with the K^+ or Na^+ counterions (in contrast to what was observed by UV-vis and EPR spectroscopy). Specifically, we hypothesize that in a non-aqueous and noncoordinating solvent like 1,2-DFB, the Lewis basic SO_3^- group interacts strongly with the more Lewis acidic Na^+ ion and thus exists as a "tighter" ion-pair when compared to K^+. This enhanced ion-pairing to Na^+ mitigates the anionic electrostatic effect of the SO_3^- groups, which ultimately leads to an anodic shift of the redox potential.

3.5 Characterization of $[CuOH]^{2+}$ complexes

Owing to the reversible nature of the cyclic voltammograms in 1,2-DFB solvent, the chemical oxidation of $[K(18\text{-}C\text{-}6)]_3[^{SO3}LCuOH]$ was investigated in 1,2-DFB at -25 °C and the reaction was monitored using UV-Vis spectroscopy in a similar manner as reported for the previous $[CuOH]^{2+}$ complexes.[8,13,14] Treatment of a 0.1 mM solution of $[K(18\text{-}C\text{-}6)]_3[^{SO3}LCuOH]$ with 1 eq. of $[Fc][BAr^F{}_4]$ resulted in the immediate formation of characteristic intense charge transfer features with a broad peak centered around ~610 nm (ε = 12,500 M^{-1} cm^{-1}) attributed to the generation of the one-electron oxidized $[CuOH]^{2+}$ complex (Figure 3.14, left).[8,13,14] Titration experiments revealed a 1:1 reaction stoichiometry with the oxidant (Figures 3.14, right), confirming that oxidation of the copper(II)-hydroxide precursor proceeds cleanly *via* a one-electron process. The product is reactive and the corresponding absorption bands decay fully within 2-3 hours at -25 °C and immediately upon warming. Additionally, the rates of decay at lower temperatures were enhanced upon the addition of external substrates containing C-H bonds that can be activated (see below). All of these observations are consistent with the prior reports of generation of analogous $[CuOH]^{2+}$ complexes.[13,14]

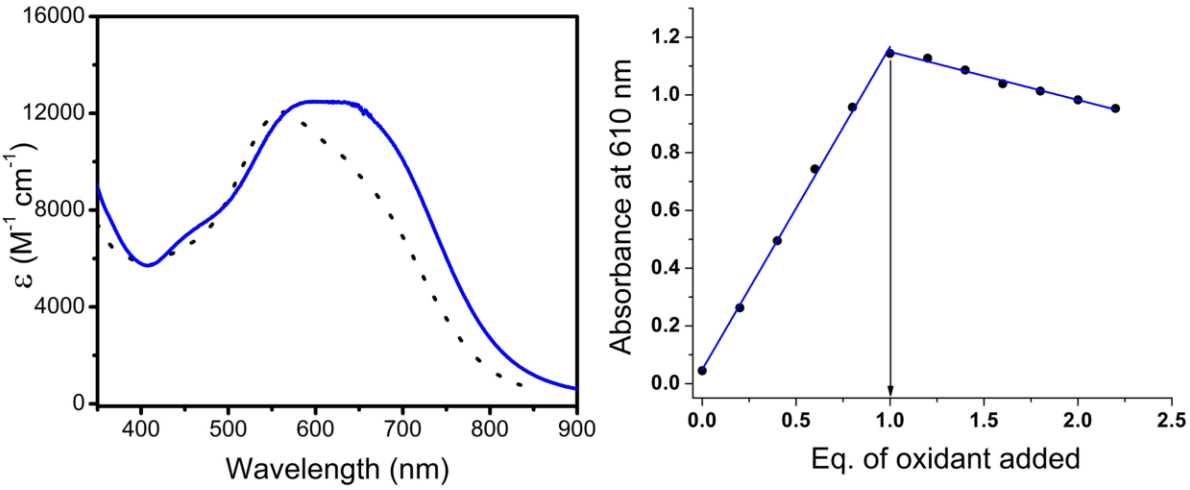

Figure 3.14. (Left) UV-Vis spectrum obtained upon the oxidation of [K(18-C-6)]$_3$[^{SO3}LCuOH] (blue trace). The UV-Vis absorption feture for [LCuOH] is depicted as the black dashed trace for comparison. (Right) Titration curve with oxidant, revealing a 1:1 reaction stoichiometry.

We repeated the one-electron oxidation reactions in the presence of 100 eq. of [Na(15-C-5)]OTf (Figure 3.15). As expected from the cyclic voltammetry experiments, [Fc][BAr$^F_4$] was unable to effect the one-electron oxidation, and hence a stronger oxidant [AcFc][BAr$^F_4$] (which has an $E_{1/2}$ of ~0.23 V vs. Fc$^+$/Fc)[63] was used in this case. Treatment of a 0.1 mM solution of [K(18-C-6)]$_3$[^{SO3}LCuOH] in the presence of 10 mM [Na(15-C-5)]OTf with 1 eq [AcFc][BAr$^F_4$] resulted in the immediate formation of an intense absorption feature having a peak centered ~566 nm (ε = 10,600 M^{-1} cm^{-1}). The one-electron oxidized species also is only moderately stable as was observed previously, its stability being somewhat lower than the former. Also, the absorption feature is slightly blue-shifted in comparison to the former. It was demonstrated previously that the charge transfer features arise from a LMCT from the electron-rich aryl-ring HOMO to the Cu(III) LUMO.[8,14] We speculate that the subtle difference between the observed LMCT features in the presence or absence of [Na(15-C-5)]OTf is due to different interactions between the pendant sulfonates and Na$^+$ and K$^+$, which result in subtle electronic perturbations to the aryl-based HOMO.

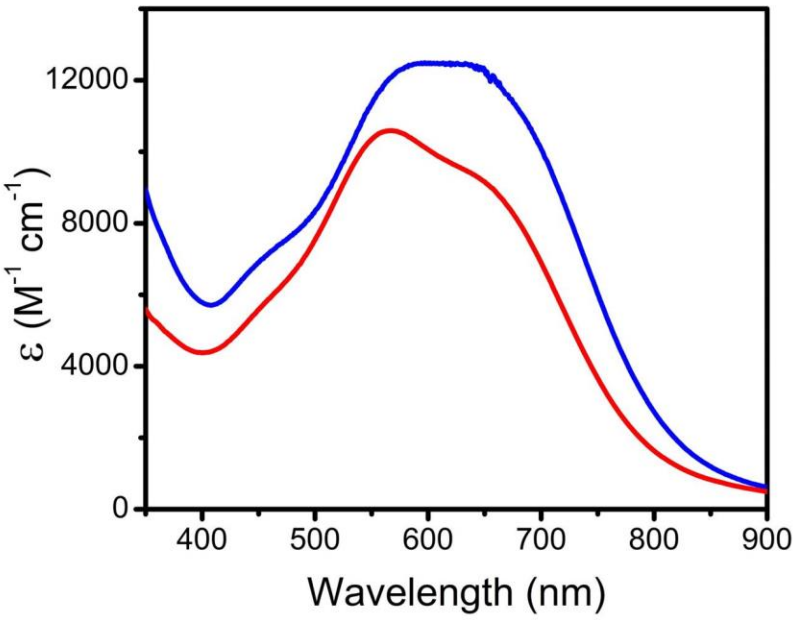

Figure 3.15. Overlay showing the difference in the LMCT features observed upon the one-electron oxidation of $[K(18\text{-}C\text{-}6)]_3[^{SO3}LCuOH]$ in the absence (blue trace) and presence of 100 eq. [Na(15-C-5)]OTf (red trace).

3.6 Evaluation of HAT thermodynamics via determination of the O-H BDE in the copper(II)-aqua complex $[^{SO3}LCuOH_2]^{2-}$

It was previously demonstrated (Chapter 2, Section 2.4.2) that ligand electronic perturbations affect the O-H BDE in the $[CuOH_2]^{2+}$ complexes, which in turn perturbs the HAT kinetics for the $[CuOH]^{2+}$ complexes. In order to understand how the anionic pendant SO_3^- on the supporting ligand affects the HAT reactivity of the $[CuOH]^{2+}$ complexes, we sought to determine the O-H BDE in $[K(18\text{-}C\text{-}6)]_2$ $[^{SO3}LCuOH_2]$ using the following two methods.

3.6.1 Determination of O-H BDE via cross HAT experiments between $LCuOH_2$ and $[K(18\text{-}C\text{-}6)]_2[^{SO3}LCuOH]$

We envisioned that the BDE of the O-H bond in the copper(II)-aqua complex $[^{SO3}LCuOH_2]^{2-}$ could be determined by measuring the equilibrium constant for the HAT cross reaction depicted in Scheme 3.3 and using the known BDE of $LCuOH_2$.[13] By

measuring the amounts of the various species after mixing $[^{SO3}LCuOH_2]^{2-}$ and $[LCuOH_2]$, the K_{eq} value may be calculated.

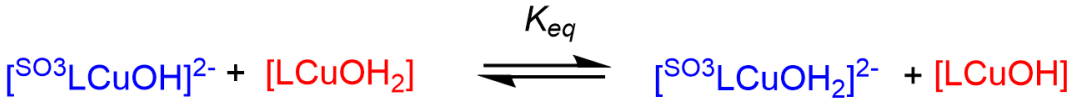

Scheme 3.3. Cross-HAT scheme.

Assuming a negligible contribution from entropy and using Eq. 3.1-3.3, K_{eq} can then be used to approximate the enthalpy of the reaction, which is equal to the difference in BDEs (ΔBDE) of the corresponding aqua species, namely $[^{SO3}LCuOH_2]^{2-}$ and $LCuOH_2$.

$$BDE(^{SO3}LCu(OH_2)) - BDE\left(LCu(OH_2)\right) = \Delta BDE \qquad \text{eq. 3.1}$$

$$\Delta BDE = \Delta H° \approx \Delta G° = -RT\ln K_{eq} \qquad \text{eq. 3.2}$$

$$BDE(^{SO3}LCu(OH_2)) = \Delta H° - BDE(LCu(OH_2)) \qquad \text{eq. 3.3}$$

Thus, given that the BDE of the parent $LCuOH_2$ complex is known, the O-H BDE of $[^{SO3}LCuOH]^{2-}$ can be computed (Eq. 3.3), and importantly, calibrated directly against the parent system. This method was used previously to determine the BDE of the complex $^{NO2}LCuOH_2$.[14] Additionally, the use of this method was previously validated in the case of $^{pipMe}LCuOH_2$, as the BDE value obtained from this method is in excellent agreement with that obtained from the independent BDE measurement (using the method described in Section 2.2.[14]

In the experiments, treatment of a 0.1 mM solution of $[K(18\text{-}C\text{-}6)]_2[^{SO3}LCuOH]$ in 1,2-DFB at -25 ºC with 0.25-2.5 eq of $LCuOH_2$ resulted in shifts in λ_{max} from 610 nm to 568 nm, close to the λ_{max} of pure LCuOH at 563 nm (Figure 3.16) and consistent with H-atom abstraction from $LCuOH_2$ by $[K(18\text{-}C\text{-}6)]_2[^{SO3}LCuOH]$ according to Scheme 3.3 above.

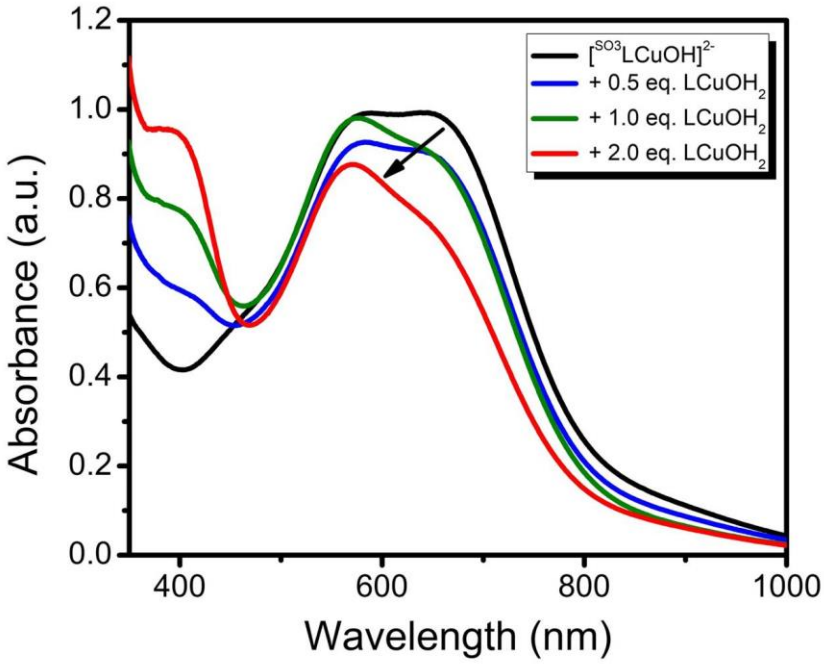

Figure 3.16. Changes in the UV-Vis absorption spectrum of $[K(18\text{-}C\text{-}6)]_2[^{SO3}LCuOH]$ with increasing equivalents of $LCuOH_2$.

The UV-vis spectra at the point of equilibrium for each of the above reactions were then modeled as the sum of two dominant absorbing components, namely $[K(18\text{-}C\text{-}6)]_2[^{SO3}LCuOH]$ and LCuOH, using the program OriginLab. Specifically, the absorbance data for the experimental equilibrium spectra were fit to Eq. 3.4 below, where Y is the experimental absorbance data, X1 and X2 are the respective absorbance data for $[K(18\text{-}C\text{-}6)]_2[^{SO3}LCuOH]$ and LCuOH at a known concentration (0.1 mM), and W1 and W2 are unitless weighting parameters, which are determined from the fitting procedure.

$$Y = W1(X1) + W2(X2) \qquad \text{eq. 3.4}$$

Representative spectral overlays of the experimental and component spectra are shown in Figure 3.17. According to Scheme 3.3, the respective $[CuOH_2]^{2+}$ species are also present in solution. However, given the weak absorbance of the respective $[CuOH_2]^{2+}$ compounds relative to the much more strongly absorbing $[CuOH]^{2+}$ species, the contributions to the absorbance from the $[CuOH_2]^{2+}$ species were taken to be negligible and thus were not included in this model. From the fitted weighting parameters

and the known concentrations (0.1 mM) of the component $[CuOH]^{2+}$ spectra used in the modeling procedure, the equilibrium concentrations of $[^{SO3}LCuOH]^{2-}$ and LCuOH were determined according to Eqs. 3.5 and 3.6.

$$\left[^{SO3}LCuOH\right]_{eq} = W1 \times \left[^{SO3}LCuOH\right]_{X1} \quad \text{eq. 3.5}$$

$$[LCuOH]_{eq} = W2 \times [LCuOH]_{X2} \quad \text{eq. 3.6}$$

According to Scheme 3.3, the expression for K_{eq} is given by Eq. 3.7

$$K_{eq} = \frac{[^{SO3}LCuOH_2]_{eq}[LCuOH]_{eq}}{[^{SO3}LCuOH]_{eq}[LCuOH_2]_{eq}} \quad \text{eq. 3.7}$$

This equation can be rewritten in terms of the equilibrium concentrations of $[^{SO3}LCuOH]^{2-}$ and LCuOH, as well as the initial concentration of the added $LCuOH_2$ ($[LCuOH_2]_0$), allowing K_{eq} to be determined according to Eq. 3.8.

$$K_{eq} = \frac{([LCuOH]_{eq})^2}{[^{SO3}LCuOH]_{eq}([LCuOH_2]_0 - [^{SO3}LCuOH]_{eq})} \quad \text{eq. 3.8}$$

The above treatment yielded a $K_{eq} = 4.2 \pm 1.8$, which corresponds to a ΔBDE of ~ 0.8 kcal mol^{-1}. Given that the O-H BDE of the $LCuOH_2$ complex is 90 ± 3 kcal mol^{-1}, the O-H BDE of the $[^{SO3}LCuOH_2]^{2-}$ complex is ~ 91 ± 3 kcal mol^{-1}. This relatively high value of the BDE is comparable to that for the previously reported complex $^{NO2}LCuOH_2$.[14] It should be noted here that while the obtained BDE of the O-H bond in $[K(18\text{-}C\text{-}6)]_2[^{SO3}LCuOH_2]$ is very close to that in $LCuOH_2$ (within error of each other), this cross HAT experiment establishes the relative ordering unambiguously. Given that the ΔBDE (Eq. 3.1) is positive, we can clearly conclude that the O-H bond strength in $[K(18\text{-}C\text{-}6)]_2[^{SO3}LCuOH_2]$ is in fact higher, albeit by a small amount. Additionally, this high BDE value should provide a significant thermodynamic driving force for HAT reactions where $[^{SO3}LCuOH_2]^{2-}$ acts as the H-atom abstractor.

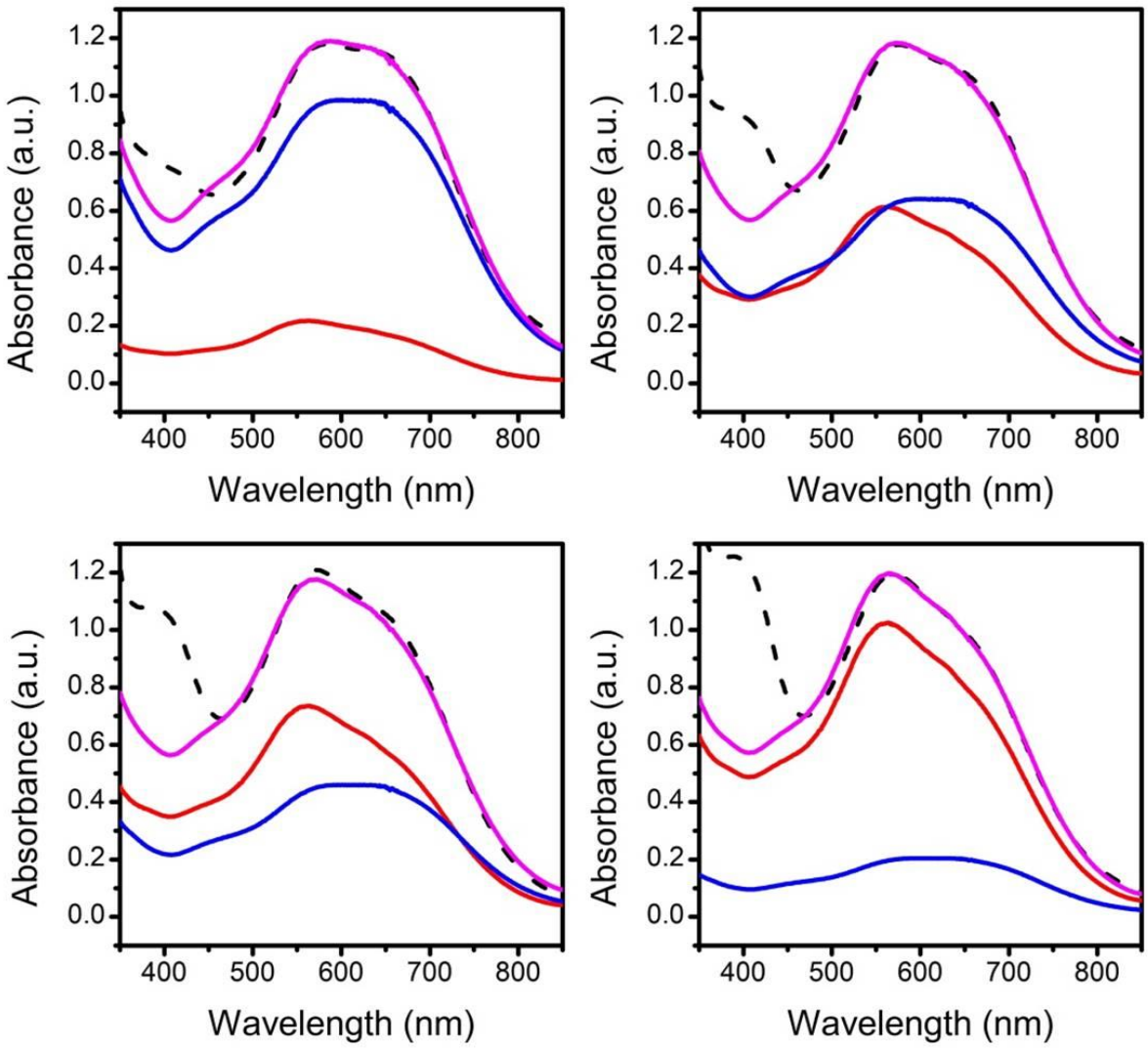

Figure 3.17. Representative deconvolution traces depicting the modeled spectra and experimental spectra. In all cases, the black dashed trace represents the experimental equilibrium spectrum, the red trace represents LCuOH, the blue trace represents $[^{SO3}\text{LCuOH}]^{2-}$ and the pink trace represents the overall modeled spectrum.

3.6.2 Determination of the O-H BDFE (Bond Dissociation Free Energy) in water through the determination of the basicity and redox potential of [K(18-C-6)]$_3$[^{SO3}LCuOH]

As has been described elaborately in previous sections (Chapter 1, Section 1.3), the BDFE or BDE can be determined from the PCET square scheme if the pK_a and $E_{1/2}$ of one of the sides of the square scheme are known. Accordingly, because [K(18-C-

6)]$_3$[^{SO3}LCuOH] is soluble in water, we independently determined the O-H BDFE for [^{SO3}LCuOH]$^{2-}$ in water through the determination of the pK_a of [^{SO3}LCuOH$_2$]$^{2-}$ and the $E_{1/2}$ for the [^{SO3}LCuOH]$^{2-}$/[^{SO3}LCuOH]$^{3-}$ redox couple.

The pK_a of [^{SO3}LCuOH$_2$]$^{2-}$ was determined through UV-vis titrations in water. The UV-vis spectra for a known concentration (1 mM) of [K(18-C-6)]$_3$[^{SO3}LCuOH] was measured in water across the pH range of 4.75-11.35, where the pH was adjusted by using either KOH or $HClO_4$ and measured using a pH probe. The representative traces are shown below in Figure 3.18.

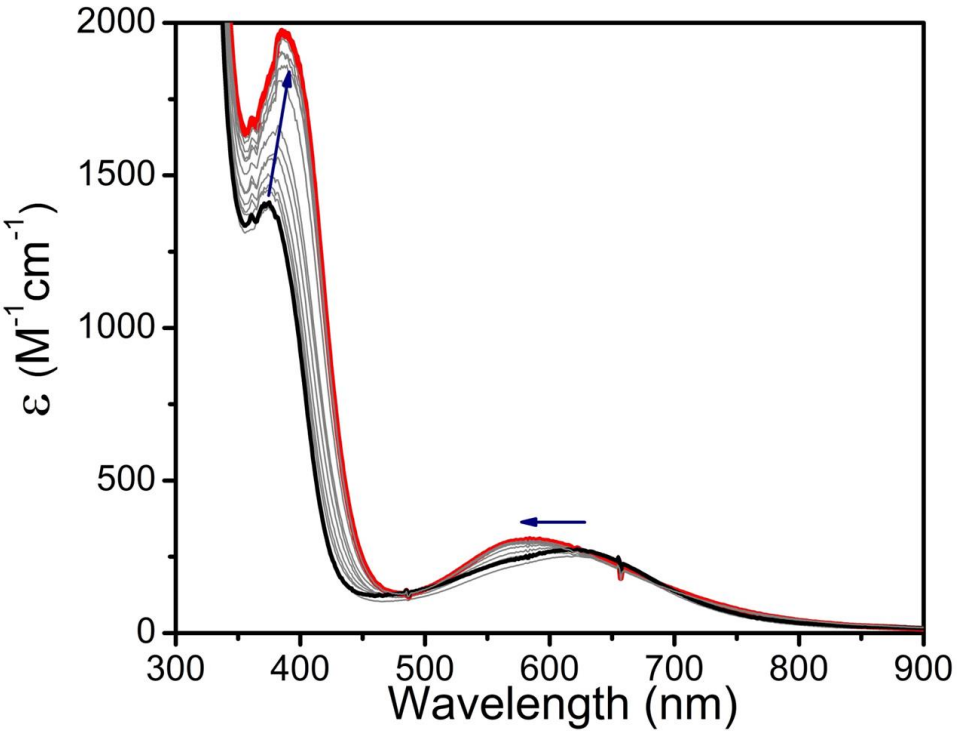

Figure 3.18. (Left) UV-vis spectra of [K(18-C-6)]$_3$[^{SO3}LCuOH] in water at a pH of 4.75 (red trace) and at pH of 11.35 (black trace). (Right) Observed changes in the UV-Vis spectra during the course of the titration from pH 11.35 to pH 4.75.

Figure 3.18 clearly shows that there are observable changes in the UV-vis spectra as a function of the pH. Going from basic pH to acidic pH shifts the *d-d* band to slightly lower wavelengths. On the other hand, the changes in the charge transfer region are more prominent, showing a shift to lower wavelengths coupled with an increase in the

intensity. The intermediate equilibrium spectra were deconvoluted using the protocol described above in Section 3.6.1 using the two components at pH 4.75 (pure copper(II)-aqua) and pH 11.35 (pure copper(II)-hydroxide) and the relative proportions of these were determined. With these proportions and the measured pH of the solution at the equilibrium points, the pK_a of $[K(18\text{-}C\text{-}6)]_2[^{SO3}LCuOH_2]$ was found to be 10.1 ± 0.2. This result is in good agreement with reported pK_a values obtained for other copper(II)-aqua complexes in water, which range from 7-13.[45] It is instructive to compare this number to the pK_a values obtained for the previously characterized analogous $[CuOH_2]^{2+}$ complexes (namely, $LCuOH_2$, $^{NO2}LCuOH_2$ and $^{pipMe}LCuOH_2$) under non-aqueous conditions, which range from ~17-20 (in THF).[13,14] In the previous cases, the higher values are an artifact of using THF solvent (in comparison to water in the current experiment), and it has been well documented that non-polar, non-protic solvents like THF have an accentuating effect on the observed basicity, owing to the low dielectric constant of the solvent medium which inhibits ionization.[44] Thus, we conclude that the lower evaluated pK_a of $[K(18\text{-}C\text{-}6)]_2[^{SO3}LCuOH_2]$ in water is not indicative of the lower intrinsic basicity of the corresponding $[CuOH]^+$ species relative to the previously characterized analogs.

The determination of the $E_{1/2}$ for the one-electron redox potential corresponding to the $[^{SO3}LCuOH]^{2-}/[^{SO3}LCuOH]^{3-}$ couple through detailed pH dependent cyclic voltammetry measurements in water proved challenging, owing to the significant overlap between this oxidative feature and the solvent oxidation window. While this might be indicative of catalytic water oxidation that is coupled with the oxidation of the $[^{SO3}LCuOH]^{3-}$, thorough analysis needs to be done to verify this notion.[45b,64] Nevertheless, an approximate $E_{1/2}$ could be determined (Figure 3.19) from the cyclic voltammograms in water (at pH 10) and it was found to be 0.75 V (vs. NHE).

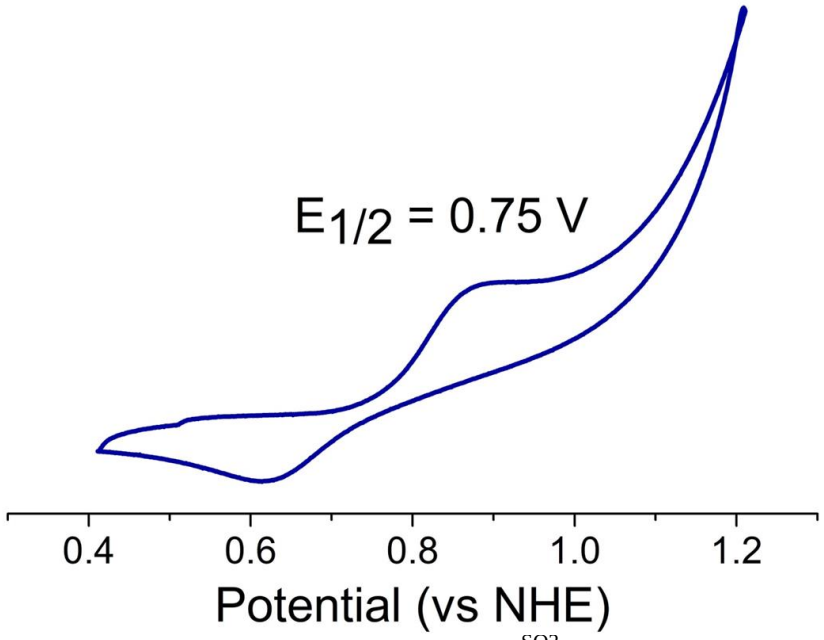

Figure 3.19. Cyclic Voltammogram of $[K(18\text{-}C\text{-}6)]_3[^{SO3}LCuOH]$ in water recorded at pH 10. Conditions : 2 mM analyte, 0.1 M $NaClO_4$ supporting electrolyte, Glassy Carbon working electrode, Scan rate 100mV/s

Using this $E_{1/2}$, the above pK_a, the known C_G (associated with the $H^+/H^\bullet$ standard reduction potential in water, C_G = 57.6 kcal mol^{-1})[16] and using Eq. 3.9 below

$$BDE\ (kcal\ mol^{-1}) = 1.37pK_a + 23.06E° + C_G \qquad \text{eq. 3.9}$$

the BDFE of the O-H bond in $[^{SO3}LCuOH_2]^{2-}$ was evaluated to be 89 ± 1 kcal mol^{-1}. This BDFE determined in water is in good agreement with the BDE of 91 kcal mol^{-1} determined from the non-aqueous measurements.

3.7 Kinetics of HAT from 9,10-dihydroantracene (DHA) performed by $[CuOH]^{2+}$

Given the high O-H BDE value of the copper(II)-aqua complex ($[^{SO3}LCuOH_2]^{2-}$) that would be formed as a result of HAT to $[CuOH]^{2+}$, we sought to explore the HAT reactivity between DHA and $[^{SO3}LCuOH]^{2-}$ in 1,2-DFB at -25 °C using a similar protocol to that employed for the analogous copper(III)-hydroxide complexes.[13,14] Oxidation of a pre-mixed solution of $[K(18\text{-}C\text{-}6)]_3[^{SO3}LCuOH]$ and varying equivalents of DHA (pseudo first order conditions) with $[Fc][BAr^F{}_4]$ resulted in the growth and subsequent decay of

the LMCT band at 610 nm diagnostic for [^{SO3}LCuOH]$^{2-}$ (Figure 3.20, left). Concomitant with the decay of this feature was the growth of sharp bands at 358 and 379 nm, indicative of the formation of anthracene (Figure 3.20, left). The absorbance vs. time plots for the feature at 610 nm were fit to a single exponential decay function, giving an observed rate constant (k_{obs}). Plotting k_{obs} against the concentration of DHA yielded the second-order rate constant for the reaction as the slope of the line (Figure 3.20, right (inset)).

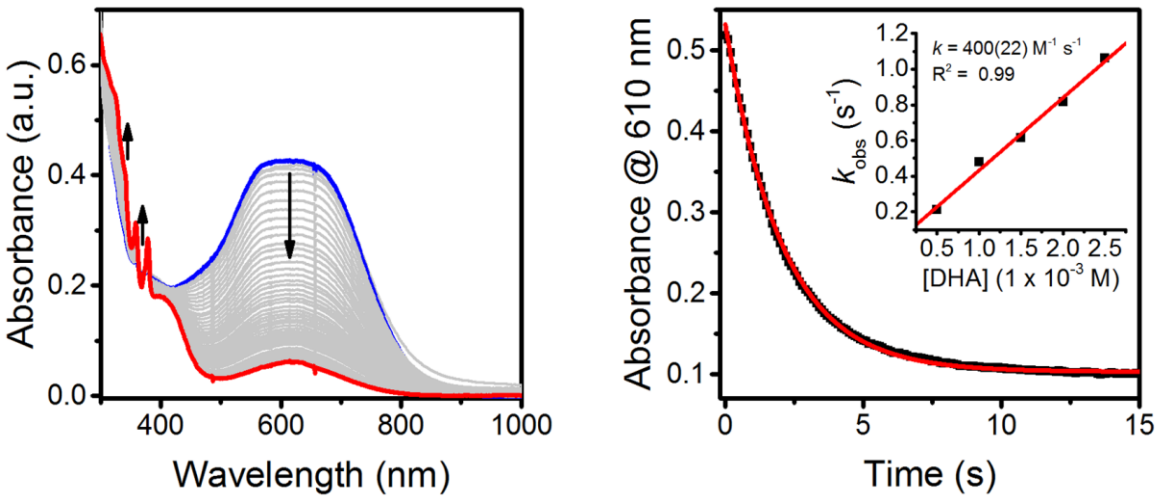

Figure 3.20. (Left) Representative UV-vis spectrum over time for the reaction of [K(18-C-6)]$_2$[^{SO3}LCuOH] with 10 eq of DHA at -25 °C. (Right) Representative absorbance vs. time plots showing the single exponential fit in red and the corresponding second-order plot.

The second-order rate constant for the HAT reaction with DHA was found to be 400(22) M^{-1} s^{-1}. This high rate of HAT from the weak C-H bonds of DHA is in line with the relatively high BDE (thermodynamic driving force) measured in the previous section. Additionally, the reactions with DHA-d_4 were also measured under identical conditions and the KIE (k_H/k_D) value was found to be 12. This relatively high value of the KIE is indicative of (1) C-H bond scission being the rate determining step of the reaction, and (2) significant non-classical quantum tunneling contributions in the HAT step. These

observations are all congruent with those for the previously reported $[CuOH]^{2+}$ complexes.[14]

In order to probe if secondary coordination sphere ionic interactions affect the HAT rates, the reactions were repeated under identical conditions in the presence of 100 eq [Na(15-C-5)]OTf. In a typical experiment, a pre-mixed solution of 0.05 mM $[K(18\text{-}C\text{-}6)]_3[^{SO3}LCuOH]$, 5 mM [Na(15-C-5)]OTf and excess DHA (pseudo-first order conditions) in 1,2-DFB was oxidized using 1 eq. $[AcFc][BAr^F{}_4]$ at -25 °C, and the reaction was monitored using UV-vis spectroscopy. The second order rate constant in this case (500(30) M^{-1} s^{-1}) was found to be slightly higher than the case lacking added [Na(15-C-5)]OTf (Figure 3.21). Complicating the comparison of these rate constants is the possibility that the solvent dielectric properties are changed because of the differences in ionic strength, which might be a significant effect for charged species like $[^{SO3}LCuOH]^{2-}$. In order to test this hypothesis, we performed a control reaction, where we repeated the experiments in the presence of 100 eq. $[Bu_4N]PF_6$. The observed rate constant in this case is found to be 300(12) M^{-1} s^{-1} (a *lower* value when compared to that in the absence of any added electrolyte). Furthermore, when the same experiments were performed in the presence of 100 eq [(K(18-C-6)]OTf, the second order rate constant also had an identical value of 300(30) M^{-1} s^{-1}. These findings suggest that any rate alteration due to changes in the ionic strength of the medium is independent of the nature of the added electrolyte. More importantly, these control experiments indicate that the rate enhancement observed in the case of addition of [Na(15-C-5)]OTf is not a consequence of alteration of the ionic strength of the reaction medium, but instead is due to more specific interactions of [Na(15-C-5)]OTf with the copper reagent. We postulate that the increased ionic interaction of the $[Na(15\text{-}C\text{-}5)]^+$ with the anionic SO_3^- groups, particularly in a non-protic solvent like DFB, causes it to exist as a "tighter ion-pair", which mitigates the electrostatic effects of the anionic SO_3^- moiety to some extent (higher than in the case of the $[K(18\text{-}C\text{-}6)]^+$ counter ion). This is also manifested in the

change in the reduction potential of the $[CuOH]^{2+}/[CuOH]^{+}$ couple by ~180 mV (Section 3.4.3), which effectively makes the $[Na(15\text{-}C\text{-}5)]_2[^{SO3}LCuOH]$ a stronger oxidant. We suggest that this intrinsic increase in the oxidation potential might translate into a higher thermodynamic driving force for the HAT reaction, which causes the subtle increase in the rates of HAT from DHA evidenced for the *in situ* generated $[Na(15\text{-}C\text{-}5)]_2[^{SO3}LCuOH]$.

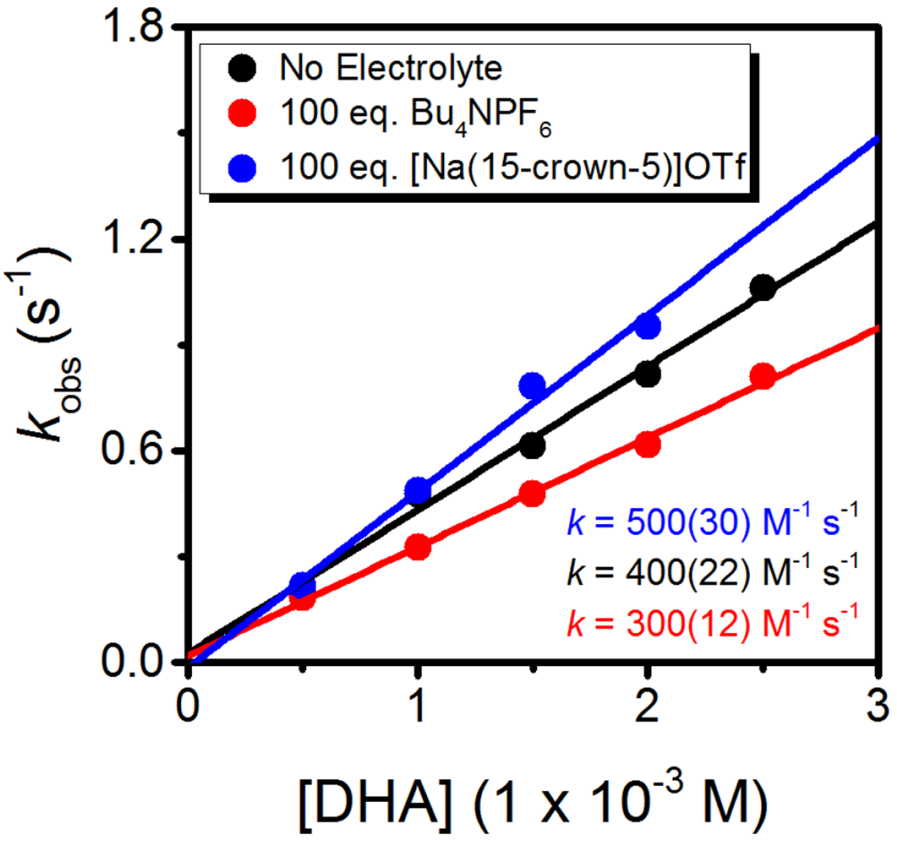

Figure 3.21. Second order plots depicting the variation in the rates of HAT from DHA to $[^{SO3}LCuOH]^{2-}$ as a function of the added electrolyte.

3.8 Summary and conclusions

A novel *para*-sulfonate functionalized pyridine dicarboxamide ligand framework was synthesized with the aim of probing the effects of such anionic substituents on the properties of the corresponding $[CuOH]^{2+}$ complexes. Structural characterization of the copper(II)-hydroxide and other copper(II)-complexes with this ligand revealed that the

pendant anionic SO_3^- functionality is involved in secondary coordination sphere interactions with Lewis acidic sites. Detailed thermodynamic and kinetic analysis in light of proton-coupled-electron transfer chemistry revealed that the corresponding copper(III)-hydroxide complexes are efficient HAT reagents owing the high BDE of the O-H bond in the corresponding copper(II)-aqua complexes. Additionally, it was observed that alteration of the counter cation from [K(18-crown-6)] to the more Lewis acidic Na(15-crown-5)] causes a considerable increase (~180 mV) in the oxidation potential of the $[CuOH]^+$ species, and we hypothesize that this increase is due to differential ion-pairing effects in the two cases. Interestingly, this differential ion-pairing is manifested in the form of subtle observable differences in the HAT reactivity of these species with DHA. The intriguing effect of such distally placed charged residues in affecting the chemistry at the metal center, by means of interactions with Lewis acidic sites, is potentially relevant to how the reactivity patterns in the active sites of enzymes may be modulated by such charged residues which are ubiquitous in the protein active sites.

3.9 Experimental section

Materials and Methods. All reagents and solvents were purchased from commercial sources and used as received unless otherwise noted. Tetrahydrofuran (THF) and diethyl ether was passed through solvent purification columns containing activated alumina and used directly (Glass Contour, Laguna, California). 1,2-Difluorobenzene (DFB), acetonitrile, and dichloromethane were dried over calcium hydride and vacuum distilled.. All solvents were stored over 3 Å molecular sieves in a N_2 filled glove-box prior to use. All samples for kinetic measurements were prepared in a Vacuum Atmospheres glove-box under an inert atmosphere of nitrogen. HPLC grade water was degassed by sparging with N_2 for 15 min prior to use in titration experiments. Elemental analyses were performed by Robertson Microlit Laboratory (Ledgewood, NJ). UV-vis spectra were obtained using an HP8453 (190-1100) diode array spectrophotometer.

Variable temperature UV-vis experiments were performed using a Unisoku low temperature cell holder. Cyclic voltammograms were recorded using an EC Epsilon potentiostat from BASi, a glassy-carbon working electrode, and a Ag^+/Ag reference electrode; they were referenced internally using decamethylferrocene. The final potentials were then converted vs. the standard Fc^+/Fc couple using standard conversion factors.[51] Aqueous cyclic voltammetry experiments were recorded using the AgCl/Ag(s) electrode and the final potentials were then converted vs. the normal hydrogen electrode using standard conversion factors. X-ray diffraction measurements were collected with Cu Kα radiation or Mo Kα source and a Bruker D8 Photon II CPAD diffractometer using normal parabolic mirrors as monochromators. EPR spectra were recorded on a CW X-band Elexsys E500 EPR spectrometer equipped with an Oxford ESR 910 liquid helium cryostat. All spectra were recorded at a temperature of 30 K at a microwave frequency of 9.64 GHz under the following conditions: microwave power of 0.063 mW (30 K); modulation amplitude of 9.8 G; modulation frequency of 100 kHz. Chemical shifts (δ) for ^1H and ^{13}C NMR spectra were referenced to residual protium in the deuterated solvent (^1H) or the characteristic solvent resonances of the solvent nuclei (^{13}C). The compounds DHA-d_4,[33k] and $[Fc][BAr^F{}_4]$[48] and $[AcFc][BAr^F{}_4]$[14] were synthesized using previously reported procedures.

Synthesis of 4-amino-3,5-diisopropylbenzenesulfonic acid hydrochloride. 2,6-diisopropylaniline dihydrogen sulfate (10.0 g, 0.036 mol) was suspended in 150 ml 1,2-dichlorobenzene and the contents were refluxed at 170 °C for 6 h. After the reaction mixture cooled down to room temperature, it was poured over crushed ice and 50 ml de-ionized water was added to it. To the resulting slurry NaOH pellets were added until the pH of the aqueous layer was ~13. The aqueous extract was separated and the solvents were removed *in vacuo* to reduce the volume to one-third of the starting volume. The aqueous extract was then acidified by dropwise addition of conc. HCl until the pH is ~4. *The acidification process is exothermic, so it is ensured that the solution remains cool by*

placing it on a salt-ice bath. The white solid that precipitated out was isolated by filtration and washed thoroughly with copious amounts of diethyl ether and dried thoroughly (7.20 g, 70.0%). ^{1}H NMR (DMSO-d_6, 400 MHz): δ 7.46 (2H, s), 3.25 (2H, quintet), 1.17 (24H, d) ppm.^{13}C{^{1}H} NMR (DMSO-d_6, 101 MHz): 146.68, 140.78, 127.71, 121.41, 27.30, 23.63 ppm. Anal. Calcd. for $C_{12}H_{20}ClNO_3S$: C, 49.07; H, 6.86; N, 4.77; Cl, 12.07. Found: C, 49.18; H, 7.15; N, 4.82; Cl, 11.98.

Synthesis of ((*i*Pr)$_2$EtNH)$_2$(^{SO3}LH$_2$). 4-amino-3,5-diisopropylbenzenesulfonic acid hydrochloride (2.00 g, 6.81 mmol) was suspended in anhydrous THF (70 ml) under an atmosphere of Ar(g) and the mixture was cooled on an ice-bath. *N*,*N*-diisopropylethylamine (2.2 ml) was added to the mixture and the contents were stirred for 20 min. Then, pyridine-2,6-dicarbonyl dichloride (0.69 g, 3.40 mmol) was added to the reaction mixture in small portions, following which a further 3.5 ml of *N*,*N*-diisopropylethylamine was added to it and the contents were stirred at 0 °C for 30 min. Then the resulting pale-yellow slurry was stirred at room temperature for 48 h under an atmosphere of Ar(g), which eventually led to the formation of a yellow oily substance with a clear supernatant solution. Then the solvent was removed *in vacuo* to ~20 ml and the resulting supernatant was decanted off to isolate a yellow sticky oily substance. This was dissolved in minimum MeOH and to this solution, excess anhydrous THF was added dropwise while cooling the contents on an ice-bath. This resulted in the formation a fine whitish solid suspension which assumed a more crystalline consistency after vigorous trituration in THF over the course of 1 h. Then the contents were filtered through a fine porosity glass frit to isolate a white solid which was washed thoroughly with cold THF and diethyl ether and dried thoroughly (1.60 g, 55.0%). Slow evaporation of a MeOH solution of the solid yielded X-ray quality prismatic crystals. ^{1}H NMR (D_2O, 400 MHz): δ 8.36 (2H, d), 8.25 (1H, t), 7.66 (4H, s), 3.67 (4H, quintet), 3.18-3.04 (8H, m), 1.31-1.28 (30H, m) 1.10 (24H, d) ppm. ^{13}C{^{1}H} NMR (D_2O, 101 MHz): 165.75, 147.92, 147.73, 142.86, 140.35, 133.19, 125.92, 121.00, 54.32, 42.51, 28.83, 17.69, 16.22, 12.11 ppm.

Anal. Calcd. for $C_{47}H_{77}N_5O_8S_2$: C, 62.43; H, 8.58; N, 7.74. Found: C, 62.16; H, 8.30; N, 7.74.

Synthesis of [K(18-crown-6)]$_3$[^{SO3}LCuOH]. $^{SO3}LH_2$ (0.200 g, 0.221 mmol) was dissolved in degassed HPLC grade water (15 ml) taken in a schlenk flask and to this, a solution of KOH (1.00 M, 0.500 ml) was added and the contents were stirred under an atmosphere of Ar(g) for 15 min, following which copper(II) triflate (0.080 g, 0.221 mmol) was added to the solution to form a blue colored solution. After 10 min of stirring, a further additional amount of KOH solution (1.00 M, 0.500 ml) was added to the reaction mixture and the solution was stirred at room temperature for 30 min. The solvents were then removed under reduced pressure while heating to 40 °C without exposing the solution to atmosphere, following which degassed acetone (10 ml) was added to the flask by using a canula. The contents were triturated for 15 min which led to the precipitation of a blue-purple solid. Then the supernatant solution was removed from the flask using a canula. This process was repeated three times and the resulting solid was dried thoroughly under vacuum. The solid was then transferred to a nitrogen filled glove-box and excess anhydrous THF and 18-crown-6 were added to the solid and the contents were triturated thoroughly overnight. The blue solid that precipitated out was isolated by filtration, washed thoroughly with copious amounts of THF and diethyl ether and dried thoroughly (0.210 g, 58.0%). X-ray quality blue needle shaped crystals were obtained by vapor diffusion of diethyl ether into a solution of the solid in 1,2-diflurobenzene (DFB) at -19 °C. UV-vis (DFB, 25 °C) λ_{max}, nm (ε, M^{-1} cm^{-1}): 383(2100), sh; 597 (350). Anal. Calcd. for $C_{67}H_{108}CuK_3N_3O_{27}S_2$: C, 49.29; H, 6.67; N, 2.57. Found: C, 49.04; H, 7.09; N, 2.17.

Synthesis of [(Et_4N)$_2$(^{SO3}LCu)]$_2$. $^{SO3}LH_2$ (0.200 g, 0.221 mmol) was dissolved in degassed HPLC grade water (10 ml) taken in a schlenk flask and to this, a solution of Et_4NOH (1.40 M in water, 0.320 ml, 0.448 mmol) was added and the contents were stirred under an atmosphere of Ar(g) for 15 min, following which copper(II) triflate

(0.080 g, 0.221 mmol) was added to the solution to form a blue-green colored solution. After 10 min of stirring, a further additional amount of Et_4NOH (1.40 M in water, 0.320 ml, 0.448 mmol) was added to the reaction mixture and the solution was stirred at room temperature for 30 min. The solvents were then removed under reduced pressure to give ~2 ml solution while heating to 40 °C without exposing the solution to atmosphere, following which degassed acetone (10 ml) was added to the flask by using a canula. The contents were triturated for 15 min which led to the precipitation of a blue-green solid. Then the supernatant solution was removed from the flask using a canula. This process was repeated two times. Then excess acetone (20 ml) is added to the reaction mixture and the contents are stirred overnight under Ar(g) to afford a fine forest green solid, which is isolated by filtration and washed thoroughly with boiling acetone. The solid is then dried thoroughly under vacuum (0.120 g, 56.0%). X-ray quality fine green needle shaped crystals were obtained by slow evaporation from a saturated solution of the compound in a water:acetone (5:95 v/v) solvent mixture. Anal. Calcd. for $C_{94}H_{150}Cu_2N_{10}O_{16}S_4$: C, 58.45; H, 7.83; N, 7.25. Found: C, 58.13; H, 8.09; N, 7.52.

Synthesis of [Na(15-crown-5)]$_3$[^{SO3}LCuCl]. $[(Et_4N)_2(^{SO3}LCu)]_2$ (0.100 g, 0.052 mmol) is suspended in CH_2Cl_2 (10 ml) and to it NaCl (0.018 g, 0.309 mmol) and excess 15-crown-5 is added and the reaction mixture is stirred for 30 min. Over the course of the reaction the solids gradually dissolve to afford a deep green solution. The solvents are then removed *in vacuo* to isolate a greasy deep green solid. This is dissolved in !2 ml acetone and then excess diethyl ether (~15 ml) is added to the solution to precipitate a deep green amorphous solid, which is isolated by filtration and dried thoroughly (0.110 g, 72.2%). Anal. Calcd. for $C_{61}H_{95}ClCuN_3Na_3O_{23}S_2$: C, 49.82; H, 6.51; N, 2.86. Found: C, 50.18; H, 6.92; N, 2.95.

Procedure for preparation of aqueous EPR samples. A 5 mM solution of [K(18-crown-6)]$_3$[^{SO3}LCuOH] in degassed HPLC grade water containing 0.1 M $NaClO_4$ was transferred into a low volume thin walled glass capillary tube. The open end of the

capillary tube was then sealed using a blow-torch and the capillary tube was placed in ice to slowly freeze the solution. Then the capillary containing the frozen sample was transferred into a standard EPR tube containing toluene. The EPR tube was finally slowly frozen by submerging it in a dewar containing liquid N_2. This EPR tube was then used for sample collection. In all cases, the observed spectra was taken and the recorded blank spectra (obtained by sample preparation in a similar manner as above containing *only* 0.1 M $NaClO_4$ and *no* copper sample) was subtracted from it to get the spectra of the copper sample.

General Procedure for the generation of the $[CuOH]^{2+}$ species. A solution of a known concentration of $[K(18\text{-crown-}6)_3][^{SO3}LCuOH]$ in 1,2-diflurobenzene(DFB) was taken in a UV-cuvette under N_2 and cooled to -25 °C for 10 min. Following this, 1 eq of $[Fc][BAr^F{}_4]$ was added to the solution in order to generate the corresponding $[CuOH]^{2+}$ at -25 °C in 1,2-diflurobenzene, characterized by the immediate appearance of the corresponding charge transfer bands at 610 nm. In the case of the runs with [Na(15-crown-5)]OTf, an identical procedure is used only with the modification of 100 eq of the electrolyte solution being added to the solution of $[K(18\text{-crown-}6)_3][^{SO3}LCuOH]$, after which 1 eq $[AcFc][BAr^F{}_4]$ is added.

General Procedure for cross HAT reactions for the determination of the BDE. A solution of a known concentration of $[K(18\text{-crown-}6)]_3[^{SO3}LCuOH]$ in 1,2-DFB was taken in a UV-cuvette under N_2 and cooled to -25 °C for 10 min. Following this, one equivalent of $[Fc][BAr^F{}_4]$ was added to the solution in order to generate the corresponding $[CuOH]^{2+}$ ($[K(18\text{-crown-}6)]_2[^{SO3}LCuOH]$) at -25 °C in 1,2-DFB, characterized by the immediate appearance of the corresponding charge transfer bands at 610 nm. To this cooled solution under N_2, was added known concentrations of the copper(II)-aqua complex $[LCuOH_2]$ and the corresponding reaction was monitored by UV-vis spectroscopy. In all cases, spectral deconvolution of the final equilibrium spectra was performed by a non-linear regression routine employing standard spectra of the pair

of $[CuOH]^{2+}$ involved in the reaction as the two components. The relative weights of the two components derived from the fitting were then utilized to calculate the equilibrium concentrations of all the species, which were then used to estimate the equilibrium constant.

General Procedure for Kinetic Studies of Substrate Activation by 6 in 1,2-difluorobenzene. Under an N_2 atmosphere, a 3.0 mL cuvette was charged with 1.8 mL of a known concentration of substrate (DHA, DHA-*d*$_4$ or 1,4-CHD) solution in 1,2-difluorobenzene. The cuvette was cooled at -25 °C for approximately 10 min, after which 0.1 mL of a 1 mM stock solution of $[K(18\text{-crown-6})]_3[^{SO3}LCuOH]$ was added. After 2 min, to this was added 0.1 mL (1 mM solution) of $[Fc][BAr^F_4]$, which resulted in the immediate growth of an intense charge transfer band centered around 610 nm, consistent with the formation of $[K(18\text{-crown-6})]_2[^{SO3}LCuOH]$. Decay of this feature was monitored over time by UV-vis spectroscopy, by collecting spectra at every 0.1 s time intervals. In all cases decay traces at 610 nm were fit to a single exponential decay function to obtain the pseudo-first order rate constants (k_{obs}). Second order rate constants were then extracted from plots of k_{obs} vs. substrate concentration.

General Procedure for Kinetic Studies of Substrate Activation by 6 in 1,2-difluorobenzene in the presence of external electrolyte. Under an N_2 atmosphere, a 3.0 mL cuvette was charged with 1.7 mL of a known concentration of substrate (DHA) solution in 1,2-difluorobenzene. The cuvette was cooled at -25 °C for approximately 10 min, after which 0.1 mL of a 1 mM stock solution of $[K(18\text{-crown-6})]_3[^{SO3}LCuOH]$, followed by addition of a 0.1 mL of a 10 mM stock solution of the electrolyte ($[Bu_4N]PF_6$ or [Na(15-crown-5)]OTf). After 2 min, to this was added 0.1 mL (1 mM solution) of $[AcFc][BAr^F_4]$, which resulted in the immediate growth of an intense charge transfer band centered around 610 nm or 567 nm respectively, consistent with the formation of the corresponding $[CuOH]^{2+}$ species. Decay of this feature was monitored over time by UV-vis spectroscopy, by collecting spectra at every 0.1 s time intervals. In all cases

decay traces at 610 nm or 567 nm were fit to a single exponential decay function to obtain the pseudo-first order rate constants (k_{obs}). Second order rate constants were then extracted from plots of k_{obs} vs. substrate concentration.

Chapter 4

A Mechanistic Dichotomy In Reactions Of The Copper(III)-Hydroxide Unit With Phenols[a]

[a] The results presented in this chapter were previously published in:

Debanjan Dhar[†], Gereon M. Yee[†], Todd F. Markle, James M. Mayer*, and William B. Tolman*. Reactivity of the Copper(III)-Hydroxide Unit With Phenols. *Chem. Sci.* **2017**, *8*, 1075-1085.

[†]*These authors contributed equally to this work.*

4.1 Introduction

Detailed study of the structural and spectroscopic properties and reactivity of copper-oxygen complexes can provide important insights into the nature of putative intermediates in oxidation catalysis.[7] Recently a new copper-oxygen motif comprising a $[CuOH]^{2+}$ core was identified by the Tolman group, examples of which include LCuOH, ^{pipMe}LCuOH, and ^{NO2}LCuOH.[8,13,14] These were prepared in solution *via* the one-electron oxidation of the correpsonding anionic copper(II)-hydroxide complexes ($[Bu_4N][LCuOH]$, $[Bu_4N][^{pipMe}LCuOH]$, and $[Et_4N][^{NO2}LCuOH]$ respectively) at low temperature (Scheme 4.1). The oxidized complexes were postulated on the basis of spectroscopy and theory to be best described as copper(III)-hydroxide species.[8,13,14,58] Despite their weak oxidizing ability (LCuOH: $E_{1/2}$ = -0.074 V vs. Fc^+/Fc in THF), the complexes react rapidly with C-H bonds of hydrocarbon substrates; for example, 9,10-dihydroanthracene (DHA) is converted cleanly to anthracene at high rates (e.g. for LCuOH, k = 1.1(1) M^{-1} s^{-1} at -80 °C in CH_2Cl_2),[14] with concomitant formation of the respective copper(II)-aqua complex ($LCu(OH_2)$, $^{pipMe}LCu(OH_2)$, and $^{NO2}LCu(OH_2)$).

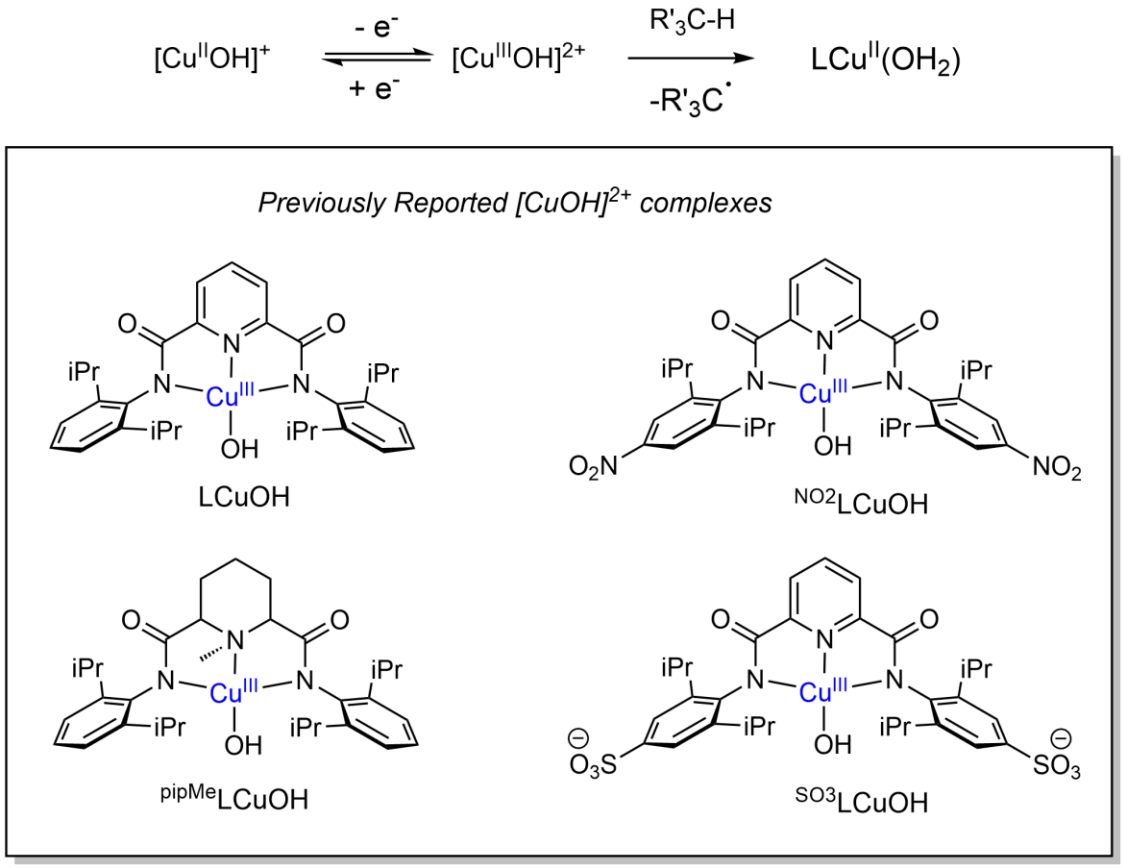

Scheme 4.1. Synthesis and reactivity of $[CuOH]^{2+}$ complexes.

The O-H bond dissociation enthalpies (BDE) of the aqua complexes were experimentally determined to lie in the range of 88-91 kcal mol^{-1} (details discussed in Chapters 2 and 3 previously),[13,14] high values that rationalize, at least in part, the fast rates of reactions of copper(III)-hydroxide complexes with DHA and the observation that even stronger C-H bonds may be attacked, including those of cyclohexane (C-H BDE ~ 99 kcal mol^{-1}). The high O-H BDE values for $LCu(OH_2)$, $^{pipMe}LCu(OH_2)$, and $^{NO2}LCu(OH_2)$ arise from high basicity of the hydroxide ($pK_a(LCu(OH_2))$ = 18.8 ± 1.8 in THF)[13] offsetting the poor oxidizing power of the complexes, properties which may be traced to the strongly electron donating di-carboxamide supporting ligand framework. Kinetic data and computations support the notion that the reactions of $[CuOH]^{2+}$ with organic substrates proceed *via* a hydrogen atom transfer (HAT) with a significant tunneling contribution to

the reaction rate.[14] The rate of HAT from DHA is fastest for ^{NO2}LCuOH, which has a slightly higher O-H BDE as a result of a higher reduction potential that offsets its weaker basicity.[14] Additionally, as previously described in Chapter 3, an analogous $[CuOH]^{2+}$ species has also been characterized using a ligand framework that incorporates pendant anionic sulfonate groups, and it is shown to perform very rapid HAT from DHA, having rates comparable to the previously characterized $[CuOH]^{2+}$ complexes. The O-H BDE in the corresponding $[CuOH_2]^{2+}$ is found to be ~ 91 kcal mol^{-1}, demonstrating that such $[CuOH]^{2+}$ complexes have a high propensity to act as efficient HAT reagents, which is a consequence of the intrinsic thermodynamic driving force afforded by these high bond strengths. Importantly, the observed high reactivity of the copper(III)-hydroxide core in these complexes provides a clear precedent for its possible involvement as an intermediate in oxidation catalysis.[13]

The extent of coupling of the proton and electron transfer involved in the attack at X-H (X = C, N, O) bonds by transition metal-oxo/hydroxo species is a fundamentally important mechanistic issue, particularly given the significance of atom transfer reactions in biology and catalysis.[1,16-18,65] Two extremes may be envisioned: concerted proton-electron transfer (CPET) or sequential proton and electron transfer (PT/ET or ET/PT depending on which occurs first). For reactions with C-H bonds of substrates that are relatively difficult to oxidize (remove electrons) or deprotonate, the sequential processes are disfavored and tightly coupled, or CPET paths are typical (although there are exceptions).[18,22,27,66] A CPET mechanism is consistent with the available evidence for the reactions of the above copper(III)-hydroxide complexes with C-H bonds.[8,13,14] We hypothesized, however, that the high basicity of the hydroxide ligands in these complexes might underlie some contributions from PT/ET processes in reactions with more acidic N-H or O-H bonds.

To test this notion, we chose to examine the reactivity of LCuOH and ^{NO2}LCuOH with phenols, substrates that have garnered extensive attention because of their

importance in biological proton, electron, and atom transfer processes.[67] By varying the *para* substituents on the phenols, the reduction potentials and acidity of the phenols could be varied over a significant range (Scheme 4.2, Table 4.1), enabling these effects on the reaction rates to be evaluated for the two complexes LCuOH and ^{NO2}LCuOH that have different O-H BDE's and DHA reaction rates.[14] In this chapter, I will present the results of these reactivity studies, and in particular the findings from kinetics experiments that implicate CPET processes for all but the most acidic phenol substrates, for which evidence is provided that PT/ET is involved. The results expand upon previous work[13,14] defining the kinetics and thermodynamics of reactions of the $[CuOH]^{2+}$ unit that is important for understanding its potential involvement in oxidation catalysis.

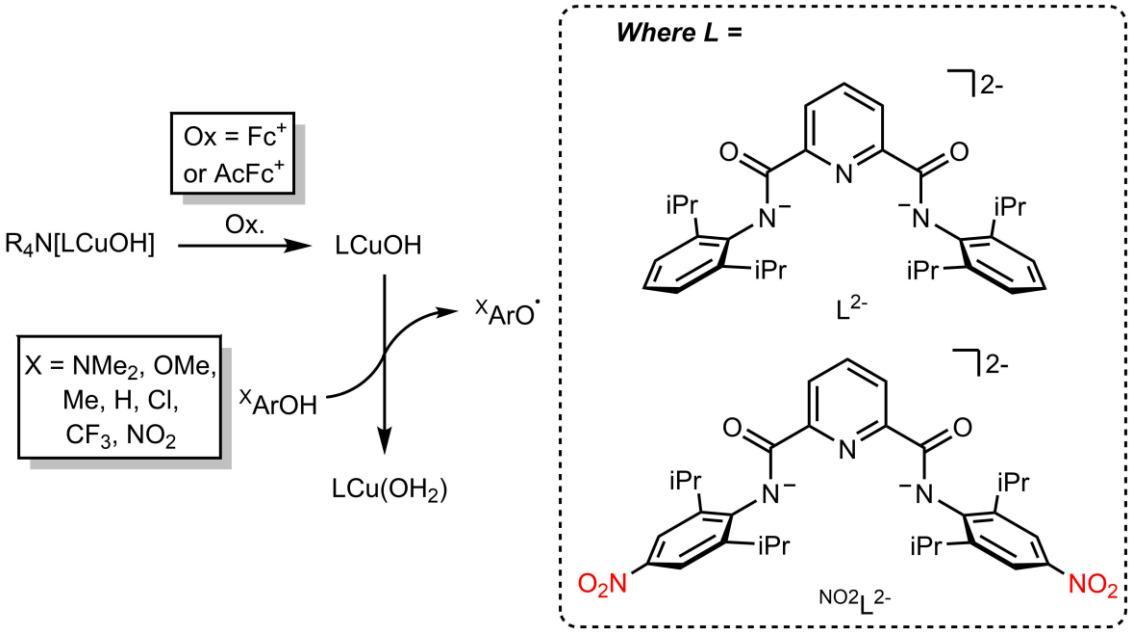

Scheme 4.2. Scheme of Reactions of $[CuOH]^{2+}$ with *para*-substituted phenols.

Table 4.1. Thermodynamic properties of *para*-subsituted phenols ^{X}ArOH.[a]

X	BDFE (kcal mol^{-1})	pK_a(ROH)	$E_{1/2}$(RO$^{\bullet}$/RO^{-})[b]	pK_a(ROH$^{+\bullet}$)	$E_{1/2}$(ROH$^{+\bullet}$/ROH)[b]
NMe_2	78.7	19.8	-0.847	6.3	-0.045
OMe	83.0	19.1	-0.618	-5.6	0.850
Me	87.1	18.9	-0.428	-4.0	1.10
H	88.3	18.0	-0.325	-7.7	1.20
Cl	88.7	16.75	-0.232	-11	1.40
NO_2	93.1	10.8	0.314	-9.5	1.90
CF_3	93.7	15.2[c]	0.079[c]	-	-

[a] Measured in DMSO, from Ref. 16 unless otherwise stated. [b] V vs. Fc^{+}/Fc. [c] From Ref. 68.

4.2 Stopped-flow kinetics experiments

4.2.1 Overview of experimental setup and kinetic workup

The reactions of LCuOH and ^{NO2}LCuOH with phenols ^{X}ArOH (Scheme 4.2) were monitored using double-mixing stopped-flow UV-vis spectroscopy at -80 °C in THF. In a typical experiment, in the first mixing event equimolar solutions of the copper(II)-hydroxide complex (Bu_4N[LCuOH] or Et_4N[^{NO2}LCuOH]) were combined in a 1:1 ratio with the appropriate oxidant in THF ([Fc]BAr^F_4 in the case of Bu_4N[LCuOH]; [AcFc]BAr^F_4 in the case of Et_4N[^{NO2}LCuOH]). The solution was then aged (4 s for Bu_4N[LCuOH] and 0.1 s for Et_4N[^{NO2}LCuOH]) to ensure complete oxidation to LCuOH or ^{NO2}LCuOH, respectively, which was verified independently from single mixing experiments and the appearance of the diagnostic ligand-to-metal charge-transfer (LMCT) feature associated with the $[CuOH]^{2+}$ core (λ_{max}, nm (ε, M^{-1} cm^{-1}) = 548 (10,000) or 500 (13,300) for LCuOH or ^{NO2}LCuOH, respectively). In the subsequent second-mixing event, the aged solution of LCuOH or ^{NO2}LCuOH was combined with a solution of the phenol substrate, and the rapid decay of the LMCT band corresponding to LCuOH or ^{NO2}LCuOH was monitored. For the reactions starting with LCuOH, both stoichiometric (1 eq of ^{X}ArOH relative to LCuOH) and pseudo first-order conditions (5-

100 eq of ^{X}ArOH relative to LCuOH) were used, except in the case for ^{NMe2}ArOH, the reactions with which were exceptionally fast and could be monitored only under stoichiometric conditions. Most of the reactions of phenols with ^{NO2}LCuOH were too rapid to be measured under pseudo first-order conditions, so all reactions were measured under stoichiometric conditions for consistency.

4.2.2 Reactions of LCuOH with ^{X}ArOH

Representative UV-vis spectra as a function of time for reactions of LCuOH with ^{X}ArOH are shown in Figure 4.1 (left). For the pseudo first-order reactions performed with excess substrate, decay traces of the absorbance at a single wavelength (548 nm) generally fit well to a single exponential decay function, consistent with a first-order decay process involving a single kinetic step (Figure 4.1 (right)). These rate constants were corroborated using multi-wavelength global analysis (Figure 4.4),[69] which yielded k_{obs} values in excellent agreement with those determined from the single-wavelength analysis (within 10% deviation). Plots of k_{obs} versus $[^{X}ArOH]_0$ were then fit to a linear regression, revealing an excellent linear dependence, and the slopes of these fits were taken as the second-order rate constants (k) for the reactions (Table 4.2, Figures 4.2-4.4).
to a single exponential decay function.

Table 4.2. Second-order rate constants for pseudo first-order reactions of LCuOH with ^{X}ArOH.

X	LCuOH[a,b]	LCuOH[a,c]
NMe_2	-	-
OMe	$(3.0 \pm 0.5) \times 10^5$	$(2.7 \pm 0.4) \times 10^5$
Me	$(8.9 \pm 1.3) \times 10^3$	$(9.6 \pm 1.4) \times 10^3$
H	$(3.9 \pm 0.6) \times 10^2$	$(3.9 \pm 0.6) \times 10^2$
Cl	$(6.5 \pm 1.0) \times 10^2$	$(6.4 \pm 1.0) \times 10^2$
NO_2	$(2.6 \pm 0.4) \times 10^2$	$(2.1 \pm 0.3) \times 10^2$
NO_2	-	$(1.7 \pm 0.2) \times 10^{3d}$
CF_3	$(3.0 \pm 0.5) \times 10^1$	$(1.8 \pm 0.3) \times 10^1$
CF_3	-	$(8.4 \pm 1.3) \times 10^{2d}$

[a] *k* has units of M^{-1} s^{-1}; errors are reported either as the statistical error from the fits or as a flat 15%, whichever is larger. [b] Pseudo first-order analysis of single wavelength absorbance vs. time traces. [c] From global fits to pseudo first-order UV-vis spectra using Olis Global Works™ program. [d] Second-order rate constant obtained for the A→B→C model as determined from global fits.

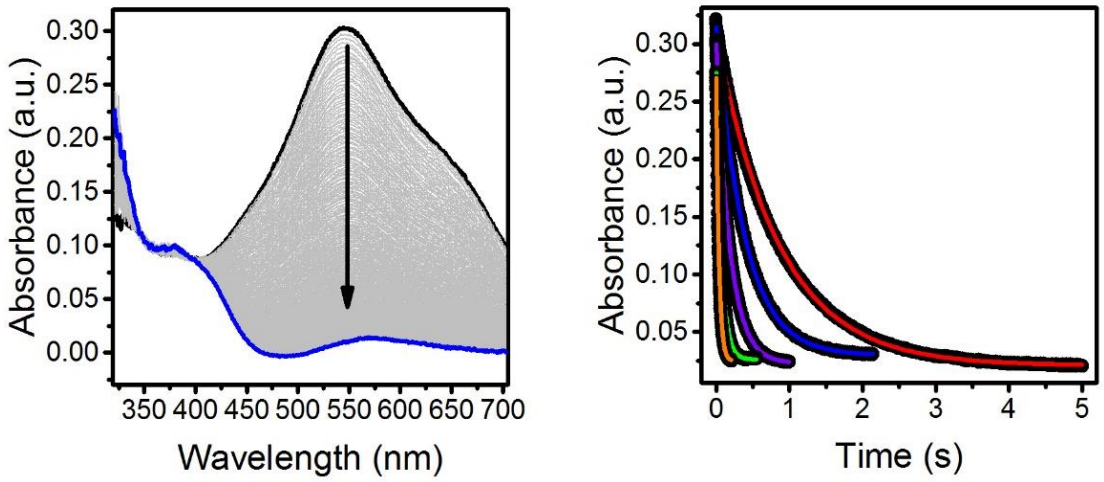

Figure 4.1. (Left) Representative pseudo first-order UV-vis decay trace of LCuOH in the presence of ^{Me}ArOH, as monitored by stopped-flow studies. The final blue spectrum matches that of the LCu(THF) adduct (see Figure 4.15 below), which forms as a result of ligand exchange with LCu(OH_2). (Right) Representative fits of the absorbance at 548 nm to a single exponential decay function.

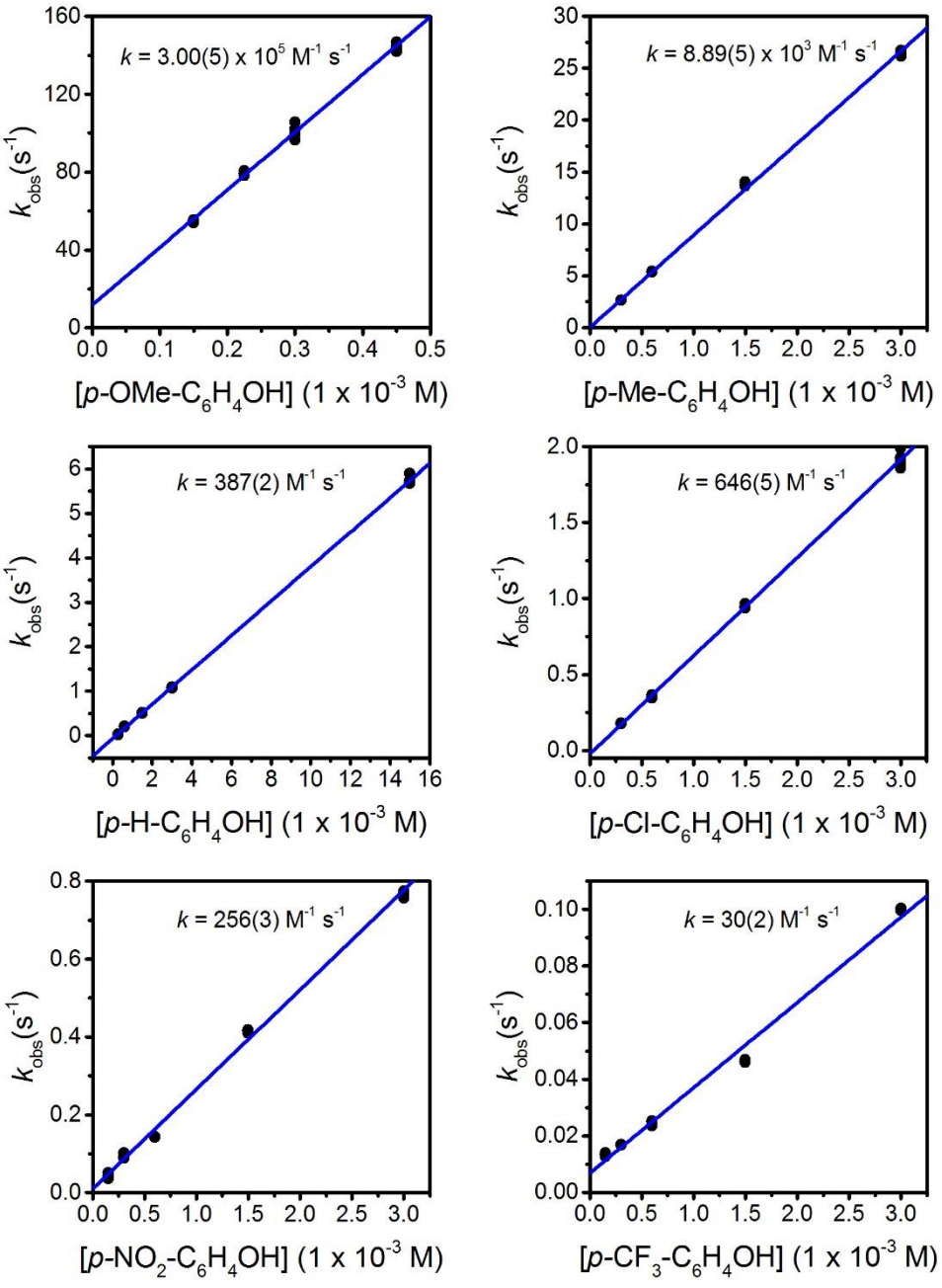

Figure 4.2. Second-order plots for pseudo-first-order reactions of LCuOH with *p*-OMe- (top left), *p*-Me- (top right), *p*-H- (middle left), *p*-Cl- (middle right), *p*-NO_2- (bottom left), and *p*-CF_3-phenol (bottom right). Pseudo first-order rate constants (k_{obs}) were determined using single wavelength analysis, exemplified in Figure 4.1 above.

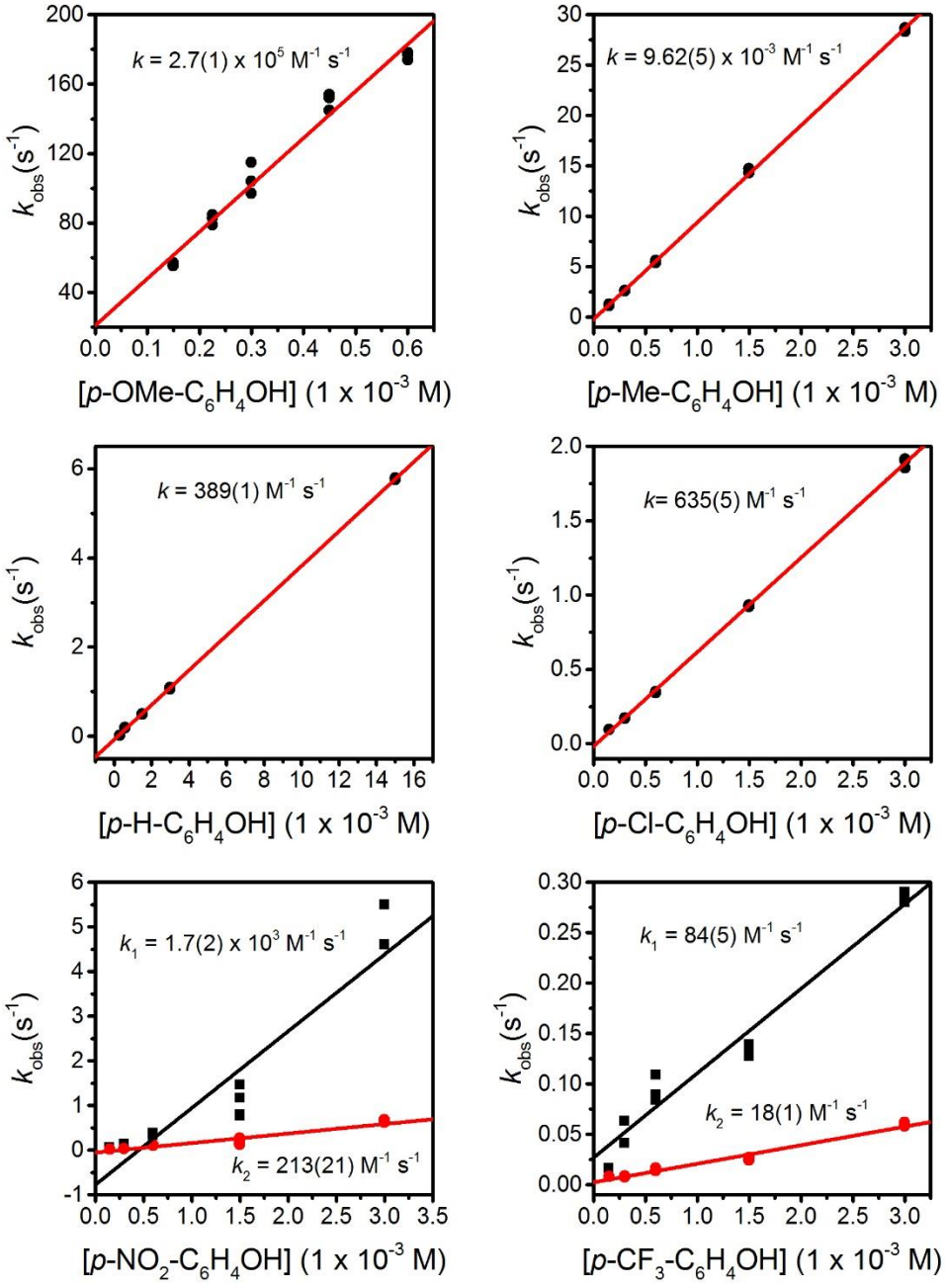

Figure 4.3. Second-order plots for pseudo-first-order reactions of LCuOH with *p*-OMe- (top left), *p*-Me- (top right), *p*-H- (middle left), *p*-Cl- (middle right), *p*-NO_2- (bottom left), and *p*-CF_3-phenol (bottom right). Pseudo first-order rate constants (k_{obs}) determined from global fitting with Olis Global Works™ program, exemplified in Figure 4.4 below.

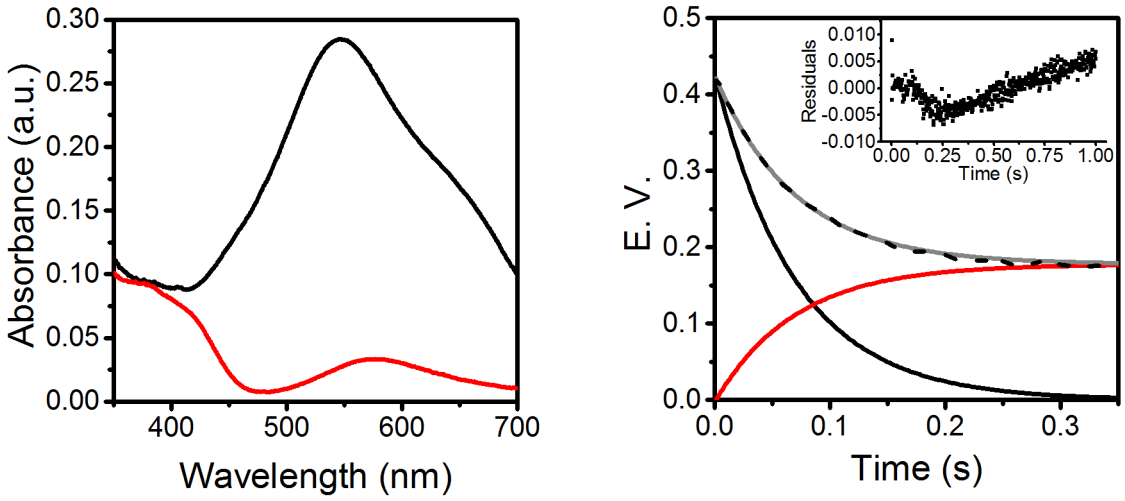

Figure 4.4. (Left) Representative spectral components obtained from the global kinetic analysis using Olis Global Works™ for ^{Me}ArOH reacting with LCuOH under pseudo-first-order conditions in which reactant is in black and product is in red. (Right) The relative contribution of the respective spectral components (or eigenvectors, E.V.) to the overall observed spectrum over the course of time, which is representative of the time course evolution of the various species involved in the reaction. The inset shows the residuals as a function of time.

The reactions of LCuOH with ^{CF3}ArOH and ^{NO2}ArOH differed from those with the other phenols with respect to kinetic behavior and product(s). In the reaction with ^{NO2}ArOH a new feature at 400 nm appeared concomitant with the decay of the LMCT feature for LCuOH at 548 nm (Figure 4.5, left). Single-wavelength analysis of the growth of the 400 nm feature revealed a second-order rate constant identical to that for the decay of LCuOH (Figure 4.5, right).

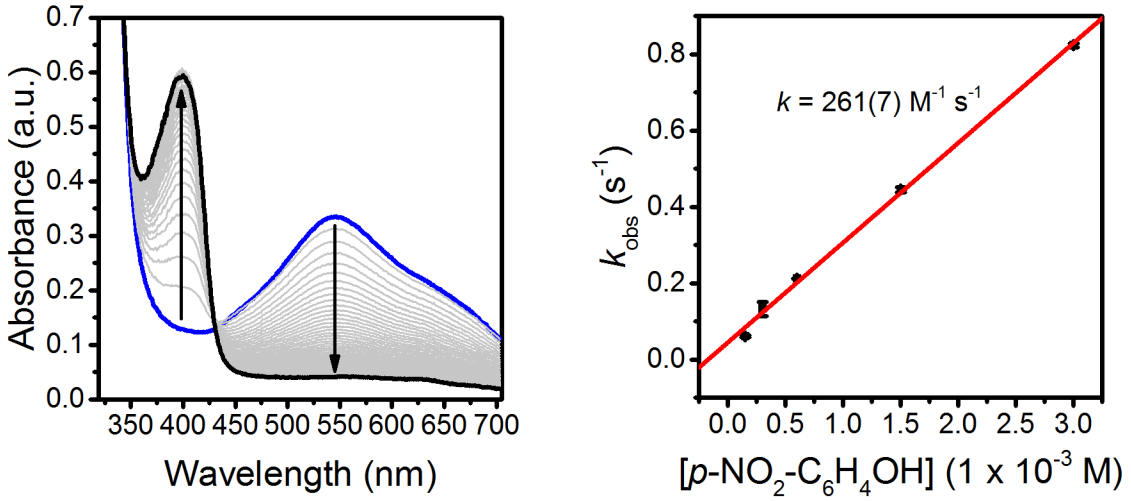

Figure 4.5. (Left) Representative UV-vis spectra as a function of time (1 ms to 100 s) for the reaction of LCuOH (prepared by reaction of Bu_4N[LCuOH] with [Fc]BAr^F_4) with ^{NO2}ArOH (5 equiv). Only selected data shown for clarity. (Right) The plot of k_{obs} vs. [^{NO2}ArOH]$_0$ for the growth of the feature at 400 nm.

For the reactions of LCuOH with ^{CF3}ArOH and ^{NO2}ArOH under pseudo-first-order conditions, only moderately satisfactory single exponential fits could be obtained for the decay traces at 548 nm. However, plotting of this k_{obs} vs. [^{X}ArOH]$_0$ revealed a linear dependence that enabled determination of the second-order rate constant (Figures 4.2-4.3). Interestingly, and in contrast to the spectral data collected for the more electron-rich phenols, the full UV-vis kinetic data for the reactions of LCuOH with ^{NO2}ArOH and ^{CF3}ArOH could only be satisfactorily fit using multicomponent analyses[69] to a stepwise kinetic model involving the formation of an intermediate (A → B→ C) (Figures 4.6-4.9). This fit is statistically improved relative to the simpler single-step fit applicable to the reactions of the other phenol substrates, and suggests differing mechanisms for reactions with p-NO_2- and p-CF_3-phenol (discussed in further detail below).

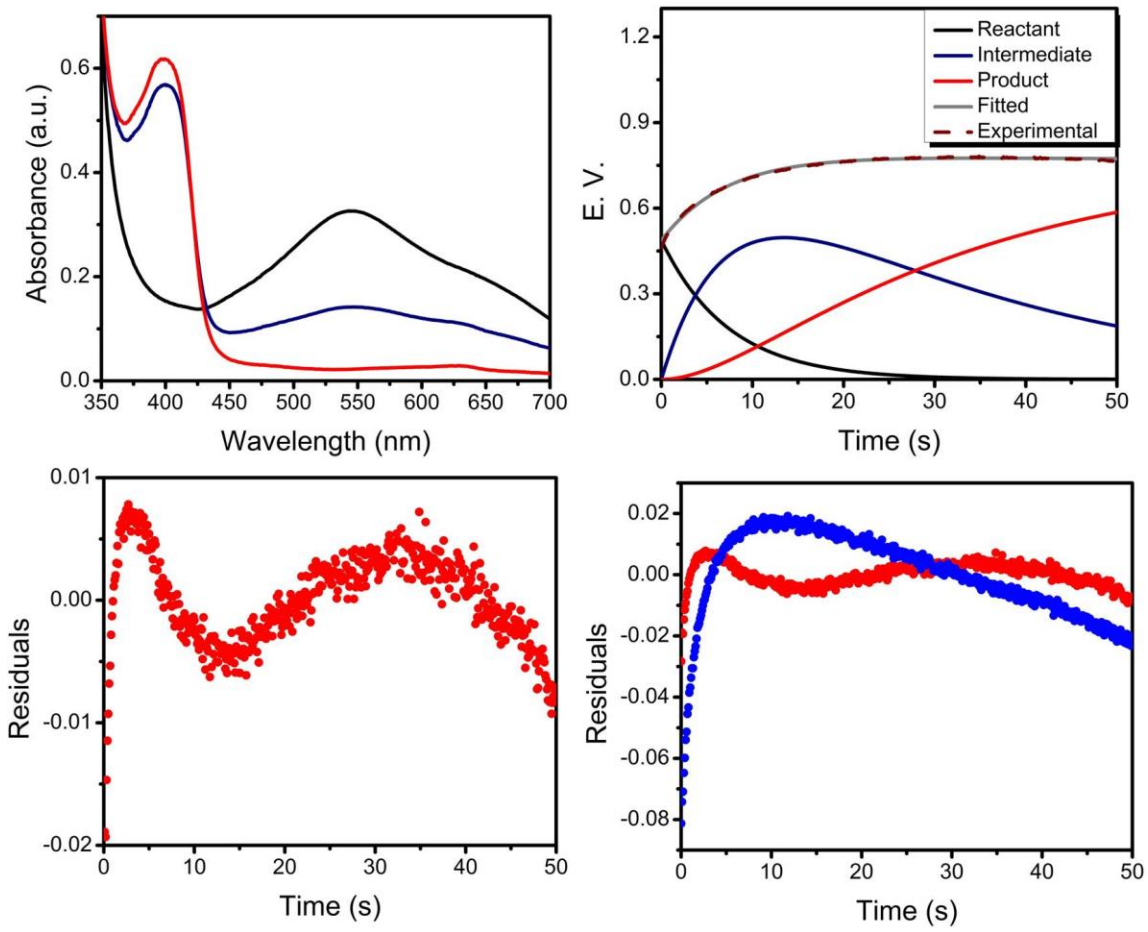

Figure 4.6. Representative spectral components obtained from the global kinetic analysis using Olis Global Works for *p*-NO_2-phenol reacting with LCuOH under pseudo-first order conditions when the kinetic model A→ B → C involving an intermediate C is used; reactant is in black, intermediate is in navy and product is in red (top left). Relative contribution of the respective spectral components (or eigen vectors, E.V.) to the overall observed spectrum over the course of time; this represents the time course evolution of the various species involved in the reaction (top right). Plot of residuals (bottom left). Overlay of residuals from a step-wise mechanism (red) and the mechanism involving a single kinetic step (blue, bottom right).

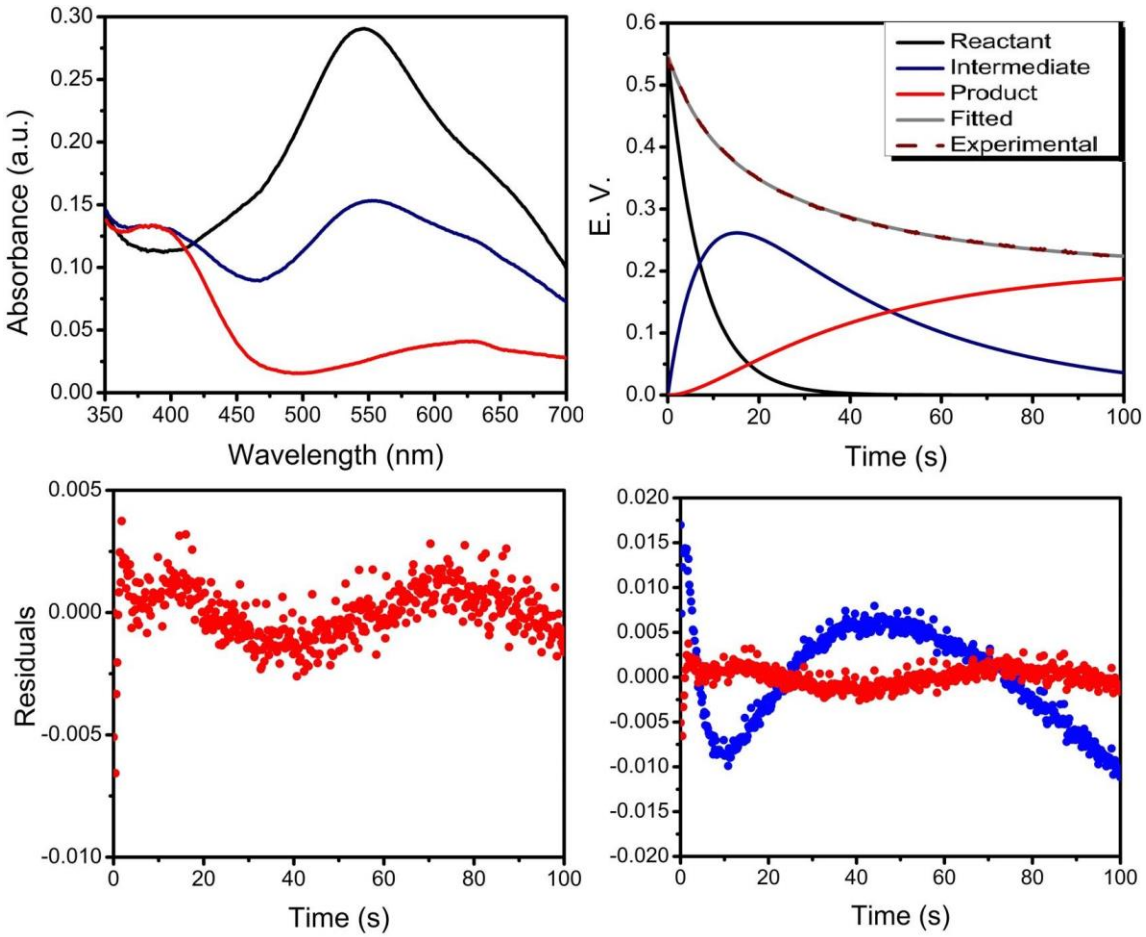

Figure 4.7. Representative spectral components obtained from the global kinetic analysis using Olis Global Works for *p*-CF_3-phenol reacting with LCuOH under pseudo-first order conditions when the kinetic model A→ B → C involving an intermediate C is used; reactant is in black, intermediate is in navy and product is in red (top left). Relative contribution of the respective spectral components (or eigen vectors, E.V.) to the overall observed spectrum over the course of time; this represents the time course evolution of the various species involved in the reaction (top right). Plot of residuals (bottom left). Overlay of residuals from a step-wise mechanism (red) and the mechanism involving a single kinetic step (blue, bottom right).

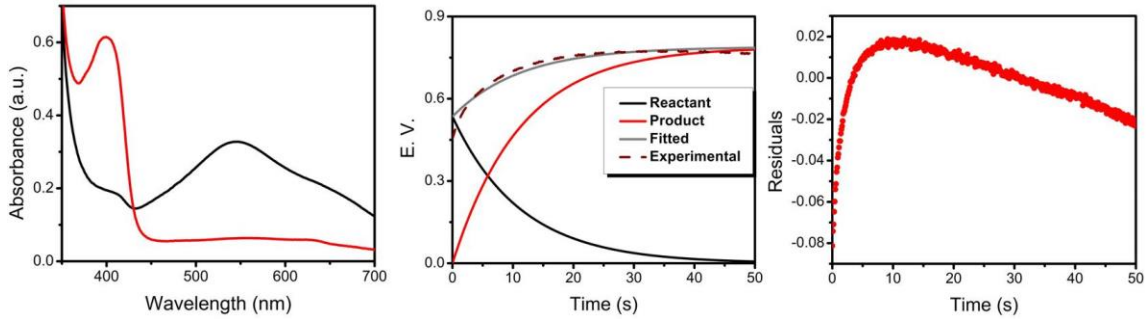

Figure 4.8. Representative spectral components obtained from the attempted global kinetic analysis using a simple kinetic model (A→ B) on Olis Global Works for *p*-NO_2-phenol reacting with LCuOH under pseudo-first order conditions in which reactant is in black and product is in red (left). Relative contribution of the respective spectral components (or eigen vectors, E.V.) to the overall observed spectrum over the course of time; this represents the time course evolution of the various species involved in the reaction (center). Plot of residuals indicating a systematic error in the fits (right).

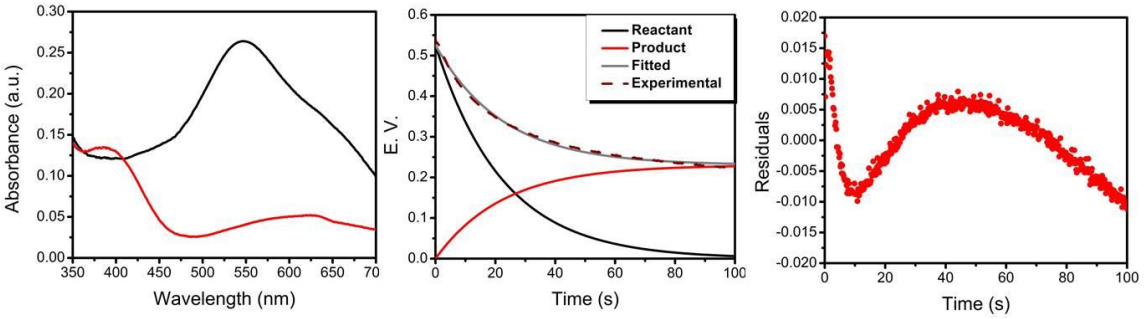

Figure 4.9. Representative spectral components obtained from the attempted global kinetic analysis using a simple kinetic model (A→ B) on Olis Global Works for *p*-CF_3-phenol reacting with LCuOH under pseudo-first order conditions in which reactant is in black and product is in red (left). Relative contribution of the respective spectral components (or eigen vectors, E.V.) to the overall observed spectrum over the course of time; this represents the time course evolution of the various species involved in the reaction (center). Plot of residuals indicating a systematic error in the fits (right).

For the stoichiometric (1:1) runs, *k* values were determined using the method of initial rates. The initial 5-10% of each concentration vs. time profile was fit by linear regression analysis to obtain an initial reaction rate, which was then divided by the square of the initial concentration of the copper complex to obtain the second-order rate constant (Table 4.3, Figures 4.10). The rates of reaction with ^{NMe2}ArOH were exceptionally fast (complete in less than 8 μs), and only the first 3 data points were usable (Figure 4.11).

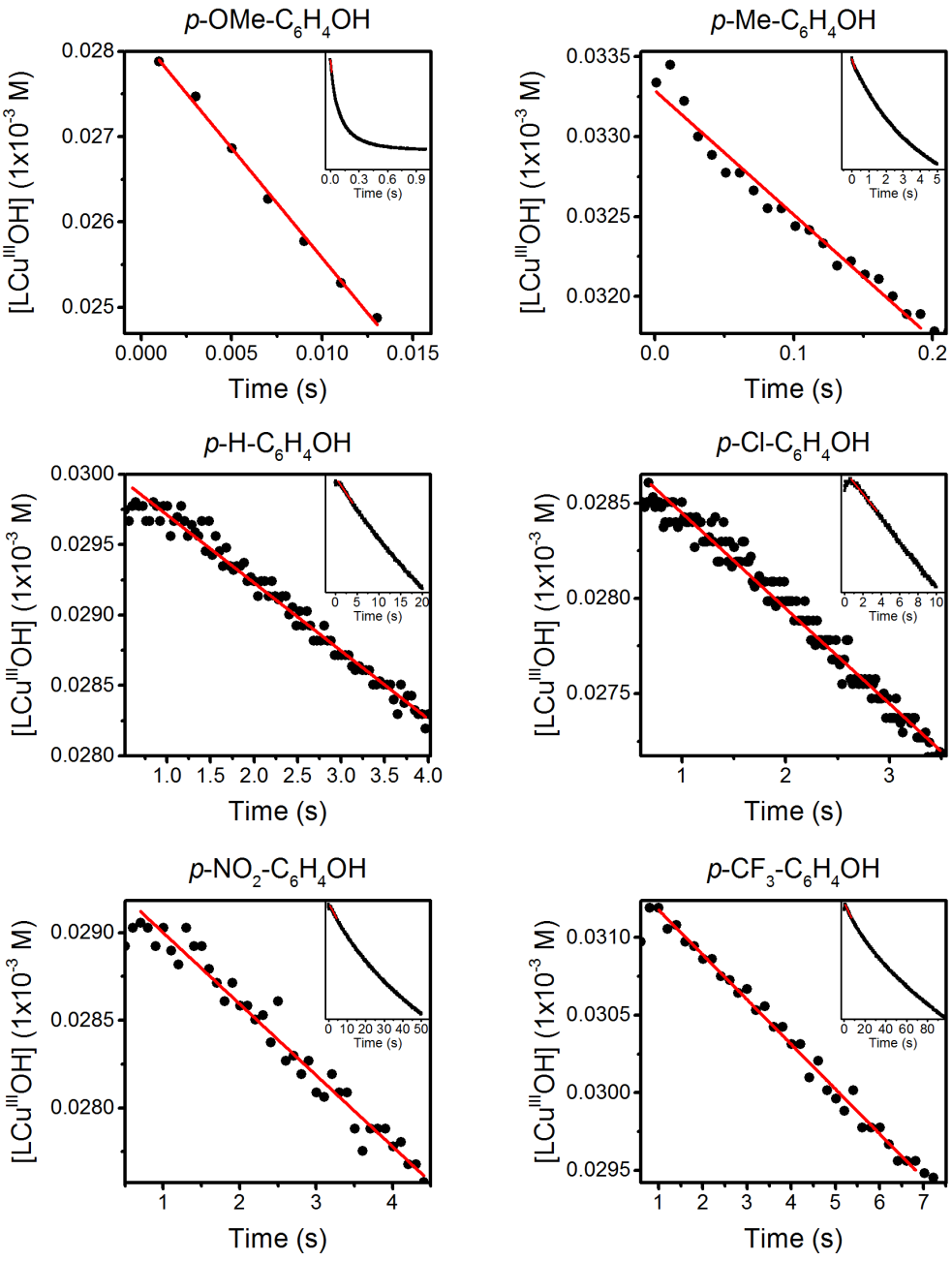

Figure 4.10. Plots of [LCuOH] vs. time (black) along with linear fits to the first 5% of data (10% in the case of *p*-OMe-phenol) for stoichiometric reactions of LCuOH with *p*-OMe- (top left), *p*-Me- (top right), *p*-H- (middle left), *p*-Cl- (middle right), *p*-NO_2- (bottom left), and *p*-CF_3-phenol (bottom right).

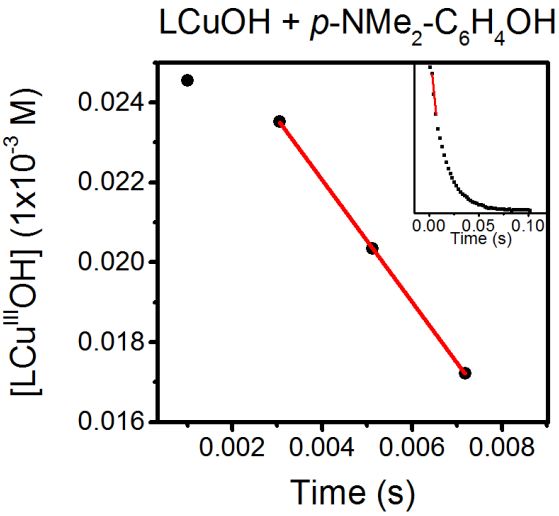

Figure 4.11. Plots of [$LCu^{III}OH$] vs. time (black) along with linear fits (red) to the first three-four data points for stoichiometric reactions of LCuOH (in red).

Table 4.3. Second-order rate constants for stoichiometric reactions of LCuOH with ^{X}ArOH determined from initial rates

X	LCuOH[a]
NMe_2	$(1.9 \pm 0.3) \times 10^6$
OMe	$(3.0 \pm 0.5) \times 10^5$
Me	$(7.0 \pm 1.1) \times 10^3$
H	$(5.1 \pm 0.8) \times 10^2$
Cl	$(5.7 \pm 0.9) \times 10^2$
NO_2 [b]	$(1.9 \pm 0.3) \times 10^2$
NO_2	$(4.6 \pm 0.7) \times 10^2$
CF_3 [b]	$(3.0 \pm 0.5) \times 10^1$
CF_3	$(3.0 \pm 0.5) \times 10^2$

[a] k has units of M^{-1} s^{-1}; errors are reported either as the statistical error from the fits or as a flat 15%, whichever is larger. [b] Determined from fits to mixed first- and second-order equation (Eq. 4.2). Values of k_1 for reactions with LCuOH was found to be $(4.7 \pm 0.3) \times 10^{-3}$ s^{-1}.

Comparison of the k values obtained from the reactions of LCuOH with ^{NO2}ArOH and ^{CF3}ArOH, under both pseudo-first-order and stoichiometric conditions, revealed a significant discrepancy in the rate constants. Thus, while satisfactory fits to the single wavelength data for stoichiometric reactions with these substrates could be obtained using the initial rates method, we observed that the second-order rate constants from this analysis were significantly higher than those obtained from the pseudo-first-order

analysis described above. We hypothesized that the rate of decay of LCuOH in the stoichiometric reactions was enhanced by an added component: attack at the C-H bonds of THF (a phenomenon described previously).[13,14] We suggest that this also occurs in the pseudo-first-order runs, but is accounted for in the self-decay component of the reaction observed as a non-zero *y*-intercept in the second-order *k* vs. $[^{X}ArOH]_0$ plots, which also agree with the previously measured sefl-decay rates. Equations that model this additional pathway by incorporating an added first-order self-decay component were used to fit the data (Eq. 4.1 and Eq. 4.2).

$$-\frac{d[\mathrm{LCu^{III}OH}]}{dt} = rate_1 + 2rate_2 = k_1[\mathrm{LCu^{III}OH}] + 2k_2[\mathrm{LCu^{III}OH}]^2 \qquad \text{eq. 4.1}$$

$$[\mathrm{LCu^{III}OH}]_t = \frac{k_1[\mathrm{LCu^{III}OH}]_0 \mathrm{e}^{-k_1 t}}{k_1 + 2k_2[\mathrm{LCu^{III}OH}]_0(1-\mathrm{e}^{-k_1 t})} \qquad \text{eq. 4.2}$$

These fits (Figures 4.12) yielded second-order rate constants in good agreement with those determined from the pseudo-first-order analyses above (Figures 4.2 and 4.3), thus validating the model that includes the self-decay (THF attack) process. Additionally, the rates of THF activation obtained from these fits are in good agreement with the independently measured self-decay rates of LCuOH in THF, which further corroborates the use of this additional kinetic pathway. Thus, in all cases, the rate constants obtained for the stoichiometric reactions with LCuOH were within error of those obtained from the pseudo first-order experiments described above, lending credence to the use of this method for the reactions of ^{NO2}LCuOH, which could not be corroborated by pseudo first-order measurements.

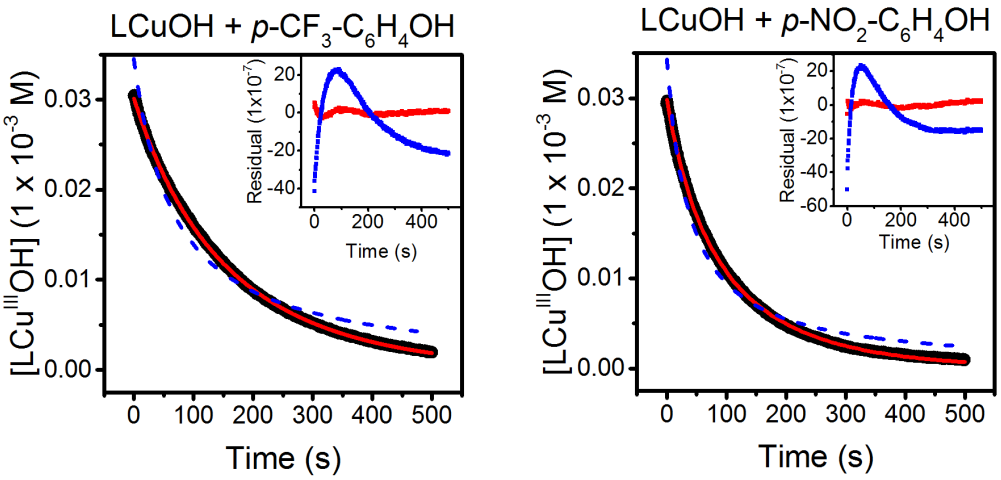

Figure 4.12. Representative concentration vs. time plots for reactions of LCuOH with *p*-CF_3- (left) and *p*-NO_2-phenol, displaying fits to Eq.4.2 (solid red) and 4.5 (dashed blue), along with the corresponding residual plots (inset). The improved fits to the expanded kinetic model are evident from the residuals.

4.2.3 Reactions of ^{NO2}LCuOH with ^{X}ArOH

As discussed earlier, the reactions of the phenolic substrates with ^{NO2}LCuOH could only be monitored under stoichiometric conditions owing to exceedingly high reaction rates. However, the use of the rate constants using stoichiometric runs was validated in the reactions of LCuOH and hence, the analysis described in Section 4.2.2 above was extended to the reactions with ^{NO2}LCuOH. The corresponding rate constants obtained from this analysis (Figures 4.13-4.15) are listed below in Table 4.4.

Table 4.4. Second-order rate constants for stoichiometric reactions of ^{NO2}LCuOH with ^{X}ArOH determined from initial rates

X	^{NO2}LCuOH [a]
NMe_2	$(6.7 \pm 1.0) \times 10^6$
OMe	$(1.8 \pm 0.3) \times 10^6$
Me	$(1.0 \pm 0.2) \times 10^6$
H	$(1.8 \pm 0.3) \times 10^5$
Cl	$(1.4 \pm 0.2) \times 10^5$
NO_2 [b]	$(8.2 \pm 2.6) \times 10^2$
NO_2	$(1.7 \pm 0.5) \times 10^3$
CF_3 [b]	$(3.0 \pm 1.5) \times 10^2$
CF_3	$(7.6 \pm 3.1) \times 10^2$

[a] k has units of M^{-1} s^{-1}; errors are reported either as the statistical error from the fits or as a flat 15%, whichever is larger. [b] Determined from fits to mixed first- and second-order equation (Eq. 4.2). Values of k_1 for reactions ^{NO2}LCuOH were found to be $(8.0 \pm 0.4) \times 10^{-3}$ s^{-1}.

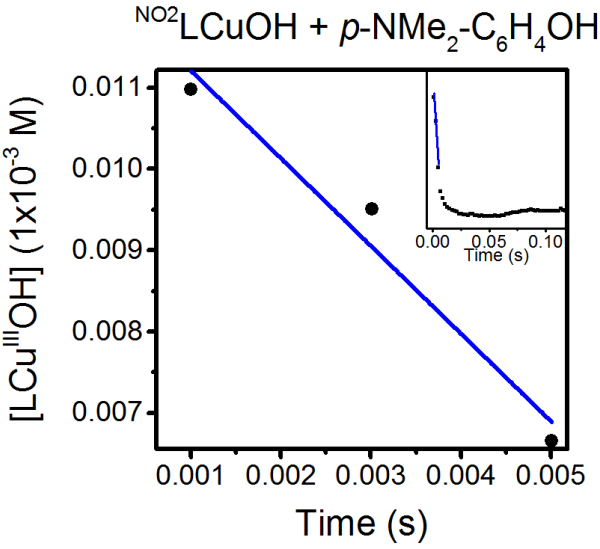

Figure 4.13. Plots of ^{NO2}LCuOH vs. time (black) along with linear fits (blue) to the first three-four data points for stoichiometric reactions with *p*-NMe_2-phenol.

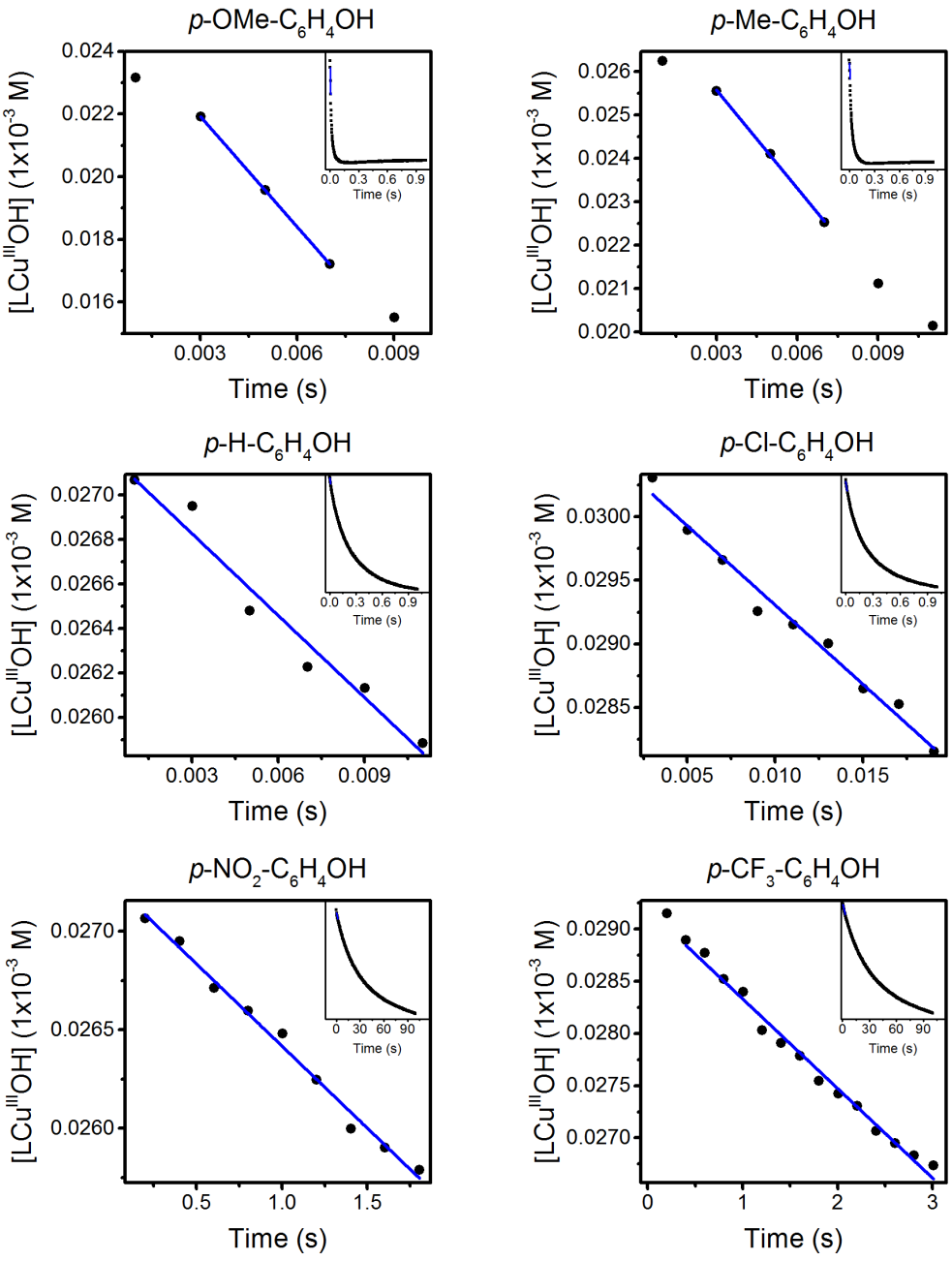

Figure 4.14. Plots of [^{NO2}LCuOH] vs. time (black) along with linear fits to the first 5% of data (10% in the case of *p*-OMe-phenol) for stoichiometric reactions of ^{NO2}LCuOH with *p*-OMe- (top left), *p*-Me- (top right), *p*-H- (middle left), *p*-Cl- (middle right), *p*-NO_2- (bottom left), and *p*-CF_3-phenol (bottom right).

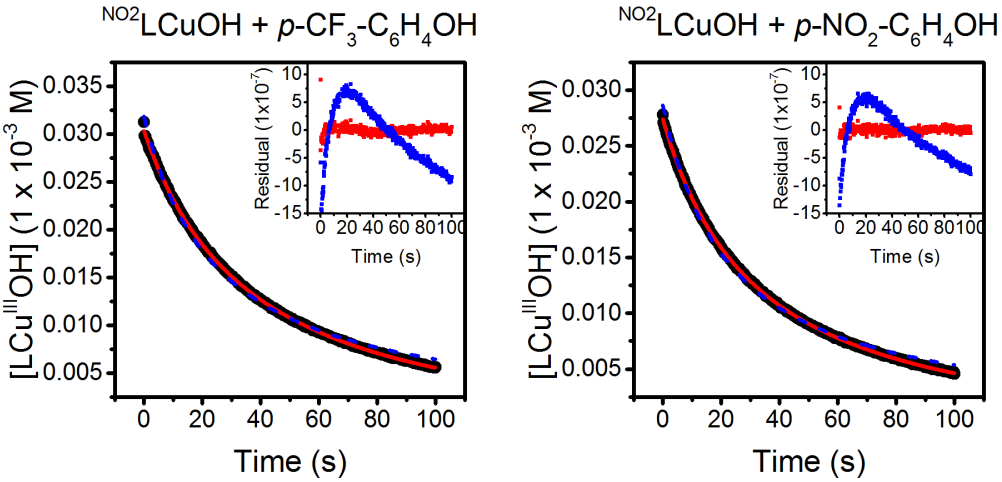

Figure 4.15. Representative concentration vs. time plots for reactions of ^{NO2}LCuOH with *p*-CF_3- (left) and *p*-NO_2-phenol, displaying fits to Eq. 5.2 (solid red) and Eq. 5.5 (dashed blue), along with the corresponding residual plots (inset). The improved fits to the expanded kinetic model are evident from the residuals.

4.2.4 Implication of the rates of reaction of LCuOH and ^{NO2}LCuOH with ^{X}ArOH

For ease of comparison, the rate constants for the reaction between the phenolic substrates and the two $[CuOH]^{2+}$ complexes are summarized in Table 4.5.[15] Inspection of *k* values given in Tables 4.5 highlights key findings from these experiments. With the same phenol, *k* values for reactions of ^{NO2}LCuOH were 3.5-460 times greater than those of LCuOH. Significant rate differences were previously observed for reactions of LCuOH and ^{NO2}LCuOH with C-H bonds, and the cause for this was attributed to the higher BDE for the O-H bond formed in the product copper(II)-aqua complex ^{NO2}LCu(OH_2) compared to that of LCu(OH_2).[14] For each complex, *k* values over the range of phenols were found to vary by 3-4 orders of magnitude as a function of *para*-substituents (Table 4.5) and for runs with the more electron-rich phenols (X = NMe_2, OMe, Me, H, and Cl), the data fit well to a kinetic model involving a single-step (A → B). These kinetic findings are consistent with a CPET (concerted proton electron transfer) mechanism for transfer of an H-atom from the phenolic substrates to LCuOH and ^{NO2}LCuOH. This mechanistic assignment is corroborated by product analysis described below. However,

the data obtained for reactions between LCuOH and the most electron-deficient phenols (X = NO_2, CF_3) were more accurately modeled using a mechanism involving an intermediate species (A → B → C). Coupled with the clear observation of a product CT feature at 400 nm in the UV-vis spectrum for reactions between LCuOH and ^{NO2}ArOH, these results suggest a more complicated pathway compared to what was seen for the more electron-rich phenols. See below for further discussion.

Table 4.5. Second-order rate constants (k) for the reactions of LCuOH and ^{NO2}LCuOH with ^{X}ArOH at –80 ºC.[a]

X	LCuOH (THF)[b]	^{NO2}LCuOH (THF)[c]
NMe_2	$(1.9 \pm 0.3) \times 10^6$ [c]	$(6.7 \pm 1.0) \times 10^6$
OMe	$(3.0 \pm 0.5) \times 10^5$	$(1.8 \pm 0.3) \times 10^6$
Me	$(8.9 \pm 1.3) \times 10^3$	$(1.0 \pm 0.2) \times 10^6$
H	$(3.9 \pm 0.6) \times 10^2$	$(1.8 \pm 0.3) \times 10^5$
Cl	$(6.5 \pm 1.0) \times 10^2$	$(1.4 \pm 0.2) \times 10^5$
NO_2	$(2.6 \pm 0.4) \times 10^{2d}$	$(8.2 \pm 2.6) \times 10^2$
CF_3	$(3.0 \pm 0.5) \times 10^{1d}$	$(3.0 \pm 1.5) \times 10^2$

[a] All values in units $M^{-1}\,s^{-1}$. In all cases, uncertainties are taken as 15% or as the standard error, whichever is greater. [b] Values determined from the pseudo-first-order analysis for all reactions except for that for X = NMe_2, in which case the rate constant from the stoichiometric analysis was used. See text for details. [c] Determined from the method of initial rates for X = NMe_2, OMe, Me, H, and Cl; for X = NO_2 and CF_3, determined from the mixed first- and second-order fits (Eq. 4.2). See text for details. [d] Determined from the single-wavelength analysis. See text for details.

4.3 Analysis of products for reactions with ^{X}ArOH with X = NMe_2, OMe, Me, H, and Cl

Based on the related reactivity with C–H bonds[8,13,14] the reactions of LCuOH and ^{NO2}LCuOH with phenols ^{X}ArOH (X = NMe_2, OMe, Me, H, and Cl) very likely yield the respective phenoxyl radicals, which would be expected to undergo subsequent radical coupling reactions.[70,71] Attempts to identify such products from batch reactions were successful in the case of the reactions of LCuOH and ^{NO2}LCuOH with ^{Me}ArOH;

Pummerer's ketone[72] was identified by GC/MS in approximately 35 and 16% yield, respectively (Scheme 4.3; see Experimental Section for details). It should be noted here that in all cases it is assumed that the rates measured correspond to the rate of the HAT/CPET reaction between $[CuOH]^{2+}$ and $^{X}ArOH$. It is also possible that the organic product of this reaction could further react with additional equivalents of $[CuOH]^{2+}$, but we assume here that such secondary reactions are negligible.

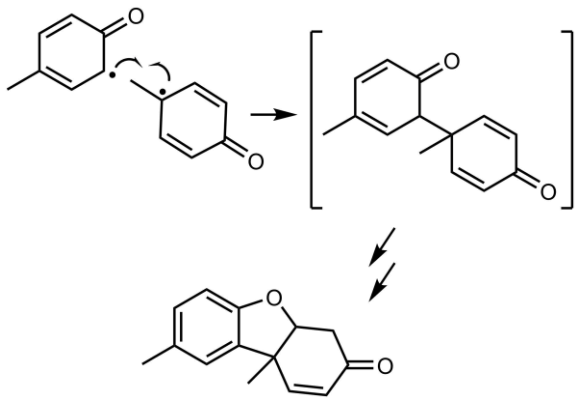

Scheme 4.3. Formation of Pummerer's ketone from the *ortho-para* coupling of two *p*-cresol phenoxyl radicals (only one resonance form of each of the reacting radicals is shown).

We can only speculate that our inability to identify radical coupling products from the reactions with the other phenols is due to their decay *via* a variety of pathways, as has been suggested in related studies.[70,71,73] Further corroboration of phenoxyl radical generation came from EPR spectroscopic analysis of the product mixtures after reaction of TEMPOH and 2,4,6-tri-*t*-butylphenol with LCuOH and ^{NO2}LCuOH; signals due to the respective nitroxyl and phenoxyl radicals were observed (Figure 4.16).

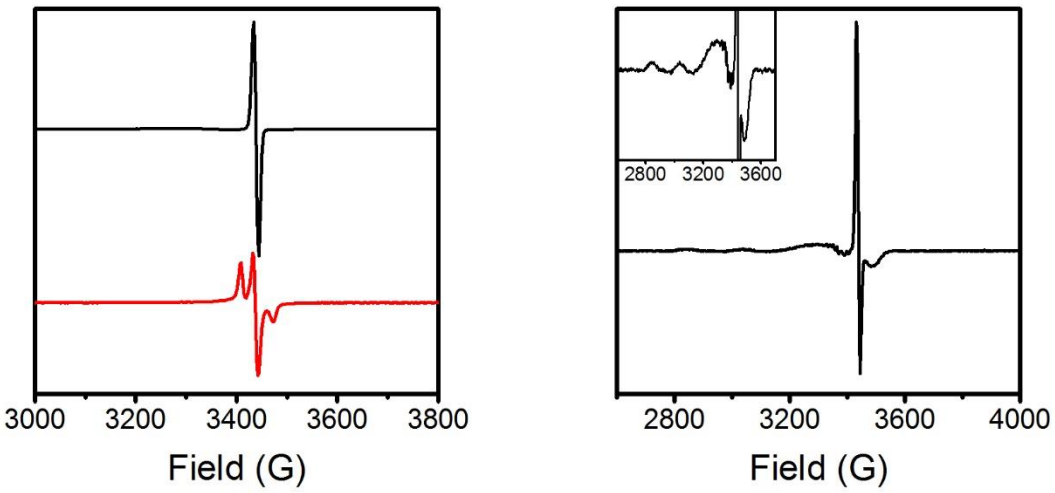

Figure 4.16. (Left) EPR spectra for reactions of LCuOH with 2,4,6-tri-*t*-butylphenol (black) and TEMPOH (red), confirming the formation of organic radical species in these reactions (conditions: 1 mM concentration, 77 K, 0.0002 mW microwave power). (Right) Product EPR spectrum for the reaction of ^{NO2}LCuOH with 2,4,6-tri-*t*-butylphenol confirming the formation of phenoxyl radical in this reaction (conditions: 0.1 mM concentration, 30 K, 0.063 mW microwave power). The inset shows a zoomed-in view to highlight the copper features that are also observed.

Quantification of the latter by UV-vis spectroscopy indicated an ~ 80% yield for reaction with LCuOH (Figure 4.17). Additionally, the inorganic decay product in all of the reactions with LCuOH, except in the case of ^{NMe2}ArOH, is the corresponding copper(II)-THF adduct formed as a result of ligand exchange of the coordinated water in LCu(OH_2) with the THF solvent. This phenomenon has been described in detail previously (Section 2.2.1.1)[13] and is further corroborated in these cases by comparison with the UV-vis absorption features of the copper(II)-THF adduct (Figure 4.18, left). The UV-vis decay spectra for reactions with ^{NO2}LCuOH (Figure 4.18, right) are distinct from any of the known complexes with this ligand, and we can only speculate that the product mixtures for these reactions likely contain some mixture of LCu(S) species, where S = H_2O, THF, or ^{X}ArOH.

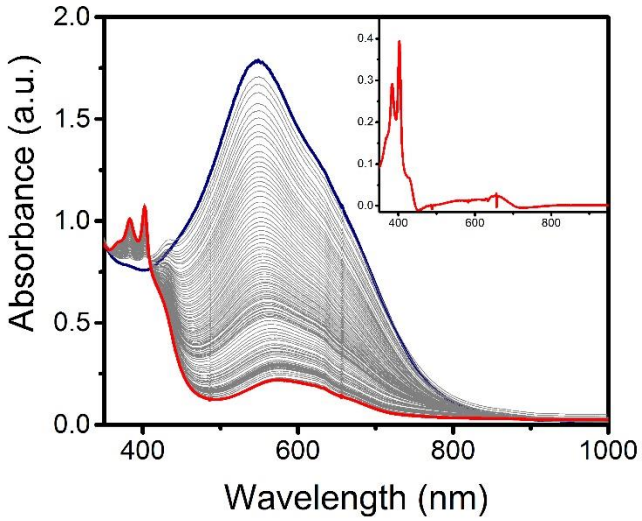

Figure 4.17. UV-vis traces of reaction between LCuOH and 2 eq 2,4,6-tri-*t*-butylphenol in THF monitored at -80 °C. The inset shows the spectrum of the phenoxyl radical obtained after subtracting out the spectral contribution from other species in solution.

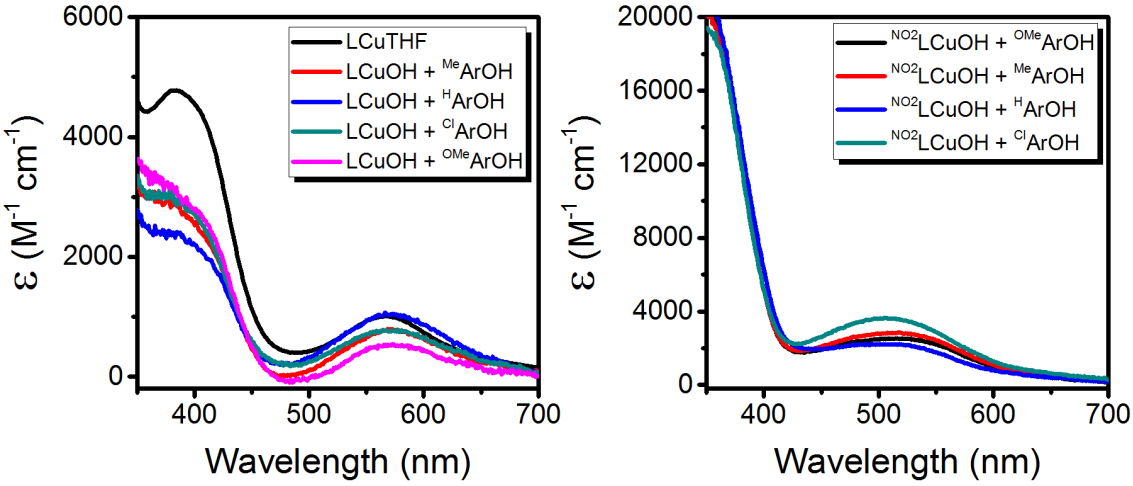

Figure 4.18. (Left) Final decay spectra of pseudo first-order stopped-flow reactions between LCuOH and ^{Me}ArOH (red), ^{H}ArOH (blue), ^{Cl}ArOH (green), and ^{OMe}ArOH (pink), all overlayed with an independent spectrum of LCu(THF) (black), supporting the identity of this species as the final inorganic product from these reactions. (Right) Final decay spectra of stoichiometric stopped-flow reactions between ^{NO2}LCuOH and ^{OMe}ArOH (black), ^{Me}ArOH (red), ^{H}ArOH (blue), and ^{Cl}ArOH (green).

In the case of reactions between LCuOH/^{NO2}LCuOH and ^{NMe2}ArOH, the final decay spectra are distinctly different from those of the other phenols in that there is a charge-transfer feature in the NIR region (Figure 4.19). This feature is stable at -80 °C,

and in the case of reactions with ^{NO2}LCuOH, even persists to some extent after sitting at room temperature overnight. This feature is tentatively assigned as some sort of copper-based phenoxyl adduct on the basis of comparions with previous reports of similar copper(II)-phenoxyl complexes[74] and the known enhanced stability of the ^{NMe2}ArO$^{\bullet}$ phenoxyl radical in comparison to the other phenoxyl radicals.[71] A detailed study of this putative copper-phenoxyl is presented in Chapter 5.

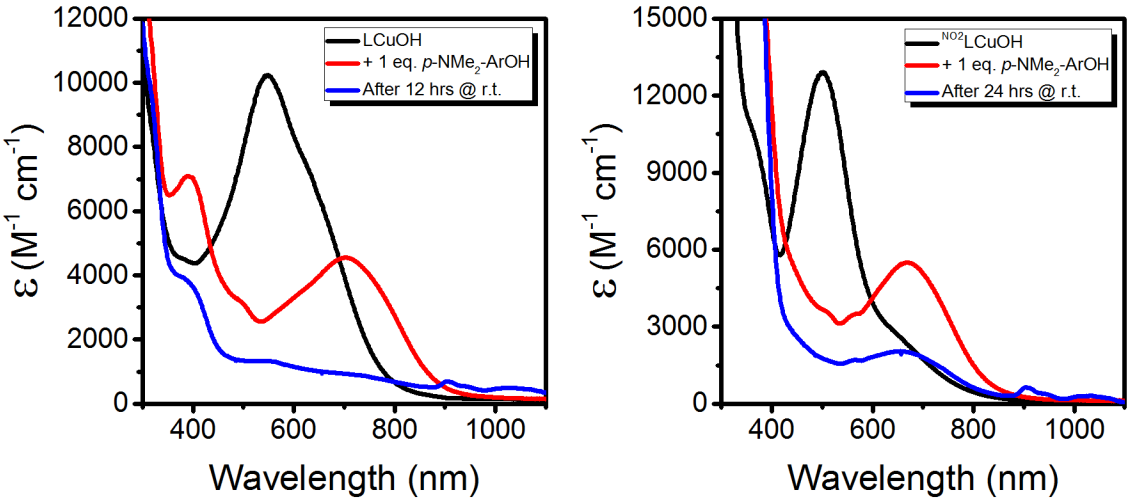

Figure 4.19. UV-vis traces showing the reaction between LCuOH (left) or ^{NO2}LCuOH (right) with 1 eq. of ^{NMe2}ArOH and the corresponding decay spectra after prolonged warming at room temperature. The starting spectra of LCuOH/^{NO2}LCuOH are shown in black, the resulting spectra after the addition of 1 eq. of ^{NMe2}ArOH are shown in red, and the decay spectra are shown in blue.

4.4 Analysis of Products for Reactions with ^{X}ArOH with X = NO_2 and CF_3

For reactions of LCuOH and ^{NO2}LCuOH with ^{NO2}ArOH and ^{CF3}ArOH, attempts to quantify any C-C coupled products were also unsuccessful. However, the necessity for a more complicated kinetic model as elucidated by the global fitting analysis, as well as the observed growth of an intense CT feature for the reaction of LCuOH with ^{NO2}ArOH, aroused suspicions of possibilities of other types of products in these cases. Previous reports of nitrophenolate formation have shown that the anion is characterized by an intense CT band in the ~ 400 nm region.[75] Thus, we tentatively assigned the CT band at

400 nm as corresponding to formed nitrophenolate anion in solution, and this assignment was corroborated by comparison to an independently synthesized sample of $[Bu_4N][^{NO2}ArO]$ dissolved in THF (Figure 4.20). The approximate yield of $^{NO2}ArO^-$ is estimated to be ~55% with respect to the starting copper concentration. It is hypothesized that $^{NO2}ArO^-$ is also formed upon reaction of ^{NO2}LCuOH with ^{NO2}ArOH, but we were unable to verify this idea because of overlapping features in the UV-vis spectra that obfuscated the 400 nm band. Additionally, for the stoichiometric reactions of ^{NO2}LCuOH with ^{NO2}ArOH it is expected that the CT feature corresponding to the $^{NO2}ArO^-$ at 400 nm, if present, would be significantly less intense than for reactions of LCuOH with ^{NO2}ArOH, due to the significant contribution from self-decay in THF. The observation of $^{NO2}ArO^-$ as a reaction product further suggests a mechanism that is distinct from a CPET pathway in this case, as it implicates some sort of an acid-base reaction. That can only be rationalized by a discrete proton transfer mechanism.

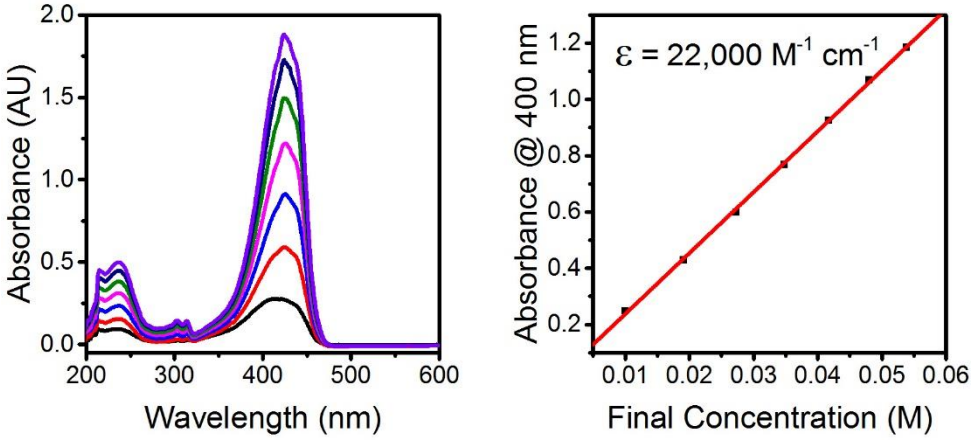

Figure 4.20. UV-vis spectra of varying concentrations of $^{NO2}ArO^-$ (left) and corresponding Beer's law plot (right) of the absorbance at 400 nm for $[Bu_4N][^{NO2}ArO]$.

Also in contrast to reactions with the more electron-rich phenols, reactions of ^{NO2}ArOH and ^{CF3}ArOH gave final UV-vis spectra distinct from that of the LCu(THF) species as described before and shown in Figure 4.21. More interestingly, for the

reactions of both substrates with LCuOH, a conspicuous absorption feature is observed in the approximate range of 625-630 nm. This absorption feature is in good agreement with that for Fc^+ ($\lambda_{max}(\varepsilon)$ = 623 nm (1000 M^{-1} cm^{-1}); see Figure 4.22, left), the oxidant used to generate LCuOH from [Bu_4N][LCuOH]. Indeed, signals in the product EPR spectrum at g = 4.32, 2.04, and 1.54 (Figure 4.22, right)[76] corroborate the presence of Fc^+, which was quantified by standard addition titration (Figure 4.23) using UV-vis spectroscopy and it is estimated that the amount of Fc^+ regenerated is ~ 90 % of the starting copper concentration. This curious observation suggests that Fc^+ is somehow regenerated in these reactions, again highlighting a level of mechanistic complexity in the reactions with the acidic phenols in contrast to those the electron-rich phenols.

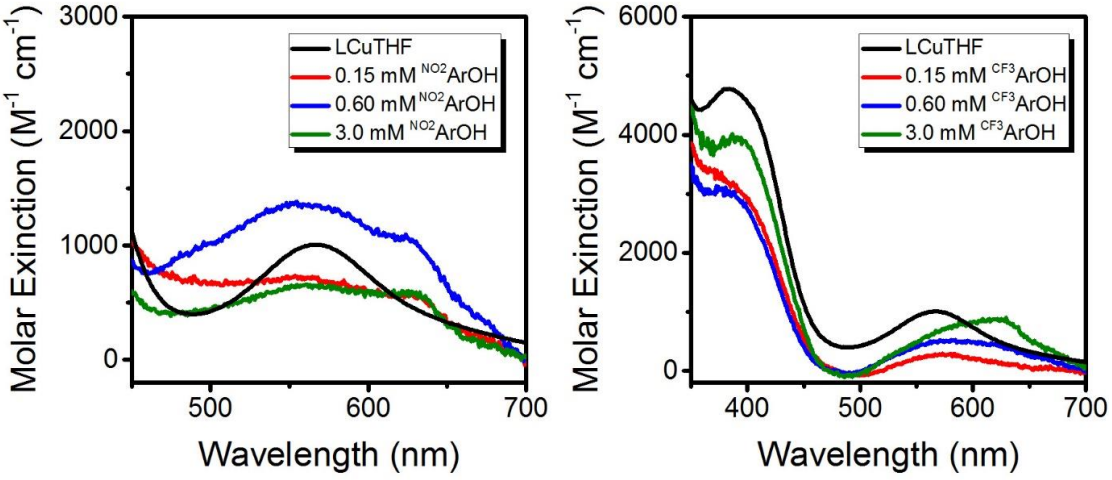

Figure 4.21. Final decay spectra of pseudo first-order stopped-flow reactions between LCuOH and ^{NO2}ArOH (left) and ^{CF3}ArOH (right) at the concentrations listed. Molar extinction values were approximated by using the total copper concentration (0.03 mM). The spectra are overlayed with that of the LCu(THF) adduct for comparison.

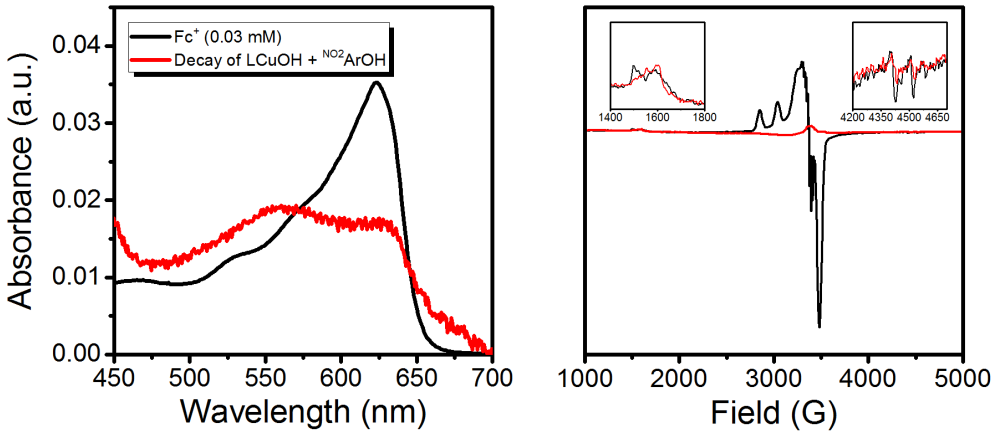

Figure 4.22. (Left) Overlay of the UV-vis spectra for a 0.03 mM solution of [Fc][BAr^F_4] (black) with the product solution of the reaction between LCuOH and 100 eq. of ^{NO2}ArOH (red). (Right) An overlay of the EPR spectra for a 1 mM [Fc]BAr^F_4 solution (red) and the product solution of the reaction of LCuOH and 2 eq. of ^{NO2}ArOH (black) with the features due to Fc^+ shown in the insets.

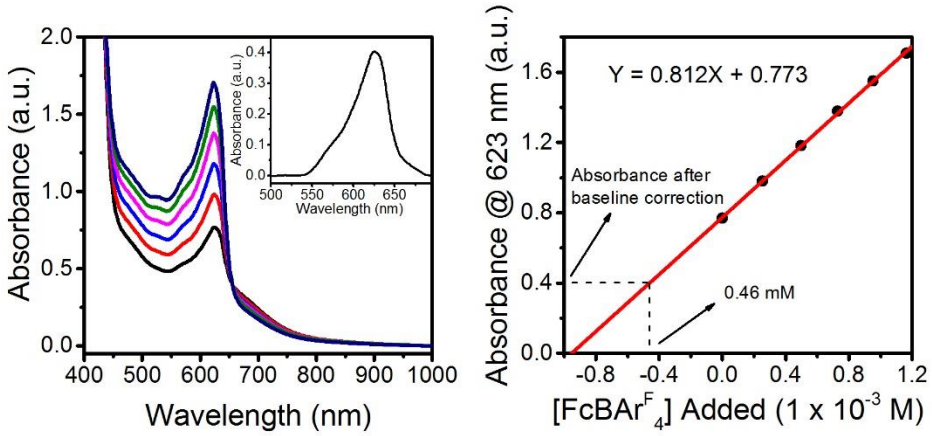

Figure 4.23. (Left) UV-vis spectrum of the product mixture for the reaction between LCuOH and ^{NO2}ArOH in THF at -80 °C (black spectrum; total Cu concentration is 0.5 mM), as well as the corresponding spectra of the same solution upon the addition [Fc]BAr^F_4 in of 0.25 eq. (red spectrum), 0.5 eq. (blue spectrum), 0.75 eq (pink spectrum), 1.0 eq. (green spectrum), and 1.25 eq (purple spectrum) increments. The inset shows the original product mixture after baseline correction, which was done to approximate the absorbance solely due to Fc^+ in the product mixture. (Right) Standard addition plot for the addition of [Fc][BAr^F_4] to the product mixture corresponding to the UV-vis absorption changes shown in the figure to the left. The absorbance after baseline correction was used to approximate the concentration of Fc^+ in the product mixture from the linear fit.

4.5 Evidence for a PT Mediated Pathway

To rationalize the production of $^{NO2}ArO^-$, several possible mechanisms (Scheme 4.4) were considered.[15] Initial HAT (i.e. CPET) could yield the copper(II)-aqua complex $LCu(OH_2)$ and the phenoxyl radical $^{NO2}ArO^{\bullet}$ ("HAT" in Scheme 4.4). This radical might then undergo reduction by ferrocene (formed in the initial reaction used to generate the reactant LCuOH) to produce $^{NO2}ArO^-$ and Fc^+ ($E_{1/2}$ for $^{NO2}ArO^{\bullet}$/ $^{NO2}ArO^-$ is 0.314 V vs. Fc^+/Fc).[16] Alternatively, $LCu(OH_2)$ and $^{NO2}ArO^{\bullet}$ might participate in a redox equilibrium to yield the copper(III)-aqua complex $[LCu(OH_2)]^+$ and $^{NO2}ArO^-$ ("ET").

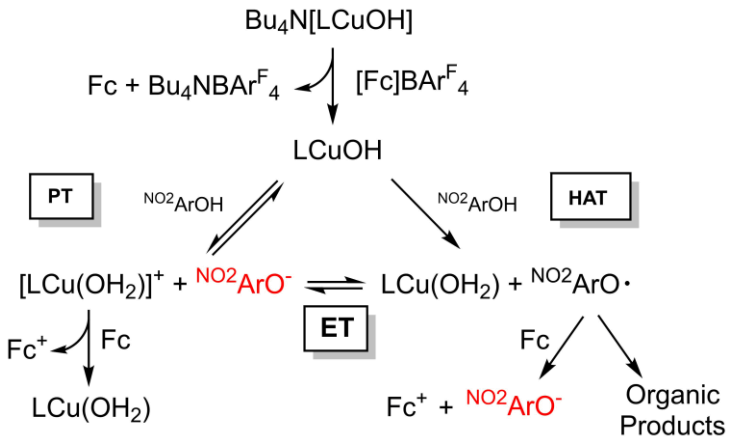

Scheme 4.4. Mechanisms that would yield the phenolate $^{NO2}ArO^-$.

While such an equilibrium seems plausible given the very close $E_{1/2}$ values for the $ArO^{\bullet}/ArO^-$ (0.314 V vs. Fc^+/Fc) and Cu^{III}/Cu^{II} couples for the copper(III)-aqua species (0.345 V vs. Fc^+/Fc),[13] it is likely that alternate decay pathways for the highly reactive phenoxyl radical[77] would drive this equilibrium to the right, and thus the equilibrium concentrations of $[LCu(OH_2)]^+$ and $^{NO2}ArO^-$ should be miniscule. Alternately, $^{NO2}ArO^-$ could also form *via* direct proton transfer between LCuOH and $^{NO2}ArOH$ ("PT"). In such a scenario, $[LCu(OH_2)]^+$ would now either (a) be reduced by ferrocene present in the reaction mixture or (b) react *via* the "ET" pathway to form the phenoxyl radical. Central to several of the above hypotheses is the involvement of $[LCu(OH_2)]^+$, which had

previously only been implicated in cyclic voltammetry experiments.[13] It was hypothesized that if the quenching of $^{NO2}ArO^{\bullet}$ and/or $[LCu(OH_2)]^+$ by ferrocene could be avoided, we might be able to observe $[LCu(OH_2)]^+$ and thus provide independent evidence in favor of it being a feasible intermediate in the reaction of LCuOH with $^{NO2}ArOH$.

4.5.1 Identification of $[LCu(OH_2)]^+$ as an intermediate in reactions of LCuOH with $^{X}ArOH$ (X = NO_2 or CF_3)

To probe the above mentioned hypotheses, the reactions between LCuOH and $^{NO2}ArOH$ were repeated using stronger oxidants, namely tri-*p*-tolylamminium radical-cation $[(p\text{-tolyl})_3N^{+\bullet}]$ ($E_{1/2}$ = 0.38 V vs. Fc^+/Fc) and thianthrenium radical cation $[C_{12}H_8S_2^{+\bullet}]$ ($E_{1/2}$ = 0.86 V vs. Fc^+/Fc),[63] the reduced forms of which would not be able to reduce the formed phenoxyl radical or $[LCu(OH_2)]^+$. Treatment of a THF solution of $[Bu_4N][LCuOH]$ with 1 eq of $[(p\text{-tolyl})_3N]PF_6$ or $[C_{12}H_8S_2][PF_6]$ (dissolved in acetonitrile for solubility/stability purposes) at -80 °C led to the growth of the typical feature at 548 nm associated with formation of LCuOH (Figure 4.24, black spectrum). Upon addition of $^{NO2}ArOH$ (5 eq) to this solution, the absorption feature at 400 nm associated with $^{NO2}ArO^-$ still appeared and the characteristic LMCT feature for LCuOH decreased in intensity and shifted slightly (λ_{max} = 550 nm, Figure 4.24, blue spectrum). This spectroscopic feature was stable for minutes upon standing at -80 °C, but bleached upon warming to room temperature (Figure 4.24, red spectrum), consistent with it being associated with a reactive intermediate.

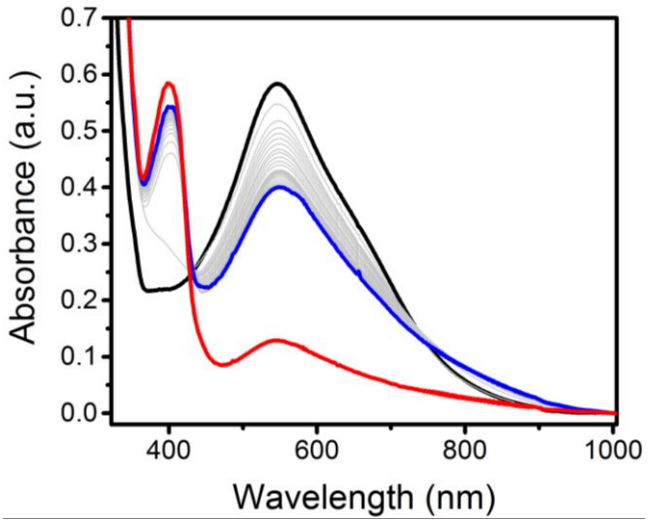

Figure 4.24. UV-vis spectra for the reaction of LCuOH (prepared by reaction of $[Bu_4N][LCuOH]$ with $(p\text{-tolyl})_3N^{+\bullet}$) with $^{NO2}ArOH$ in THF at -80 °C. (Black) initial spectrum of LCuOH. (Grey) intermediate spectra as a function of time (4-834 s). (Blue) final spectrum stable at -80 °C. (Red) spectrum resulting from warming to room temperature.

It is noteworthy that the feature at 400 nm is lower in intensity when compared to the experiments using Fc^+ as the oxidant; the yield of $^{NO2}ArO^-$ can be approximated to be ~30% with respect to the starting copper concentration. Taken together, all of these observations support the hypothesis that the reduced ferrocene, present in the reaction mixture (from the initial oxidation of $[Bu_4N][LCuOH]$) is involved in subsequent reactions.

Additional experiments were performed to further evaluate the nature of the intermediate involved in the reaction of LCuOH with $^{NO2}ArOH$. To test the feasibility of the intermediacy of $[LCu(OH_2)]^+$, a solution of LCuOH (generated by the reaction of $[Bu_4N][LCuOH]$ with $[C_{12}H_8S_2][PF_6]$ in THF at -80 °C) was treated with the weak acid 2,4,6-trimethylpyridinium triflate (Figure 4.25, left). The resulting UV-vis spectrum is similar to that shown in Figure 4.24 (blue). An analogous spectrum was also obtained upon reaction of LCu(THF) dissolved in wet acetone or THF (conditions known to yield $LCu(OH_2)$)[13] with $[C_{12}H_8S_2][PF_6]$ at -80 °C (Figure 4.25, right), again consistent with the intermediate being $[LCu(OH_2)]^+$.

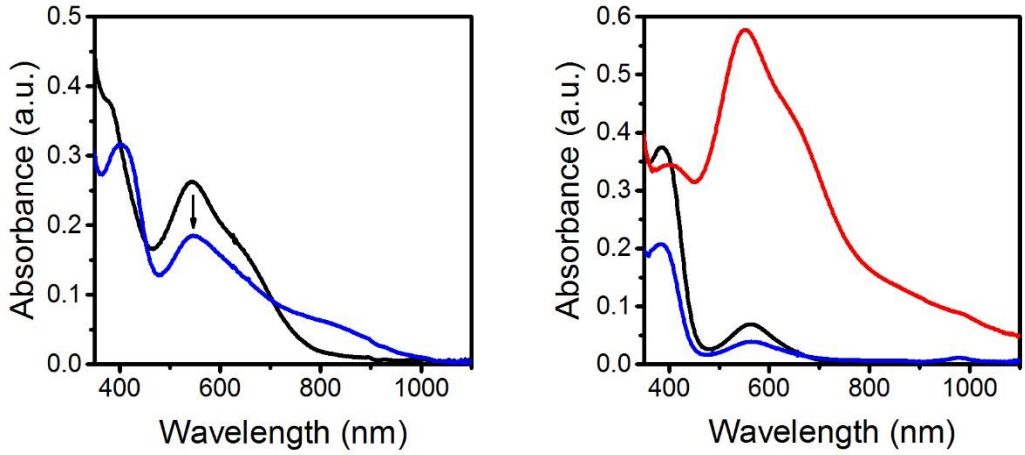

Figure 4.25. (Left) UV-Vis traces for the reaction between LCuOH (black spectrum; generated by addition of 1 eq. of $[C_{12}H_8S_2]PF_6$ to a 0.1 mM solution of $[Bu_4N][LCuOH]$ in THF at -80 °C) and 1 eq of 2,4,6-trimethylpyridinium triflate (blue spectrum) in THF at -80 °C. (Right) UV-vis absorption spectrum of the independently generated $[LCu(OH_2)]^+$ intermediate, formed by the addition of 1 eq of $[C_{12}H_8S_2]PF_6$ oxidant to a 0.1 mM solution of $LCu^{II}(THF)$ dissolved in wet Acetone (red) at -80 ºC. The starting spectra of LCu(THF) in dry and wet acetone are shown in black and blue, respectively.

Alternatively, it is possible that $[LCu(THF)]^+$, formed as a result of a ligand exchange with the solvent, could be present in the above reactions. To evaluate this possibility, we reacted LCu(THF) in anhydrous THF with $[C_{12}H_8S_2][PF_6]$ at -80 °C ($E_{1/2}$ of $[LCu(THF)]^+/[LCu(THF)]$ is 0.735 vs. Fc^+/Fc).[13] In this case, however, the UV-vis spectrum of the resulting solution differed significantly from that in Figure 4.24 (Figure 4.26, left). A third possibility is that the intermediate is the complex LCu(^{NO2}ArO), formed by ligand exchange with $^{NO2}ArO^-$. To evaluate this hypothesis, we independently synthesized $[Bu_4N][LCu(^{NO2}ArO)]$, characterized it fully (including by X-ray crystallography; Figure 4.27), and treated a solution of it in THF with $[(p\text{-tolyl})_3N][PF_6]$ at -80 °C. The UV-vis spectrum obtianed in this case (Figure 4.26, right) was also distinct from that observed in Figure 4.24 and this clearly ruled out LCu(^{NO2}ArO) as the intermediate. Detailed studies on the charcterization of LCu(^{NO2}ArO) will be presented in Chapter 5.

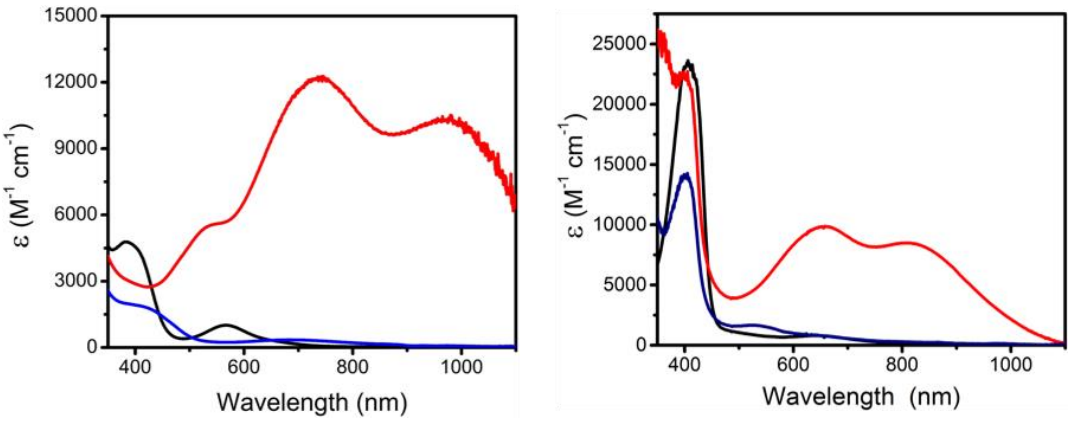

Figure 4.26. (Left) UV-vis absorption spectra of $LCu^{II}(THF)$ in THF (black), $[LCu^{III}(THF)]^{+}$ in THF generated by addition of 1 eq of $[C_{12}H_8S_2]PF_6$ (red), and the corresponding decay spectrum of the oxidized species upon warming up to room temperature (blue). All spectra were recorded at -80 ºC. (Right) UV-Vis absorption spectra of a THF solution of $Bu_4N[LCu^{II}OAr^{NO2}]$ (black), after the addition of 1 eq of $[(p\text{-tolyl})_3N]PF_6$ (red), and the final decay spectrum of the oxidized species after warming up to room temperature (blue). All spectra were recorded at -80 °C.

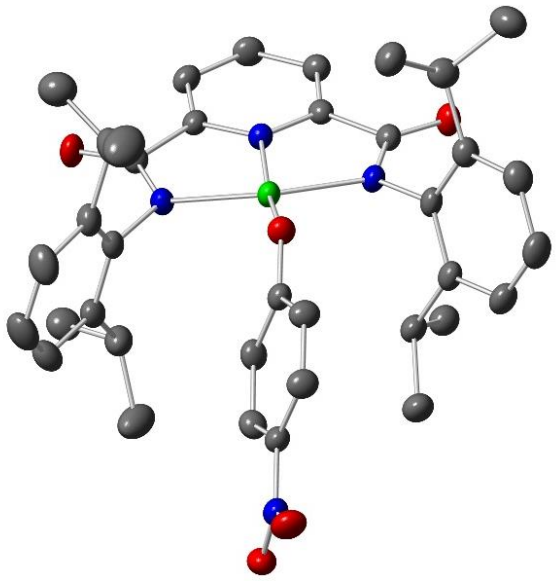

Figure 4.27. Crystal structure of $[Bu_4N][LCuOAr^{NO2}]$ with thermal ellipsoids drawn at 50% probability. Green, blue, red, and gray atoms represent Cu, N, O, and C, respectively. H-atoms, counter-ion, and solvent molecules omitted for clarity.

It is also noteworthy that the UV-vis spectrum of the intermediate extracted from the kinetic modeling using multi-component global fitting agrees well with the

independent spectra for $[LCu(OH_2)]^+$ (Figure 4.28). While the spectra are not a perfect match, they all reproduce the CT feature, characteristic of copper(III) intermediates with the pyridine di-carboxamide ligand framework. The LMCT band of LCuOH has been previously shown to be highly solvent dependent in the presence of coordinating solvents, and so it is hypothesized that the presence of other coordinating species in the control experiments (e.g. 2,4,6-trimethylpyridine, water, and excess phenol) are likely causes of the subtle observed differences in the UV-vis spectra. We also considered the possibility that this intermediate could be due to the formation of some precursor complex between LCuOH and ^{NO2}ArOH. Such species have been implicated in select transition metal based oxidations of phenols, often as a rationale for observed saturation behavior in these systems.[78] However, we view this idea to be unlikely on the basis of (a) the formation of $^{NO2}ArO^-$ concomitant with formation of the intermediate, (b) the persistence of the intermediate, and (c) thermodynamic arguments (presented below).

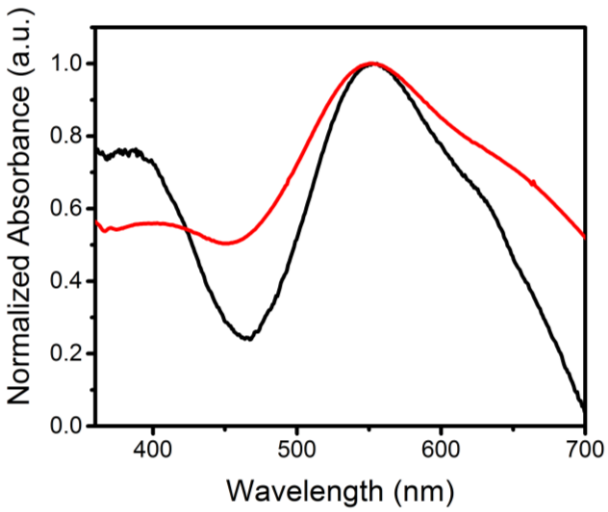

Figure 4.28. Overlay of the UV-vis spectra corresponding to the intermediate identified from global fitting of the reaction between LCuOH (from stopped-flow studies, generated by treatment of Bu_4N[LCuOH] with 1 eq. of Fc^+) and ^{NO2}ArOH (black) and the experimentally measured spectrum of $[LCu^{III}(OH_2)]^+$ generated by treatment of LCu(THF) in wet acetone with 1 eq. of $[C_{12}H_8S_2]PF_6$ at -80 ºC (red). The spectra are normalized.

Taken together, the more complex kinetic model required to fit the data and the direct spectroscopic observations of the intermediate in independent reactions supports the feasibility of $[LCu(OH_2)]^+$ as the intermediate in reactions of LCuOH with ^{NO2}ArOH. This conclusion is not undermined by the fact that when Fc^+ is used as an oxidant to generate LCuOH, the spectroscopic features associated with $[LCu(OH_2)]^+$ are not observed upon subsequent reaction with ^{NO2}ArOH; the absence of said features may be rationalized by postulating that $[LCu(OH_2)]^+$ is reduced *in situ* by ferrocene present in the reaction mixture. This postulate is further supported by identification of Fc^+ in the UV-vis and EPR spectra of the product mixtures and the known reduction potential of the $[LCu(OH_2)]^+/LCu(OH_2)$ couple in THF ($E_{1/2}$ = 0.345 V vs. Fc^+/Fc).[13]

The persistence of the intermediate feature at low temperatures suggests that the most plausible pathway to formation of $[LCu(OH_2)]^+$ is initial PT from ^{NO2}ArOH to LCuOH. Also in favor of an initial proton transfer step is the fact that Fc^+ is regenerated in the reactions between LCuOH and ^{CF3}ArOH at high substrate concentrations (Figure 4.21, right). Given that the approximate pK_a difference (ΔpK_a) between $[LCu(OH_2)]^+$ and ^{CF3}ArOH is 3.5, proton transfer would be expected to be significant only at high concentrations of ^{CF3}ArOH, consequently leading to the regeneration of Fc^+ only under such circumstances. It is also noteworthy that control reactions with ^{Me}ArOH as substrate and using $[(p\text{-tolyl})_3N][PF_6]$ or $[C_{12}H_8S_2][PF_6]$ as the oxidant did not yield any observable intermediate; instead, the features of LCuOH decayed rapidly as was observed in the stopped-flow studies (Figure 4.29). All the data support the hypothesis that the reactions of LCuOH with ^{NO2}ArOH and ^{CF3}ArOH proceed through a different mechanism when compared to the other phenols, namely one mediated by an initial proton transfer, which is further explored in thermodynamic arguments below.

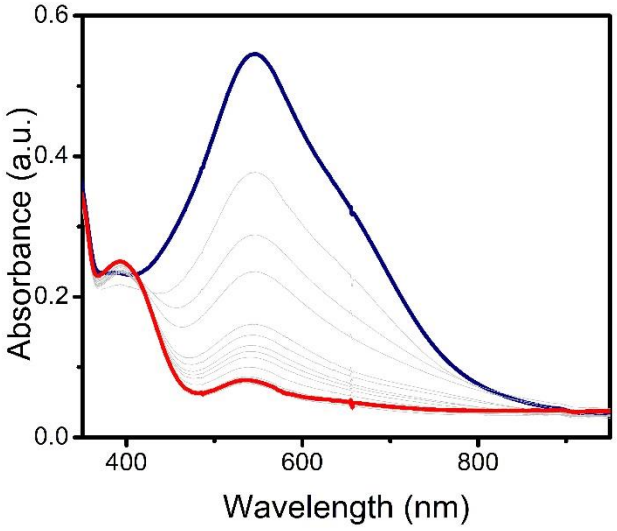

Figure 4.29. UV-Vis traces on treatment of LCuOH (generated by oxidation of $[Bu_4N][LCuOH]$ with $(p\text{-tolyl})_3NPF_6$)) with 2 eq *p*-cresol monitored in THF at -80 °C.

For the reactions of ^{NO2}LCuOH with ^{NO2}ArOH, the evidence in favor of a divergent mechanism is less clear. In these reactions, data indicating the formation of $^{NO2}ArO^-$, regeneration of $[AcFc^+]$, and the presence of an intermediate are all lacking. The lack of evidence for aqua adduct $[LCu(OH_2)]^+$ may derive from the decreased basicity of ^{NO2}LCuOH relative to LCuOH (~2 pK_a units).[14] This decreased propensity for proton transfer from ^{NO2}ArOH to ^{NO2}LCuOH would be offset by a slightly increased thermodynamic driving force for CPET. Thus, it is postulated that while proton transfer might indeed be induced at higher substrate concentrations (as is suggested for the reaction between LCuOH and ^{CF3}ArOH), its overall contribution in altering the mechanism of the reaction cannot be established unambiguously. Nonetheless, on the basis of the linear free energy plots discussed below, we hypothesize that the reaction between ^{NO2}LCuOH and ^{NO2}ArOH might also involve a degree of an initial proton transfer.[15]

4.5.2 Linear free energy relationships and thermodynamic arguments

Arguments in favor of a PT mediated pathway can also be made by using linear free energy relationships (LFERs). Because the thermodynamic data (pK_a, $E_{1/2}$, BDFE) for the phenols were obtained in DMSO[16,68] (Table 4.1), and no such data is available in THF (the solvent used to acquire the kinetic data for the reactions of LCuOH and ^{NO2}LCuOH with the phenols) we sought to convert rate constants measured in THF to the corresponding values in DMSO. Solvent effects on HAT reactions from phenols in a variety of solvents have been examined previously, and an empirical equation was developed that correlates the rates of such reactions across different solvents (Eq. 4.3).[22c,79] In this equation, (i) k^S(ArOH/X) denotes the HAT rate constant for reaction of the phenol (ArOH) with a reagent X in a given solvent S, (ii) k^o(ArOH/X) denotes the HAT rate constant in an alkane solvent and is unique to the particular reactant pair, (iii) β_2^H (unique to solvent S) represents a general thermodynamically related scale of hydrogen-bond acceptor abilities for different solvents in CCl_4, and (iv) α_2^H (unique to phenol ArOH) represents a general thermodynamically related scale of phenol hydrogen bond donor strength. Using reported values of α_2^H (Table 4.6) and β_2^H (0.51 for THF and 0.78 for DMSO),[80] we subtracted forms of Eq. 4.3 (one for THF and one for DMSO) and included the β_2^H values to yield Eq. 4.4. The rate constants in DMSO were then calculated from the corresponding rate constants in THF (Table 4.5) using Eq. 4.4; these are listed below in Table 4.7. An implicit assumption made in using these conversions is that the abstractor behaves identically in the two solvents. While Ingold and co-workers have previously demonstrated that such kinetic solvent effects are independent of the nature of the abstractor,[79] we acknowledge that this might not be completely true for the $[CuOH]^{2+}$ complexes, as they could act as potential hydrogen bond donors and behave differently in THF and DMSO. However, this is expected to be a systematic trend for a given abstractor and hence these conversions are useful in predicting trends across their reactions with a series of phenols.

$$\log(k^{S}_{\underline{ArOH}}) = \log(k^{o}_{\underline{ArOH}}) - 8.3\alpha_2^H\beta_2^H \quad \text{eq. 4.3}$$

$$\log k_{\mathrm{DMSO}} = \log k_{\mathrm{THF}} - 2.241\alpha_2^H \quad \text{eq. 4.4}$$

Table 4.6. Hydrogen bond donor activities of the phenols used in this study.

Phenol	4-CF_3	4-NO_2	4-Cl	4-H	4-Me	4-OMe	4-NMe_2
α [a]	0.724	0.787	0.670	0.596	0.569	0.573	0.57[b]

[a] From Ref. 79a,79b,80. [b] Determined from Hammett parameters as discussed in Ref. 80.

Table 4.7. Second-order rate constants (k) for the reactions of LCuOH and ^{NO2}LCuOH with ^{X}ArOH at –80 ºC, converted from THF to DMSO.[a]

X	LCuOH (DMSO)[b]	^{NO2}LCuOH (DMSO)[b]
NMe_2	1.0×10^5	3.5×10^5
OMe	1.6×10^4	9.4×10^4
Me	4.7×10^2	5.3×10^4
H	1.8×10^1	8.3×10^3
Cl	2.0×10^1	4.4×10^3
NO_2	4.5×10^0	1.4×10^1
CF_3	7.2×10^{-1}	7.0×10^0

[a] All values in units $M^{-1}\,s^{-1}$. [b] Estimated from the experimental values in THF (Table 4.5) using an empirical correlation of phenol rate constants with solvent hydrogen bonding properties (Eqs. 4.3 and 4.4; see text). Given that the uncertainties in α and β are unknown, no uncertainties are reported for the DMSO values.

Plots of logk_{DMSO} versus log$K$, $E_{1/2}$, and pK_a are shown in Figure 4.30. Here k is the second-order rate constant of the reaction in DMSO (from Table 4.7), $E_{1/2}$ is the redox potential of the ^{X}ArOH in DMSO ($E_{1/2}(ROH^{+\bullet}/ROH)$ in Table 4.1), and pK_a is for the phenol in DMSO (Table 4.1). The equilibrium constant K is for the reaction between LCuOH or ^{NO2}LCuOH with the phenol ^{X}ArOH to form LCu(OH_2) or ^{NO2}LCu(OH_2) and the phenoxyl radical ^{X}ArO$^{\bullet}$, and was determined from the approximate ΔG_{CPET} (defined as the difference in the bond dissociation free energy for the phenol O-H and the BDE of the corresponding copper(II)-aqua complex) at T = 298 K.

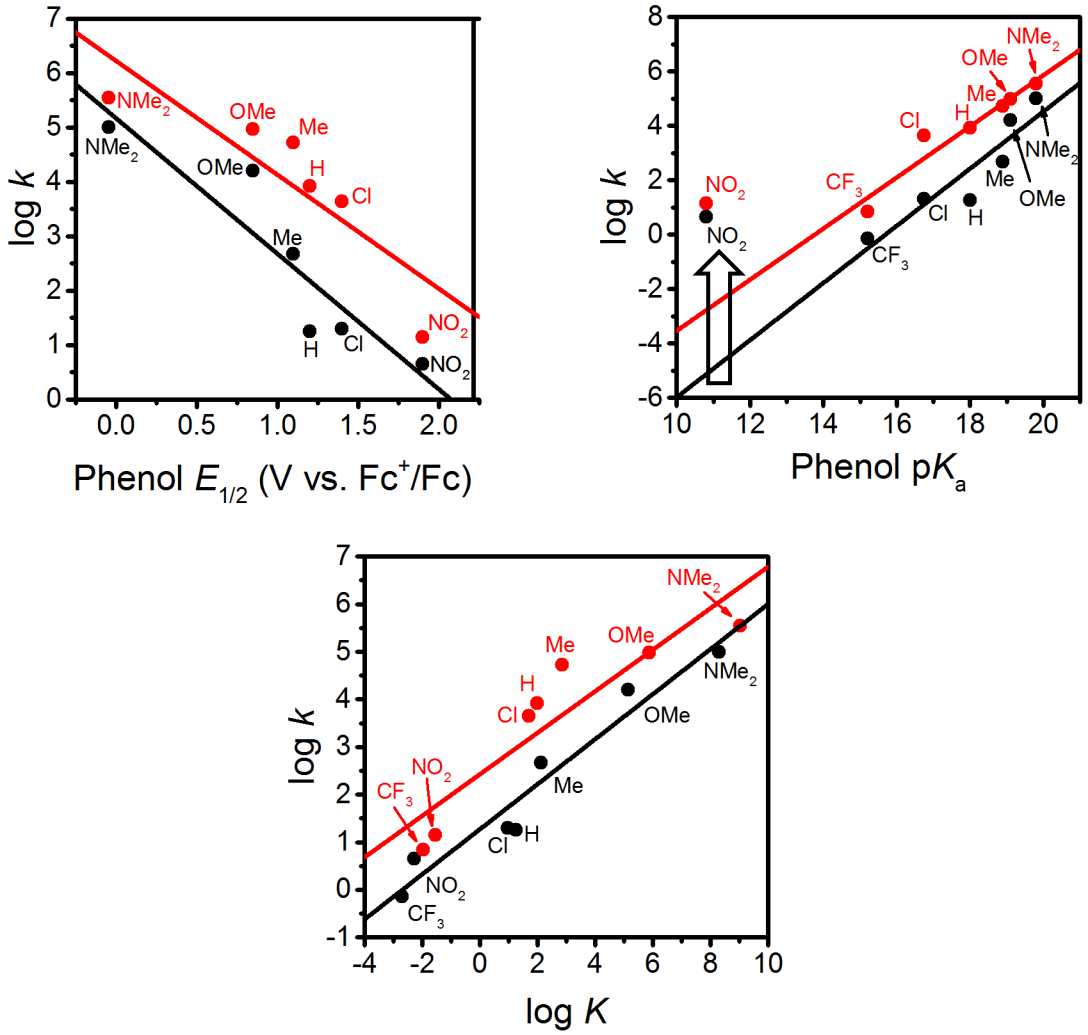

Figure 4.30. (Top Left) Plots of logk_{DMSO} vs. $E_{1/2}$(^{X}ArOH$^{+\bullet}$/^{X}ArOH) (X indicated) for their reactions with LCuOH (black) and ^{NO2}LCuOH (red). Linear fits have slopes of -2.5 (R^2 = 0.84) and -2.1 (R^2 = 0.76), respectively. (Top Right) Plots of logk_{DMSO} vs. pK_a of the phenols ^{X}ArOH (X indicated) for their reactions with LCuOH (black) and ^{NO2}LCuOH (red). Linear fits do not include the data points for X = NO_2 and have slopes of 1.1 (R^2 = 0.85) and 0.94 (R^2 = 0.93), respectively. The wide arrow indicates the X = NO_2 outliers. (Bottom) Plots of logk_{DMSO} vs. logK_{CPET} for reactions of LCuOH (black) and ^{NO2}LCuOH (red) with phenols ^{X}ArOH (X labeled). Linear fits have slopes of 0.47 (R^2 = 0.94) and 0.44 (R^2 = 0.84), respectively. Adapted from Ref 15.

The linear correlation between log$k$ and log$K$ (Figure 4.30, bottom) seems to support a similar mechanism operating across all the phenol substrates. The unitless slope of 0.47 and 0.44 for this Brønsted-type plot shows that an increase of K_{CPET} of 10^2 gives an increase in k_{CPET} of roughly 10, with the value of roughly ½ being consistent with a

relationship between driving force and kinetic barrier that is within the typical low-driving force Marcus regime ($\Delta G° \ll 2\lambda$) and is in line with what has been observed for other cases of PCET.[16,22,26,79d] The plots of log*k* vs. $E_{1/2}(^{X}ArOH^{+\bullet}/^{X}ArOH)$ (Figure 4.30, top left) may also be fit to straight lines, although the fits are of lower quality, with slopes of -2.5 V^{-1} (R^2 = 0.84) and -2.1 V^{-1} (R^2 = 0.76). Converting from relative reduction potentials to relative equilibrium constants for ET from ^{X}ArOH to LCuOH or ^{NO2}LCuOH gives respective unitless slopes of 0.17 and 0.12, which reflect that these reactions are not very sensitive to the reduction potential of the phenols. The slope of the plot of log*k* vs. phenol pK_a (Figure 4.30, top right, with linearity only achieved by omitting the data point for X = NO_2) is unusual. Even though the reactions involve removal of the phenolic proton, the more acidic phenols in general react *slower*. For example, ^{NMe2}ArOH is three orders of magnitude less acidic than ^{Cl}ArOH, but it reacts 5000 and 800 times faster for LCuOH and ^{NO2}LCuOH, respectively. Thus the Brønsted plot has a *positive* slope, of 1.1. This result rules out an initial proton step for these phenols, as this would have more acidic phenols reacting faster. The points for X = NO_2 are anomalous in the plots of log*k* vs. pK_a (Figure 4.30, top right). The rate constants for reactions with this phenol are significantly faster—by greater than four orders of magnitude—than that predicted by the linear dependence displayed by the other substrates. Interestingly, and in contrast to what we observe, in the case of other examples for which a consistent CPET mechanism was established, plots of log*k* vs. pK_a, $E_{1/2}$, and BDFE *all* displayed good linear correlations across all substrates.[70,81]

We interpret the data presented in Figure 4.30 (top right) to indicate that while a common CPET mechanism is followed by most of the phenols, for the most acidic phenol with X = NO_2, initial proton transfer followed by a subsequent electron transfer (PT/ET) likely occurs competitively with the CPET pathway.[30b,c,82] The observation of the aquo complex $[LCu(OH_2)]^+$ as an intermediate shows that CPET is not the only process occurring for this phenol. Still, the fact that the rate constant for the reaction

shows a good linear correlation with the driving force for a CPET reaction (Figure 4.30, bottom) is intriguing and suggests that the reaction likely proceeds by both pathways at comparable rates. Detailed kinetic modeling is complicated by the involvement of the reduced form of the initial ferrocenium oxidant, with some of the phenoxyl radical apparently generated *via* a CPET mechanism being reduced by Fc, thus increasing the apparent yield of the phenolate. The higher yields of $^{NO2}ArO^-$ when Fc^+ is used as an oxidant are consistent with this notion. For the stronger oxidants, however, any phenolate formed is probably from the initial PT pathway in the PT/ET mechanism.

Thermodynamic arguments also support the possibility for PT in the reactions of $^{X}ArOH$ (X = NO_2 and CF_3), comparing the free energies for PT and CPET as a function of the X substituent in $^{X}ArOH$ (Figure 4.31). ΔG_{CPET} is estimated as the difference of the phenol BDFE and the BDE of the copper(II)-aqua complex, $LCu(OH_2)$. ΔG_{PT} is roughly approximated as the difference of the phenol pK_a in DMSO and the pK_a of the copper(III)-aqua complex $LCu(OH_2)$ in THF, which should capture the trend (the various phenol pK_as likely being shifted by a constant amount between DMSO and THF) and should be more negative than the true value in THF (the less polar solvent disfavoring the formation of charged species in the equilibrium $ArOH + LCuOH \rightleftharpoons ArO^- + LCuOH_2^+$). Figure 4.31 shows that ΔG_{PT} is greater than ΔG_{CPET} by a significant amount for most of the phenols, consistent with CPET being more favorable than the corresponding PT/ET process. However, for X = NO_2 and CF_3, ΔG_{PT} comes much closer and is likely comparable to ΔG_{CPET}, so PT may be thermodynamically competitive with CPET in these cases. It has been suggested that under such circumstances, there can be a change in the nature of the transition-state; "*valence bond mixing creates a concerted reaction with PT character, followed by ET.*"[66] In this case, however, competitive pathways are indicated by the appearance of phenoxide and aquo complexes as intermediates, rather than the evolution of a single transition state.

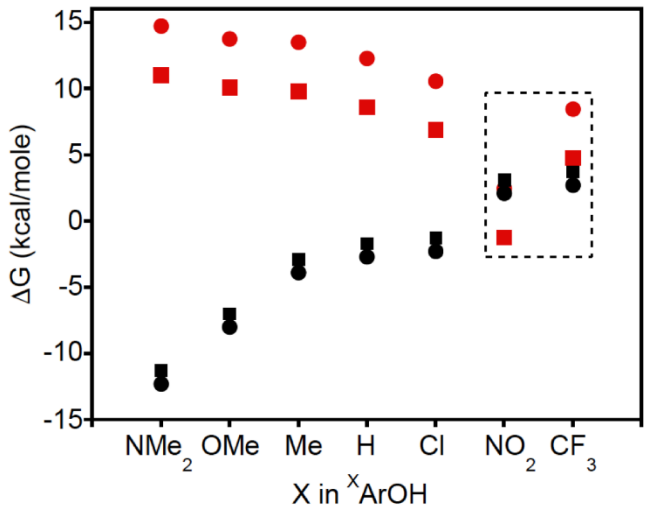

Figure 4.31. The plot of Δ*G* for corresponding PT (red) or CPET (black) reactions with LCuOH (squares) and ^{NO2}LCuOH (circles). The dashed region represents where there is potential for thermodynamic overlap (i.e., both PT and CPET are feasible).

In general, metal-mediated PCET reactions involving initial PT from single donor site to single acceptor site are rare. In one case, manganese(III)- and iron(III)-oxo complexes featuring extremely basic oxo ligands were shown to change mechanism from CPET to PT in their reactions with phenols.[33a] Notably, however, product analysis showed that the subsequent electron transfer after PT did not occur, even with fairly reducing phenolic substrates. Other studies report initial proton transfer occurring in aqueous PCET reactions of substituted phenols at higher pH, but these reactions are often reminiscent of sequential-proton-loss-electron-transfer (SPLET) in which hydroxide (or buffer) serves to deprotonate the phenol before one-electron oxidation of the phenoxide.[83] Still other reports of PT-initiated PCET reactions involving ruthenium(IV)-oxo or osmium(III)-amino complexes have also been shown to involve exogenous hydroxide as a proton acceptor.[84] In such systems it is difficult to distinguish between a concerted and sequential process. Most common are examples in which metal-mediated phenol-based oxidations have been shown to proceed *via* concerted processes. These include reactions mediated by metal-superoxo,[85a] -oxo,[85b] and -hydroxo/-alkoxo species,[78a] as well as metal based oxidants featuring pendant basic functionalities, which are often an amine or

carboxylate group.[86] In some cases an "ET-first" type mechanism has been proposed, as in the case of two μ-peroxo-/μ-oxo-dicopper species.[70] There are also some studies which report a change in mechanism from a concerted process to a sequential ET/PT process, induced by increasing the overall driving force for electron transfer either by (1) increasing the reduction potential of the H-atom abstractor or by (2) decreasing the oxidation potential of the phenolic substrate.[30b,85b] In one instance mechanistic changeover has even been induced by simply changing the temperature.[30a] A unifying theme amongst all of the above examples is that the transition metal based oxidants are supported by neutral/monoanionic ligand frameworks and possess an overall cationic charge. Consequently, the reactive species most commonly behave as electrophiles in these studies, thus precluding pathways involving an initial PT step.

These characteristics contrast with those of LCuOH, which is a reasonably strong base (estimated pK_a ~ 11.7 for $[LCu(OH_2)]^+$ in THF).[13] By analogy to the above cases in which an "ET-first" mechanism was induced by decreasing the oxidation potential of the phenolic substrate (i.e. making the substrate more electron-rich), it is proposed that decreasing the pK_a of the phenolic substrate (making it more electron-poor) induces a "PT-first" mechanism in the reaction between LCuOH and ^{NO2}ArOH. As an illustration of this point, it is instructive to compare this reaction with that between a ruthenium(III)-pterin complex and ^{NO2}ArOH, which is proposed to proceed *via* a CPET pathway.[78e] The thermodynamic driving force for a CPET reaction in both these cases is very similar (BDE of $LCu(OH_2)$ is 90 kcal mol^{-1} while that for the N-H bond formed in the ruthenium-pterin complex is ~89 kcal mol^{-1}). However, the ruthenium(III)-pterin is significantly less basic (pK_a ~12 in MeCN) than ^{NO2}ArOH (pK_a ~20.7 in MeCN), which results in an unfavorable thermodynamic driving force for a proton transfer from ^{NO2}ArOH in that solvent (~9 pK_a units, ~ 12 kcal mol^{-1}). Consequently, the reaction proceeds through the more feasible CPET mechanism. In contrast, the copper(III)-aqua complex ($[LCu(OH_2)]^+$) has a pK_a of ~ 11.7 (in THF), so proton transfer from ^{NO2}ArOH

(pK_a ~13.1 in THF) to LCuOH is much more energetically favorable, and thus contribution from a PT/ET pathway is much more feasible.

The above argument raises an important question: If the thermodynamic driving force of the CPET pathway is comparable to that for the corresponding PT pathway, what factors determine the contribution from each pathway in the overall mechanism of the reaction? Computational studies aimed at addressing such a dichotomy between concerted and sequential PT/ET pathways suggest that factors such as intrinsic proton transfer barrier and nature of the coupling between the proton and electron are often key determinants under such circumstances.[87] While in many cases the CPET pathway is strongly favored, such a mechanistic cross-over seems plausible, particularly in cases where the free energies are competitive and where the proton transfer occurs between electronegative O or N atoms so that the intrinsic barrier is small. For instance, a gas phase study focused on understanding such competition between PT versus HAT in reactions of enol radical cations and aldehydes concluded that when the enthalpies of the PT and HAT (ΔH_{PT} and ΔH_{HAT}, respectively) were similar, the PT pathway dominated. The authors attribute this to a much more stable transition state involving H-bonding in the case of PT and a non-negligible intrinsic barrier in the case of the HAT pathway.[88] While this system is significantly different than the solution phase studies discussed above, it serves to highlight the importance of such factors as the nature of the transition-state and intrinsic barriers in the phenol reactions of LCuOH, and in these types of PCET reactions in general.

4.6 Summary and conclusions

The reactivity of the copper(III)-hydroxide complexes LCuOH and ^{NO2}LCuOH in THF with a series of phenols ^{X}ArOH with *para*-substituents X having a range of electron donor capabilities was probed using low temperature stopped-flow methods. Second-order rate constants for the reactions were measured and found to vary over a wide range

(~10^5 s^{-1}). For X = NMe_2, OMe, Me, H, and Cl, direct formation of phenoxyl radical species is implicated, whereas for X = NO_2 (and likely for CF_3 as well), the phenolate $^{X}ArO^-$ formed and the kinetics for decay of LCuOH and ^{NO2}LCuOH were best fit to a model involving the formation of an intermediate identified tentatively on the basis of independent experiments as the copper(III)-aqua complex $[LCu(OH_2)]^+$. These results, in conjunction with evaluation of the trends in log*k* as a function of the phenol thermodynamic parameters log*K*, $E_{1/2}$, and pK_a are consistent with a CPET mechanism for the series X = NMe_2, OMe, Me, H, and Cl, but with an additional contribution from sequential PT/ET for the most acidic phenols with X = NO_2 and CF_3. These results serve to elucidate the finer nuances of the hydrogen atom abstraction ability of the reactive copper(III) hydroxide species, particularly highlighting the important role of its basicity in such reactions. More generally, these findings provide significant insights into fundamental aspects of the reactivity of the $[CuOH]^{2+}$ core, which may play a key role in oxidations promoted by enzymes and other catalysts.

4.7 Experimental section

Materials and Methods. All reagents and solvents were purchased from commercial sources and used as received unless otherwise noted. Tetrahydrofuran (THF) was either dried over sodium/benzophenone, and vacuum distilled, or passed through activated alumina columns and plumbed directly into glove-box for direct use. Acetonitrile was dried over calcium hydride and vacuum distilled. Diethyl ether was passed through solvent purification columns (Glass Contour, Laguna, California). All solvents were stored over 3 Å molecular sieves in an N_2 filled glove-box before use. Metal complexes were synthesized and manipulated in a Vacuum Atmospheres glove-box under an inert atmosphere of N_2 or through the use of standard Schlenk-line techniques. HPLC grade water was degassed by sparging with N_2 for 15 min before use in titration experiments. Elemental analyses were performed by Robertson Microlit

Laboratory (Ledgewood, NJ). UV-vis spectra were obtained using an HP8453 (190-1100) diode array spectrophotometer. Variable temperature UV-vis experiments were performed using a Unisoku low temperature cell holder. Double mixing stopped flow UV-Vis absorption spectroscopy experiments were carried out on a TgK Scientific Double mixing Cryo Stopped-Flow instrument using a Xenon light source and a Kineta Scan Photodiode Array detector. X-ray diffraction measurements were collected with Cu Kα radiation and a Bruker D8 Photon II CPAD diffractometer using normal parabolic mirrors as monochromators. All GC-MS experiments were conducted on an Agilent Technologies 7890A GC system and 5975C VL MSD. The GC column was an HP-5 ms with dimensions 30 m x 0.25 mm. EPR spectra were recorded on a CW X-band Elexsys E500 EPR spectrometer equipped with an Oxford ESR 910 liquid helium cryostat. All spectra were recorded at a temperature of 30 or 77 K and ~~at~~ (redundant preposition) a microwave frequency of 9.64 GHz under the following conditions: microwave power of 0.063 mW (30 K) or 0.0002 mW (77 K); modulation amplitude of 9.8 G; modulation frequency of 100 kHz. Chemical shifts (δ) for ^{1}H and ^{13}C NMR spectra were referenced to residual protium in the deuterated solvent (^{1}H) or the characteristic solvent resonances of the solvent nuclei (^{13}C). Compounds LCu(MeCN), LCuOH, ^{NO2}LCuOH,[8,13,14] [Fc]BAr$^{F}_{4}$,[48] [AcFc]BAr$^{F}_{4}$,[14] (*p*-tolyl)$_3$NPF$_6$,[63] [$C_{12}H_8S_2$]PF$_6$,[63] and *p*-dimethylaminophenol[89] were synthesized as described previously

[Bu$_4$N][^{NO2}ArO]. *4*-$NO_2C_6H_4OH$ (0.695 g, 5.00 mmol) was dissolved in anhydrous Et_2O (5 ml), and to this a solution of Bu_4NOH in MeOH (1.0 M, 5.0 ml, 5.0 mmol) was added. The yellow solution was stirred at room temperature for 30 min, after which the solvents were removed *in vacuo*. The resulting bright yellow solid was then suspended in anhydrous Et_2O (20 mL) and further stirred for 30 min, after which the residue was isolated by filtration and washed with excess Et_2O and dried thoroughly (1.62 g, 85.0%). ^{1}H NMR (DMSO-d_6, 400 MHz): δ_H 7.70 (2H, d), 5.87(2H, d), 3.14-

3.18(8H, m), 1.49-1.61 (8H, m), 1.31 (8H, m), 0.93 (12H, t) ppm. $^{13}C\{^{1}H\}$ NMR (DMSO-d_6, 100 MHz): δ_C 127.51, 119.37, 57.51, 23.05, 19.20, 13.48 ppm.

[Bu_4N][LCu(^{NO2}ArO)]. LCu(MeCN) (0.150 g, 0.255 mmol) and [Bu_4N][^{NO2}ArO] (0.098 g, 0.255 mmol) were suspended in anhydrous Et_2O (15 ml) and stirred for 30 min. After this, anhydrous THF (3 ml) was added to the suspension to facilitate dissolution of all solids, and the resulting solution was allowed to stir at room temperature for 12 h. During the course of the reaction, an olive green solid precipitated out of the reaction mixture. This solid was isolated by filtration and washed with copious amounts of anhydrous Et_2O and dried thoroughly (0.210 g, 88.7 %). X-ray quality crystals were obtained as green blocks by vapor diffusion of Et_2O into a concentrated solution of the compound in THF. UV-vis (THF, -80 °C) λ_{max}, nm (ε, M^{-1} cm^{-1}): 412 (23,100), 648 (800). Anal. Calcd for $C_{53}H_{77}CuN_5O_5.Et_2O$: C, 68.33; H, 8.75; N, 6.99. Found: C, 68.38; H, 8.66; N, 6.91.

Synthesis of 2,4,6-trimethylpyridinium Triflate.: Dry HCl (g) (generated by dropwise addition of concentrated H_2SO_4 to NaCl) was passed through a stirring solution of 2,4,6-trimethylpyridine in Et_2O, yielding the 2,4,6-trimethylpyridinium hydrochloride salt as a white powder which was isolated by vacuum filtration, washed with Et_2O, and dried *in vacuo*. After taking this solid into an N_2 filled glovebox, the hydrochloride salt (0.250 g, 1.59 mmol) and AgOTf (0.450 g, 1.75 mmol) were transferred to a 20 mL vial and dissolved in dry acetonitrile (10 mL), resulting in the immediate formation of a white precipitate (AgCl). After stirring for approximately 45 min, the suspension was passed through a syringe filter to remove AgCl, and the solvents were removed *in vacuo* to give a white oily solid. Trituration with 10-15 mL of dry Et_2O was followed by removal of the solvents *in vacuo*, and this was repeated three times, ultimately giving a white solid that was dried thoroughly *in vacuo* (0.350 g, 81.1%). ^{1}H NMR (DMSO-d_6, 400 MHz): δ_H 14.88 (1H, s), 7.58 (2H, s), 2.63 (6H, s), 2.49 (3H, s) ppm. $^{13}C\{^{1}H\}$ NMR (DMSO-d_6, 100 MHz): δ_C 159.07, 152.35, 125.52, 21.80, 19.43 ppm.

General procedure for double mixing stopped-flow monitoring of the reaction between LCuOH and 4-substituted phenols. In a N_2 filled glovebox, 0.12 mM stock solutions of Bu_4N[LCuOH] and [Fc]$BAr^F{}_4$ in THF were prepared, along with stock solutions of the phenols, which ranged from 0.3-6 mM (5-100 eq.). Solutions were transferred to gas tight syringes fitted with luer-lock tips and transferred to the stopped flow syringes after thorough washing of the syringes and mixing lines with degassed THF (2.5 mL). A typical run involved initial 1:1 mixing of 0.12 mM solutions of Bu_4N[LCuOH] and [Fc]$BAr^F{}_4$, yielding a reaction mixture which was aged for 4 s (to ensure full conversion of Bu_4N[LCuOH] to LCuOH as confirmed by single mixing experiments between LCuOH and [Fc]$BAr^F{}_4$). This was followed by a second 1:1 mixing event between the oxidized mixture and substrate solution, resulting in a final concentration of copper and substrate of 0.03 mM and 0.15-3 mM, respectively. Each mixing event resulted in a half-fold dilution of the starting solutions, and thus stock solutions of Bu_4N[LCuOH] and [Fc]$BAr^F{}_4$ were prepared at four times the final concentration, whereas substrate stocks were prepared at twice the final concentration. After the final mixing event, UV-Vis snapshots were collected over the course of the reaction using an integration time of 0.002 s (except in the case of reactions involving 4-$Me_2NC_6H_4OH$ and 4-$MeOC_6H_4OH$, where an integration time of 0.0015 s was used).

Given that LCuOH exhibits a characteristic charge-transfer (CT) band at 548 nm (10,000 M^{-1} cm^{-1}), monitoring of the absorbance of this feature over time provided a nice handle by which to determine the rates of these reactions. In all cases, plots of absorbance vs. time fit well to a single exponential decay function (Eq. 4.5), yielding pseudo first-order rate constants (k_{obs}). Plots of k_{obs} vs. substrate concentration revealed a linear dependence, indicative of second-order kinetics (for each kinetic step), and the slopes of these plots were taken as the second-order rate constant (k, see equation Eq. 4.6).

$$[\mathrm{LCu^{III}OH}]_t = [\mathrm{LCu^{III}OH}]_0 e^{-k_{obs}t} \qquad \text{eq 4.5}$$

$$k_{obs} = k_{self-decay} + k[\mathrm{Substrate}]_0 \qquad \text{eq 4.6}$$

In addition to the method described above, global-fitting was also performed using the program Olis Global Works™.[69] In all cases, the rate constants provided from these fits are analogous to k_{obs} described above, and plotting these values against substrate concentration yielded very similar second-order rate constants when compared to those obtained from the single-wavelength analysis.

General procedure for double mixing stopped-flow monitoring of the stoichiometric reactions of LCuOH and ^{NO2}LCuOH with 4-substituted phenols. In a N_2 filled glove box, 0.12 mM stock solutions of Bu_4N[LCuOH], Et_4N[^{NO2}LCuOH], [Fc]BAr^F_4, and [AcFc]BAr^F_4 were prepared in THF, along with 0.06 mM stock solutions of the phenols. Solutions were transferred to gas tight syringes fitted with luer-lock tips and transferred to the stopped flow syringes after thorough washing of the syringes and mixing lines with degassed THF (2.5 mL). A typical run involved initial 1:1 mixing of 0.12 mM solutions of Bu_4N[LCuOH]/Et_4N[^{NO2}LCuOH] and [Fc]BAr^F_4/[AcFc]BAr^F_4, yielding a reaction mixture which was aged for a set time (to ensure full conversion of Bu_4N[LCuOH]/Et_4N[^{NO2}LCuOH] to LCuOH/^{NO2}LCuOH as confirmed by single mixing experiments between Bu_4N[LCuOH]/Et_4N[^{NO2}LCuOH] and [Fc]BAr^F_4/[AcFc]BAr^F_4). This was followed by a second 1:1 mixing event between the oxidized mixture and substrate solution, resulting in a final concentration of 0.03 mM in both copper and substrate. Each mixing event resulted in a half-fold dilution of the starting solutions, and thus stock solutions of Bu_4N[LCuOH]/Et_4N[^{NO2}LCuOH] and [Fc]BAr^F_4/[AcFc]BAr^F_4 were prepared at four times the final concentration (0.12 mM), whereas substrate stocks were prepared at twice the final concentration (0.06 mM). After the final mixing event, UV-vis snapshots were collected over the course of the reaction using an integration time of 0.002 s (except in the case of reactions involving 4-$Me_2NC_6H_4OH$ and 4-$MeOC_6H_4OH$, where an integration time of 0.0015 s was used). The absorbance of the charge-transfer feature associated with either LCuOH/^{NO2}LCuOH (λ_{max}(ε, M^{-1} cm^{-1}) = 548(10,000) or 500(13,300) nm for LCuOH/^{NO2}LCuOH, respectively) was monitored

over time, and the decay absorbance trace was converted to concentration using the Beer-Lambert equation. The initial 5-10% of the data was fit to a linear regression providing reaction rates (M/s) that were divided by the square of the LCuOH concentration to give the second-order rate constant *k* (Eq. 4.7).

$$-\frac{d[\mathrm{LCu^{III}OH}]}{dt} = k[\mathrm{LCu^{III}OH}][\mathrm{Substrate}] = k[\mathrm{LCu^{III}OH}]^2 \qquad \text{eq. 4.7}$$

Comparison of the second-order rate constants obtained from the stoichiometric reactions with those from the pseudo-first-order analysis reveals some clear discrepancies, specifically with regard to reactions with 4-NO_2- and 4-CF_3-phenol. These reactions are the slowest and include some significant contribution from self-decay in THF (discussed in detail previously). In order to account for this, the data for these two runs were also fit to a mixed first and second-order rate law to include a first-order self-decay component (Eq. 4.8). Under conditions for which $[\mathrm{LCu^{III}OH}]_0$ = $[\mathrm{Substrate}]_0$, this can be approximated by Eq. 4.9, for with the integrated rate law is given by Eq. 4.2. Using this analysis, second-order rate constants were obtained that agreed much more closely with those obtained from the pseudo first-order experiments. Additionally, the rate constant obtained for self-decay from the fit is in good agreement with the independent self-decay rate measurements.

The justification for the use of Eq. 4.9. The rate law for the mixed first and second-order reaction is given by Eq. 5.8.

$$-\frac{d[\mathrm{LCu^{III}OH}]}{dt} = k_1[\mathrm{LCu^{III}OH}] + k_2[\mathrm{LCu^{III}OH}][\mathrm{Substrate}] \qquad \text{eq. 4.8}$$

When $[\mathrm{LCu^{III}OH}]_0$ = $[\mathrm{Substrate}]_0$, we can approximate $k_2[\mathrm{LCu^{III}OH}][\mathrm{Substrate}]$ = $k_2[\mathrm{LCu^{III}OH}]^2$. Thus the chemical equations for the first and second-order steps are given directly below, along with their corresponding rate equations

$$\mathrm{LCu^{III}OH} \rightarrow \mathrm{X}, \mathrm{rate}_1 = k_1[\mathrm{LCu^{III}OH}]$$

$$LCu^{III}OH + LCu^{III}OH \rightarrow Y, \text{rate}_2 = k_2[LCu^{III}OH]^2$$

Given that the second step involves the reaction of 2 molecules of $LCu^{III}OH$, $-d[LCu^{III}OH]/dt$ for the second step is 2x rate_2. Thus the overall rate of change of $[LCu^{III}OH]$ can be written as

$$-\frac{d[LCu^{III}OH]}{dt} = rate_1 + 2rate_2 = k_1[LCu^{III}OH] + 2k_2[LCu^{III}OH]^2 \qquad \text{eq. 4.9}$$

For which the integrated rate law is given by Eq. 4.2 (see Section 4.2.1 above)

$$[LCu^{III}OH]_t = \frac{k_1[LCu^{III}OH]_0 e^{-k_1 t}}{k_1 + 2k_2[LCu^{III}OH]_0(1 - e^{-k_1 t})} \qquad \text{Eq. 4.2}$$

It is important to note that while the stoichiometric data for reactions of LCuOH/^{NO2}LCuOH with ^{NO2}ArOH and ^{CF3}ArOH indeed fit better to Eq. 4.2, we have assumed in applying the rate Eq. 4.9 that over the course of the reaction, $[LCu^{III}OH]_t$ = $[\text{Substrate}]_t$. While we acknowledge that this is not actually the case, we posit that $[LCu^{III}OH]_t$ and $[\text{Substrate}]_t$ do not diverge significantly over the course of the reaction; the change in $[LCu^{III}OH]_t$ due to self-decay, though significant, is still relatively small.

For the faster reactions, fits to Eq. 4.2 were of lower quality and gave physically unreasonable values, a reflection of the diminishing contribution of self-decay to the overall rate. Thus, this correction was only applied to reactions with the 4-NO_2- and 4-CF_3-phenols.

Identification of Radical Species in reactions of LCuOH 2,4,6-tri-*t*-butylphenol and TEMPOH. A dry 2 mm EPR tube was capped with a rubber septum and cooled in a liquid N_2/acetone bath under active Ar flow. The tube was charged with $[Fc]BAr^F{}_4$ (0.3 mL at 1.67 mM concentration) *via* syringe and allowed to cool for approximately 5-10 min. A solution of Bu_4N[LCuOH] (0.1 mL, 5 mM in THF) was subsequently added, giving a deep purple solution, which was mixed by slow sparging

with Ar gas. To this mixture was added 0.1 mL of substrate (10 mM TEMPOH or 2,4,6-tri-*t*-butylphenol in THF), and the solution was sparged with Ar gas for approximately 15-20 min at -80 ºC, after which the solution was frozen in liquid N_2 under active Ar flow. These samples were then analyzed by EPR spectroscopy to identify the presence of organic radical species in solution (conditions: 1 mM final concentration, 77 K, 0.0002 mW microwave power).

Identification of Radical Species in UV-vis reactions of ^{NO2}LCuOH with 2,4,6-tri-*t*-butylphenol. In a N_2 filled glove-box, a 3 mL cuvette was charged with 1.8 mL of dry THF and 0.1 mL of a 2 mM solution of $Bu_4N[^{NO2}LCuOH]$. The cuvette was capped with a rubber septum, taken out of the glove-box, and cooled in the spectrometer at -80 ºC for 10 minutes under a slow Ar flow. To the cooled solution was added $[AcFc]BAr^F_4$ (0.1 mL, 2 mM), which resulted in the growth of a charge-transfer feature at 513 nm, characteristic of ^{NO2}LCuOH. To this solution was added 0.1 mL of 2 mM 2,4,6-tri-*t*-butylphenol, which resulted in the rapid decay of this feature. Once this feature had completely decayed, an aliquot of this solution was transferred to a 2 mm EPR tube and analyzed by EPR spectroscopy for the presence of organic radical products in solution (conditions: 0.1 mM concentration, 30 K, 0.063 mW microwave power).

EPR Identification of Fc^+ in the product solutions of reactions between LCuOH and ^{NO2}ArOH. A dry 2 mm EPR tube was capped with a rubber septum and cooled in a liquid N_2/acetone bath (~ -80 ºC) under active N_2 flow. The tube was charged with $[Fc]BAr^F_4$ (0.1 mL, 3 mM in THF) *via* syringe and allowed to cool for approximately 5-10 min. A solution of $Bu_4N[LCuOH]$ (0.1 mL, 3 mM in THF) was subsequently added, giving a deep purple solution, which was mixed by slow sparging with N_2 gas. To this mixture was added 0.1 mL of substrate (3 mM ^{NO2}ArOH), and the solution was slowly sparged with N_2 gas for approximately 15-20 min at -80 ºC, after which the solution was frozen in liquid N_2 under active N_2 flow. These samples were then analyzed by EPR spectroscopy to identify the presence of Fc^+ in solution

(conditions: 1 mM concentration, 30 K, 2 mW microwave power). For comparison, a 1 mM sample of [Fc]BAr^F_4 in THF was prepared and recorded under the same conditions.

UV-Vis Quantification of 2,4,6-tri-*t*-butylphenoxyl Radical in Reactions of LCuOH with 2,4,6-tri-*t*-butylphenol. In a N_2 filled glovebox, a 3 mL cuvette was charged with 1.8 mL of THF. The cuvette was capped with a rubber septum, taken out of the glovebox, and cooled in the spectrometer at -80 ºC under a slow Ar flow. To this was added 0.1 mL of a 2 mM solution of Bu_4N[LCuOH] in THF, followed by 0.1 mL of a 2 mM solution of [AcFc]BAr^F_4, which resulted in the immediate growth of a charge-transfer band centered at 548 nm, characteristic of LCuOH. Subsequent addition of 0.1 mL of 4 mM 2,4,6-tri-*t*-butylphenol resulted in the decay of this feature and the appearance of sharp charge-transfer features centered near 400 nm, indicative of the formation of 2,4,6-tri-*t*-butylphenoxyl radical. This species was quantified using the measured absorbance and the known molar extinction coefficient.[90]

General procedure for analysis of products from reactions of LCuOH and ^{NO2}LCuOH with substituted phenols.: This procedure is adapted from the previously reported procedure. In a N_2 filled glovebox, 5.4 mL of a THF solution of Bu_4N[LCuOH] or Et_4N[^{NO2}LCuOH] (5.56 mM) and a magnetic stir bar were transferred to a 20 mL vial that was capped with a rubber septum secured with copper wire. This was taken out of the glovebox and cooled to -80 ºC in an acetone/liquid N_2 bath under a slow, active flow of N_2, supplied through a needle *via* the Schlenk line. After cooling for approximately 10 min, 0.3 mL of a THF solution of [Fc]BAr^F_4 or [AcFc]BAr^F_4 (100 mM) was quickly added with stirring, resulting in a deep purple colored solution. After waiting for approximately 30 s, a THF solution of *p*-cresol was quickly added (0.3 mL @ 200 mM), resulting in a rapid color change to a more brown/green color. This solution was allowed to stir for an additional 30 min at low temperature before $HClO_4$ (0.2 mL @ 4 M) was added to quench the reaction, followed by warming of the solution to room temperature. After adding 2-5 mL of H_2O, THF was removed by rotary evaporation, after which the

remaining aqueous mixture was extracted with ethyl acetate (3 x 10 mL). The combined organic phases were washed with brine (2 x 10 mL), dried over Na_2SO_4 and filtered, and finally concentrated to dryness by rotary evaporation, generally giving an oily/solid residue. To the product mixture was added 2 mL of acetone, 1 mL of which was filtered through a 0.2 µm syringe filter into a GC-MS vial that was spiked with 0.05 mL of 25 mM 1,3,5-trimethoxybenzene in acetone as an internal standard.

Final quantification was then performed using GC-MS to measure the percentage of product in the sample relative to an internal standard, which was measured against a calibration curve. This curve was prepared using a coupled phenol surrogate, namely 2,2'-biphenol, given its ready availability and chemical similarity to the expected C-C coupled phenol products. The standard method used for all runs involved injection into an initial oven temperature of 50 °C (held for 2 min) followed by a 20 °C min^{-1} ramp to 70 °C (held for 6 min), followed by a 20 °C min^{-1} ramp to 150 °C (held for 3 min), followed by a final 20 °C min^{-1} ramp to 250°C (held for 8 min). The flow rate of He carrier gas was 1 mL/min and the inlet temperature was 250 °C.

General procedure for the generation of $[LCu(OH_2)]^+$ by oxidation:. A 3 mL cuvette capped with a rubber septum was charged with anhydrous acetone (1.95 mL) and degassed HPLC grade water (0.05 mL) under Ar. The cuvette was cooled at -80 ºC for 10 min, after which a solution of LCu(THF) in acetone (0.1 mL, 2 mM) was added. Subsequent addition of a MeCN solution of $[C_{12}H_8S_2]PF_6$ (0.1 mL, 2 mM) resulted in the immediate growth of an intense charge-transfer feature centered at ~ 550 nm, for which the UV-vis spectrum was recorded.

General procedure for the generation of $[LCu(OH_2)]^+$ by protonation of LCuOH. In a N_2 filled glove-box, a 3 mL cuvette was charged with THF (1.8 mL) and a THF solution of Bu_4N[LCuOH] (0.1 mL, 1 mM), and capped with a rubber septum. The cuvette was then taken out of the glove-box and cooled at -80 ºC for 10 min, after which ~~an~~ a MeCN solution of $[C_{12}H_8S_2]PF_6$ (0.1 mL, 1 mM) was added, resulting in the growth

of an LMCT band at 548 nm characteristic of LCuOH. Subsequently, a THF solution of 2,4,6-trimethylpyridinium triflate (0.1 mL, 1 mM) was added,and the UV-vis spectrum was recorded.

General procedure for the observation of intermediate $[LCu(OH_2)]^+$ in reactions of LCuOH with ^{NO2}ArOH and ^{Me}ArOH. In a N_2 filled glove-box, a 3 mL cuvette was charged with THF (1.8 mL) and a THF solution of Bu_4N[LCuOH] (0.1 mL, 1 mM), and capped with a rubber septum. The cuvette was then taken out of the glove-box and cooled at -80 ºC for 10 min, after which an MeCN solution of either $[(p\text{-tolyl})_3N]PF_6$ or $[C_{12}H_8S_2]PF_6$ (0.1 mL, 1 mM) was added, resulting in the growth of an LMCT band at 548 nm characteristic of LCuOH. Subsequently, a THF solution of either ^{NO2}ArOH or ^{Me}ArOH (0.1 mL, 2 mM) was added and UV-vis spectra were monitored over time.

General procedure for the oxidation of LCu(THF) with $[C_{12}H_8S_2]PF_6$ in THF. In a N_2 filled glove-box, a 3 mL cuvette was charged with THF (1.8 mL) and a THF solution of LCu(THF) (0.1 mL, 2 mM), and capped with a rubber septum. The cuvette was then taken out of the glove-box and cooled at -80 ºC for 10 min, after which 0.05 mL aliquots of ~~an~~ a MeCN solution of $[C_{12}H_8S_2]PF_6$ (0.1 mL, 1 mM) were added, resulting in the growth of multiple intense charge-transfer features centered at ~ 534, 735, and 992 nm. The resulting UV-vis spectrum was recorded.

General procedure for the oxidation of $Bu_4N[LCuOAr^{NO2}]$ with $[(p\text{-tolyl})_3N]PF_6$ in THF. In a N_2 filled glove-box, a 3 mL cuvette was charged with THF (2.4 mL) and a THF solution of $Bu_4N[LCuOAr^{NO2}]$ (0.1 mL, 1 mM), and capped with a rubber septum. The cuvette was then taken out of the glove-box and cooled at -80 ºC for 10 min, after which a MeCN solution of $[(p\text{-tolyl})_3N]PF_6$ (0.1 mL, 1 mM) was added, resulting in the growth of two intense charge-transfer features centered at ~ 656 and 814 nm. The resulting UV-vis spectrum was recorded.

Chapter 5

Targeting Mononuclear Copper(III)-Phenolate Complexes

5.1 Introduction

The chemistry of copper-phenolate complexes has been explored in great detail, particularly with the aim of modeling the active sites of enzymes like galactose oxidase.[2e,74c,91] The active site of galactose oxidase consists of a five-coordinate mononuclear copper center having a distorted square pyramidal coordination geometry, which has two bound histidine and tyrosine residues and a fifth labile aqua ligand.[91] It has been proposed that the key catalytic intermediate that is responsible for the oxidation of galactose is a copper(II)-tyrosyl ligand radical unit that is formed by a two-electron oxidation of the copper(I)-tyrosinate precursor, which is also believed to be the resting state of the enzyme.[91] Hence, the oxidation chemistry of copper(II)-phenolate compounds has garnered specific interest within the bioinorganic community, particularly owing to the intrinsic redox non-innocent nature of the bound phenolate ligand. The redox non-innocent nature of the bound phenolate implies that upon oxidation one could either access a copper(II)-phenoxyl radical or a copper(III)-phenolate moiety.[92] The fundamental importance of assignment of the correct spectroscopic oxidation state of the metal and the accurate description of the electronic structure of metal complexes of redox non-innocent ligand frameworks, particularly in relevance to accurately elucidating its chemical properties, has been discussed elaborately in the literature.[93] While most literature precedents support the formation of a copper(II)-phenoxyl species upon oxidation,[91,92] there are two examples of copper complexes supported by salen-based ligand frameworks where the oxidation is proposed to be metal centered. Figure 5.1 shows the X-ray structure of the only structurally characterized copper(III)-phenolate complex, [Cu**Sal**][SbF_6]).[94] Detailed spectroscopic analysis including resonance Raman, X-Ray absorption and UV-vis absorption spectroscopies, coupled with computational

studies were used to accurately assign the one-electron oxidation of the copper(II)-salen precursor as being metal centered. However, in all these studies the phenolate group is a part of the supporting ligand backbone and examples of well-defined copper(III)-phenolate complexes bearing a discrete phenolate ligand are thus far unknown. It has also been previously demonstrated that within an analogous series of nickel(II)-salen complexes generated using varying electronic substitutions, the center of oxidation (metal centered vs. ligand-centered) and the extent of localization/de-localization of the ligand radical (in the case of ligand-centered oxidations) is dependent on the nature of the electronic substituent and/or the nature of the linker.[95]

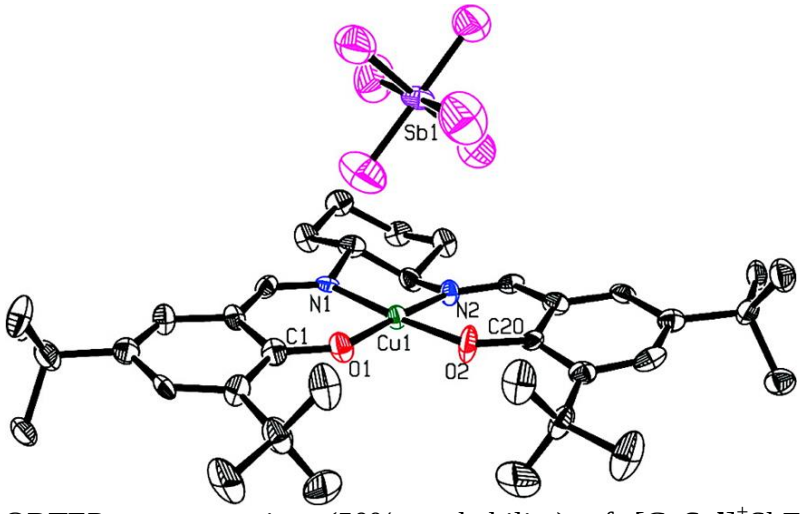

Figure 5.1. ORTEP representation (50% probability) of [Cu**Sal**]$^{+}$SbF$_6^{-}$, excluding hydrogen atoms. Selected interatomic distances (Å) and angles (deg): Cu(1)−O(1), 1.831(6); Cu(1)−O(2), 1.838(6); Cu(1)−N(1), 1.877(6); Cu(1)−N(2), 1.880(6); N(1)−C(7), 1.290(9); N(2)−C(14), 1.292(10); O(1)−C(1), 1.317(10); O(2)−C(20), 1.317(9); O(1)−Cu(1)−O(2), 86.5(3); O(1)−Cu(1)−N(1), 94.3(3); O(2)−Cu(1)−N(2), 93.8(3); N(1)−Cu(1)−N(2), 85.7(3). Adapted from Ref. 94a.

While investigating the hydrogen atom transfer reactivity of copper(III)-hydroxide and alkylperoxide complexes supported by the strongly electron donating pyridine-2,6-dicarboxamide supporting ligand framework with phenolic substrates, we reported the transient generation of putative high-valent copper-phenolates as possible reaction intermediates.[15,96] The supporting pyridine-2,6-dicarboxamide ligand framework had been previously successfully used in the Tolman group for the generation of

analogous high-valent copper(III) species like the aforementioned copper(III)-hydroxide and formally copper(III)-alkylperoxide complexes (Chapter 1, Section 1.2).[8,13,14,96] Notably, the one-electron oxidation potential of the copper(III/II) couple for the hydroxide complex is -0.076 (V vs. Fc^{+}/Fc), and it was suggested that the strong electron donation from the di-anionic ligand is key in stabilizing the high-valent copper(III) center.[8] Inspired by these observations, we sought to investigate the independent synthesis and spectroscopic properties of the putative high-valent copper-phenolates supported by the pyridine-2,6-dicarboxamide ligand framework. We hypothesized that by altering the electronic substitution on the phenolic moiety we could systematically tune the center of oxidation from a ligand-centered oxidation (in the case of electron rich phenolate moieties) to a metal-centered oxidation (in the case of electron deficient phenolate groups) to afford copper(II)-phenoxyl or copper(III)-phenolate complexes, respectively (Scheme 5.1). The synthesis and spectroscopic characterization of a series of analogous copper(II)-phenolate complexes with varying electronic substitutions on the phenol (*para*-NMe_2, *para*-OMe, *para*-H and *para*-NO_2) will be presented first. Subsequently, the oxidation chemistry of these compounds will be explored using multiple spectroscopic methods, with the ultimate aim of assessing whether the electronic structure of such species are best described as a copper(III)-phenolate or a copper(II)-phenoxyl (Scheme 5.1) and whether one could truly achieve a systematic modulation of the center of oxidation depending on the nature of the involved phenolate.

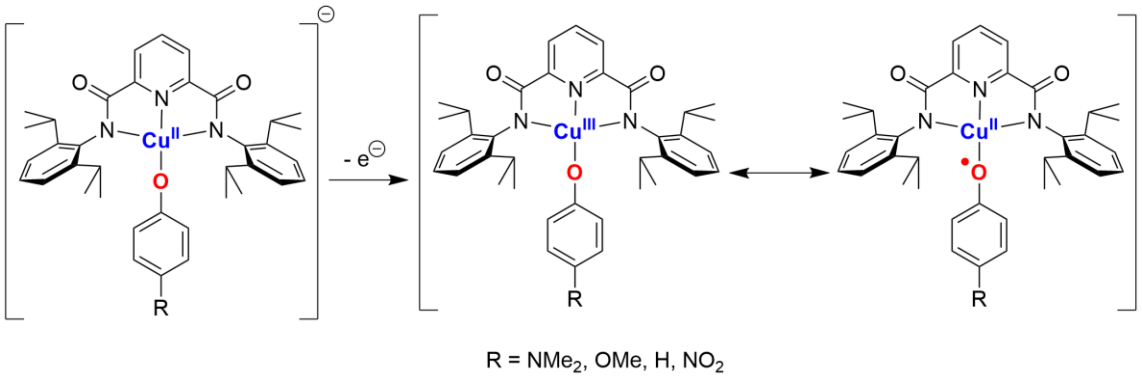

Scheme 5.1. The copper(II)-phenolate complexes presented in this chapter and the possible electronic descriptions of the one-electron oxidized species

5.2 Synthesis and characterization of copper(II)-phenolate complexes

5.2.1 Synthesis and structural characterization

A series of copper(II)-phenolate complexes were synthesized in high yield and purity in one of two ways (Scheme 5.2). The first procedure for the synthesis of the copper(II)-phenolate complexes [R'$_4$N][LCuOAr^R] (R = NO_2 [**1a**]$^-$, R = H [**1b**]$^-$, OMe [**1c**]$^-$) involved treating a suspension of the copper(II)-acetonitrile adduct in Et_2O/THF mixture (5:1 v/v) with 1 eq of the corresponding tetraalkylammonium phenolate salt, which led to the precipitation of the corresponding copper(II)-phenolate complex as an amorphous solid that was isolated by filtration. The second route involved treatment of [Bu_4N][LCuOH] with an excess (2 eq) of the corresponding phenol in a THF/Et_2O mixture (5:1 v/v) in the presence of a desiccant (3 Å molecular sieves), followed by isolation of the resulting copper(II)-phenolate complex as a solid. This second route takes advantage of the high basicity of [Bu_4N][LCuOH] in non-polar solvents like THF (pK_a of $LCuOH_2$ = 18.8)[13] and was employed for the synthesis of [Bu_4N][LCuOAr^{NMe2}] ([Bu_4N][**1d**]).[96] This latter route was preferred over the previous one owing to difficulties associated with isolating the tetraalkylammonium phenolate salt for ^{NMe2}ArOH as a solid. Excess phenol and desiccant were used to ensure complete conversion to the desired product. It is noteworthy that while [R'$_4$N][**1a-c**] were not synthesized using this method,

in situ test reactions between [Bu_4N][LCuOH] and ^{R}ArOH (R = NO_2, H, OMe) in THF solvent yielded solutions with UV-vis spectra identical to those obtained by dissolution of the independently isolated [R'$_4$N][**1a-c**] in THF, validating that this method would be equally applicable for the synthesis of these compounds.

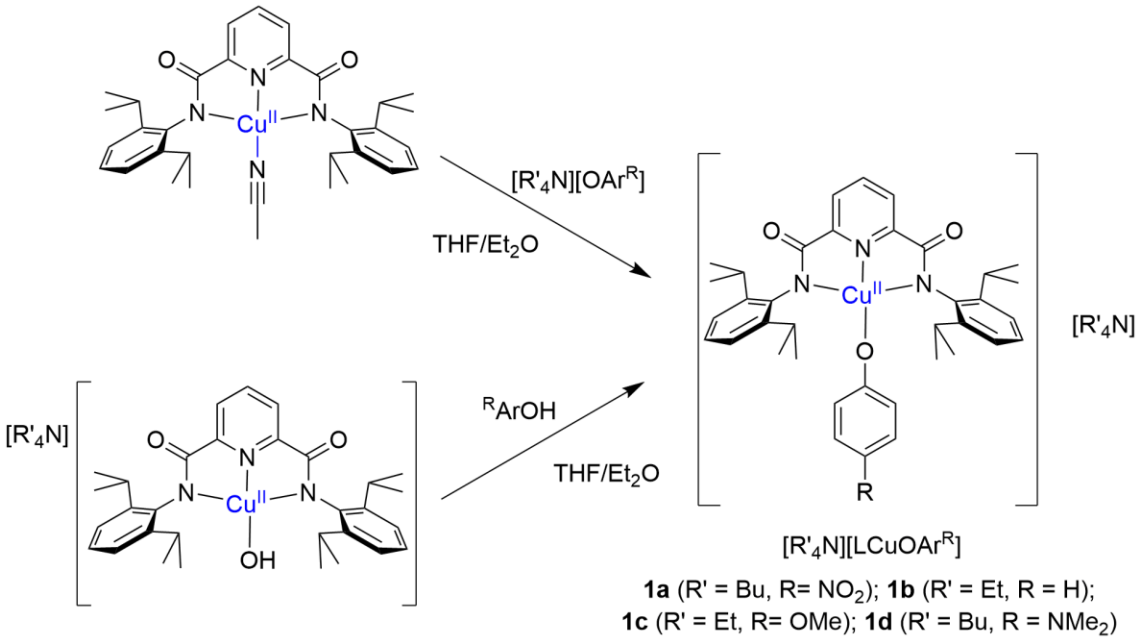

Scheme 5.2. Synthetic route for the generation of the copper(II)-phenolate complexes.

While all the compounds [R'$_4$N][**1a-d**] were structurally characterized using single crystal X-Ray diffraction, the quality of the single crystal X-ray diffraction data for [Bu_4N][**1d**] was not high enough to accurately evaluate bond metrics and draw structural arguments. Nevertheless, one can definitely ascertain bond connectivity from the data and make rough estimations of the bond metrics. Additionally, high-resolution mass spectrometry was used in this case to unambiguously confirm its chemical identity. The X-Ray crystal structures of the anionic portions of compounds [R'$_4$N][**1a-d**] are depicted in Figure 5.2 and the relevant bond metrics are summarized in Table 5.1. The Cu-N and Cu-O bond distances (~1.9 Å for $N_{pyridine}$, ~2.0 Å for N_{amide}, and ~1.9 Å for $O_{phenolate}$) are standard and within range of those expected for analogous square planar copper(II)

complexes.[14,96-97] The Cu(II) ion all the compounds adopts a similar distorted square-planar geometry evidenced by τ_4 values ranging between 0.17 and 0.24 (τ_4 is 0 for ideal square-planar and 1 for ideal tetrahedral geometry, respectively).[41] Nevertheless, a subtle trend in the geometry deviating from square-planarity as the bound phenolate ligand becomes more electron poor is observed, with [**1a**]$^-$ being the most distorted. Additionally, a subtle trend is also observed in the bond angle subtended by the phenolate C-O bond and the Cu-O bond, giving CuOC bond angles of 128.88, 121.55 and 115.41 for [**1a**]$^-$, [**1b**]$^-$ and [**1c**]$^-$ respectively. While it is tempting to rationalize the trend on the basis of phenolate ligand electronic influences, the trend is sufficiently subtle to also be simply attributed to crystal packing effects in the solid state structures.

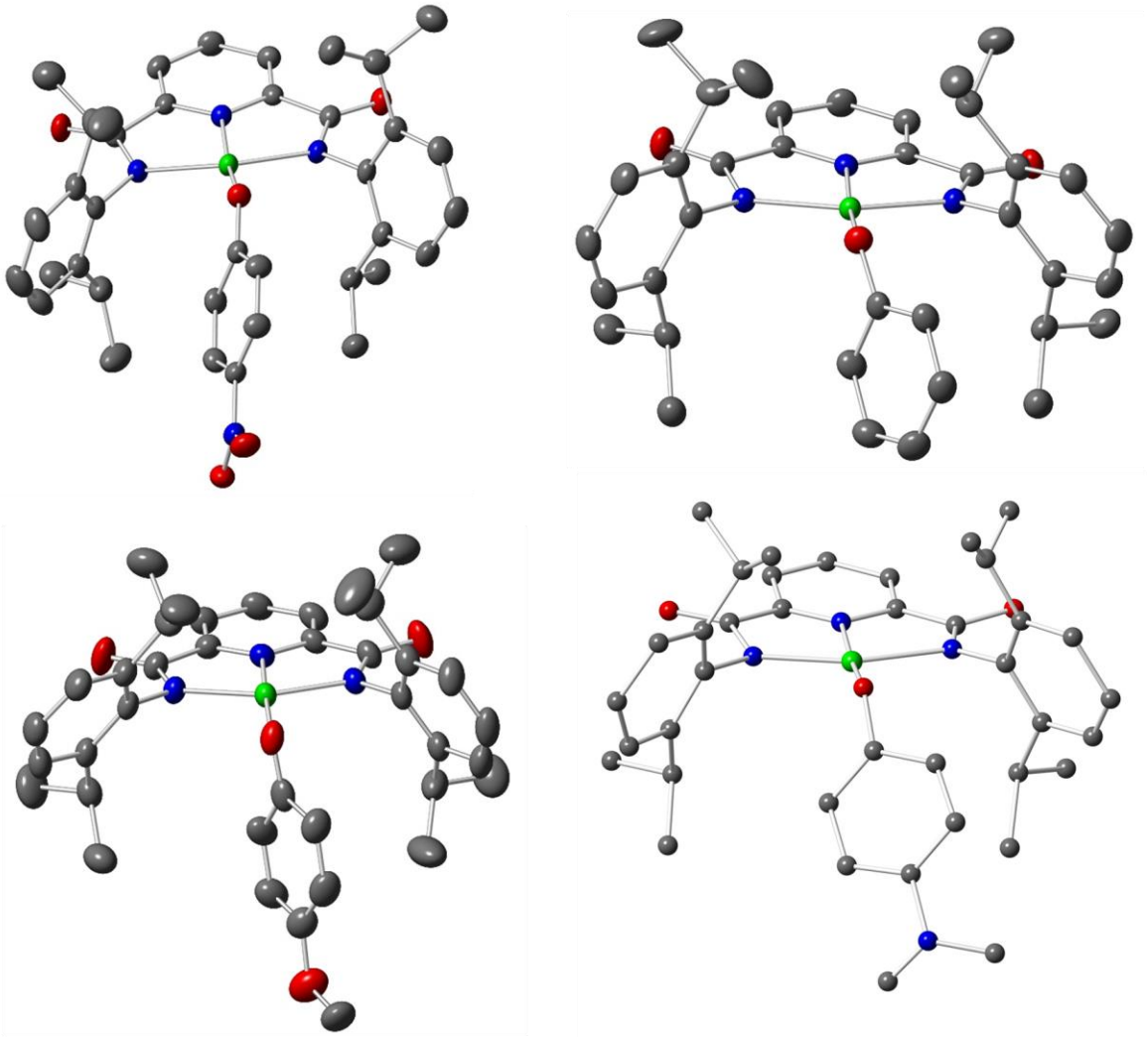

Figure 5.2. Representation of the X-ray crystal structure of the anionic components of [R'$_4$N][**1a-d**], showing all nonhydrogen atoms as 50% thermal ellipsoids where counterions and solvents have been omitted for clarity. (Top left) [Bu$_4$N][**1a**], (Top right) [Et$_4$N][**1b**], (Bottom left) [Et$_4$N][**1c**], and (Bottom right) [Bu$_4$N][**1d**] depicted as a ball and stick model. Relevant bond Cu-N/O bond distances are listed in Table 5.1.

Table 5.1. Structural parameters for the compounds [Bu_4N][**1a**], [Et_4N][**1b**], [Et_4N][**1c**] and [Bu_4N][**1d**].

	Cu-O[a]	Cu-N_{Py}[a]	Cu-N_{Am}[a]	τ_4[b]
[Bu_4N][1a]	1.8976(11)	1.9240(13)	2.0002(13), 2.0029(13)	0.24
[Et_4N][1b]	1.8767(13)	1.9296(14)	2.0063(15), 2.0219(15)	0.19
[Et_4N][1c]	1.9136(17)	1.9248(19)	2.0259(19), 2.0130(19)	0.17
[Bu_4N][**1d**][c]	1.876(8)	1.947(11)	1.992(13), 2.081(12)	~0.17

[a] in Å, [b] Tau for 4-coordinate (0 for square planar and 1 for tetrahedral, 41)
[c] Bond metrics obtained from a low resolution (1 Å) structure, hence the high estimated standard deviation in the bond length values

5.2.2 Spectroscopic characterization of the copper(II)-phenolate complexes

5.2.2.1 UV-vis absorption spectroscopy

The solution state UV-Vis spectra of the copper(II)-phenolate compounds [R'_4N][**1a-d**] recorded in THF at -80 °C are shown in Figure 5.3. All the spectra are consistent with typical distorted square planar copper(II)-phenolate complexes, with observable *d-d* transitions in the visible region and phenolate-to-Cu(II) charge transfer features in the lower wavelength region.[74c,91] The complex [Bu_4N][**1a**] also has a distinctly strong absorption feature at ~407 nm which we assign as an intra-ligand charge transfer in the nitrophenolate fragment on the basis of literature precedent.[75]

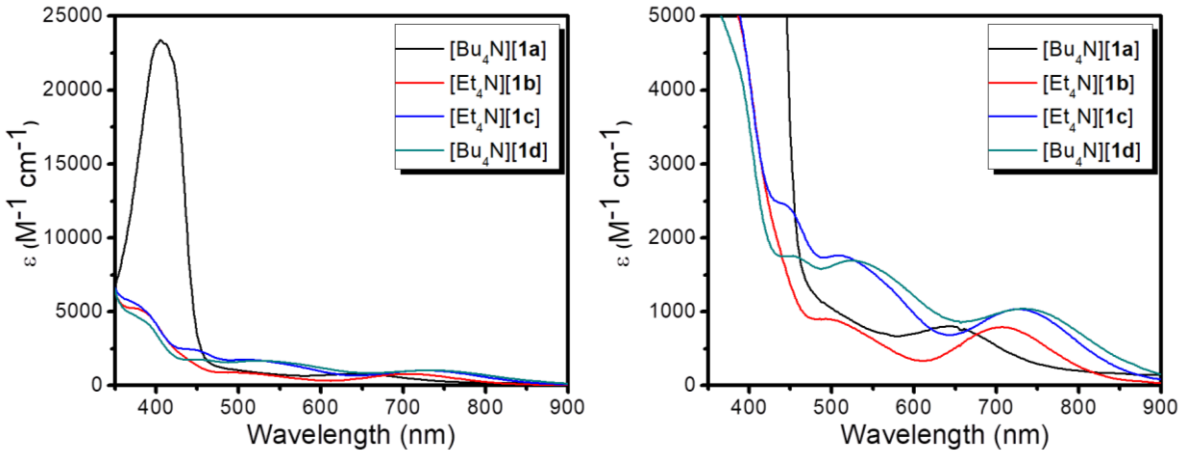

Figure 5.3. UV-Vis absorption spectrum of the copper(II)-phenolate compounds [R'$_4$N][**1a-d**] in THF at -80 °C showing the entire wavelength region (left) and expanded *d-d* region (right).

When looking at the expanded *d-d* region of the UV-Vis absorption spectrum of all the copper(II)-phenolate complexes (Figure 5.3, right), it is evident that all the compounds except for [Bu$_4$N][**1a**] have very similar absorption features. For [Bu$_4$N][**1a**], there is only one conspicuous *d-d* transition feature as opposed to the two observed for the other compounds. Additionally, the lowest energy *d-d* transition is blue shifted for this compound, having a λ_{max} ~ 645 nm as opposed to λ_{max} ~ (710 – 735) nm for [R'$_4$N][**1b-d**]. We hypothesize that this anomaly might be a consequence of the subtle geometric perturbation around the copper(II)-center observed for [Bu$_4$N][**1a**]. This result agrees with previous reports of UV-Vis absorption spectra for copper(II)-phenolates, where it is generally observed that electron donating phenolates tend to show absorption features at lower energies due to an increase in energy of the filled phenolate orbitals.[74c]

5.2.2.2 EPR spectroscopy

The EPR spectra of compounds [R'$_4$N][**1a-d**] (frozen samples in THF solvent, 30 K) are as expected for mononuclear Cu(II) compounds (Figure 5.4), displaying pseudo-axial signals (g_z ~ 2.2 and $g_{x/y}$ ~ 2.02-2.05) with rich superhyperfine coupling attributed to the ligand N atoms that are magnetically isolated from the nearby H atoms. The

parameters from spectral simulation (Figure 5.5) are summarized in Table 5.2 and Table 5.3.

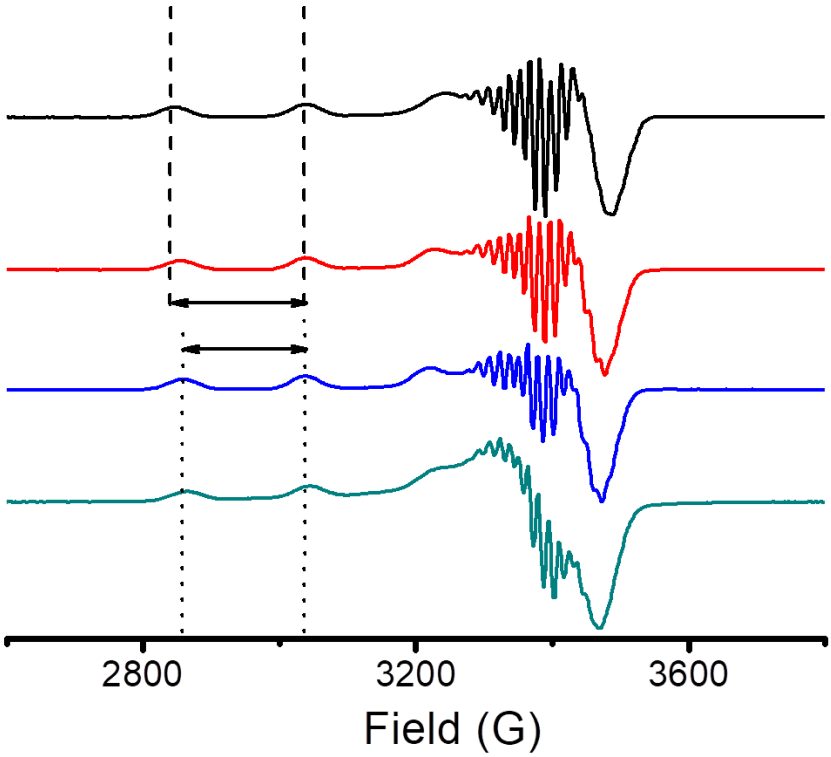

Figure 5.4. X-band EPR spectra of frozen solutions of samples [R'$_4$N][**1a-d**] recorded at 30 K where black trace represents [Bu$_4$N][**1a**], red trace represents [Et$_4$N][**1b**], blue trace represents [Et$_4$N][**1c**], and cyan trace represents [Bu$_4$N][**1d**]. The dashed lines depict the Cu hyperfine splitting constants A_z for [Bu$_4$N][**1a**] and dotted lines depict that for [Bu$_4$N][**1d**].

Table 5.2. Simulated g-values for EPR spectra of corresponding copper complexes [R'$_4$N][**1a-d**]

Compound	g(x)	g(y)	g(z)
[Bu$_4$N][**1a**]	2.022	2.052	2.198
[Et$_4$N][**1b**]	2.023	2.055	2.200
[Et$_4$N][**1c**]	2.020	2.052	2.203
[Bu$_4$N][**1d**]	2.037	2.048	2.197

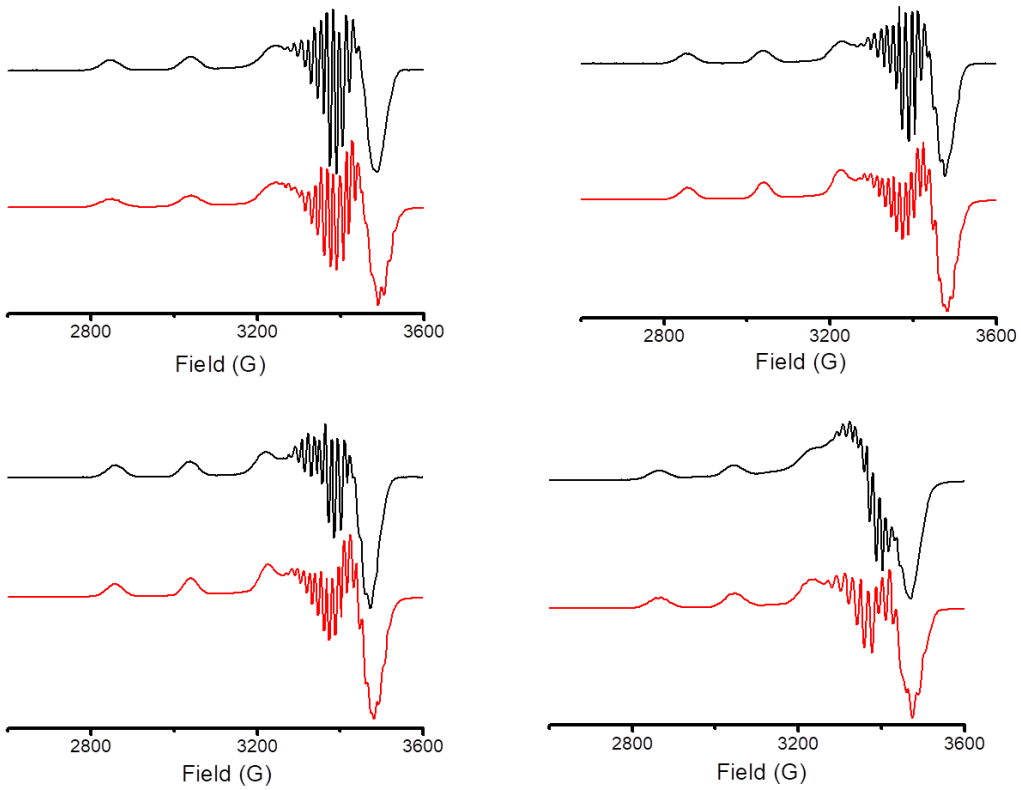

Figure 5.5. Experimental (black) and Simulated (red) spectra for [Bu_4N][**1a**] (top left), [Et_4N][**1b**] (top right), [Et_4N][**1c**] (bottom left), and [Bu_4N][**1d**] (bottom right).

Table 5.3. Simulated hyperfine parameters[a] for Cu, amido N (N_{am}), and pyridyl N (N_{py}) nuclei for complexes [R'$_4$N][**1a-d**].

		[Bu_4N][**1a**]	[Et_4N][**1b**]	[Et_4N][**1c**]	[Bu_4N][**1d**]
A_{Cu}	xx	115	100	95	80
	yy	115	100	95	80
	zz	580	554	545	537
A_{am}	xx	40	40	40	50
	yy	40	40	40	60
	zz	45	30	30	50
A_{py}	xx	40	40	40	50
	yy	40	40	40	60
	zz	45	30	45	40

[a] Hyperfine splitting reported with units of MHz.

Despite the high degree of similarity in the EPR spectra for the copper(II)-phenolate complexes, there is a subtle systematic trend in the Cu hyperfine splitting constants as a function of the electronic substitution on the coordinated phenolate ligand.

This trend is evident from the linear correlation in the plot of the $A_z(Cu)$ vs. the Hammett constant (σ_{para} which serves as a measure of the electron donating/withdrawing ability of the bound phenolate moeity)[53] depicted in Figure 5.6. Such correlations between the Cu hyperfine splitting constant and degree of electron donation from the supporting ligand framework were previously observed in a series of copper(II)-hydroxide complexes supported by pyridine/piperidine di-carboxamido ligand frameworks (discussed in Section 2.4, Chapter 2).[14] In the previous work, it was observed that increased donation from the supporting ligand framework enhances the Cu hyperfine splitting, which DFT calculations showed aligns with an increase in the Mulliken spin density on the Cu center.[14] Interestingly, however, in the present series of compounds [R'$_4$N][**1a-d**], this trend seems to be reversed; the Cu hyperfine splitting constant increases as the phenolate ligand becomes more electron poor, with the electron withdrawing *p*–NO_2 substituent in [Bu_4N][**1a**] causing the largest splitting and the most electron rich *p*–NMe_2 substituent in [Bu_4N][**1d**] inducing the lowest splitting constant. In the absence of more detailed analysis, such as that which would be facilitated by DFT calculations, for example, we currently have no explanation for this divergence from the previous results.

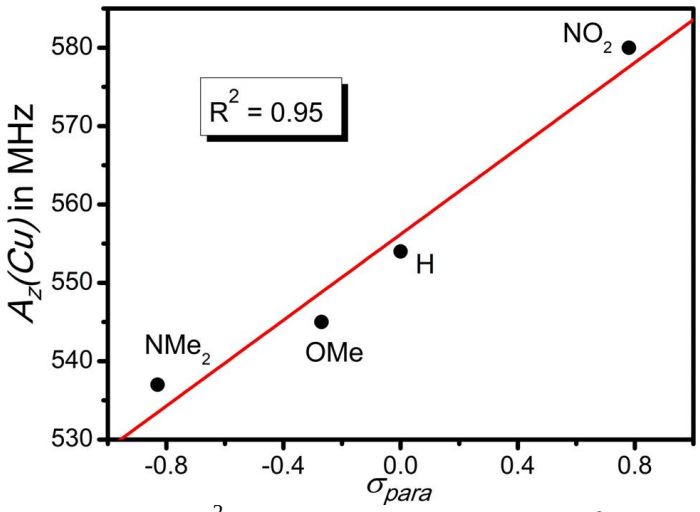

Figure 5.6. Linear correlation (R^2= 0.95) between the $A_z(Cu)$ for [R'$_4$N][LCuOAr^R] and σ_{para}(R).

5.2.2.3 Cyclic voltammetry

The electrochemical behavior of [R'$_4$N][**1a-d**] was investigated in THF solvent at room temperature with [Bu$_4$N][PF$_6$] as the supporting electrolyte using cyclic voltammetry (Figure 5.7). As expected, the redox potentials of the copper(II)-phenolate complexes are strongly dependent on the nature of the substituents on the phenolate ligand, with the most electron withdrawing *p*–NO$_2$ substituent having the highest redox potential (0.237 V vs. Fc$^+$/Fc) and the most electron donating *p*–NMe$_2$ having the lowest redox potential (-0.639 V vs. Fc$^+$/Fc).

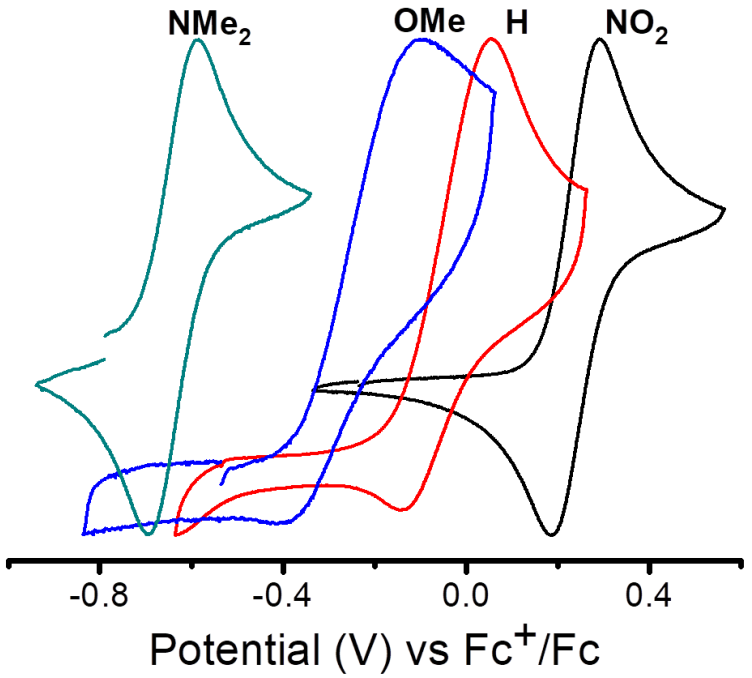

Figure 5.7. Overlay of the cyclic voltammograms of [R'$_4$N][**1a-d**] in THF solvent ([Bu$_4$N][PF$_6$] as the supporting electrolyte supporting electrolyte, referenced internally with decamethylferrocene, potentials reported against Ferrocene); black trace represents [Bu$_4$N][**1a**] (Scan rate 50 mV/s), red trace represents [Et$_4$N][**1b**] (Scan rate 1000 mV/s), blue trace represents [Et$_4$N][**1c**] (Scan rate 2000 mV/s), and cyan trace represents [Bu$_4$N][**1d**] (Scan rate 50 mV/s).

There are significant differences in the electrochemical behavior, however, with the extent of reversibility of the redox event being a notable disparity. The cyclic voltammograms for [Bu$_4$N][**1a**] and [Bu$_4$N][**1d**] are best described as being quasi-

reversible (with ΔE defined as E_{pa}–E_{pc}, which increased slightly with faster scan rates and had values of 110 mV and 100 mV, respectively, at a scan rate of 50 mV/s). At the low scan rate of 50 mV/s, the one-electron oxidation event has near ideal i_{pa}/i_{pc} values of 0.99. In contrast, the voltammograms for [Et_4N][**1b-c**] are irreversible, depicting only minimal cathodic current at high scan rates (Figure 5.8), thus allowing determination of only approximate $E_{1/2}$ values. These results imply that one-electron oxidation of [Et_4N][**1b-c**] (at room temperature) leads to the formation of some species that is highly unstable towards a subsequent chemical event. The $E_{1/2}$ values for the copper(II)-phenolate complexes along with the literature values of the redox potential of the free phenoxyl/phenolate couple[16] are summarized in Table 5.4.

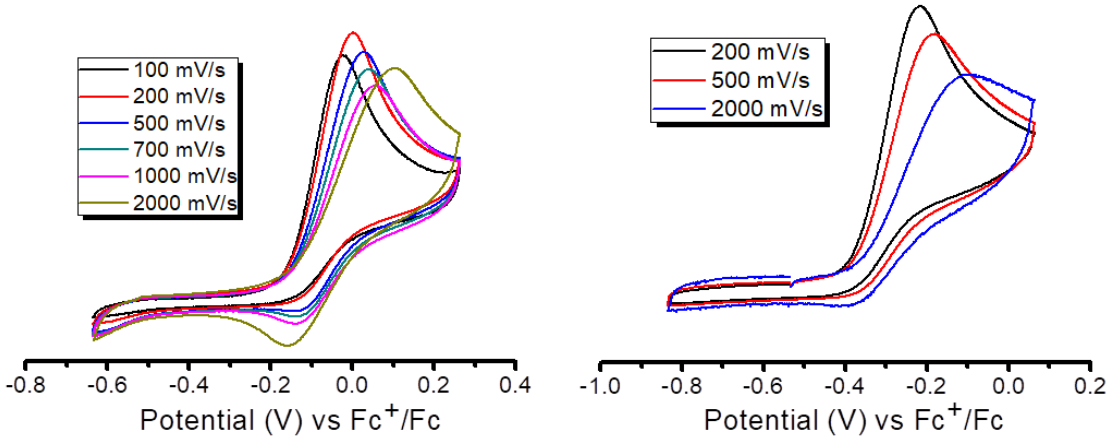

Figure 5.8. Cyclic voltammograms of [Et_4N][**1b**] (left) and [Et_4N][**1c**] (right) depicting the nature of the scan rate dependence.

Table 5.4. Redox potential for the one-electron oxidation of [R'$_4$N]**[1a-d**] along with the redox potential for the one-electron oxidation of the corresponding free phenolate species

	$E_{1/2}$ ($ArO^{\cdot}/ArO^{-}$)[a,b]	$E_{1/2}$ of first redox couple in [R'$_4$N][**1a-d**][b,c]	ΔE = [$E_{1/2}$(Cu) – $E_{1/2}$(ArO^{-})]
[Bu_4N][**1a**]	0.314	0.237	-0.077
[Et_4N][**1b**]	-0.325	-0.026	0.299
[Et_4N][**1c**]	-0.618	-0.248	0.370
[Et_4N][**1d**]	-0.847	-0.639	0.208

[a] in DMSO (Ref 16). [b] vs. Fc^+/Fc. [c] in THF

A closer analysis of the redox potential values in Table 5.4 reveals that for compounds [R'$_4$N]**[1b-d**], the redox potential for the one-electron oxidation is significantly higher (0.3-0.4 V) than the redox potential for the one-electron oxidation of the corresponding free phenolate anion. This can be easily rationalized if the center of the oxidation is phenolate ligand, as binding of an electrophilic Cu(II)-center is expected to reduce the electron density on the phenolate ring, thus making it more difficult to oxidize when compared to the free phenolate. However, [Bu_4N][**1a**] is anomalous in this regard because the free *p*–NO_2-phenolate has a higher oxidation potential than when bound to the copper(II)-center. While this result might seem counterintuitive at a first glance, it further reinforces the strongly electron donating nature of the pyridine-di-carboxamide ligand framework which can stabilize high-valent copper complexes. Thus, qualitatively speaking it appears that there might be something intrinsically different about the nature of the oxidation for [Bu_4N][**1a**] when compared to the other analogs in the series. It is worth noting here, however, that this is only a qualitative argument, as the redox potential values of the copper complexes and free phenolate anions were not measured in the same solvent.

5.3 Characterization of the corresponding one-electron oxidized complexes of the copper(II)-phenolate compounds

Following the successful synthesis and spectroscopic characterization of the copper(II)-phenolate complexes [R'$_4$N][**1b-d**], we sought to examine the spectroscopic properties of the corresponding one-electron oxidized complexes with the aim of accurately determining if these oxidized complexes are best described as a copper(II)-phenoxyl species or a copper(III)-phenolate species.

5.3.1 UV-Vis absorption spectroscopy

5.3.1.1 One-electron oxidation of [Bu_4N][**1a**]

In order to gain insight into the identity of the species formed upon the 1-electron oxidation of [Bu_4N][**1a**] observed by cyclic voltammetry, chemical oxidation of the complex was evaluated using UV-Vis absorption spectroscopy in THF solvent at -80 °C (Figure 5.9). In a typical experiment, a solution of 0.1 mM [Bu_4N][**1a**] in THF in a UV-Vis cuvette packed in the glove-box was cooled to -80 °C, after which 1 eq of [(*p*-tolyl)$_3$N]PF_6 ($E_{1/2}$ = 0.38 V vs. Fc^+/Fc, dissolved in CH_3CN for solubility and stability purposes)[63] was added. The addition of the oxidant led to the immediate growth of intense charge transfer features in the visible and near-IR region with strong absorptions at 657 nm (ε = 10,000 M^{-1} cm^{-1}) and 828 nm (ε = 8,500 M^{-1} cm^{-1}). While the oxidized species is relatively stable at -80 °C ($t_{1/2}$ ~ 4 h, consistent with the observed high reversibility in the cyclic voltammetry experiments), it decays immediately upon warming to room temperature. The intense absorption features observed are reminiscent of the ligand to metal charge transfer transitions observed for the mononuclear copper(III)-hydroxide/alkylperoxide unit supported by the same ligand framework.[8,14,96] Also, the two prior literature reports of putative copper(III)-phenolate complexes supported by salen based ligand frameworks also depict such strong LMCT transitions in the 500-600 nm range.[94] These spectroscopic signatures are distinct from the literature reports of copper(II)- and zinc(II)-phenoxyl radical complexes, which generally show the π-π^* transitions associated with the phenoxyl radical at ~400 nm with relatively broad and low intensity absorptions at higher wavelengths.[91] These observations suggest that the one-electron oxidation of [Bu_4N][**1a**] leads to the formation of a novel copper(III)-phenolate complex rather than a copper(II)-phenoxyl species (Scheme 5.1).

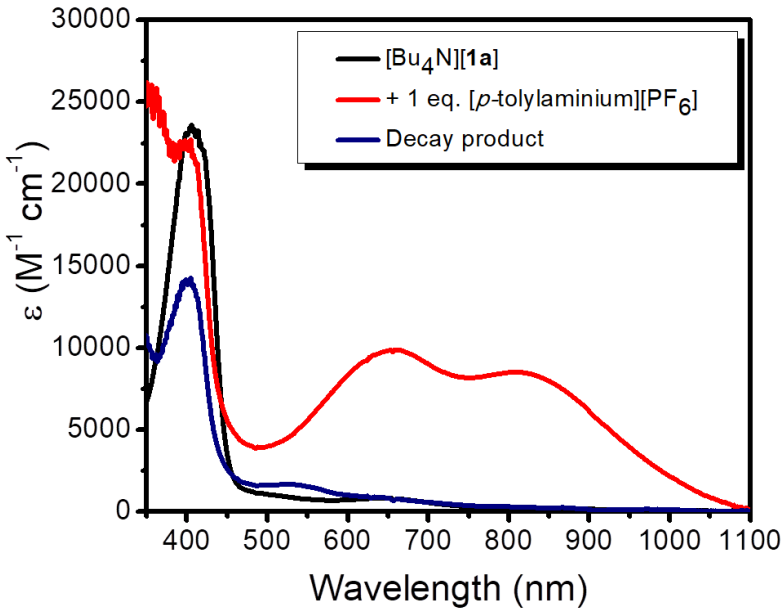

Figure 5.9. UV-Vis absorption spectra for the one-electron oxidation of $[Bu_4N]$[**1a**] in THF at -80 °C to yield [**1a**], where black trace represents the starting compound, red trace represents the oxidation product and navy trace represents the decay product.

5.3.1.2 One-electron oxidation of $[Et_4N]$[**1b-c**]

The chemical oxidations of $[Et_4N]$[**1b-c**] were also monitored using UV-Vis absorption spectroscopy in THF solvent at -80 °C (Figure 5.10). In a typical experiment, 0.1 mM solutions of $[Et_4N]$[**1b-c**] in THF solvent prepared inside the glove-box were cooled to -80 °C inside a UV-vis cuvette, after which 1eq of oxidant ($[AcFc][BAr^F_4]$ in the case of $[Et_4N]$[**1b**] and $[Fc][BAr^F_4]$ in the case of $[Et_4N]$[**1c**]) was added. In both cases, the immediate appearance of multiple intense charge transfer features was observed in the visible and near IR region. In the case of **1b**, absorption features are observed at 462 nm ($\varepsilon = 6{,}400\ M^{-1}\ cm^{-1}$), 625 nm ($\varepsilon = 12{,}300\ M^{-1}\ cm^{-1}$), 732 nm ($\varepsilon = 14{,}000\ M^{-1}\ cm^{-1}$) and 842 nm ($\varepsilon = 16{,}300\ M^{-1}\ cm^{-1}$). The generated species is moderately stable at -80 °C ($t_{1/2}$ ~ 30 min), but decays rapidly upon warming to higher temperatures. The generated species for $[Et_4N]$[**1c**] is less stable and decays rapidly even at -80 °C ($t_{1/2}$ ~ 25 s). The absorption features for **1c** are observed at 442 nm ($\varepsilon = 5{,}800\ M^{-1}\ cm^{-1}$), 575 nm ($\varepsilon = 7{,}900\ M^{-1}\ cm^{-1}$), 637 nm ($\varepsilon = 7{,}500\ M^{-1}\ cm^{-1}$), and 878 nm

($\varepsilon = 18{,}400\ M^{-1}\ cm^{-1}$). The observed instability for **1b** and **1c** is also in agreement with the observed irreversibility in the cyclic voltammograms.

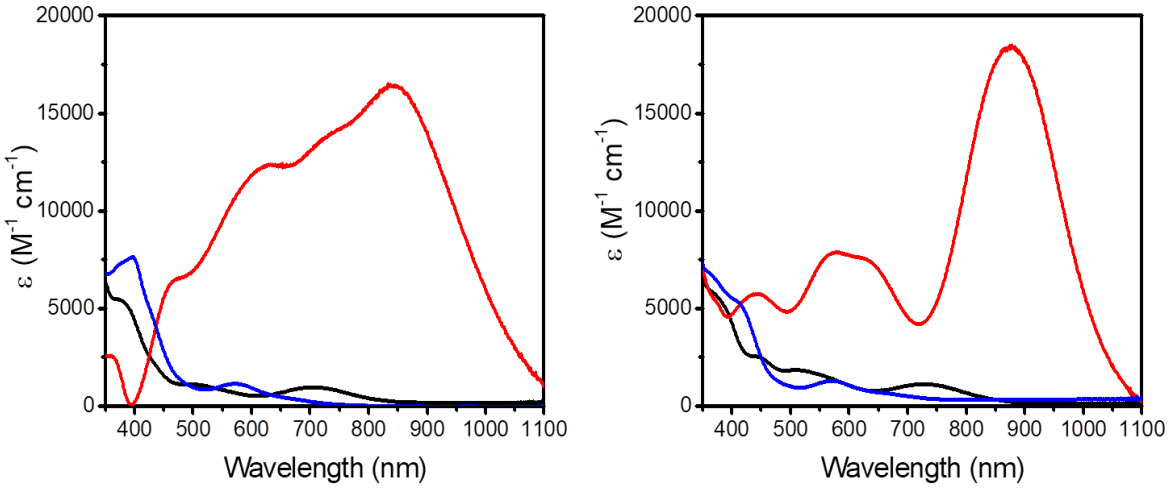

Figure 5.10. (Left) UV-Vis absorption spectra for the one-electron oxidation of [Et_4N][**1b**] in THF at -80 °C to yield [**1b**]. (Right) UV-Vis absorption spectra for the one-electron oxidation of [Et_4N][**1c**] in THF at -80 °C to yield [**1c**]; In both cases, the black trace represents the starting compound, red trace represents the oxidation product and blue trace represents the decay product.

It is worth noting here that while both **1b** and **1c** possess intense LMCT features generally associated with the putative generation of copper(III)-species, in both cases charge transfer features are also present in the ~400-500 nm range, which are generally diagnostic absorption fetaures for the formation of copper(II)-phenoxyl type intermediates.[74a,91,98] Thus, in these cases, the conclusions from UV-vis absoprtion spectroscopy are ambiguous, perhaps suggesting the possibility of both copper(III)-phenolate and copper(II)-phenoxyl species being present. In this regard, it is worth noting that a temperature dependent valence tautomerism between a copper(III)-phenolate and copper(II)-phenoxyl has previously been proposed in the literature.[94] Unfortunately, attempts to explore this possibility for [**1b-c**] have thus far been unsuccessful owing to the thermal instability of the oxidized species.

5.3.1.3 One-electron oxidation of [Bu_4N][**1d**]

The one-electron oxidation of [Bu_4N][**1d**] in THF solvent at -80 °C, was also monitored suing UV-Vis absorption spectroscopy by treating a 0.1 mM solution of [Bu_4N][**1d**] prepared inside the glove-box with 1 eq of [Fc][BAr^F_4]. Upon oxidation, charge transfer transitions appear (Figure 5.11) with features at 390 nm ($\varepsilon = 10{,}000\ M^{-1}\ cm^{-1}$), 500 nm ($\varepsilon = 5{,}800\ M^{-1}\ cm^{-1}$), and 710 nm ($\varepsilon = 8{,}900\ M^{-1}\ cm^{-1}$). In contrast to [**1a-c**], the most intense absorption features for [**1d**] are observed at significantly lower wavelengths and are more in line with well documented absorption features for metal-phenoxyl type species.[91,94,98]

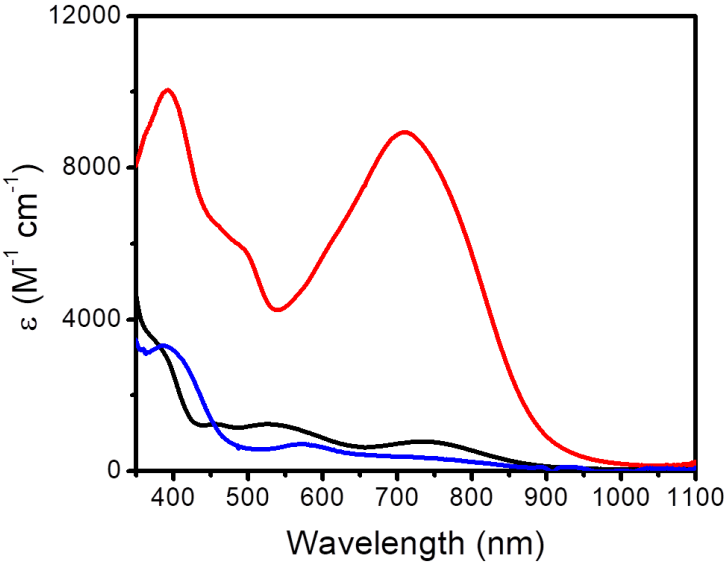

Figure 5.11. UV-Vis absorption spectra for the one-electron oxidation of [Bu_4N][**1d**] in THF at -80 °C to yield [**1d**], where the black trace represents the starting compound, red trace represents the oxidation product and blue trace represents the decay product.

For example, Figure 5.12 (adapted with permission from Ref 98a) shows the UV-Vis absorption spectra for a reported mononuclear copper(II)-phenolate complex, [$L^{tbu2}Cu(CH_3CN)$]OTf, using a triazacyclononane (TACN) based ligand framework.[98a] The one-electron oxidized version of this complex, described as a copper(II)-phenoxyl species, displays charge transfer features in the 400 nm region, very similar to that for **1d**. Additionally, **1d** is significantly more stable in comparison to the other analogs, even at

room temperature ($t_{1/2}$ ~ 6 h). This is line with literature proposals of enhanced stability of copper(II)-phenoxyl species with electron donating substituents on the phenolate ring.[71] It has been suggested that the increased stability is a consequence of the stabilization of the hole on the ligand (phenolate moiety) as a result of the electron donating substituent.[74a] All of these results imply that the intrinsic nature of the oxidation product in the case of **1d** is distinct from those for **1a-c**, and we hypothesize that **1d** is best described as being a copper(II)-phenoxyl species. This notion is rationalized by the fact that the coordinated phenolate ligand in [Bu_4N][**1d**] is extremely electron rich, such that oxidation is most likely to happen at the coordinated phenolate and not on the copper center.

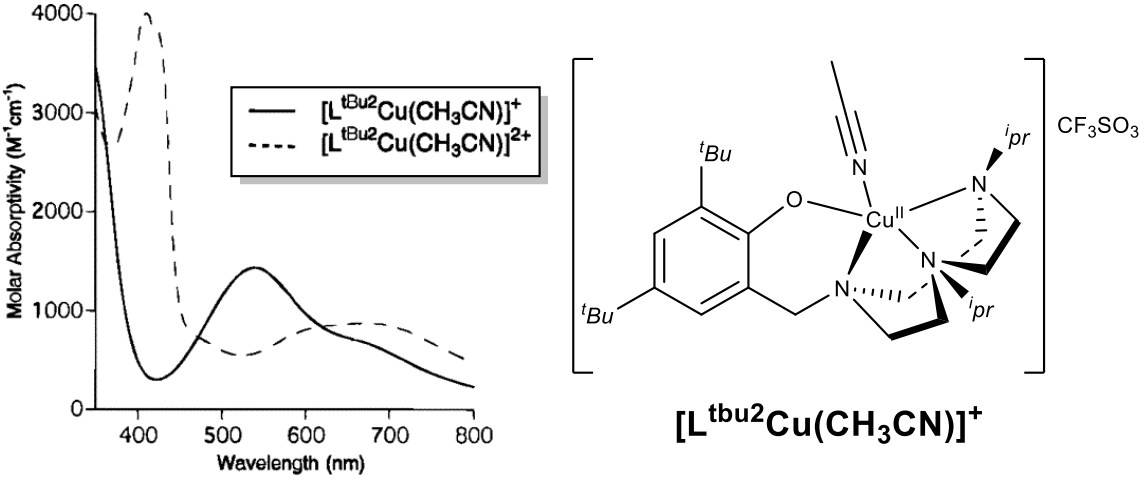

Figure 5.12. UV-vis absorption spectra for copper(II)-phenolate (solid line) and copper(II)-phenoxyl (dashed line) for a TACN based ligand framework. Adapted with permission from Ref 98a.

5.3.2 EPR spectroscopy

The X-band EPR spectra for the one-electron oxidized complexes for [R'$_4$N**][1a-d**] do not display a signal in both perpendicular and parallel mode at 30 K, except for less than 5% of a Cu(II) signal (based on spin integration of the starting copper(II)-complexes). The observation of EPR silence agrees with previous reports for the copper(III)-hydroxide and formally copper(III)-alkylperoxide complexes supported by the pyridine di-carboxamide ligand framework.[8,14,96] This finding is consistent with either

(1) a $S = 0$ ground state indicating a copper(III)-phenolate species or antiferromagnetic coupling between Cu(II) and a phenoxyl radical, or (2) a $S = 1$ ground state achieved by ferromagnetic coupling between the copper and ligand radical electron.[92,99]

5.3.3 Resonance Raman spectroscopy

The Resonance Raman spectroscopy of the complexes was explored in collaboration with Nicole Gagnon, the details of which will be discussed in her Ph.D. Thesis. In this section, I will summarize the key findings from these experiments with the aim of elucidating how these findings lead to the unambiguous determination of the center of oxidation for the one-electron oxidized species.

It is well documented in the literature that copper(II)-phenoxyl complexes have a diagnostic C-O stretch in the 1400-1500 cm^{-1} range,[91,98] while copper(II)-phenolate complexes have the corresponding stretch in the 1250-1290 cm^{-1} range.[100] The higher energy for the former has been attributed to the development of partial C-O double bond character in the phenoxyl radical. For example, the C-O stretching frequency for the Cu-tyrosyl radical in the active site of galactose oxidase is 1487 cm^{-1}.[101] Based on literature precedent, we hypothesized that examination of the vibrational spectroscopic data for the copper(II)-phenolate complexes and their one-electron oxidized counterparts would enable unambiguous identification of the latter as either copper(III)-phenolate or copper(II)-phenoxyl species. We focused on [Bu_4N][**1a**] and [Bu_4N][**1d**], the two extremities within the series, to avoid possible ambiguities associated with the possible presence of both types of species for the oxidized forms of **1b** and **1c**. The Resonance Raman spectra of [Bu_4N][**1a**] and [Bu_4N][**1d**] and their corresponding one-electron oxidized counterparts are shown in Figure 5.13 and the key vibrations and their proposed assignments are summarized in Table 5.5.

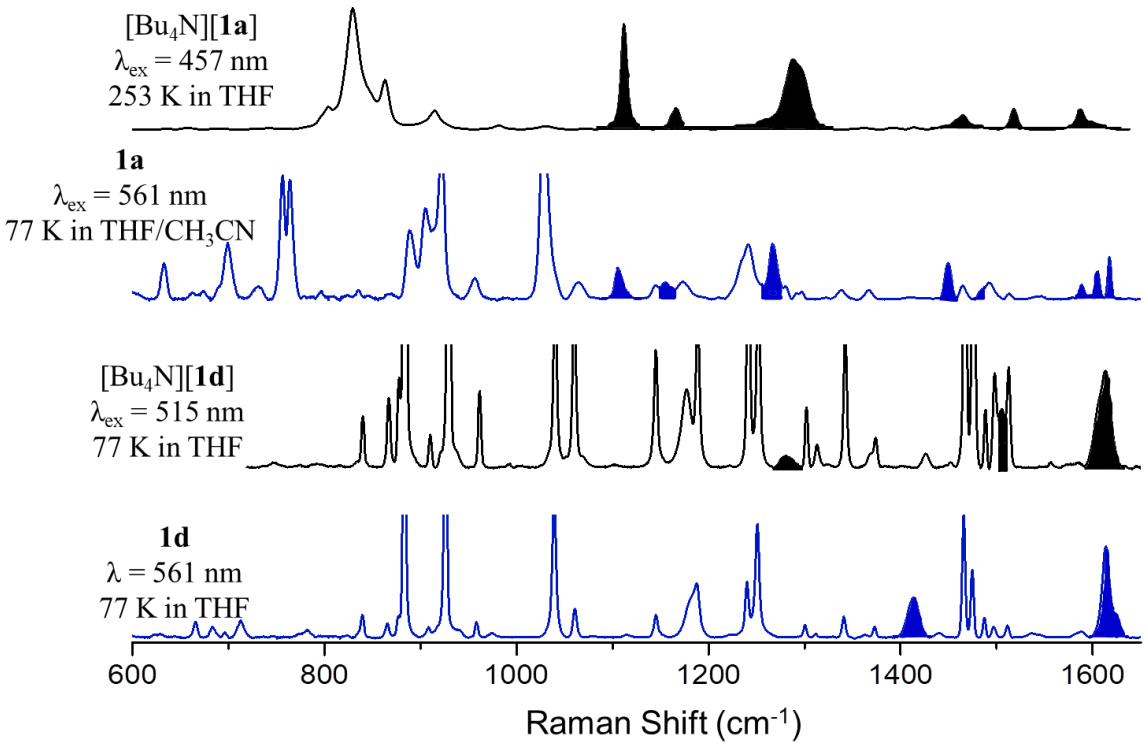

Figure 5.13. Resonance Raman spectra of [Bu_4N][**1a**], **1a**, [Bu_4N][**1d**] and **1d** with the relevant stretching frequencies highlighted (all samples are recorded at 5mM concentration).

Table 5.5. Relevant vibrational frequencies in the Resonance Raman spectra (in cm^{-1}) and the proposed assignments for the corresponding vibrations.

[Bu_4N][**1a**]	**1a**	[Bu_4N][**1d**]	**1d**	**Proposed assignment**
1112, 1166	1107, 1156	-	-	C-H bend
1288	1266	1280	1413	C-O stretch
1465, 1518, 1586, 1597	1449, 1486, 1588, 1604	1505, 1614	1614, 1660	C-C stretch
-	634	-	-	Cu-O stretch

As evident from Figure 5.12 and Table 5.5, the resonance Raman spectra for the copper(II)-phenoate complexes contain multiple stretches in the 1450-1600 cm^{-1} range, corresponding to C-C vibrations in the coordinated phenolate that undergo resonance enhancement.[100] The tentative assignment for the C-O stretch for [Bu_4N][**1d**] is at 1280 cm^{-1}. Upon one-electron oxidation of [Bu_4N][**1d**], this feature disappears and a new

vibration is observed at 1413 cm^{-1}, which is consistent with the formation of a copper(II)-phenoxyl species. This finding indicates that in the case of the copper(II)-phenolate complex with the *para*-NMe_2 substituent, one-electron oxidation leads to the generation of a copper(II)-phenoxyl species. In the case of [Bu_4N][**1a**], the putative C-O stretch is proposed to be at 1288 cm^{-1}. Interestingly, in this case, one-electron oxidation does not lead to the observable growth of any new vibration in the 1400 cm^{-1} range. All the vibrations in this region are conserved from the starting compound, which is indicative of only subtle alterations in the C-C stretches of the phenolate moiety upon oxidation. The absence of any new feature clearly argues against formation of a phenoxyl species upon oxidation. Additionally, the C-O stretch (previously at 1288 cm^{-1} for [Bu_4N][**1a**]), is conserved and is only shifted to a slightly lower frequency of 1266 cm^{-1}. This result indicates that the C-O bond is relatively unperturbed compared to the copper(II)-phenolate **1a**. We propose that the slight decrease in bond order is a consequence of the phenolate being coordinated to Cu(III) instead of Cu(II). Also, we note the appearance of a new feature at at 635 cm^{-1} which we tentatively assign as a Cu(III)-O(phenolate) stretch on the basis of its similarity to the Cu-O stretch of 630 cm^{-1} for the copper(III)-hydroxide species.[58] All of these results support the notion that one-electron oxidation of the copper(II)-phenolate complex bearing the electron withdrawing *para*-NO_2 substituent leads to the formation of a copper(III)-phenolate species.

5.4 Summary and conclusions

A series of analogous copper(II)-phenolate complexes, [$Cu(^{X}OAr)]^{+}$, differing only with respect to the nature of the *para*-substituent on the phenolic moiety have been synthesized and spectroscopically characterized. Examination of the spectroscopic characteristics of the copper(II)-precursors reveals interesting trends in multiple spectroscopic properties. The spectroscopic properties of the corresponding one-electron oxidized complexes also were examined. Importantly, it was demonstrated that tuning the

nature of the phenolate causes a modulation in the behavior of the oxidized complexes with respect to the center of oxidation. In the case of the copper(II)-phenolate bearing the electron withdrawing *para*-NO_2 substituent, cyclic voltammetry experiments reveal that the one-electron redox potential of the $[Cu(^{NO2}OAr)]^{2+}/[Cu(^{NO2}OAr)]^{+}$ couple is *lower* than the one-electron redox potential of the $[^{NO2}OAr]^{\bullet}/[^{NO2}OAr]^{-}$ pair, thus suggesting that the center of oxidation has shifted to the metal. This is corroborated by UV-vis and resonance Raman spectroscopy, where the spectrum of the $[Cu(^{NO2}OAr)]^{2+}$ complex depicts signatures distinct from the other analogs in the series which resemble reported copper(II)-phenoxyl complexes. Particularly noteworthy is the absence of the C-O phenoxyl stretch in the resonance Raman spectrum for the $[Cu(^{NO2}OAr)]^{2+}$ moiety, which indicates that the one-electron oxidized copper(II)-phenolate is a copper(III)-phenolate complex and *not* a copper(II)-phenoxyl unit. In summary, for the electron donating phenolate ligands the oxidized complexes are best described as "copper(II)-phenoxyl" species, while for electron withdrawing phenols, the more accurate description of the corresponding oxidized complex is a "copper(III)-phenolate". These results show that it is possible to tune the center of oxidation by merely altering the electronic nature of the phenolate in a series of closely related complexes. Further work is currently underway to buttress this argument using other spectroscopic methods like X-ray Absorption spectroscopy (in collaboration with the group of Prof. Serena DeBeer) and theoretical calculations.

5.5 Experimental section

Materials and Methods. All reagents and solvents were purchased from commercial sources and used as received unless otherwise noted. Tetrahydrofuran (THF) and diethyl ether was passed through solvent purification columns containing activated alumina and used directly (Glass Contour, Laguna, California). Acetonitrile and dichloromethane were dried over calcium hydride and vacuum distilled.. All solvents

were stored over 3 Å molecular sieves in a N_2 filled glove-box prior to use. All samples for kinetic measurements were prepared in a Vacuum Atmospheres glove-box under an inert atmosphere of nitrogen. Elemental analyses were performed by Robertson Microlit Laboratory (Ledgewood, NJ). UV-vis spectra were obtained using an HP8453 (190-1100) diode array spectrophotometer. Variable temperature UV-vis experiments were performed using a Unisoku low temperature cell holder. Cyclic voltammograms were recorded using an EC Epsilon potentiostat from BASi, a glassy-carbon working electrode or Platinum working electrode, and a Ag^+/Ag reference electrode; they were referenced internally using decamethylferrocene. The final potentials were then converted vs. the standard Fc^+/Fc couple using standard conversion factors.[51] X-ray diffraction measurements were collected with Cu Kα radiation or Mo Kα source and a Bruker D8 Photon II CPAD diffractometer using normal parabolic mirrors as monochromators. EPR spectra were recorded on a CW X-band Elexsys E500 EPR spectrometer equipped with an Oxford ESR 910 liquid helium cryostat. All spectra were recorded at a temperature of 30 K at a microwave frequency of 9.64 GHz under the following conditions: microwave power of 0.063 mW (30 K); modulation amplitude of 9.8 G; modulation frequency of 100 kHz. Chemical shifts (δ) for ^1H and ^{13}C NMR spectra were referenced to residual protium in the deuterated solvent (^1H) or the characteristic solvent resonances of the solvent nuclei (^{13}C). The ligand H_2L and the corresponding metal complexes $[Bu_4N][LCuOH]$ and LCu(MeCN) were synthesized using previously reported procedures.[8] The compounds $(p\text{-tolyl})_3NPF_6$,[63] and *p*-dimethylaminophenol[89] were synthesized using previously reported procedures.

Synthesis of $[Bu_4N][^{NO2}ArO]$. *4*-$NO_2C_6H_4OH$ (0.695 g, 5.00 mmol) was dissolved in anhydrous Et_2O (5 mL) and to this a solution of Bu_4NOH in MeOH (1.0 M, 5.0 mL, 5.0 mmol) was added. The yellow solution was stirred at room temperature for 30 min, after which the solvents were removed *in vacuo*. The resulting bright yellow solid was then suspended in anhydrous Et_2O (20 mL) and further stirred for 30 min, after

which the residue was isolated by filtration and washed with excess Et_2O and dried thoroughly (1.62 g, 85.0%). ^{1}H NMR (DMSO-d_6, 400 MHz): δ_H 7.70 (2H, d), 5.87(2H, d), 3.14-3.18(8H, m), 1.49-1.61 (8H, m), 1.31 (8H, m), 0.93 (12H, t) ppm. $^{13}C\{^1H\}$ NMR (DMSO-d_6, 100 MHz): δ_C 127.51, 119.37, 57.51, 23.05, 19.20, 13.48 ppm. HR-MS (ESI, MeOH) *m/z*: Calcd. for $[C_6H_4NO_3]^-$ 138.019; found 123.021.

Synthesis of [Et$_4$N][^{OMe}ArO]. *4*-$CH_3OC_6H_4OH$ (0.540 g, 4.35 mmol) was dissolved in anhydrous degassed acetone (20 mL) taken in a Schlenk flask and to this a solution of degassed Et_4NOH in water (1.40 M, 3.10 mL, 4.34 mmol) was added and the contents were stirred under an atmosphere of Ar(g) for 30 min. Removal of the solvents from the reaction mixture yielded a brown oily residue. This residue was then taken up in anhydrous degassed acetone (5 mL) and the solvents were removed *in vacuo* while heating to 70 °C to give a yellowish solid. The solid was then triturated with degassed anhydrous Et_2O (10 mL) under an atmosphere of Ar(g), after which the supernatant yellow solution was decanted. This procedure was repeated twice and the residual solid was isolated by filtration, washed with copious amounts of Et_2O and dried thoroughly to yield an off-white solid (0.370 g, 33.5%). ^{1}H NMR (DMSO-d_6, 400 MHz): δ_H 6.48 (2H, d), 6.29 (2H, d), 3.55 (3H, s), 3.15 (8H, q), 1.12 (12H, t) ppm. $^{13}C\{^1H\}$ NMR (DMSO-d_6, 100 MHz): δ_C 162.04, 146.98, 117.37, 114.77, 55.92, 51.49, 7.12 ppm. HR-MS (ESI, MeOH) *m/z*: Calcd. for $[C_7H_7O_2]^-$ 123.045; found 123.041.

Synthesis of [Et$_4$N][^{H}ArO]. This compound was synthesized using a modified vesrion of a previously reported procedure.[102] C_6H_5OH (0.404 g, 4.30 mmol) was dissolved in anhydrous degassed acetone (15 mL) taken in a schlenk flask and to this a solution of degassed Et_4NOH in water (1.40 M, 3.10 mL, 4.34 mmol) was added and the contents were stirred under an atmosphere of Ar(g) for 30 min. Removal of the solvents from the reaction mixture yielded a pale yellow solid. The solid was then triturated with degassed anhydrous Et_2O (20 mL) during which it assumes an off-white color and a fine powdery consistency. The contents are then filtered on a fine frit to isolate an off-white

solid, which is washed thoroughly with Et_2O and dried (0.900 g, 93.8%). ^1H NMR (DMSO-d_6, 400 MHz): δ_H 6.71 (2H, m), 6.15 (2H, d), 5.90 (1H, t), 3.16 (8H, q), 1.13 (12H, t) ppm. $^{13}C\{^1H\}$ NMR (DMSO-d_6, 100 MHz): δ_C 171.17, 128.49, 118.91, 107.70, 51.47, 7.14 ppm. These are similar to the characterization data reported previously.[102]

Synthesis of [Bu_4N][LCu(^{NO2}ArO)]. LCu(MeCN) (0.150 g, 0.255 mmol) and [Bu_4N][^{NO2}ArO] (0.098 g, 0.255 mmol) were suspended in anhydrous Et_2O (15 mL) and stirred for 30 min. After this, anhydrous THF (3 mL) was added to the suspension to facilitate dissolution of all solids and the resulting solution was allowed to stir at room temperature for 12 h. During the course of the reaction an olive green solid precipitated out of the reaction mixture. This solid was isolated by filtration and washed with copious amounts of anhydrous Et_2O and dried thoroughly (0.210 g, 88.7 %). X-ray quality crystals were obtained as green blocks by vapor diffusion of Et_2O into a concentrated solution of the compound in THF. UV-vis (THF, -80 °C) λ_{max}, nm (ε, M^{-1} cm^{-1}): 412 (23,100), 648 (800). Anal. Calcd for $C_{53}H_{77}CuN_5O_5.Et_2O$: C, 68.33; H, 8.75; N, 6.99. Found: C, 68.38; H, 8.66; N, 6.91.

Synthesis of [Et_4N][LCu(^{H}ArO)]. LCu(MeCN) (0.150 g, 0.255 mmol) and [Et_4N][^{H}ArO] (0.057 g, 0.255 mmol) were suspended in anhydrous Et_2O (15 mL) and stirred for 20 min. After this, anhydrous THF (5 mL) was added to the suspension to facilitate dissolution of all solids and the resulting solution was allowed to stir at room temperature for 12 h. During the course of the reaction a brown solid precipitated out of the reaction mixture. This pale-brown solid was isolated by filtration and washed with copious amounts of anhydrous Et_2O and dried thoroughly (0.175 g, 90.0 %). X-ray quality crystals were obtained as brown needles by vapor diffusion of Et_2O into a concentrated solution of the compound in CH_2Cl_2. UV-vis (THF, -80 °C) λ_{max}, nm (ε, M^{-1} cm^{-1}): 372 (5,250), 496 (900), 707 (790). Anal. Calcd for $C_{45}H_{62}CuN_4O_3.Et_2O$: C, 69.68; H, 8.59; N, 6.63. Found: C, 69.32; H, 8.50; N, 6.55.

Synthesis of [Et_4N][LCu(^{OMe}ArO)]. LCu(MeCN) (0.150 g, 0.255 mmol) and [Bu_4N][^{NO2}ArO] (0.065 g, 0.255 mmol) were suspended in anhydrous Et_2O (15 mL) and stirred for 30 min. After this, anhydrous THF (3 mL) was added to the suspension to facilitate dissolution of all solids and the resulting solution was allowed to stir at room temperature for 12 h. During the course of the reaction a dark brown solid precipitated out of the reaction mixture. This solid was isolated by filtration and washed with copious amounts of anhydrous Et_2O and dried thoroughly (0.180 g, 88.0 %). X-ray quality crystals were obtained as brown needles by vapor diffusion of Et_2O into a concentrated solution of the compound in THF. UV-vis (THF, -80 °C) λ_{max}, nm (ε, M^{-1} cm^{-1}): 373 (5,620), 447 (2,430), 518 (1,750), 730 (1,030). Anal. Calcd for $C_{46}H_{64}CuN_4O_3$: C, 69.01; H, 8.06; N, 7.00. Found: C, 68.92; H, 8.06; N, 6.85.

Synthesis of [Bu_4N][LCu(^{NMe2}ArO)]. Solid [Bu_4N][LCuOH] (150 mg, 0.186 mmol) and 38 mg (0.279 mmol) of 4-dimethylamino-phenol was mixed along with activated 3 Å molecular sieves in a 20 mL vial inside a N_2 filled dry box. To this mixture 10 mL of anhydrous THF was added, which resulted in the immediate formation of a deep purple solution. After stirring for 30 min. the reaction mixture was syringe-filtered using a 25 mM diameter, 0.2 µm hydrophobic polytetrafluoroethylene (PTFE) syringe filter, into a separate vial to remove all the molecular sieve particulate. The residual pulverized sieves were rinsed with anhydrous THF (3 x 2 mL) to extract all adhered compound and the resulting solution was syringe-filtered analogously and combined with the original filtrate. The combined solution was then concentrated *in vacuo* to ~ 2 mL and to the resulting solution excess diethyl ether (Et_2O, ~ 15 mL) was added and the mixture was stirred vigorously. The fine solid that precipitated out was isolated by filtration on a fine-pore size frit and washed with copious amounts of Et_2O and dried thoroughly to yield a deep purple colored solid (155 mg, 90 %). X-ray quality crystals were obtained by layering of pentane on a saturated THF solution of the complex inside the freezer at -20 °C. UV-vis (THF, -80 °C) λ_{max}, nm (ε, M^{-1} cm^{-1}): 377 (4,660), 456 (1,750), 526 (1,690),

735 (1,040). HR-MS (ESI, MeCN) *m/z*: Calcd. for $[C_{39}H_{47}CuN_4O_3]^-$ 682.294; found 682.187.

References

1. (a) Punniyamurthy, T.; Velusamy, S.; Iqbal, J. Recent Advances in Transition Metal Catalyzed Oxidation of Organic Substrates with Molecular Oxygen. *Chem. Rev.* **2005,** *105*, 2329-2364. (b) Newhouse, T.; Baran, P. S. If C-H Bonds Could Talk: Selective C-H Bond Oxidation. *Angew. Chem., Int. Ed.* **2011,** *50*, 3362-3374. (c) Wencel-Delord, J.; Droge, T.; Liu, F.; Glorius, F. Towards mild metal-catalyzed C-H bond activation. *Chem. Soc. Rev.* **2011,** *40*, 4740-4761. (d) Yee, G. M.; Tolman, W. B. Transition Metal Complexes and the Activation of Dioxygen. In *Sustaining Life on Planet Earth: Metalloenzymes Mastering Dioxygen and Other Chewy Gases*; Kroneck, P. M. H., Sosa Torres, M. E., Sigel, A., Sigel, H., Sigel, R. K. O., Eds.; Metal Ions in Life Sciences Series; Springer: Cham, Switzerland, 2015; Vol. 15, pp 131-204. (e) Arakawa, H.; Aresta, M.; Armor, J. N.; Barteau, M. A.; Beckman, E. J.; Bell, A. T.; Bercaw, J. E.; Creutz, C.; Dinjus, E.; Dixon, D. A.; et al. Catalysis Research of Relevance to Carbon Management: Progress, Challenges, and Opportunities. *Chem. Rev.* **2001**, *101*, 953-996.
2. (a) Holm, R. H.; Kennepohl, P.; Solomon, E. I. Structural and Functional Aspects of Metal Sites in Biology. *Chem. Rev.* **1996**, *96*, 2239-2314. (b) Meunier, B. *Biomimetic Oxidations Catalyzed by Transition Metal Complexes*; Imperial College Press: London, 2000. (c) Balcells, D.; Clot, E.; Eisenstein, O. C-H Bond Activation in Transition Metal Species from a Computational Perspective. *Chem. Rev.* **2010**, *110*, 749-823. (c) Gunay, A.; Theopold, K. H. C-H bond Activations by Metal Oxo Compounds. *Chem. Rev.* **2010**, *110*, 1061-1081. (d) Lewis, J. C. Artificial Metalloenzymes and Metallopeptide Catalysts for Organic Synthesis. *ACS Catal.* 2013, *3*, 2954-2975. (e) Que, L., Jr.; Tolman, W. B. Biologically inspired oxidation catalysis. *Nature* **2008**, *455*, 333–340. (f) Martell, A. E.;

Sawyer, D. T.; *Oxygen Complexes and Oxygen Activation by Transition Metals*.; Plenum: New York, 1988.

3. (a) Ray, K.; Heims, F.; Schwalbe, M.; Nam, W. High-Valent Metal-Oxo Intermediates in Energy Demanding Processes: From Dioxygen Reduction to Water Splitting. *Curr. Opin. Chem. Biol.* **2015,** *25*, 159-171. (b) Engelmann, X.; Monte-Perez, I.; Ray, K. Oxidation Reactions with Bioinspired Mononuclear Non-Heme Metal-oxo complexes. *Angew. Chem. Int. Ed.* **2016**, *55*,7632 -7649. (c) Decker, A.; Solomon, E. I. Dioxygen Activation by Copper, Heme and Non-Heme Iron Enzymes: Comparison of Electronic Structures and Reactivities. *Curr. Opin. Chem. Biol.* **2005,** *9*, 152-163.

4. (a) Solomon, E. I.; Heppner, D. E.; Johnston, E. M.; Ginsbach, J. W.; Cirera, J.; Qayyum, M.; Kieber-Emmons, M. T.; Kjaergaard, C. H.; Hadt, R. G.; Tian, L. Copper Active Sites in Biology. *Chem. Rev.* **2014,** *114*, 3659-3853. (b) Solomon, E. I.; Sarangi, R.; Woertink, J. S.; Augustine, A. J.; Yoon, J.; Ghosh, S. O_2 and N_2O Activation by Bi-, Tri-, and Tetranuclear Cu Clusters in Biology. *Acc. Chem. Res.* **2007,** *40*, 581-591.

5. (a) Ali, M. E.; Rahman, M. M.; Sarkar, S. M.; Hamid, S. B. A. Heterogeneous Metal Catalysts for Oxidation Reactions. *J. Nanomaterials* **2014,** *2014*, 1-23. (b) Ren, Y.; Wang, M.; Chen, X.; Yue, B.; He, H. Heterogeneous Catalysis of Polyoxometalate Based Organic–Inorganic Hybrids. *Materials* **2015,** *8*, 1545-1567. (c) van der Vlugt, J. I.; Meyer, F. Homogeneous Copper-Catalyzed Oxidations. In *Organometallic Oxidation Catalysis*; Meyer, F., Limberg, C., Eds.; Topics in Organometallic Chemistry Series; Springer-Verlag: Berlin, 2007**;** Vol. 22, pp 191-240. (d) Allen, S. E.; Walvoord, R. R.; Padilla-Salinas, R.; Kozlowski,

M. C. Aerobic Copper-Catalyzed Organic Reactions. *Chem. Rev.* **2013,** *113*, 6234-6458.

6. (a) Hematian, S.; Garcia-Bosch, I.; Karlin, K. D. Synthetic Heme/Copper Assemblies: Toward an Understanding of Cytochrome *c* Oxidase Interactions with Dioxygen and Nitrogen Oxides. *Acc. Chem. Res.* **2015,** *48*, 2462-2474. (b) Thorseth, M. A.; Tornow, C. E.; Tse, E. C. M.; Gewirth, A. A., Cu Complexes that Catalyze the Oxygen Reduction Reaction. *Coord. Chem. Rev.* **2013**, *257*, 130-139.

7. (a) Elwell, C. E.; Gagnon, N. L.; Neisen, B. D.; Dhar, D.; Spaeth, A. D.; Yee, G.M.; Tolman, W. B. Copper-Oxygen Complexes Revisited: Structures, Spectroscopy, and Reactivity. *Chem. Rev.*, **2017**, *117*, 2059-2107. (b) Mirica, L. M.; Ottenwaelder, X.; Stack, T. D. P. Structure and Spectroscopy of Copper−Dioxygen Complexes. *Chem. Rev.* **2004,** *104*, 1013-1046. (c) Lewis, E. A.; Tolman, W. B. Reactivity of Dioxygen−Copper Systems. *Chem. Rev.* **2004,** *104*, 1047-1076. (d) Tolman, W. B. Using Synthetic Chemistry to Understand Copper Protein Active Sites: A Personal Perspective. *J. Biol. Inorg. Chem.* **2006,** *11*, 261-271. (d) *Copper-Oxygen Chemistry;* Karlin, K. D.; Itoh, S.; Rokita, S., Eds.; Wiley Series of Reactive Intermediates in Chemistry and Biology; John Wiley & Sons, Inc.: Hoboken, NJ, 2011; Vol. 4. (e) Solomon, E. I.; Ginsbach, J. W.; Heppner, D. E.; Kieber-Emmons, M. T.; Kjaergaard, C. H.; Smeets, P. J.; Tian, L.; Woertink, J. S. Copper Dioxygen (Bio)inorganic Chemistry. *Faraday Discuss.* **2011,** *148*, 11-39. (f) Haack, P.; Limberg, C. Molecular Cu^{II}-O-Cu^{II} Complexes: Still Waters Run Deep. *Angew. Chem., Int. Ed.* **2014,** *53*, 4282-4293. (g) Gagnon, N.; Tolman, W. B. $[CuO]^{+}$ and $[CuOH]^{2+}$ Complexes: Intermediates in Oxidation Catalysis? *Acc. Chem. Res.* **2015,** *48*, 2126-2131. (h) Lee, J. Y.; Karlin, K. D. Elaboration of Copper–Oxygen Mediated C–H Activation

Chemistry in Consideration of Future Fuel and Feedstock Generation. *Curr. Opin. Chem. Biol.* **2015,** *25*, 184-193. (i) Serrano-Plana, J.; Garcia-Bosch, I.; Company, A.; Costas, M. Structural and Reactivity Models for Copper Oxygenases: Cooperative Effects and Novel Reactivities. *Acc. Chem. Res.* **2015**, *48*, 2397-2406.

8. Donoghue, P. J.; Tehranchi, J.; Cramer, C. J.; Sarangi, R.; Solomon, E. I.; Tolman, W. B. Rapid C–H Bond Activation by a Monocopper(III)–Hydroxide Complex. *J. Am. Chem. Soc.* **2011,** *133*, 17602-17605.

9. (a) Nam, W. High-Valent(IV)-Oxo Complexes of Heme and Non-Heme Ligands in Oxygenation Reactions. *Acc. Chem. Res.*, **2007**, *40*, 522-531. (b) Krebs, C.; Fujimori, D. G.; Walsh, C. T.; Bollinger, J. M. Jr. Non-heme Fe(IV)-Oxo intermediates. *Acc. Chem. Res.* **2007**, *40*, 484-492. (c) Costas, M.; Mehn, M. P.; Jensen, M. P.; Que, L. Dioxygen activation at mononuclear nonheme iron active sites: enzymes, models, and intermediates. *Chem. Rev.* **2004**, *104*, 939-986. (d) Fujii, H. Electronic structure and reactivity of high-valent oxo iron porphyrins. *Coord. Chem. Rev.* **2002**, *226*, 51-60. (e) Groves, J. T. High-valent iron in chemical and biological oxidations. *J. Inorg. Biochem.* **2006**, *100*, 434-447. (f) McDonald, A. R.; Que, L., Jr. High-Valent Nonheme Iron-Oxo Complexes: Synthesis, Structure, and Spectroscopy. *Coord. Chem. Rev.* **2013**, *257*, 414-428. (g) Que, L., Jr. The road to non-heme oxoferryls and beyond. Acc. Chem. Res. **2007**,*40*, 493-500. (h) Borovik, A. S.; Zart, M. K.; Zinn, P. J. in *Activation of Small Molecules: Organometallic and Bioinorganic Perspectives*, ed. W. B. Tolman, Wiley-VCH, Weinheim, 2006, p. 187. (i) Borovik, A. S. Role of Metal–Oxo Complexes in the Cleavage of C-H bonds. *Chem. Soc. Rev.* **2011**, *40*, 1870–1874.

10 . (a) Kamachi, T.; Kihara, N.; Shiota, Y.; Yoshizawa, K. Computational Exploration of the Catalytic Mechanism of Dopamine β-Monooxygenase: Modeling of Its Mononuclear Copper Active Sites. *Inorg. Chem.* **2005,** *44*, 4226-4236. (b) Yoshizawa, K.; Kihara, N.; Kamachi, T.; Shiota, Y. Catalytic Mechanism of Dopamine β-Monooxygenase Mediated by Cu(III)-Oxo. *Inorg. Chem.* **2006,** *45*, 3034-3041. (c) Gherman, B. F.; Heppner, D. E.; Tolman, W. B.; Cramer, C. J. Models for Dioxygen Activation by the Cu_B Site of Dopamine *β*-Monooxygenase and Peptidylglycine *α*-Hydroxylating Monooxygenase. *J. Biol. Inorg. Chem.* **2006,** *11*, 197-205. (d) Huber, S. M.; Ertem, M. Z.; Aquilante, F.; Gagliardi, L.; Tolman, W. B.; Cramer, C. J. Generating Cu^{II}-Oxyl/Cu^{III}-Oxo Species from Cu^{I}-α-Ketocarboxylate Complexes and O_2: In Silico Studies on Ligand Effects and C-H-Activation Reactivity. *Chem.—Eur. J.* **2009,** *15*, 4886-4895. (e) Rijs, N. J.; González-Navarrete, P.; Schlangen, M.; Schwarz, H. Penetrating the Elusive Mechanism of Copper-Mediated Fluoromethylation in the Presence of Oxygen through the Gas-Phase Reactivity of Well-Defined $[LCuO]^+$ Complexes with Fluoromethanes ($CH_{(4-n)}F_n$, n = 1-3). *J. Am. Chem. Soc.* **2016,** *138*, 3125-3135.

11. (a) Kim, S.; Ståhlberg, J.; Sandgren, M.; Paton, R. S.; Beckham, G. T. Quantum Mechanical Calculations Suggest that Lytic Polysaccharide Monooxygenases Use a Copper-Oxyl, Oxygen-Rebound Mechanism. *Proc. Natl. Acad. Sci. U. S. A.* **2014,** *111*, 149-154. (b) Hedegard, E. D.; Ryde, U. Targetting the reactive intermediate in polysaccharide monooxygenase. *J. Biol. Inorg. Chem.* **2017,** *22*, 1029-1037.

12. (a) Rezabal, E.; Gauss, J.; Matxain, J. M.; Berger, R.; Diefenbach, M.; Holthausen, M. C. Quantum Chemical Assessment of the Binding Energy of CuO^+ *J. Chem. Phys.* **2011**, *134*, 064304-1-064304-13. (b) Fiedler, A.; Schröeder, D.; Shaik, S.;

Schwarz, H. Electronic Structures and Gas-Phase Reactivities of Cationic Late-Transition-Metal Oxides. *J. Am. Chem. Soc.* **1994**, *116*, 10734-10741. (c) Schröder, D.; Holthausen, M. C.; Schwarz, H. Radical-Like Activation of Alkanes by the Ligated Copper Oxide Cation (Phenanthroline)CuO^+. *J. Phys. Chem. B.* **2004**, *108*, 14407-14416.(d) Dietl, N.; van der Linde, C.; Schlangen, M.; Beyer, M. K.; Schwarz, H. Diatomic $[CuO]^+$ and Its Role in the Spin-Selective Hydrogen- and Oxygen-Atom Transfers in the Thermal Activation of Methane. *Angew. Chem. Int. Ed.* **2011**, *50*, 4966-4969. (e) Dietl, N.; Schlangen, M.; Schwarz, H. Thermal Hydrogen-Atom Transfer from Methane: The Role of Radicals and Spin States in Oxo-Cluster Chemistry. *Angew. Chem. Int. Ed.* **2012**, *51*, 5544-5555.

13. Dhar, D.; Tolman, W. B. Hydrogen Atom Abstraction from Hydrocarbons by a Copper(III)-Hydroxide Complex. *J. Am. Chem. Soc.* **2015,** *137*, 1322-1329.
14. Dhar, D.; Yee, G. M.; Spaeth, A. D.; Boyce, D. W.; Zhang, H.; Dereli, B.; Cramer, C. J.; Tolman, W. B. Perturbing the Copper(III)-Hydroxide Unit through Ligand Structural Variation. *J. Am. Chem. Soc.* **2016,** *138*, 356-368.
15. Dhar, D.; Yee, G. M.; Markle, T. F., Mayer, J. M.; Tolman, W. B. Reactivity of the Copper(III)-Hydroxide Unit with Phenols *Chem. Sci.* **2017**, *8*, 1075-1085.
16. Warren, J. J.; Tronic, T. A.; Mayer, J. M. Thermochemistry of Proton-Coupled Electron Transfer Reagents and its Implications. *Chem. Rev.* **2010,** *110*, 6961-7001.
17. (a) Huynh, M. H. V.; Meyer, T. J. Proton-coupled electron transfer. *Chem. Rev.* **2007**, *107*, 5004-5064. (b) Weinberg, D. R.; Gagliardi, C. J.; Hull, J. F.; Murphy, C. F.; Kent, C. A.; Westlake, B. C.; Paul, A.; Ess, D. H.; McCafferty, D. G.; Meyer, T. J. Proton-coupled electron transfer. *Chem. Rev.* **2012**, *112*, 4016-4093.

18. (a) *Hydrogen-Transfer Reactions*; Hynes, J. T.;Klinman, J. P.;Limbach, H.-H.;Schowen, R. L., Eds.; Wiley-VCH Verlag GmbH & Co. KGaA, 2006. (b) Costentin, C. Electrochemical Approach to the Mechanistic Study of Proton-Coupled Electron Transfer. *Chem. Rev.* **2008,** *108*, 2145-2179.

19. (a) Meunier, B.; de Visser, S. P.; Shaik, S. Mechanism of oxidation reactions catalyzed by Cytochrome P450 Enzymes *Chem. Re*v. **2004**, *104*, 3947-3980. (b) Shaik, S.; Kumar, D.; de Visser, S. P.; Altun, A.; Theil, W. Theoretical perspective on the Structure and Mechanism of Cytochrome P450 Enzymes *Chem. Re*v. **2005**, *105*, 2279-2328.

20. (a) Bordwell, F. G.; Cheng, J.-P.; Harrelson, J. A., Jr. Homolytic Bond dissociation Energies in solution from equilibrium acidity and electrochemical data. *J. Am. Chem. Soc.* **1988**, *110*, 1229-1231. (b) Wayner, D. M.; Parker, V. D. Bond energies in solution from electrode potentials and thermochemical cycles: A simplified and general approach. *Acc. Chem. Res.* **1993**, *26*, 287-294.

21. Tilset, M. In *Electron Transfer in Chemistry*; Balzani, V., Ed.; Wiley-VCH: Weinheim, Germany, 2001.

22. (a) Mayer, J. M. Proton-coupled electron transfer: A reaction chemist's view. *Annu. Rev. Phys. Chem.* **2004,** *55*, 363-390. (b) Mayer, J. M. Hydrogen Atom Abstraction by Metal-Oxo Complexes: Understanding the Analogy with Organic Radical Reactions. *Acc. Chem. Res.* **1998,** *31*, 441-450. (c) Warren, J. J.; Mayer, J. M. Predicting organic hydrogen atom transfer rate constants using the Marcus cross relation. *Proc. Natl. Acad. Sci. U. S. A.* **2010,** *107*, 5282-5287.

23. (a) Mader, E. A.; Davidson, E. R.; Mayer, J. M. Large Ground-State Entropy Changes for Hydrogen Atom Transfer Reactions of Iron Complexes. *J. Am. Chem. Soc.* **2007,** *129*, 5153-5166. (b) Mader, E. A.; Manner, V. W.; Markle, T.

F.; Wu, A.; Franz, J. A.; Mayer, J. M. Trends in Ground-State Entropies for Transition Metal Based Hydrogen Atom Transfer Reactions. *J. Am. Chem. Soc.* **2009,** *131*, 4335-4345.

24. (a) Bronsted, J. N. Acid and Basic Catalysis. *Chem. Rev.* **1928,** *5*, 231-338. (b) Bell, R. P.; Higginson, W. C. E. The Catalyzed Dehydration of Acetaldehyde Hydrate, and the Effect of Structure on the Velocity of Protolytic Reactions. *Proc. R. Soc. A.* **1949,** *197*, 141-159.

25. (a) Evans, M. G.; Polanyi, M. Further considerations on the thermodynamics of chemical equilibria and reaction rates. *Trans. Faraday Soc.* **1936**, *32*, 1333-1360. (b) Bell, R. P. The Theory of Reactions Involving Proton Transfers. *Proc. R. Soc. A.* **1936**, *154*, 414-429.

26. (a) Mayer, J. M. Understanding Hydrogen Atom Transfer: From Bond Strengths to Marcus Theory. *Acc. Chem. Res.* **2011,** *44*, 36-46. (b) Mayer, J. M. Simple Marcus-Theory-Type Model for Hydrogen-Atom Transfer/Proton-Coupled Electron Transfer. *J. Phys. Chem. Lett.* **2011,** *2*, 1481-1489. (c) Warren, J. J.; Mayer, J. M. Moving protons and electrons in biomimetic systems. *Biochemistry* **2015,** *54*, 1863-1878.

27. (a) Hammes-Schiffer, S. Theory of Proton-Coupled Electron Transfer in Energy Conversion Processes. *Acc. Chem. Res.* **2009,** *42*, 1881-1889. (b) Hammes-Schiffer, S.; Soudackov, A. V. Proton-Coupled Electron Transfer in Solution, Proteins, and Electrochemistry. *J. Phys. Chem. B* **2008,** *112*, 14108-14123. (c) Hammes-Schiffer, S.; Stuchebrukhov, A. A. Theory of Coupled Electron and Proton Transfer Reactions. *Chem. Rev.* **2010,** *110*, 6939-6960. (d) Lai, W.; Li, C.; Chen, H.; Shaik, S. Hydrogen-Abstraction Reactivity Patterns from A to Y: The Valence Bond Way. *Angew. Chem. Int. Ed.* **2012,** *51*, 5556-5578.

28. (a) Mayer, J. M.; Rhile, I. J. Thermodynamics and kinetics of proton-coupled electron transfer: stepwise vs. concerted pathways. *Biochimica et Biophysica Acta*. **2004**, *1655*, 51-58. (b) Roth, J. P.; Mayer, J. M. Hydrogen Transfer Reactivity of a Ferric Bi-imidazoline Complex That Models the Activity of Lipoxygenase Enzymes. *Inorg. Chem.* **1999,** *38*, 2760-2761.

29. Parsell, T. H.; Yang, M. Y.; Borovik, A. S. C–H Bond Cleavage with Reductants: Re-Investigating the Reactivity of Monomeric MnIII/IV-Oxo Complexes and the Role of Oxo Ligand Basicity. *J. Am. Chem. Soc.* **2009**, *131*, 2762–2763.

30. (a) Jung, J.; Kim, S.; Lee, Y.-M.; Nam, W.; Fukuzumi, S. Switchover of the Mechanism between Electron Transfer and Hydrogen-Atom Transfer for a Protonated Manganese(IV)-Oxo Complex by Changing Only the Reaction Temperature. *Angew. Chem., Int. Ed.* **2016,** *55*, 7450-7454. (b) Ohzu, S.; Ishizuka, T.; Kotani, H.; Kojima, T. Reactivity of Ru(III)-hydroxo complex in substrate oxidation in water. *Chem. Commun.* **2014**, *50*, 15018-15021. (c) Morimoto, Y.; Park, J.; Suenobu, T.; Lee, Y.-M.; Nam, W.; Fukuzumi, S. Mechanistic Borderline of One-Step Hydrogen Atom Transfer versus Stepwise Sc^{3+}-Coupled Electron Transfer from Benzyl Alcohol Derivatives to a Non-Heme Iron(IV)-Oxo Complex. *Inorg. Chem.* **2012,** *51*, 10025-10036. (d) Park, J.; Morimoto, Y.; Lee, Y.-M.; Nam, W.; Fukuzumi, S. Proton-Promoted Oxygen Atom Transfer vs. Proton-Coupled Electron Transfer of a Non-Heme Iron(IV)-Oxo Complex. *J. Am. Chem. Soc.* **2012,** *134*, 3903-3911.

31. (a) Glickman, M. H.; Klinman, J. P. Lipoxygenase Reaction Mechanism: Demonstration That Hydrogen Abstraction from Substrate Precedes Dioxygen Binding during Catalytic Turnover. *Biochemistry* **1996,** *35*, 12882-12892. (b) Neidig, M. L.; Wecksler, A. T.; Schenk, G.; Holman, T. R.; Solomon, E. I. Kinetic

and Spectroscopic Studies of N694C Lipoxygenase: A Probe of the Substrate Activation Mechanism of a Nonheme Ferric Enzyme. *J. Am. Chem. Soc.* **2007,** *129*, 7531-7537. (c) Green, M. T.; Dawson, J. H.; Gray, H. B. Oxoiron(IV) in chloroperoxidase compound II is basic: implications for P450 chemistry. *Science* **2004**, *304*, 1653-1656.

32. Cho, K.-B.; Hirao, H.; Shaik, S.; Nam, W. To rebound or dissociate? This is the mechanistic question in C-H hydroxylation by heme and nonheme metal-oxo complexes. *Chem. Soc. Rev.* **2016,** *45*, 1197-1210.

33. (a) Gupta, R.; Borovik, A. S. Monomeric $Mn^{III/II}$ and $Fe^{III/II}$ Complexes with Terminal Hydroxo and Oxo Ligands: Probing Reactivity via O−H Bond Dissociation Energies *J. Am. Chem. Soc.* **2003**, *125*, 13234-13242. (b) Wang, K.; Mayer, J. M. Oxidation of Hydrocarbons by $[(phen)_2Mn(\mu\text{-}O)_2Mn(phen)_2]^{3+}$ via Hydrogen Atom Abstraction. *J. Am. Chem. Soc.* **1997,** *119*, 1470-1471.(c) Goldsmith, C. R.; Stack, T. D. P. Hydrogen Atom Abstraction by a Mononuclear Ferric Hydroxide Complex: Insights into the Reactivity of Lipoxygenase. *Inorganic Chemistry* **2006,** *45*, 6048-6055.(d) Goldsmith, C. R.; Cole, A. P.; Stack, T. D. P. C-H Activation by a Mononuclear Manganese(III) Hydroxide Complex: Synthesis and Characterization of a Manganese-Lipoxygenase Mimic? *J. Am. Chem. Soc.* **2005,** *127*, 9904-9912. (e) Gardner, K. A.; Kuehnert, L. L.; Mayer, J. M. Hydrogen Atom Abstraction by Permanganate: Oxidations of Arylalkanes in Organic Solvents *Inorg. Chem.* **1997**, *36*, 2069-2078. (f) Yin, G.; Danby, A. M.; Kitko, D.; Carter, J. D.; Scheper, W. M.; Busch, D. H. Understanding the Selectivity of a Moderate Oxidation Catalyst: Hydrogen Abstraction by a Fully Characterized, Activated Catalyst, the Robust Dihydroxo Manganese(IV) Complex of a Bridged Cyclam. *J. Am. Chem. Soc.* **2007,** *129*,

1512-1513. (g) Yin, G.; Danby, A. M.; Kitko, D.; Carter, J. D.; Scheper, W. M.; Busch, D. H. Oxidative Reactivity Difference among the Metal Oxo and Metal Hydroxo Moieties: pH Dependent Hydrogen Abstraction by a Manganese(IV) Complex Having Two Hydroxide Ligands *J. Am. Chem* . *Soc.* **2008**, *130*, 16245-16253. (h) Moyer, B. A.; Meyer, T. J. Properties of the oxo/aqua system $(bpy)_2(py)RuO^{2+}/(bpy)_2(py)Ru(OH_2)^{2+}$ *Inorg. Chem.* **1981**, *20*, 436-444. (i) Lebeau, E. L.; Binstead, R. A.; Meyer, T. J. Mechanistic Implications of Proton Transfer Coupled to Electron Transfer *J. Am. Chem. Soc.* **2001**, *123*, 10535-10544. (j) Bryant, J. R.; Mayer, J. M. Oxidation of C−H Bonds by $[(bpy)_2(py)Ru^{IV}O]^{2+}$ Occurs by Hydrogen Atom Abstraction *J. Am. Chem. Soc.* **2003**, *125*, 10351-10361. (k) Goldsmith, C. R.; Jonas, R. T.; Stack, T. D. P. C-H bond activation by a ferric methoxide complex: Modeling the rate-determining step in the mechanism of lipoxygenase. *J. Am. Chem. Soc.* **2002,** *124*, 83-96. (l) Wang, D.; Zhang, M.; Bühlmann, P.; Que, L., Jr. Redox Potential and C−H Bond Cleaving Properties of a Nonheme Fe^{IV}═O Complex in Aqueous Solution *J. Am. Chem. Soc.* **2010**, *132*, 7638-7644. (m) Lansky, D. E.; Goldberg, D. P. Hydrogen Atom Abstraction by a High-Valent Manganese(V)-OxoCorrolazine *Inorg. Chem.* **2006**, *45*, 5119-5125. (n) Sastri, C. V.; Lee, J.; Oh, K.; Lee, Y. J.; Lee, J.; Jackson, T. A.; Ray, K.; Hirao, H.; Shin, W.; Halfen, J. A.; Kim, J.; Que, L.; Shaik, S.; Nam, W. Axial ligand tuning of a nonheme iron(IV)-oxo unit for hydrogen atom abstraction. *Proc. Natl. Acad. Sci. (USA)* **2007**, *104*, 19181-19186. (o) Gao, H.; Groves, J. T. Fast Hydrogen Atom Abstraction by a Hydroxo Iron(III) Porphyrazine. *J. Am. Chem. Soc.* **2017**, *139*, 3938-3941.

34. (a) Espenson, J. H. Chemical Kinetics and Reaction Mechanisms, McGraw-Hill Companies, New York, Second Edition, 2002. (b) Kwart, H. Temperature

dependence of the primary kinetic hydrogen isotope effect as a mechanistic criterion. *Acc. Chem. Res.* **1982**, *15*, 401-408.

35. (a) Kohen, A.; Klinman, J. P. Enzyme Catalysis: Beyond Classical Paradigms. *Acc. Chem. Res.***1998**, *31*, 397-404. (b) Klinman, J. P. Importance of protein dynamics during enzymatic C-H bond cleavage catalysis. *Biochemistry* **2013,** *52*, 2068-2077. (c) Sharma, S. C.; Klinman, J. P. Experimental Evidence for Hydrogen Tunneling when the Isotopic Arrhenius Prefactor (A_H/A_D) is Unity. *J. Am. Chem. Soc.* **2008,** *130*, 17632-17633.

36. (a) Jonsson, T.; Glickman, M. H.; Sun, S.; Klinman, J. P. Experimental Evidence for Extensive Tunneling of Hydrogen in the Lipoxygenase Reaction: Implications for Enzyme Catalysis. *J. Am. Chem. Soc.* **1996**, *118*, 10319-10320. (b) Hu, S.; Sharma, S. C.; Scouras, A. D.; Soudackov, A. V.; Carr, C. A. M.; Hammes-Schiffer, S.; Alber, T.; Klinman, J. P. Extremely elevated room-temperature kinetic isotope effects quantify the critical role of barrier width in enzymatic C-H activation. *J. Am. Chem. Soc.* **2014**, *136*, 8157-8160.

37. (a) Mandal, D.; Ramanan, R.; Usharani, D.; Janardanan, D.; Wang, B.; Shaik, S. How Does Tunneling Contribute to Counterintuitive H-Abstraction Reactivity of Nonheme Fe(IV)O Oxidants with Alkanes? *J. Am. Chem. Soc.* **2015,** *137*, 722-733. (b) Kwon, Y. H.; Mai, B. K.; Lee, Y.-M.; Dhuri, S. N.; Mandal, D.; Cho, K.-B.; Kim, Y.; Shaik, S.; Nam, W. Determination of Spin Inversion Probability, H-Tunneling Correction, and Regioselectivity in the Two-State Reactivity of Nonheme Iron(IV)-Oxo Complexes. *J. Phys. Chem. Lett.* **2015,** *6*, 1472-1476. (c) Mandal, D.; Shaik, S. Interplay of Tunneling, Two-State Reactivity, and Bell–Evans–Polanyi Effects in C–H Activation by Nonheme Fe(IV)O Oxidants. *J. Am. Chem. Soc.* **2016,** *138*, 2094-2097.

38. Hirao, H.; Que, L., Jr.; Nam, W.; Shaik, S. A two-state reactivity rationale for counterintuitive axial ligand effects on the C-H activation reactivity of nonheme Fe^{IV}=O oxidants. *Chem. - Eur. J.* **2008,** *14*, 1740-1756.

39. Cappellani, E. P.; Drouin, S. D.; Jia, G.; Maltby, P. A.; Morris, R. H.; Schweitzer, C. T. Effect of the Ligand and Metal on the pKa Values of the Dihydrogen Ligand in the Series of Complexes [M(H2)H(L)2]+, M = Fe, Ru, Os, Containing Isosteric Ditertiaryphosphine Ligands, L. *J. Am. Chem. Soc.* **1994,** *116*, 3375-3388.

40. Garrido, G.; Koort, E.; Rafols, C.; Bosch, E.; Rodima, T.; Leito, I.; Roses, M. Acid-Base Equilibria in Nonpolar Media. Absolute pKa Scale of Bases in Tetrahydrofuran. *J. Org. Chem.* **2006,** *71*, 9062-9067.

41. Yang, L.; Powell, D. R.; Houser, R. P. Structural variation in copper(i) complexes with pyridylmethylamide ligands: structural analysis with a new four-coordinate geometry index, τ_4. *Dalton Transactions* **2007**, 955-964.

42. DigiSim 3.03b from BASi Analytical instruments.

43. *Handbook of Bond Dissociation Energies in Organic compounds*; Luo, Y., Ed.; CRC Press: New York, USA, 2002, pp. 11-93.

44. (a) Abdur-Rashid, K.; Fong, T. P.; Greaves, B.; Gusev, D. G.; Hinman, J. G.; Landau, S. E.; Lough, A. J.; Morris, R. H. An Acidity Scale for Phosphorus-Containing Compounds Including Metal Hydrides and Dihydrogen Complexes in THF: Toward the Unification of Acidity Scales *J. Am. Chem. Soc.* **2000**, *122*, 9155-9171. (b) Barbosa, J.; Barrón, D.; Bosch, E.; Rosés, M. Resolution of acid strength in tetrahydrofuran of substituted benzoic acids. *Anal. Chim. Acta* **1992**, *265*, 157-165. (c) Barrón, D.; Bosch, E.; Rosés, M. Acid–base behaviour of substituted phenolic substances and resolution of acid strength in tetrahydrofuran *Anal. Chim. Acta* **2000**, *403*, 339-347.

45. (a) Gilson, R.; Durrant, M. C. Estimation of the pKa values of water ligands in transition metal complexes using density functional theory with polarized continuum model solvent corrections. *Dalton Trans.* **2009**, 10223-10230. (b) Coggins, M. K.; Zhang, M.-T.; Chen, Z.; Song, N.; Meyer, T. J. Single-Site Copper(II) Water Oxidation Electrocatalysis: Rate Enhancements with HPO42- as a Proton Acceptor at pH 8. *Angew. Chem., Int. Ed.* **2014,** *53*, 12226-12230.

46. Bell, S. R.; Groves, J. T. A Highly Reactive P450 Model Compound I. *J. Am. Chem. Soc.* **2009,** *131*, 9640-9641.

47. Bakac, A. Hydrogen Atom Abstraction by Metal−Oxo and Metal−Superoxo Complexes: Kinetics and Thermodynamics. *J. Am. Chem. Soc.* **2000**, *122*, 1092-1097.

48. BAr^F_4 represents $[B[3.5\text{-}(CF_3)_2C_6H_3]_4]^-$. This anion was used preferentially over the conventional PF_6^- because of enhanced solubility and stability. $Fc[BAr^F_4]$ was synthesized using the reported procedure : Bras, J. L.; Jiao, H.; Meyer, W. E.; Hampel, F.; Gladysz, J. A. Synthesis, crystal structure, and reactions of the 17-valence-electron rhenium methyl complex $[(\eta^5\text{-}C_5Me_5)Re(NO)(P(4\text{-}C_6H_4CH_3)_3)(CH_3)][B(3,5\text{-}C_6H_3(CF_3)_2)_4]$: experimental and computational bonding comparisons with 18-electron methyl and methylidene complexes. *J. Organomet. Chem.* **2000**, *616*, 54-66.

49. Yee, G. M. Probing the Effects of Ligand Electronic Variation on the Hydrogen Atom Transfer Reactivity of the Copper(III)-Hydroxide Core. Ph. D. Dissertation, University of Minnesota, MN, 55455.

50. (a) Hall, H. K., Jr. Steric effects on the base strengths of cyclic amines. *J. Am. Chem. Soc.* **1957,** *79*, 5444-5447. (b) Hall, H. K., Jr. Correlation of the base strengths of amines. *J. Am. Chem. Soc.* **1957,** *79*, 5441-5444. (c) Kaljurand, I.;

Kuett, A.; Soovaeli, L.; Rodima, T.; Maeemets, V.; Leito, I.; Koppel, I. A. Extension of the Self-Consistent Spectrophotometric Basicity Scale in Acetonitrile to a Full Span of 28 pK_a Units: Unification of Different Basicity Scales. *J. Org. Chem.* **2005,** *70*, 1019-1028. (d) Uudsemaa, M.; Kanger, T.; Lopp, M.; Tamm, T. pKa calculation for monoprotonated bipiperidine, bimorpholine and their derivatives in H2O and MeCN. *Chem. Phys. Lett.* **2010,** *485*, 83-86.

51. Noviandri, I.; Brown, K. N.; Fleming, D. S.; Gulyas, P T..; Lay, P. A.; Masters, A. F..; Philips, L. The Decamethylferrocenium/Decamethylferrocene Redox Couple: A Superior Redox Standard to the Ferrocenium/Ferrocene Redox Couple for Studying Solvent Effects on the Thermodynamics of Electron Transfer. *J. Phys. Chem. B* **1999**, *103*, 6713-6722.

52. (a) Wiedner, E. S.; Roberts, J. A.; Dougherty, W. G.; Kassel, W. S.; Dubois, D. L.; Bullock, R. M. Synthesis and Electrochemical Studies of Cobalt(III) Monohydride Complexes Containing Pendant Amines. *Inorg. Chem.* **2013**, *52*, 9975-9988. (b) Baron, R.; Kershaw, N. M.; Donohue, T. J.; Compton, R. G. Quantitative voltammetry of the reduction of methyl benzoate in THF reveals strong ion pairing of the radical anion with tetra-*n*-butyl cations. *J. Phys. Org. Chem.* **2009**, *22*, 247-253. (c) Baron, R.; Kershaw, N. M.; Donohue, T. J.; Compton, R. G. Electrochemistry in tetrahydrofuran and at low temperature: protocol, procedures and methods. *J. Phys. Org. Chem.* **2009**, *22*, 1136-1141.

53. Hansch, C.; Leo, A.; Taft, R. W. A Survey of Hammett Substituent Constants and Resonance and Field Parameters. *Chem. Rev.* **1991**, *91*, 165-195.

54. Boaz, N. C.; Bell, S. R.; Groves, J. T. Ferryl Protonation in Oxoiron(IV) Porphyrins and Its Role in Oxygen Transfer. *J. Am. Chem. Soc.* **2015**, *137*, 2875-2885.

55. (a) Yoshida, M.; Kondo, M.; Torii, S.; Sakai, K.; Masaoka, S. Oxygen Evolution Catalyzed by a Mononuclear Ruthenium Complex Bearing Pendant SO_3^- Groups. *Angew. Chem. Int. Ed.* **2015**, *54*, 7981 –7984. (b) Duparc, V. H.; Schaper, F. Sulfonato-imino copper(II) complexes: fast and general Chan–Evans–Lam coupling of amines and anilines. *Dalton Trans*. **2017**, *46*, 12766-12770. (c) Duparc, V. H.; Schaper, F. Sulfonato-diketimine Copper(II) Complexes: Synthesis and Application as Catalysts in Chan−Evans−Lam Couplings. *Organometallics* **2017**, *36*, 3053−3060.

56. Kanetani, F.; Yamaguchi, H. Studies of Reactions of Amines with Sulfur Trioxide (VI). Thermal Reactions of Anilinium, Dimethylanilinium, and Trimethylanilinium salts of Butylamidosulfuric Acid. *Bull. Chem. Soc. Jpn*. **1981**, *54*, 3048-3058.

57. Taylor, R.; Kennard, O.; Versichel, W. Geometry of the N-H-O=C Hydrogen Bond. 2. Three-Center ("Bifurcated") and Four-Center ("Trifurcated") Bonds. *J. Am. Chem. Soc.* **1984**, *106*, 244-248.

58. Spaeth, A. D.; Gagnon, N. L.; Dhar, D.; Yee, G. M.; Tolman, W. B. Determination of the Cu(III)-OH Bond Distance by Resonance Raman Spectroscopy Using a Normalized Version of Badger's Rule. *J. Am. Chem. Soc.* **2017**, *139*, 4477-4485.

59. Murata, M.; Kojima, M.; Kita, M.; Kashino, S.; Yoshikawa, Y. A Stable Sulfonato-Cobalt(III) Complex : Δ-[Co{$OS(O)_2CH_2CH_2NH_2$-*N*,*O*}$(en)_2$]-$(ClO_4)_2$. *Acta. Cryst*. **1997**,*C53*,1761-1762.

60. Yokota, S.; Tachi, Y.; Nishiwaki, N.; Ariga, M.; Itoh, S. A New β-Diketiminate Ligand Carrying a Functional Group on the Carbon Framework. Synthesis and

Characterization of a Linear Polymeric Copper(I) Complex. *Inorg. Chem.* **2001,** *40*, 5316-5317.

61. (a) Shannon, R. D. Revised effective ionic radii and systematic studies of interatomic distances in halides and chalcogenides. *Acta. Cryst.* **1976**, *A32*, 751-767. (b) Marcus, Y. Ionic radii in aqueous solutions. *Chem. Rev.* **1988,** *88*, 1475-1498.

62. (a) Bales, B. L.; Peric, M. EPR Line Shifts and Line Shape Changes Due to Spin Exchange of Nitroxide Free Radicals in Liquids. *J. Phys. Chem. B* **1997,** *101*, 8707-8716. (b) Bales, B. L.; Meyer, M.; Smith, S.; Peric, M. EPR Line Shifts and Line Shape Changes due to Spin Exchange of Nitroxide Free Radicals in Liquids: 6. Separating Line Broadening due to Spin Exchange and Dipolar Interactions. *J. Phys. Chem. A* **2009,** *113*, 4930-4940.

63. Connelly, N. G.; Geiger, W. E. Chemical Redox Agents for Organometallic Chemistry. *Chem. Rev.* **1996,** *96*, 877-910.

64. (a) Shen, J.; Wang, M.; Zhang, P.; Jiang, J.; Sun, L. Electrocatalytic water oxidation by copper(II) complexes containing a tetra- or pentadentate amine-pyridine ligand. *Chem. Commun.* **2017,** *53*, 4374-4377. (b) Garrido-Barros, P.; Funes-Ardoiz, I.; Drouet, S.; Benet-Buchholz, J.; Maseras, F.; Llobet, A. Redox Non-innocent Ligand Controls Water Oxidation Overpotential in a New Family of Mononuclear Cu-Based Efficient Catalysts. *J. Am. Chem. Soc.* **2015,** *137*, 6758-6761. (c) Yu, F.; Li, F.; Hu, J.; Bai, L.; Zhu, Y.; Sun, L. Electrocatalytic water oxidation by a macrocyclic Cu(II) complex in neutral phosphate buffer. *Chem. Commun.* **2016,** *52*, 10377-10380. (d) Fu, L.-Z.; Fang, T.; Zhou, L.-L.; Zhan, S.-Z. A mononuclear copper electrocatalyst for both water reduction and oxidation. *RSC Adv.* **2014,** *4*, 53674-53680.

65. (a) Costentin, C.; Robert, M.; Saveant, J.-M. Concerted Proton-Electron Transfers: Electrochemical and Related Approaches. *Acc. Chem. Res.* **2010,** *43*, 1019-1029. (b) Costentin, C.; Robert, M.; Saveant, J.-M.; Tard, C. Breaking Bonds with Electrons and Protons. Models and Examples. *Acc. Chem. Res.* **2014,** *47*, 271-280.

66. (a) Usharani, D.; Lacy, D. C.; Borovik, A. S.; Shaik, S. Dichotomous Hydrogen Atom Transfer vs. Proton-Coupled Electron Transfer During Activation of X-H Bonds (X = C, N, O) by Nonheme Iron-Oxo Complexes of Variable Basicity. *J. Am. Chem. Soc.* **2013,** *135*, 17090-17104.

67. (a) Minnihan, E. C.; Nocera, D. G.; Stubbe, J. Reversible, long-range radical transfer in E. coli class Ia ribonucleotide reductase. *Acc. Chem. Res.* **2013,** *46*, 2524-2535. (b) McEvoy, J. P.; Brudvig, G. W. Water-splitting chemistry of photosystem II. *Chem. Rev.* **2006,** *106*, 4455-4483. (c) Kaila, V. R. I.; Verkhovsky, M. I.; Wikstrom, M. Proton-Coupled Electron Transfer in Cytochrome Oxidase. *Chem. Rev.* **2010,** *110*, 7062-7081. (d) Yoshikawa, S.; Shimada, A. Reaction Mechanism of Cytochrome c Oxidase. *Chem. Rev.* **2015,** *115*, 1936-1989.

68. Bordwell, F. G.; Cheng, J. Substituent effects on the stabilities of phenoxyl radicals and the acidities of phenoxyl radical cations. *J. Am. Chem. Soc.* **1991,** *113*, 1736-1743.

69. Olis GlobalWorks 3D Analysis Software. For illustrative references see (a) Ma, Z.; Williamson, H.R.; Davidson, V.L. Roles of multiple-proton transfer pathways and proton-coupled electron transfer in the reactivity of the *bis*-Fe^{IV} state of MauG. *Proc. Natl. Acad. Sci.* **2015**, *112*, 10896-10901. (b) DeSa, R. J.; Matheson, I. B. C. A Practical Approach to Interpretation of Singular Value

Decomposition Results. *Meth. Enzymol.* **2004**, *384*, 1-8. (c) Henry, E. R.; Hofrichter, J. Singular value decomposition: Application to analysis of experimental data. *Meth. Enzymol.* **1992**, *210*, 129-192. (d) Sreerama, N.; Venyaminov, S. Y.; Woody, R. W. Analysis of Protein Circular Dichroism Spectra Based on the Tertiary Structure Classification. *Anal. Biochem.* **2001**, *299*, 271-274.

70. Osako, T.; Ohkubo, K.; Taki, M.; Tachi, Y.; Fukuzumi, S.; Itoh, S. Oxidation Mechanism of Phenols by Dicopper-Dioxygen (Cu_2/O_2) Complexes. *J. Am. Chem. Soc.* **2003,** *125*, 11027-11033.

71. Eyer, P.; Lengfelder, E. Radical formation during autoxidation of 4-dimethylaminophenol and some properties of the reaction products. *Biochem. Pharmacol.* **1984,** *33*, 1005-1013.

72. Miller, L. L.; Stewart, R. F.; Gillespie, J. P.; Ramachandran, V.; So, Y. H.; Stermitz, F. R. Synthesis of morphinandienones, a dihydrophenathrone, and Pummerer's ketones by anodic coupling. *J. Org. Chem.* **1978,** *43*, 1580-1586.

73. (a) Esguerra, K. V. N.; Fall, Y.; Lumb, J.-P. A Biomimetic Catalytic Aerobic Functionalization of Phenols. *Angew. Chem., Int. Ed.* **2014,** *53*, 5877-5881. (b) Askari, M. S.; Esguerra, K. V. N.; Lumb, J.-P.; Ottenwaelder, X. A Biomimetic Mechanism for the Copper-Catalyzed Aerobic Oxygenation of 4-tert-Butylphenol. *Inorg. Chem.* **2015,** *54*, 8665-8672.

74. (a) Verma, P.; Pratt, R. S.; Storr, T.; Wasinger, E. C.; Stack, T. D. P. Sulfanyl stabilization of copper-bonded phenoxyls in model complexes and galactose oxidase *Proc. Natl. Acad. Sci.* **2011**, *108*, 8600-18605. (b) Jazdzewski, B. A.; Holland, P. L.; Pink, M.; Young, V. G.; Spencer, D. J. E.; Tolman, W. B. Three-Coordinate Copper(II)−Phenolate Complexes *Inorg. Chem.* **2001,** *40*, 6097-6107.

(c) Jazdzewski, B. A.; Tolman, W. B. Understanding the copper–phenoxyl radical array in galactose oxidase: contributions from synthetic modeling studies *Coord. Chem. Rev.* **2000,** *200–202*, 633-685.

75. Suksai, C.; Tuntulani, T. Chromogenic anion sensors. *Chem. Soc. Rev.* **2003,** *32*, 192-202.

76. For a representative EPR spectrum of [Fc][BF_4] see Bew, S. P.; Cheesman, M. R.; Sharma, S. V. Ferrocenium salts mediate para-tert-butylcalixarene synthesis *Chem. Commun.* **2008**, *44*, 5731-5733.

77. Neta, P.; Grodlowski, J. Rate Constants for Reactions of Phenoxyl Radicals in Solution. *J. Phys. Chem. Ref. Data* **2005**, *34*, 109-199.

78. (a) Wijeratne, G. B.; Day, V. W.; Jackson, T. A. O-H bond oxidation by a monomeric Mn^{III}-OMe complex. *Dalton Trans.* **2015,** *44*, 3295-3306. (b) Wijeratne, G. B.; Corzine, B.; Day, V. W.; Jackson, T. A. Saturation Kinetics in Phenolic O-H Bond Oxidation by a Mononuclear Mn(III)-OH Complex Derived from Dioxygen. *Inorg. Chem.* **2014,** *53*, 7622-7634. (c) Rice, D. B.; Wijeratne, G. B.; Burr, A. D.; Parham, J. D.; Day, V. W.; Jackson, T. A. Steric and Electronic Influence on Proton-Coupled Electron-Transfer Reactivity of a Mononuclear Mn(III)-Hydroxo Complex. *Inorg. Chem.* **2016,** *55*, 8110-8120. (d) Mader, E. A.; Mayer, J. M. The Importance of Precursor and Successor Complex Formation in a Bimolecular Proton−Electron Transfer Reaction. *Inorg. Chem.* **2010**, *49*, 3685-3687. (e) Miyazaki, S.; Kojima, T.; Mayer, J. M.; Fukuzumi, S. Proton-Coupled Electron Transfer of Ruthenium(III)-Pterin Complexes: A Mechanistic Insight. *J. Am. Chem. Soc.* **2009,** *131*, 11615-11624.

79. (a) Snelgrove, D. W.; Lusztyk, J.; Banks, J. T.; Mulder, P.; Ingold, K. U. Kinetic Solvent Effects on Hydrogen-Atom Abstractions: Reliable, Quantitative

Predictions via a Single Empirical Equation for. *J. Am. Chem. Soc.* **2001,** *123,* 469-477. (b) Nielsen, M. F.; Ingold, K. U. Kinetic Solvent Effects on Proton and Hydrogen Atom Transfers from Phenols. Similarities and Differences. *J. Am. Chem. Soc.* **2006,** *128,* 1172-1182. (c) Litwinienko, G.; Ingold, K. U. Solvent Effects on the Rates and Mechanisms of Reaction of Phenols with Free Radicals. *Acc. Chem. Res.* **2007,** *40,* 222-230. (d) Jha, M.; Pratt, D. A. Kinetic solvent effects on peroxyl radical reactions. *Chem. Commun.* **2008**, 1252-1254. (e) Valgimigli, L.; Banks, J. T.; Ingold, K. U.; Lusztyk, J. Kinetic Solvent Effects on Hydroxylic Hydrogen Atom Abstractions Are Independent of the Nature of the Abstracting Radical. Two Extreme Tests Using Vitamin E and Phenol. *J. Am. Chem. Soc.* **1995,** *117,* 9966-9971.

80. Abraham, M. H.; Grellier, P. L.; Prior, D. V.; Duce, P. P.; Morris, J. J.; Taylor, P. J. Hydrogen bonding. Part 7. A scale of solute hydrogen-bond acidity based on log K values for complexation in tetrachloromethane. *J. Chem. Soc., Perkin Trans. 2* **1989**, 699-711.

81. (a) Nomrowski, J.; Wenger, O. S. Photoinduced PCET in Ruthenium-Phenol Systems: Thermodynamic Equivalence of Uni- and Bidirectional Reactions. *Inorg. Chem.* **2015,** *54,* 3680-3687. (b) Kundu, S.; Miceli, E.; Farquhar, E. R.; Ray, K. Mechanism of phenol oxidation by heterodinuclear Ni Cu bis(μ-oxo) complexes involving nucleophilic oxo groups. *Dalton Trans.* **2014,** *43,* 4264-4267.

82. Sjödin, M.; Styring, S.; Wolpher, J.; Xu, Y.; Sun, L.; Hammarström, L. Switching the Redox Mechanism: Models for Proton-Coupled Electron Transfer from Tyrosine and Tryptophan *J. Am. Chem. Soc.* **2005**, *127,* 3855-3863.

83. Costentin, C.; Louault, C.; Robert, M.; Saveant, J.-M. The electrochemical approach to concerted proton-electron transfers in the oxidation of phenols in water. *Proc. Natl. Acad. Sci.* **2009,** *106*, 18143-18148.

84. (a) El-Samanody, E.-S.; Demadis, K. D.; Meyer, T. J.; White, P. S. Reversible Osmium(VI) Nitrido to Osmium(II) Ammine Interconversion in Complexes Containing Polypyrazolyl Ligands. *Inorg. Chem.* **2001,** *40*, 3677-3686. (b) Lebeau, E. L.; Binstead, R. A.; Meyer, T. J. Mechanistic Implications of Proton Transfer Coupled to Electron Transfer. *J. Am. Chem. Soc.* **2001,** *123*, 10535-10544.

85. (a) Lee, J. Y.; Peterson, R. L.; Ohkubo, K.; Garcia-Bosch, I.; Himes, R. A.; Woertink, J.; Moore, C. D.; Solomon, E. I.; Fukuzumi, S.; Karlin, K. D. Mechanistic Insights into the Oxidation of Substituted Phenols via Hydrogen Atom Abstraction by a Cupric–Superoxo Complex. *Journal of the American Chemical Society* **2014,** *136*, 9925-9937. (b) Kotani, H.; Kaida, S.; Ishizuka, T.; Sakaguchi, M.; Ogura, T.; Shiota, Y.; Yoshizawa, K.; Kojima, T. Formation and characterization of a reactive chromium(V)-oxo complex: mechanistic insight into hydrogen-atom transfer reactions. *Chem. Sci.* **2015,** *6*, 945-955.

86. Warren, J. J.; Mayer, J. M. Proton-Coupled Electron Transfer Reactions at a Heme-Propionate in an Iron-Protoporphyrin-IX Model Compound. *J. Am. Chem. Soc.* **2011,** *133*, 8544-8551.

87. Kretchmer, J. S.; Miller, T. F. Tipping the Balance between Concerted versus Sequential Proton-Coupled Electron Transfer. *Inorg. Chem.* **2016,** *55*, 1022-1031.

88. Audier, H. E.; Bouchoux, G.; Mourgues, P.; Penaud-Berruyer, F. Proton and hydrogen atom transfers between ionized enols and neutral aldehydes. *Org. Mass Spectrom.* **1992,** *27*, 439-442.

89. Seim, K. L; Obermeyer. A. C.; Francis, M. B. Oxidative Modification of Native Protein Residues Using Cerium(IV) Ammonium Nitrate *J. Am. Chem. Soc.*, 2011, **133**, 16970–16976.

90. Manner, V. W.; Markle, T. F.; Freudenthal, J. H.; Roth, J. P.; Mayer, J. M. The first crystal structure of a monomeric phenoxyl radical: 2,4,6-tri-tert-butylphenoxyl radical. *Chem. Commun.* **2008**, 256-258.

91. (a) Whittaker, J. W. Free Radical Catalysis by Galactose Oxidase. *Chem. Rev.* **2003,** *103*, 2347-2364. (b) Lyons, C. T.; Stack, T. D. P. Recent advances in phenoxyl radical complexes of salen-type ligands as mixed-valent galactose oxidase models. *Coord. Chem. Re*v. **2013**, *257*, 528–540. (c) Shimazaki, Y. Recent Advances in X-Ray Structures of Metal-Phenoxyl Radical Complexes. *Adv. Mater. Phys. Chem.* **2013**, *3*, 60-71. (d) Itoh, S.; Taki, M.; Fukuzumi, S. Active site models for galactose oxidase and related enzymes. *Coord. Chem. Rev.* **2000,** *198*, 3-20. (e) Thomas, F. Ten Years of a Biomimetic Approach to the Copper(II) Radical Site of Galactose Oxidase. *Eur. J. Inorg. Chem.* **2007,** *2007*, 2379-2404.

92. (a) Kaim, W. The chemistry and biochemistry of the copper–radical interaction *Dalton Trans.* **2003**, *0*, 761-768. (b) Shimazaki, Y. Properties of the one-electron oxidized copper(II) salen-type complexes: relationship between electronic structures and reactivities. *Pure Appl. Chem.* **2014**, *86*, 163–172. (c) Shimazaki, Y.; Yamauchi O. Recent Advances in Metal-Phenoxyl Radical Chemistry. *Indian J. Chem.* **2011**, *50A*, 383-394.

93. (a) Kaim, W.; Schwederski, B. Non-innocent ligands in bioinorganic chemistry—An overview *Coord. Chem. Rev.* **2010**, *254*, 1580–1588. (b) Luca, O. R.; Crabtree, R. H. Redox active ligands in catalysis. *Chem. Soc. Rev.*, **2013**, *42*,

1440-1459. (c) Chirik, P. J.; Wieghardt, K. Radical ligands confer nobility on base metal catalysts. *Science* **2010**, *327*, 794–795.

94. (a) Storr, T.; Verma, P.; Pratt, R. C.; Wasinger, E. C.; Shimazaki, Y.; Stack, T. D. P. Defining the Electronic and Geometric Structure of One-Electron Oxidized Copper−Bis-phenoxide Complexes. *J. Am. Chem. Soc.* **2008**, *130*, 15448–15459. (b) Chiang, L.; Herasymchuk, K.; Thomas, F.; Storr, T. Influence of Electron-Withdrawing Substituents on the Electronic Structure of Oxidized Ni and Cu Salen Complexes. *Inorg. Chem.* **2015**, *54*, 5970−5980.

95. Thomas, F. Ligand-centered oxidative chemistry in sterically hindered salen complexes: an interesting case with nickel. *Dalton Trans.* **2016,** *45*, 10866-10877.

96. Neisen, B. D.; Gagnon, N. L.; Dhar, D.; Spaeth, A. D.; Tolman, W. B. Formally Copper(III)-alkylperoxo complexes as models of possible intermediates in Monooxygenase enzymes. *J. Am. Chem. Soc.* **2017**, *139*, 10220-10223.

97. Neisen, B. D.; Solntsev, P. V.; Halvagar, M. R.; Tolman, W. B. Secondary Sphere Hydrogen Bonding in Monocopper Complexes of Potentially Dinucleating Bis(carboxamide) Ligands *Eur. J. Inorg. Chem.* **2015**, *2015*, 5856−5863.

98. (a) Halfen, J. A.; Jazdzewski, B. A.; Mahapatra, S.; Berreau, L. M.; Wilkinson, E. C.; Que, L., Jr.; Tolman, W. B. Synthetic Models of the Inactive Copper(II)−Tyrosinate and Active Copper(II)−Tyrosyl Radical Forms of Galactose and Glyoxal Oxidases. *J. Am. Chem. Soc.*, **1997**, *119*, 8217-8227. (b) Sokolowski, A.; Leutbecher, H.; Weyhermuller, T.; Schnepf, R.; Bothe, E.; Bill, E.; Hildebrandt, P.; Wieghardt, K. Phenoxyl-copper(II) complexes: models for the active site of galactose oxidase. *J. Biol. Inorg. Chem.* **1997**, *2*, 444-453.

99. (a) Bleaney, B.; Bowers, K. D. Anomalous paramagnetism of copper acetate. *Proc. Royal Soc. London.***1952,** *214*, 451-465. (b) Kahn, O. Dinuclear Complexes with Predictable Magnetic Properties. *Angew. Chem. Int. Ed* **1985,** *24*, 834-850.

100. (a) Ghosh, S.; Cirera, J.; Vnace, M. A.; Ono, T.; Fujisawa, K.; Solomon, E. I. Spectroscopic and Electronic Structure Studies of Phenolate Cu(II) Complexes: Phenolate Ring Orientation and Activation Related to Cofactor Biogenesis. *J. Am. Chem. Soc.*, **2008**, 130, 16262–16273. (b) Jazdzewski, B. A.; Holland, P. L.; Pink, M.; Young, V. G., Jr.; Spencer, D. J. E.; Tolman, W. B. Three-Coordinate Copper(II)−Phenolate Complexes. *Inorg. Chem.* **2001**, *40*, 6097-6107. (c) Que, L. J. In *Biological Applications of Raman Spectroscopy*; Wiley: New York, 1988; Vol. 3, p 491. (d) Schnepf, R.; Sokolowski, A.; Müller, J.; Bachler, V.; Wieghardt, K.; Hildebrandt, P. Resonance Raman Spectroscopic Study of Phenoxyl Radical Complexes. *J. Am. Chem. Soc.* **1998,** *120*, 2352-2364. (e) Mukherjee, A.; McGlashen, M. L.; Spiro, T. G. Ultraviolet Resonance Raman Spectroscopy and General Valence Force Field Analysis of Phenolate and Phenoxyl Radical. *J. Phys. Chem.* **1995,** *99*, 4912-4917.

101. (a) Whittaker, M. M.; Whittaker, J. W. The active site of galactose oxidase. *J. Biol. Chem.* **1988**, *263*, 6074-6080. (b) Whittaker, M. M.; DeVito, V. L.; Asher, S. A.; Whittaker, J. W. Resonance Raman evidence for tyrosine involvement in the radical site of galactose oxidase. *J. Biol. Chem.* **1989**, *264*, 7104-7106. (c) McGlashen, M. L.; Eads, D. D.; Spiro, T. G.; Whittaker, J. W. Resonance Raman Spectroscopy of Galactose Oxidase: A New Interpretation Based on Model Compound Free Radical Spectra *J. Phys. Chem.* **1995**, *99*, 4918-4922.

102. Mascharak, P. K.; Armstrong, W. H.; Mizobe, Y.; Holm, R. H. Single cubane-type MFe_3S_4 clusters (M = Mo, W): synthesis and properties of oxidized and

reduced forms and the structure of $(Et_4N)_3[MoFe_3S_4(S\text{-}p\text{-}C_6H_4Cl)_4(3,6\text{-}(C_3H_5)_2C_6H_2O_2)]$. *J. Am. Chem. Soc.* **1983,** *105,* 475-483.